AKADEMIA GÓRNICZO-HUTNICZA IM. STANISŁAWA STASZICA W KRAKOWIE

DZIEDZINA NAUK ŚCISŁYCH I PRZYRODNICZYCH

DYSCYPLINA NAUKI FIZYCZNE

ROZPRAWA DOKTORSKA

Spinowa magnetorezystancja i spinowy efekt Halla w cienkowarstwowych układach hybrydowych: metal ciężki, ferromagnetyk, antyferromagnetyk

Autor: Krzysztof Grochot

Promotorzy rozprawy: prof. dr hab. Tomasz Stobiecki
prof. dr hab. Nika Spiridis

Praca wykonana w Akademii Górniczo-Hutniczej im. Stanisława Staszica w Krakowie

Wydział Fizyki i Informatyki Stosowanej AGH

Kraków, 2023

AGH UNIVERSITY OF SCIENCE AND TECHNOLOGY

FIELD OF NATURAL SCIENCES

SCIENTIFIC DISCIPLINE PHYSICAL SCIENCES

DOCTORAL THESIS

Spin Hall Magnetoresistance and Spin Hall effect in heavy metal, ferromagnet, antiferromagnet hybrid structures

Author: Krzysztof Grochot

Supervisors: prof. dr hab. Tomasz Stobiecki
prof. dr hab. Nika Spiridis

Completed in AGH University of Science and Technology,

Faculty of Physics and Applied Computer Science

Kraków, 2023

AGH UNIVERSITY OF SCIENCE AND TECHNOLOGY

WWW.AGH.EDU.PL

First edition, May 16, 2023

AGH University of Science and Technology

Declaration

(a) Authenticity of Dissertation

I hereby declare that I am the legitimate author of this Dissertation and that it is my original work.
No portion of this work has been submitted in support of an application for another degree or qualification of this or any other university or institution of higher education.
I hold the AGH University of Science and Technology harmless against any third party claims with regard to copyright violation, breach of confidentiality, defamation and any other third party right infringement.

(b) Declaration of the thesis Supervisors

This dissertation is ready to be reviewed.

Acknowledgements

I would like to express my sincere gratitude to all the people who supported me throughout my dissertation journey. First and foremost, I would like to thank my supervisors: *Prof. dr hab. Nika Spiridis* for introducing me to surface physics and providing valuable advice during synchrotron measurements and *prof. dr hab. Tomasz Stobiecki* for their invaluable guidance, feedback, and encouragement and for introducing me to the world of spintronics and magnetism. They always challenged me to think critically and creatively and inspired me to pursue excellence in my research.

I am deeply grateful to *dr hab. inż. Witold Skowroński, prof. AGH* for sharing his knowledge and experience and insight into experimental techniques.

I would like to especially thank *dr inż. Piotr Ogrodnik* and *dr Łukasz Karwacki* for supporting my research with theoretical models, their constructive comments, and good advice.

I would like to express my thank to *dr Piotr Mazalski* for magnetooptical microscopy images and inspiring scientific discussions.

I am indebted to my fellow researchers and friends: *dr inż. Stanisław Łazarski*, *dr inż. Sławomir Ziętek*, *mgr inż. Jakub Mojsiejuk*, *mgr inż. Piotr Rzeszut*, *dr hab. Jarosław Kanak*, *dr hab. Maciej Czapkiewicz*, *M.Sc. Wiesław Powroźnik*, *dr inż. Jakub Chęciński* and *dr inż. Monika Cecot* for their collaboration, camaraderie, and moral support. They made this journey more enjoyable and less stressful. I learned a lot from them and had fun working with them.

The nanofabrication processes were supported by research infrastructure from the Academic Center for Materials and Nanotechnology AGH.

This PhD thesis has been completed in the framework of the Program POWER, project No. POWR.03.02.00-00-I004/16, co-financed by the European Union. The research was funded by National Science Center Grant SPINORBITRONICS, No. UMO-2016/23/B/ST3/01430.

Finally, I would like to dedicate this work to my wife *Klaudia*, for her endless support and patience. Without her, I would not be where I am today.

Abstract

The development of new, energy-efficient storage and data processing based on electron spin is attracting widespread interest from the perspective of potential applications in so-called green IT. Heavy metals (HMs) demonstrating strong spin-orbital couplings, such as Pt and W, are being explored for use as sources of spin current. The spin current-generated spin-orbit torque (SOT) can switch the perpendicular magnetization of a ferromagnetic (FM) layer in an external magnetic field collinear to the current, but this significantly limits its practical application. The solution to this problem is to use an antiferromagnet (AFM) layer, which, due to exchange bias coupling, can break the spatial symmetry of the system and makes it possible to switch the current magnetization of the ferromagnet without an external magnetic field. The dissertation describes contributions to the experimental investigation of thin-film spintronic heterostructures of the heavy metal (HM)/FM, FM/HM/FM, and HM/FM/AFM types characterized by significant spin-orbital interactions. This thesis is based on four papers previously published in well-known scientific journals listed in the JCR database and one under preparation, in which the Author was the main experimenter.

The work is divided into two main parts, including a theoretical introduction and a discussion of the conducted experiments. The first part discusses the theoretical basis of the phenomena observed in the experiment, such as galvanomagnetic effects and effects related to spin-orbital interactions such as spin Hall magnetoresistance (SMR), current induced magnetization switching (CIMS), spin orbit coupling (SOC) in HMs, spin Hall effect (SHE), and exchange bias (ExB) interaction.

The experimental part begins with a description of the study of the HM/FM bilayer system using a series of samples in which the HM role was mainly W, Pt, and Au. At the same time, the FM layer was Co and CoFeB. The chapter discusses the results of determining the SMR and anisotropic magnetoresistance (AMR) contribution to magnetoresistance using the theoretical spin diffusion model. Next, we examine the spin Hall angle (SHA) as a function of t_{Pt} in Pt(t_{Pt})/CoFeB(2) and $[\mathrm{Pt}(\mathrm{t_{Pt}}) - \mathrm{Ti}(0.2)]_{\mathrm{m}}$ /Pt/CoFeB(2) systems (numbers in parentheses denote thickness in nanometers, m indicates number of the interface of the Pt-Ti superlattice). Finally, we analyze the shape of the current switching loop in the Pt(4)/ Co(1)/MgO(2) system using the phenomenological model considering the effect of Dzyaloshinskii–Moriya interaction (DMI).

Then we focused on the trilayer Co(1)/Pt(0- 4)/Co(1) system, where the magnetization dynamics of the Co layers, anomalous Hall effect (AHE) hysteresis loops, and spin-orbit interaction are discussed. Variable Pt thickness enables effective tuning of the ferromagnetic interlayer exchange coupling (IEC). Spin Hall magnetoresistance (SMR) and anisotropic magnetoresistance (AMR) effects were analyzed based on the spin diffusion model. The effective SOT field (field-like (H_{FL}) and damping-like (H_{DL})) and the effective SHA as a function of the thickness of

Pt were determined and analyzed. The experimental results were compared with the predictions of the spin diffusion model. The asymmetry of Co/Pt and Pt/Co interfaces, IEC, and domain structure, enables both to achieve multilevel CIMS, potentially important for SOT memory applications.

The last section discusses the experimental results of SOT-induced CIMS in Pt(W)/Co/NiO heterostructures with varying thicknesses of W and Pt layers, a perpendicularly magnetized Co layer, and an antiferromagnetic NiO layer. Using magnetization current switching, magnetoresistance measurements, and the AHE, the perpendicular and plane components of the ExB were determined. An analytical model of the critical switching current as a function of HM thickness was then fitted to the obtained results for several nanodevices from both systems. As a result, the effective SHA and the effective perpendicular anisotropy were determined. In addition, the dependence of SMR as a function of Pt thickness was reproduced by fitting the theoretical model to the experimental data. Measurements by the field harmonic method allowed us to determine the SHA as a function of HM thickness in Pt(W)/Co(0.7)/NiO systems.

In addition, technologies for fabricating Hall bar devices by optical lithography are discussed, and methods for determining the SHA by angular and field harmonic methods are demonstrated, as well as the scheme of magnetization current switching experiments and methods of magnetoresistive measurements.

Streszczenie

Opracowanie nowych, energooszczędnych technologii przechowywania i przetwarzania informacji w oparciu o spin elektronu wzbudza szerokie zainteresowanie z punktu widzenia potencjalnych zastosowań w obszarze enerooszczędnych pamięci elektronicznych wpisujących się w trend tzw. Green IT. Metale ciężkie (HM), wykazujące silne sprzężenie spinowo-orbitalne, takie jak Pt i W, są badane pod kątem wykorzystania ich jako źródła prądu spinowego. Wygenerowany prądem spinowym spinowo-orbitalny moment siły (SOT) jest w stanie przełączyć prostopadłe namagnesowanie warstwy ferromagnetycznej (FM) w zewnętrznym polu magnetycznym współliniowym z prądem, co jednak znacznie ogranicza praktyczne jego zastosowanie. Odpowiedzią na ten problem jest zastosowanie warstwy antyferromagnetycznej (AFM), która dzięki wymiennemu interfejsowemu sprzężeniu z warstwą ferromagnetyczną (tzw. exchange bias) jest w stanie złamać symetrię przestrzenną układu i umożliwić przełączenie prądowe magnetyzacji ferromagnetyka bez zewnętrznego pola magnetycznego. Praca opisuje eksperymentalne badania cienkowarstwowych heterostruktur spintronicznych typu HM/FM, FM/HM/FM oraz HM/FM/AFM charakteryzujących się znacznym oddziaływaniem spinowo-orbitalnych. Niniejsza rozprawa opiera się na czterech pracach opublikowanych wcześniej w czasopismach naukowych z listy JCR oraz jednej, która jest w przygotowaniu, w których Autor był głównym pomysłodawcą i wykonawcą podstawowych eksperymentów.

Praca podzielona jest na dwie główne części, w skład których wchodzą wprowadzenie teoretyczne oraz opis i dyskusja przeprowadzonych badań. W części pierwszej omówiono teoretyczne podstawy zjawisk obserwowanych w eksperymencie takich jak efekty galwanomagnetyczne oraz efekty związane z oddziaływaniami spinowo-orbitalnymi jak chociażby sprzężenie spinowo-orbitalne w metalach ciężkich, spinowy efekt Halla, spinowo-orbitalny moment siły oraz oddziaływanie exchange bias. Część eksperymentalną rozpoczyna opis badań układu biwarstwowego HM/FM na przykładzie szeregu próbek, w których rolę metalu ciężkiego pełniły głównie W, Pt i Au, natomiast warstwę ferromagnetyczną stanowił Co i stop CoFeB. W rozdziale tym zostały omówione wyniki badania spinowej magnetorezystancji (SMR) i anizotropowej magnetorezystancji (AMR) wraz z analizą danych eksperymentalnych z wykorzystaniem teoretycznego dyfuzyjnego modelu prądu spinowego wyznaczono udziały SMR i AMR w wypadkowej magnetorezystancji. Dodatkowo wyznaczono efektywne kąty Halla w funkcji grubości Pt w układach Pt(t_{Pt})/CoFeB(2) i $[\mathrm{Pt}(\mathrm{t_{Pt}}) - \mathrm{Ti}(0.2)]_{\mathrm{m}}$/Pt/CoFeB(2) (liczby w nawiasach podają grubości warstw w nanometrach, m jest liczbą interfejsów). Przeanalizowano także kształt pętli przełączania prądowego w układzie Pt(4)/Co(1)/MgO(2) za pomocą modelu fenomenologicznego z uwzględnieniem efektu DMI.

Następnie skupiono się na układzie trójwarstwowym Co(1)/Pt(0-4)/Co(1), gdzie

omówiona została dynamika namagnesowania warstw Co, właściwości magnetostatycznego przemagnesowania z pętli anomalnego efektu Halla AHE oraz oddziaływanie spinowo-orbitalne. Zmienna grubość Pt umożliwia efektywne dostrojenie ferromagnetycznego w sprzenia wymiennego (IEC). Efekty SMR i AMR analizowano w oparciu o model dyfuzyjnego transportu spinowego. Wyznaczono i przeanalizowano efektywne pole SOT (field-like (H_{FL}) i damping-like (H_{DL})) oraz efektywny spinowy kąt Halla w funkcji grubości Pt. Wyniki eksperymentalne zostały porównane z teoretycznymi obliczeniami modelu transportu spinowego.
Asymetria obu interfejsów: dolnego Co/Pt i górnego Pt/Co, oraz obecność IEC umożliwiają uzyskanie wielopoziomowego przełączania prądowego magnetyzacji, mającego potencjalne zastosowanie w pamięciach SOT.

W ostatnim podrozdziale omówiono wyniki eksperymentalne przełączania prądowego magnetyzacji indukowanego przez SOT w heterostrukturach Pt(W)/Co/NiO o zmiennej grubości warstw W i Pt, prostopadle namagnesowanej warstwie Co oraz antyferromagnetycznej warstwie NiO. Wykorzystując przełączanie prądowe magnetyzacji, pomiary magnetorezystacji oraz anomalny efekt Halla, wyznaczono prostopadłą i płaszczyznową składową pola exchange bias. Następnie do wyników otrzymanych dla kilku nanourządzeń z obu układów, dopasowano analityczny model krytycznego prądu przełączania w funkcji grubości metalu ciężkiego. W efekcie wyznaczono efektywny spinowy kąt Halla i efektywną anizotropię prostopadłą. Dodatkowo za pomocą dopasowania modelu teoretycznego do danych eksperymentalnych odtworzono zależność SMR w funkcji grubości Pt. Pomiary metodą harmonicznych polowych pozwoliły wyznaczyć wartości efektywnego spinowego kąta Halla w funkcji grubości HM w układach Pt(W)/Co(0.7)/NiO.

Ponadto w pracy doktorskiej omówione zostały technologie wytwarzania kompletnej heterostruktury spinowego efektu Halla metodą litografii optycznej oraz przedyskutowane zostały metody wyznaczania spinowego kąta Halla metodą harmonicznych kątowych i polowych, metody pomiarów magnetorezystancyjnych a także schemat eksperymentów przełączania prądowego magnetyzacji.

List of Publications

List of all publications with the author's contribution. The thesis is based on the publications marked in blue bold.

[P1] Ł. Karwacki, **K.Grochot**, S. Łazarski, et al. *Optimization of spin Hall magnetoresistance in heavy-metal/ferromagnetic-metal bilayers*. Sci Rep 10, 10767 (2020).
DOI: 10.1038/s41598-020-67450-3, Citations: 3, IF(2021): 4.997
KG contribution: *ideas for experimental studies of the magnetoresistance effects, fabricating Hall bar devices in the clean room, carrying out electrical measurements, experimental data processing, analyzing the results, and manuscript co-editing.*
[P2] W. Skowroński, **K. Grochot**, P. Rzeszut, et al. *Angular Harmonic Hall Voltage and Magnetoresistance Measurements of Pt/FeCoB and Pt-Ti/FeCoB Bilayers for Spin Hall Conductivity Determination.* IEEE Transactions on Electron Devices, vol. 68, no. 12, pp. 6379-6385 (2021), DOI: 10.1109/TED.2021.3122999, Citations: 1, IF(2021): 3.221
KG contribution: *nanostructurization process in clean-room of PtTi/CoFeB sample to the form of devices, performance of the harmonic data measurements and processing, manuscript co-editing.*
[P3] P. Ogrodnik, **K. Grochot**, Ł. Karwacki, et al., *Study of Spin–Orbit Interactions and Interlayer Ferromagnetic Coupling in Co/Pt/Co Trilayers in a Wide Range of Heavy-Metal Thickness.* ACS Appl. Mater. Interfaces 2021, 13, 39, 47019–47032 (2021), DOI: 10.1021/acsami.1c11675, Citations: 4, IF(2021): 10.383
KG contribution: *ideas for experimental studies of the magnetization dynamics, spin Hall magnetoresistance, and harmonic measurements, design of the device layout for magnetization switching, nanostructurization in clean-room to the form of devices, performance all electrical measurements: AHE, SD-FMR, magnetoresistance, and harmonic Hall voltage, all experimental*

data processing, cooperation in the development of theoretical models of dynamics magnetization and magnetoresistance, manuscript co-editing.

[P4] **K. Grochot**, P. Ogrodnik, P. Mazalski, et al. *Multilevel switching due to spin-orbit torques in Co/Pt/Co*, arXiv:2210.07357v1, DOI: 10.48550/arXiv.2210.07357,

KG contribution: *ideas for multilevel magnetization switching induced by current and magnetic field in a ferromagnetically coupled system, nanostructurization in clean-room to the form of devices, performance of all electrical and current-induced magnetization switching measurements, experimental data processing, developed the phenomenological domain mechanism of multilevel switching and writing draft version of the manuscript.*

[P5] **K. Grochot**, Ł. Karwacki, S. Łazarski, et al. *Current-Induced Magnetization Switching of Exchange-Biased NiO Heterostructures Characterized by Spin-Orbit Torque.* Phys. Rev. Applied 15, 014017 (2021), DOI: 10.1103/PhysRevApplied.15.014017, Citations: 8, IF(2021): 4.931

KG contribution: *ideas for fied-free CIMS using exchange bias field, design of the device layout for switching and transport measurement, nanostructurization process in clean-room, AHE, magnetoresistance and switching measurements performance, experimental data processing and fitting theoretical model, writing the draft version of the manuscript.*

[P6] S. Ziętek, J. Mojsiejuk, **K. Grochot**, et al., *Numerical model of harmonic Hall voltage detection for spintronic devices*, Phys. Rev. B 106, 024403 (2022), DOI: 10.1103/PhysRevB.106.024403, Citations: 1, IF(2021): 3.908

KG contribution: *nanostructurization process in clean-room, magnetoresistance and harmonic Hall voltage measurements performance, experimental data processing, manuscript co-editing.*

[P7] W. Skowroński, Ł. Karwacki, S. Ziętek, J. Kanak, S. Łazarski, **K. Grochot**, et al. *Determination of spin hall angle in heavy-metal/$Co-Fe-B$-based heterostructures with interfacial spin-orbit fields*, Phys. Rev. Applied 11, 024039 (2019), DOI: 10.1103/PhysRevApplied.11.024039, Citations: 27, IF(2021): 4.931

KG contribution: *nanostructurization process in clean-room, electrical measurements performance, experimental data processing, manuscript co-editing.*,

[P8] A. Kozioł-Rachwał , N. Kwiatek, W. Skowroński, **K. Grochot**, et al. *Insight into the structural and magnetotransport properties of epitaxial α-Fe2O3/Pt(111) heterostructures: Role of the reversed layer sequence*, Phys. Rev. B 106, 104419 (2022), DOI: 10.1103/PhysRevB.106.104419, Citations: 0, IF(2021): 3.908

KG contribution: *nanostructurization process in clean-room, magnetoresistance, and current-induced switching measurements, experimental data processing, manuscript co-editing.*

[P9] A. Magni, V. Basso, A. Sola, G. Soares, N. Meggiato, M. Kuepferling, W. Skowroński, S. Łazarski, **K. Grochot**, et al. *Spin Hall Magnetoresistance and Spin-Orbit Torque Efficiency in Pt/FeCoB Bilayers*, IEEE Transactions on Magnetics vol. 58, no. 2 (2022), DOI: 10.1109/TMAG.2021.3084866, Citations: 5, IF(2021): 1.848
KG contribution: *nanostructurization process in clean-room, angular harmonic Hall voltage measurements performance, angular harmonics data processing, manuscript co-editing*
[P10] S. Łazarski, W. Skowroński, **K. Grochot**, et al. *Spin-orbit torque induced magnetization dynamics and switching in a CoFeB/Ta/CoFeB system with mixed magnetic anisotropy*, Phys. Rev. B 103, 134421 (2021), DOI: 10.1103/PhysRevB.103.134421, Citations: 5, IF(2021): 3.908
KG contribution: *nanostructurization process in clean-room, electrical measurements, manuscript co-editing.*
[P11] S. Łazarski, W. Skowroński, J. Kanak, Ł. Karwacki, S. Ziętek, **K. Grochot**, et al. *Field-Free Spin-Orbit-Torque Switching in Co/Pt/Co Multilayer with Mixed Magnetic Anisotropies*, Phys. Rev. Applied 12, 014006 (2019), DOI: 10.1103/PhysRevApplied.12.014006, Citations: 28, IF(2021): 4.931
KG contribution: *nanostructurization process in clean-room, electrical measurements, manuscript co-editing.*
[P12] J. Mojsiejuk, S. Ziętek, **K. Grochot**. et al. *CMTJ: Simulation package for analysis of multilayer spintronic devices*, npj Comput Mater 9, 54 (2023), DOI: 10.1038/s41524-023-01002-x, Citations: 0, IF(2021): 12.256
KG contribution: *nanostructurization process in clean-room, FMR, current-induced magnetization switching and angular harmonics measurements, manuscript co-editing.*

Contents

List of Figures

List of Abbreviations

1

Introduction

The design of new energy-efficient data storage and processing technologies based on electron spin is of broad interest from the perspective of potential applications in so-called green information technology (IT). Heavy metals (HMs) exhibiting strong SOC, such as Pt and W, are being investigated for use as sources of spin current. A spin current-generated SOT is capable of switching the perpendicular magnetization of the FM layer in a single memory cell under an external magnetic field that is collinear with the current. This enables fast writing and reading of information in binary form, but significantly limits its practical application. To be able to realize current magnetization switching without applying an external magnetic field, it is necessary to break the inversion symmetry of the system. It may be done, for example, by using an AFM layer that induces an exchange bias field at the FM/AFM interface.

Conventional random access memory (RAM) is used as operating memory in practically all modern computers, including vast amounts in computing clusters and server centers for big data. A single cell of RAM is built from two MOS transistors, one of which plays the role of a capacitor and the other as a separating element. Due to the periodic discharge of capacitors, this type of memory requires a continuous refresh involving reading information from each cell and writing it again, generating significant access times, high power consumption, and the necessary constant power supply. It is assumed that in the broad IT industry worldwide, by 2030, between 3% and 13% of globally generated energy will be associated with the storage and sharing of information through Big Data centers [1]. These projections increase every year due to the vast and ever-growing demand for power. To solve these problems, spintronic circuits such as MRAMs or the newer generation of spin transfer torque RAM (STT-RAM) and spin-orbit torque RAM (SOT-RAM) have been looked at with hope for many years now. In the era of green IT, when great attention is paid not only to the performance of electronic devices but also to their energy efficiency, nonvolatile RAMs are becoming an excellent alternative to conventional devices. Magnetic memories do not require constant power supply and refreshing to maintain their state. The voltage (much lower than needed to power the DRAMs) is necessary only to write and read the stored information. A crucial parameter when considering the energy efficiency of RAM is the energy required to write or read information per bit. The latest generation of spin transfer torque (STT)-RAM chips will allow achieving written energy of several fJ per bit. Compared to the most widely used DDR3 1333 MHz modules, for which this oscillates around 50 pJ per bit, this is a three orders of magnitude lower.

Another area where spintronic elements may find wide application in the future is neuromorphic computing. This is the concept of creating electronic circuits that emulate the principles of the human brain. This approach aims to increase computational efficiency and reduce power consumption compared to conventional computers. Neuromorphic computing relies on two essential elements: artificial neurons and synapses, the equivalent of biological nerve cells and their connections. Artificial neurons receive input signals from other neurons and generate output signals depending on their internal state. Artificial synapses carry signals between neurons and can learn by changing the connection's strength depending on the neurons' activity. Spintronic devices are also increasingly being used as artificial synapses because they exhibit many desirable properties for neuromorphic computing. They are nonvolatile and scalable, have fast switching dynamics and low power consumption, and are compatible with standard integrated circuit technologies [2]. Today, systems using magnetic spin textures, such as domain walls or skyrmions, which are stable configurations of magnetization in FM layers, are being extensively studied. Due to their memristive behavior, magnetic spin textures can play the role of artificial neurons by using SHE to generate a spin current that can affect the movement of magnetic textures along the FM layer. If the magnetic spin texture reaches the end of the layer, it can generate a pulse (spike), which is an analogy to an action potential in biological neurons [3–7]. Today, systems using magnetic spin textures, such as domain walls or skyrmions, which are stable configurations of magnetization in FM layers, are being extensively studied.

This doctoral thesis discusses the results of researches on hybrid HM/FM bilayer thin films, FM / HM / FM trilayers, and bilayers with AFM on top of HM /FM /AFM stack. These systems can successfully find applications in many types of spintronics devices, such as low power consumption and high density magnetic RAMs like SOT-MRAM [8–11] or STT-MRAM [12–16], nanooscillators in the THz regime [17–24], or elements for neuromorphic computation, recently very popular [25, 26]. The studies focus on the characterization and comparison of SMR, SHE, and CIMS in all the types of systems mentioned above.

The dissertation is divided into five major chapters. Shortly after this *Introduction*, there is Chapter 2, which contains *Theoretical foundations* of the investigated phenomena such as *Galvanomangetic Effects in ferromagnets* (Sect. 2.1), *Spin Hall effect and Spin-Orbit Torque* (Sect. 2.2), *Current-induced magnetization switching* (Sect. 2.3), and *Exchange bias* (Sect. 2.4). Chapter 3 briefly describes the experimental methods employed. The following subsections discuss the preparation of hybrid thin films by magnetron sputtering and pulsed laser deposition (Sect. 3.1), characterization of the deposited systems using magneto-optical Kerr effect (MOKE) (Sect. 3.2), x-ray absorption spectroscopy (XAS) (Sect. 3.3) and x-ray diffraction (XRD) (Sect. 3.4). Section 3.5 describes the fabrication of nanodevices, while Sect. 3.6 discusses applied electrical detection methods. Chapter 4, which contains the most important results on the studied systems, is divided into three subsections focused on the results of SMR, SHE, and CIMS in HM/FM on the example of Pt/Co(CoFeB) and W/Co(CoFeB) systems based on the paper [P1] and Pt(t_{Pt})/CoFeB(2) and [Pt/Ti]/Pt/CoFeB(2) systems based on [P2], FM/HM/FM using the Co/Pt/Co system as an example based on the [P3, P4], and HM/FM/AFM using the W(Pt)/Co/NiO system as an example based on the paper [P5]. The Ph.D. thesis is closed by the *Summary* chapter.

2

Theoretical Foundations

The chapter discusses magnetotransport phenomena originating from the interaction between the magnetic field, magnetization, charge current, and spin current. These allow the electrical detection of spin-related effects in spintronics thin-film systems. We focus mainly on the phenomena observed in HM/FM, FM/HM/FM, and HM/FM/AFM systems when charge current flows in the presence of a magnetic field. The chapter is divided into five subsections. We begin our review with galvanomagnetic effects in ferromagnetic materials, moving on in the following subsection to describe the SHE and the SOT phenomena that are its consequence. These phenomena use CIMS described in the following subsection. The chapter ends with a discussion of the theoretical basis of exchange bias (ExB).

2.1 | Galvanomagnetic effects in ferromagnets

The charge current ($\mathbf{j_e}$) flowing through an isotropic conductor is followed by an electric field $\mathbf{E}$ defined according to Ohm's law as:

$$\mathbf{E} = \rho \mathbf{j_e}, \tag{2.1}$$

where: ρ is the resistivity and $\mathbf{j_e}$ is the current density vector.

For a thin layer of FM material placed in a magnetic field H and oriented according to the coordinate system shown in Fig.2.1, the above equation can be written as follows [27]:

$$\mathbf{E} = \rho_{\perp} \mathbf{j_e} + (\rho_{\parallel} - \rho_{\perp})\mathbf{m}(\mathbf{m} \cdot \mathbf{j_e}) + \rho_{\mathrm{H}}(\mathbf{m} \times \mathbf{j_e}), \tag{2.2}$$

where: $\rho_{\parallel}$ and $\rho_{\perp}$ is resistivity when $\mathbf{m} \parallel \mathbf{j_e}$ and $\mathbf{m} \perp \mathbf{j_e}$, respectively; ρ_{H} defines as anomalous Hall resistivity, $\mathbf{m} = \mathbf{M}/|M|$ is the magnetization unit vector whose components are: $m_{\mathrm{x}} = \sin\theta\cos\varphi$, $m_{\mathrm{y}} = \sin\theta\sin\varphi$, $m_{\mathrm{z}} = \cos\theta$.

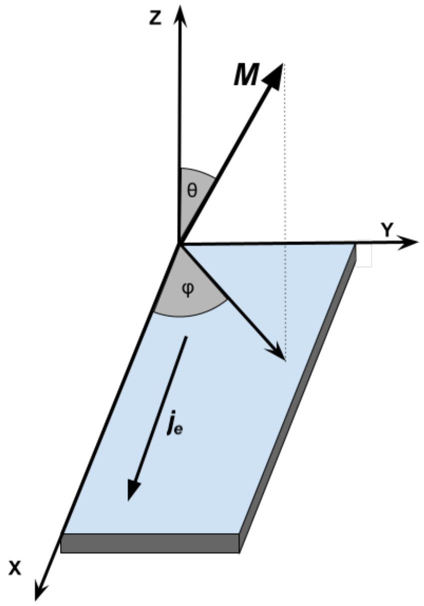

Figure 2.1: Orientation of the magnetization and current density vectors of FM thin film in the coordinate system.

For current flowing in the x direction: $\mathbf{j_e} = (j_{\mathrm{x}}, 0, 0)$, the components of the $\mathbf{E}$ vector take the form [28]:

$$E_{\mathrm{x}} = j_{\mathrm{x}}\left(\rho_{\perp} + \Delta\rho\sin^2\theta\cos^2\varphi\right), \tag{2.3}$$

$$E_{\mathrm{y}} = j_{\mathrm{x}}\left(\Delta\rho\sin^2\theta\cos\varphi\sin\varphi + \rho_{\mathrm{H}}\cos\theta\right), \tag{2.4}$$

$$E_{\mathrm{z}} = j_{\mathrm{x}}\left(\Delta\rho\sin\theta\cos\theta\sin\varphi - \rho_{\mathrm{H}}\sin\theta\sin\varphi\right) \tag{2.5}$$

where $\Delta\rho = \rho_{\parallel} - \rho_{\perp}$.

The E_{x} component determines the longitudinal magnetoresistance effect referred to as AMR discovered in 1856 by William Thomson, better known as Lord Kelvin [29]. E_{y} and E_{z} components are the transverse galvanomagnetic effects in the Hall configuration. This dissertation does not discuss Hall devices that allow measurement in the E_{z} direction.

The AMR effect is related to the energy splitting and shift in the d-orbitals because of the presence of a magnetic field, known as the Zeeman effect. Due to SOC, this effect causes a change in the charge distribution in the d-orbitals [30], leading to a variation in the resistivity of the material. The $\rho_{\|}$ is maximum when the localized d-orbitals offer maximum scattering cross section to the conducting s-electrons (s-d scattering occurs), with j $\|$ m. Instead, the $\rho_{\perp}$ is minimum when the scattering cross section is the smallest, with j $\perp$ m. Anisotropic magnetoresistance (AMR) is defined as follows:

$$AMR = \Delta\rho/\rho_{\perp} \tag{2.6}$$

The angular dependence of AMR effect can be described by the following equation in the case where magnetization lies in the plane of thin films (θ=90^o) [31]:

$$E_x = \rho_{\perp} j_{\mathrm{x}} + \Delta\rho j_{\mathrm{x}} \cos^2\varphi, \tag{2.7}$$

where φ is the angle between current and magnetization.

In the considered system, the electric field component E_{y} is given by Eq.2.4. When a thin film of a magnetic material is subjected to an in-plane magnetic field and a current flows in the x direction, Eq.2.4 describes the transverse magnetoresistance effect called planar Hall effect (PHE):

$$E_y = j_{\mathrm{x}} \Delta\rho \sin\varphi \cos\varphi. \tag{2.8}$$

In the case when the thin film is placed in a large perpendicular magnetic field H_{z} ($\theta = 0^o$), Eq.2.4 can be simplified to the following form called anomalous Hall effect (AHE):

$$E_{\mathrm{y}} = \rho_{\mathrm{H}} j_{\mathrm{x}}, \tag{2.9}$$

where anomalous Hall resistivity (ρ_H) is defined as:

$$\rho_{\mathrm{H}} = \mu_0 R_0 H + \mu_0 M_{\mathrm{S}} R_{\mathrm{S}} \tag{2.10}$$

where: R_0 is called a normal Hall coefficient and $R_{\mathrm{S}} = a\rho + b\rho^2$ is the spontaneous Hall constant. In FM materials, $R_{\mathrm{s}}/R_0 = 10^3$ [32] therefore $\mu_0 R_0 H$ term may be neglected in further considerations. a and b coefficients are related to various models of electron scattering [33], which can be classified into three categories: intrinsic, skew-scattering, and side jump. The intrinsic contribution comes from the Berry curvature term, which acts as an effective Lorentz force on electrons [34–36]. The contribution of skew scattering comes from the asymmetric scattering of electrons by impurities or phonons due to SOC [30]. The side jump contribution comes from a lateral shift of electron trajectories during scattering events due to SOC [37].

2.1.1 | Spin Hall Magnetoresistance (SMR)

SMR is a phenomenon in which a charge current ($\mathbf{j_e}$) flowing through a non-magnetic layer (e.g., a HM) generates a spin current $\mathbf{j_s} = \mathbf{j}_\uparrow - \mathbf{j}_\downarrow$ pointing toward the surface of the material, with spin polarization σ perpendicular to both the $\mathbf{j_e}$ and the $\mathbf{j_s}$. This effect is related to SHE (see Sect. 2.2), which describes the generation of a $\mathbf{j_s}$ in a non-magnetic metal layer due to the spin-orbit interaction [38]. The theoretical basis principle of SMR can be explained using the spin diffusion model [39, 40]. In this model, the $\mathbf{j_s}$ generated by SHE in a non-magnetic metal layer can diffuse into an adjacent FM layer when the magnetization is perpendicular to σ without relevant changes in HM resistivity. When the magnetization aligns parallel or antiparallel to σ, the $\mathbf{j_s}$ is reflected from the interface into HM. Here, we have the so-called inverse SHE [41], which converts spin to charge current, transforming the entering $\mathbf{j_s}$ into an additional $\mathbf{j_e}$ (different from the one already applied) that decreases and increases the longitudinal resistivity ($\mathbf{j_e} \propto -(\mathbf{j_s} \times \sigma)$). The $\mathbf{j_s}$ can induce spin accumulation at the interface between the two layers, leading to a transverse voltage across the FM layer. The magnitude of the transverse voltage depends on the spin polarization of the FM layer and the efficiency of the spin injection from the non-magnetic metal layer. In a system where the $\mathbf{j_e}$ flows along the x direction, the dependence of the longitudinal resistivity (ρ_{xx}) on the magnetization vector can be written as follows:

$$\rho_{\mathrm{xx}}(\mathbf{m}) = \rho_0 - \rho_{SMR} m_{\mathrm{y}}^2 \tag{2.11}$$

In summary, the total resistance of a system of thin-film heterostructures with a FM, focusing exclusively on the magnetoresistance effects described above, can be written as the sum of the contributions of the individual effects [42]:

$$R_{\mathrm{xx}}(\mathbf{m}) = R_0 + \Delta R_{\mathrm{AMR}} m_{\mathrm{x}}^2 + \Delta R_{\mathrm{SMR}} m_{\mathrm{y}}^2 \tag{2.12}$$

Furthermore, the R_{xx} in spherical coordinates takes the following form:

$$R_{\mathrm{xx}}(\mathbf{m}) = R_0 + \frac{1}{2}(\Delta R_{\mathrm{AMR}} + \Delta R_{\mathrm{SMR}}) \sin^2\theta + \frac{1}{2}(\Delta R_{\mathrm{AMR}} - \Delta R_{\mathrm{SMR}}) \sin^2\theta \cos 2\varphi, \tag{2.13}$$

where θ and φ are polar and azimuthal angles of the magnetization vector.

2.2 | Spin Hall Effect (SHE) and Spin-Orbit Torque (SOT)

After briefly discussing magnetoresistance and Hall effects, we will focus on selected spin-dependent phenomena in thin-film systems. First, we will characterize the SOC, which is mainly significant in HM-based systems described in the experimental section. We will then provide the theoretical basis for the SOC-based phenomenon, that is, SHE causes the conversion of the flowing charge current into a spin current. Spin accumulation at the FM interface can generate a magnetic torque acting on the magnetization vector of the ferromagnet, the so-called SOT, which is the subject of the following subsection. In the characterization of the effects mentioned above, we will mainly concentrate on the model system HM/FM, which correctly represents the real systems that are the subject of this dissertation.

2.2.1 | Spin-orbit coupling

The SOC is a relativistic effect that arises from the interaction between the spin of an electron and the magnetic field generated by its orbital motion around the nucleus [43]. This interaction is analogous to the classical phenomenon of a charged particle moving in a magnetic field. However, it takes on a quantum mechanical description because of the wave-particle duality of electrons. To simplify the description of the phenomenon, we will use the Bohr atomic model [44], where electrons circulate an atomic nucleus having Ze charge in circular orbits under the impact of the Coulomb potential.

SOC is due to the magnetic field $B_{\mathrm{SO}} = \mu_0 Zev/4\pi r^2$ that affects the electron's internal magnetic moment, associated with angular momentum (l) and spin (s). The approximate interaction energy, given by the Bohr magneton and the Bohr radius, can be written as follows after applying a few assumptions:

$$\epsilon_0 \approx \frac{\mu_0 \mu_B^2 Z^4}{4\pi a_0^3} \tag{2.14}$$

where μ_{B} is the Bohr magnetron and a_0 is the Bohr radius while Z is the atomic number of the element.

The variable Z means that the spin-orbit interaction, while weak for light elements, becomes much more important for heavy elements, especially the inner shells. The associated magnetic field is 10 T for boron, or carbon [45]. In single atoms, SOC lifts the energy degeneracy for spin-up (↑) and spin-down (↓) states. However, if the space-inversion symmetry is broken in a crystal, SOC is sufficient to lift the spin degeneracy.

2.2.2 | Spin Hall effect in HM

The previously characterized SOC effect is the origin of a wide range of phenomena in magnetism, such as magnetocrystalline anisotropy [46, 47], magnetostriction [48–52], Rashba-Edelstein effect (REE) [53–58] and SHE [41, 59–62] also theoretical papers on the spin Hall effect of 2D graphene [63]. Due to the subject matter of this dissertation, in the further description, we will focus only on the SHE in HM/FM systems. The author believes that it contributes most to the phenomena studied and described in the experimental section (see Chapter 3).

The SHE in HM is a transport phenomenon that involves the generation of spin currents and, consequently, spin accumulations on the lateral surfaces of a sample carrying electric current due to strong SOC. The sign of the spin current polarization directions is opposite on the opposing boundaries. The SHE can be quantified by a dimensionless material-dependent parameter called SHA (θ_{SH}), which measures the efficiency with which the charge-to-spin conversion is realized:

$$\mathbf{j_s} = \theta_{\mathrm{SH}}(\sigma \times \mathbf{j_e}) \tag{2.15}$$

where $\mathbf{j_s}$ and $\mathbf{j_e}$ are spin and charge current densities, respectively; σ - spin polarization.

The theoretical basis of this effect was first proposed by Dyakonov and Perel in 1971 [64]. SHE in HM can be understood by considering two possible mechanisms: extrinsic and intrinsic. The extrinsic mechanism consists of spin-dependent Mott scattering, where electrons with opposite spin scatter in two directions when they collide with spin-orbit-coupled impurities. The intrinsic mechanism does not require scattering, and the anomalous (lateral) velocity arises from SOC in the band structure itself.

The skew-scattering mechanism is one of the primary extrinsic mechanisms that involve spin-dependent Mott scattering, where electrons with opposite spin diffuse in opposite directions when colliding with impurities or defects in the material. It can be quantified by the skew-scattering angle (θ_{sk}), which depends on the scattering time (τ_{sk}) and the strength of SOC.

The following equation describes this process:

$$\mathbf{j_s} = \theta_{\mathrm{sk}}(\mathbf{j_e} \times (\nabla \times \mathbf{j_e})) \tag{2.16}$$

where θ_{sk} is the skew-scattering angle given by:

$$\theta_{\mathrm{sk}} = \frac{\hbar}{2e}\frac{\tau_{\mathrm{sk}}}{m_{\mathrm{e}}}\Gamma \tag{2.17}$$

where τ_{sk} is the time of skew scattering, m_{e} is the mass of the electron, e is the charge of the electron and Γ is the strength of SOC. The τ_{sk} is related to the scattering rate due to impurities and can be expressed as:

$$\frac{1}{\tau_{\mathrm{sk}}} = \frac{1}{\tau}\sum_i \frac{\partial V_{\mathrm{i}}}{\partial \mathbf{k}} \times \left(\frac{\partial V_{\mathrm{i}}}{\partial \mathbf{r}} \times \sigma\right) \cdot \mathbf{v} \tag{2.18}$$

where $\boldsymbol{\tau}$ is the relaxation time, V_{i} is the scattering potential due to an impurity atom, $\mathbf{k}$ is the wave vector of the electron, $\mathbf{r}$ is the position vector, $\mathbf{v}$ is the velocity vector and $\boldsymbol{\sigma}$ is the Pauli matrix representing the spin of the electron.

In this external contribution, $\mathbf{j}_{\mathrm{s}}$ is proportional to the relaxation time of the electron (average travel time between collisions). This mechanism dominates in almost perfect crystals where the relaxation time is long: a longer spin relaxation time allows the spin polarization direction to be maintained over a longer distance, resulting in a more considerable spin current density. On the contrary, a shorter spin relaxation time leads to a faster decay of the spin polarization direction, resulting in a smaller spin current density.

Therefore, the spin current in a material can be optimized by increasing the spin relaxation time, for example, by reducing the impurity density or improving the crystal quality of the material. This is important for developing efficient spintronics devices based on the spin Hall effect, where a large spin current density is necessary for the operation and functionality of the devices.

The second extrinsic mechanism is the side jump which, contrary to the abovementioned mechanism, is independent of conductivity. The side jump of SHE in HM involves a lateral shift of the electron wave packet during scattering due to impurities or defects in the material. It can be understood using a quantum mechanical picture, where an electron with a given spin experiences a phase shift due to SOC. The phase shift changes the center of mass position of the electron wave packet that depends on its spin orientation. The resulting spin current due to this process is given by:

$$\mathbf{j_s} = \theta_{\mathrm{sj}} \mathbf{j_e} \times (\mathbf{z} \times \mathbf{v_e}) \tag{2.19}$$

where θ_{sj} is the side-jump scattering angle:

$$\theta_{\mathrm{sj}} = -(\hbar/4e^2)\tau_{\mathrm{sj}} \cdot (\nabla V \times \mathbf{E}_{\mathrm{y}}) \tag{2.20}$$

where τ_{sj} is the side-jump scattering time, V is the lattice potential, and E_{y} is the y-component of the electric field ($\mathbf{E}$) induced by $\mathbf{j_e}$ in the x direction. The magnitude of the side-jump effect depends on the strength of the SOC and the degree of asymmetry in the scattering potential. This mechanism is usually expected to be weaker than internal scattering, but it can become important in certain materials and geometries. The side-jump effect is essential to interpret Hall spin measurements in heavy metals (HMs). As it contributes to the accumulation of spin at the edges of the material, it can overestimate the internal Hall spin conductivity if it is not adequately accounted for.

Last but not least, the intrinsic mechanisms of SHE in HM are due to the material's intrinsic properties, where the trajectories of the electrons are distorted as a consequence

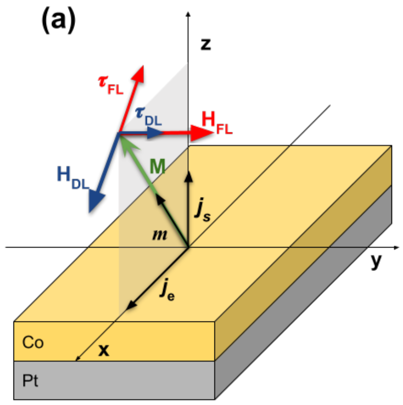

Figure 2.2: SOT damping-like and field-like torques forcing on the magnetization of the FM layer and related to them effective fields H_{DL} and H_{FL} in HM/FM systems, where HM is characterized by positive (e.g., Pt) (a) and negative (e.g., W) (b) spin Hall angle.

of the asymmetries in the material. This mechanism is based on an electron with a given spin experiencing a Berry phase [65] that acts as an effective magnetic field. The Berry phase leads to a transverse deflection of the electron trajectory that depends on its spin orientation [66]. For HMs, the intrinsic mechanism is the most crucial contribution to SHE: calculations predict a high charge-to-spin conversion efficiency and a sign change from Pt to W, which has been observed experimentally [66, 67]. The intrinsic mechanism correlates the sign of SHA with the band filling [66]. SHE is positive for metals with more than half the d band content (Pt [39, 68], Ir [69], Au and Ag [70]), and SHE is negative for HMs with less than half the d band content (Ta [71] and W [72]).

2.2.3 | Spin-Orbit Torque

The magnetization dynamics can be described by the Landau-Lifshitz-Gilbert (LLG) equation [73, 74]. Formula models the precessional motion of magnetization vector $\mathbf{m}$ in solids under the influence of an effective magnetic field H_{eff} (sum of the external magnetic field, dipolar and anisotropy fields, demagnetization, and exchange coupling fields) and a damping term. The LLG can be extended to include additional effects, such as STT, the torque induced by the spin-polarized current in the FM layer, originally proposed by Slonczewski [75]. For magnetic moment described by spherical angles (polar θ and azimuthal φ) where $\mathbf{m} = [\sin\theta\cos\varphi, \sin\theta\sin\varphi, \cos\theta]$, the equation can be written in the form as follows:

$$\frac{d\mathbf{m}}{dt} = -\gamma_e \mathbf{m} \times H_{\text{eff}} + \frac{\alpha_g}{M_S}\mathbf{m} \times \frac{d\mathbf{m}}{dt} + \gamma_e(\boldsymbol{\tau}_{\text{DL}} + \boldsymbol{\tau}_{\text{FL}}) \tag{2.21}$$

where γ_e is the gyromagnetic ratio and α_g is the Gilbert damping coefficient.

The torques $\boldsymbol{\tau}_{\text{DL}} = H_{\text{DL}}(\mathbf{m} \times \mathbf{m} \times \hat{e}_y)$ and $\boldsymbol{\tau}_{\text{FL}} = H_{\text{FL}}(\mathbf{m} \times \hat{e}_y)$ denote components of SOT effective fields damping-like (DL) and field-like (FL) where H_{DL} and H_{FL} are the torque amplitudes, respectively, $\hat{e}_y$ - polarization of the spin current at the edges

Two main models describe the interaction of spin current on the magnetization of a FM layer: STT where the $\mathbf{j_e}$ flowing through the magnetic tunneling junction (MTJ) structure of a non-magnetic layer (e.g., MgO) sandwiched by two FM layers (e.g., Co or CoFeB) possessing non-collinear magnetization becomes spin-polarized at one and, transferring its angular momentum, exerts a torque on the magnetization of the other FM layer [16, 75, 76]. Since classical MTJ systems are not the topic of this dissertation, we will not pay much attention to this mechanism in further consideration.

The second model type is SOT, which originates from the transfer of orbital angular momentum from the lattice to the spin system and is discussed in detail in the following. SOT is a current-induced magnetic torque, the source of which is the SOC. It enables efficient and effective control of magnetization of a FM layer, e.g., in bilayers with broken symmetry [68, 77, 78] and even in a single ferri- and ferromagnetic layer [79, 80].

For the first time, SOT effect was observed for the $Ni_{81}Fe_{19}$/Pt bilayer [77], where spin accumulation at the HM/FM interface was observed. This accumulation can generate magnetic torques that, interacting with the magnetization $\mathbf{m}$ of FM, can cause deterministic magnetization switching dependent on the polarity of the current flowing through the system. In the following subsections, we will focus on describing the mechanisms of this phenomenon under the assumption of an HM/FM bilayer when $\mathbf{j_e}$ flows through the system in the x direction, generating spin accumulation in the y direction. Two main mechanisms for generating SOT will be discussed in the following, specifically the bulk SHE and interfacial the REE.

2.2.3.1 | Bulk spin-orbit torque

As mentioned in the subsection dedicated to the SHE effect (see Sect.2.2.2), $\mathbf{j_e}$ flowing through a metallic layer with strong SOC generates an out-of-plane transverse $\mathbf{j_s}$ with in-plane spin polarization directed perpendicular to the $\mathbf{j_e}$. The spin current is then absorbed in the FM layer adjacent to HM, and its angular momentum is transferred to the magnetization generating SOTs [81].

The spin current $\mathbf{j_s}$ at the HM/FM interface undergoes spin filtering, which is the spin-dependent reflection and transmission of electrons. The total spin current ($\mathbf{j}_{\text{s,tot}}$)

is not conserved during the filtering process, which means that the density of the spin current flowing into the HM/FM interface from the HM side and the reflected current ($Q_{\text{in}} + Q_{\text{refl}}$) is not equal to the density of the current that has passed through the interface (Q_{trans}). Due to the need to conserve the angular momentum, the lost component of spin is transferred to the FM layer in the form of a torque [82]. The total spin torque can be expressed as follows [83]:

$$\boldsymbol{\tau}_{\text{tot}} = \frac{\hbar}{2e}(-2ReG_{\uparrow\downarrow}\mathbf{m} \times \boldsymbol{\mu_s} \times \mathbf{m} - 2ImG_{\uparrow\downarrow}\boldsymbol{\mu_s} \times \mathbf{m}), \tag{2.22}$$

where $\boldsymbol{\mu_s}$ is the total spin accumulation and $G_{\uparrow\downarrow}$ spin mixing conductance.

In general, two components of SOTs add and even in magnetization direction are observed, the previously mentioned τ_{DL} and τ_{FL}, respectively. The ratio between the DL and FL components of the SOTs is roughly determined as the ratio between the real part ($Re[G_{\uparrow\downarrow}]$) and the imaginary part ($Im[G_{\uparrow\downarrow}]$) of the spin mixing conductance, which controls the number of spins passing through the interface without reflection [83]. It has been proven that DL torque is responsible for switching magnetization [71] while FL torque is expected to promote faster propagation of the domain wall [84]. In the metallic layers, the part ($Re[G_{\uparrow\downarrow}]$) dominates over ($Im[G_{\uparrow\downarrow}]$), making DL the main torque component. In real systems, there may also be additional scattering effects, such as spin-flip or spin-memory loss, making the model more complicated [85].

2.2.3.2 | Interfacial spin-orbit torque

The second mechanism to generate SOT is based on symmetry breaking in HM/FM heterostructures where an electric field is applied. When two different materials are contacted, there is an inversion symmetry breaking along the z-direction, which modifies the hybridization of the orbitals, which, in combination with SOC, results in Rashba-Edelstein effect (REE) [58]. When REE is much stronger than the exchange interaction between spin accumulation and magnetization of the ferromagnet, the spins align in-plane and perpendicular to the wave vector. This non-equilibrium of the spin density exerts a torque on the magnetization of the FM layer through an exchange coupling at the interface, which is the FL torque [78]. If REE spin-orbit coupling is much weaker than the exchange coupling, the spins accumulate at the interface. When an electric field is applied along the x-direction, the spins tilt in response to the time-dependent orthogonal spin-orbit field, producing a non-equilibrium accumulation of spins that generates a DL torque through exchange interaction. This torque is called intrinsic due to its weak dependence on scattering [86–88]. In both cases, spin accumulation at the interface was considered. When the effects of spin diffusion away from the interface are also considered, additional contributions to SOT can be generated [81]. In addition, other mechanisms for generating SOT, such as the spin-swapping effect in weakly disordered ultrathin bilayers with electron transport in the Knudsen regime, are also known in the literature [89].

2.3 | Current-induced magnetization switching (CIMS)

Current-induced magnetization switching can be considered a milestone in developing modern spintronics. So far, it has been shown in the example of a variety of thin-film materials, such as HM underlayers [90], antiferromagnetic [91], and magnetic insulators [92], that in the presence of an external in-plane magnetic field, switching of the FM layer with effective perpendicular magnetic anisotropy ($K_{\perp,\mathrm{eff}}$) is performed. In the most straightforward macrospin approach, the mechanism of this switching is based on the joint action of damping-like torque and in-plane field H_{x}. An in-plane current pulse with a given turn induces an effective H_{DL} field, which can result in an unstable magnetization state and, consequently, switching of magnetization to the opposite state. It happens only if H_{DL} is parallel to the external field H_{x}. On the other hand, the magnetization state is stabilized when H_{DL} is antiparallel to H_{x}. Then the switching is impossible. When the polarity of the current changes, the situation reverses, resulting in bipolar switching after changing the direction of the H_{x} field. The transferred angular momentum is perpendicular to the current direction and normal to the sample plane. It is impossible to achieve switching between the $+z$ and $-z$ directions in systems with $K_{\perp,\mathrm{eff}}$ without applying an external in-plane magnetic field, which breaks the symmetry along the current direction. The following formula gives the critical switching current after Lee [93]:

$$j_{\mathrm{sw}} = \frac{2e}{\hbar}\frac{M_S t_F}{\theta_{\mathrm{SH}}}\left(\sqrt{\frac{H^2_{\mathrm{K,eff}}}{32}\left[8+20\left(\frac{H_x}{H_{\mathrm{K,eff}}}\right)^2-\left(\frac{H_x}{H_{\mathrm{K,eff}}}\right)^4-\left(\frac{H_x}{H_{\mathrm{K,eff}}}\right)\left(8+\left(\frac{H_x}{H_{\mathrm{K,eff}}}\right)^2\right)^{3/2}\right]}\right) \tag{2.23}$$

where $H_{\mathrm{K,eff}}$ is the effective perpendicular anisotropy field. For the systems analyzed in this dissertation, the magnetic field applied during the switching experiments (H_x) was significantly smaller than $H_{\mathrm{K,eff}}$ (cf. Table 1 in [P5]). It allows using a simplified formula for the critical switching current in further discussions as follows:

$$j_{\mathrm{sw}} = \frac{2e}{\hbar}\frac{M_S t_F}{\theta_{\mathrm{SH}}}\left(\frac{H_{\mathrm{K,eff}}}{2}-\frac{H_{\mathrm{x}}}{\sqrt{2}}\right). \tag{2.24}$$

Of course, the real mechanism of SOT switching is much more complicated than coherent magnetization switching employing H_{DL} and H_x interaction. In a real system, moreover, j_{sw} depends on many other factors such as DMI [94] (see in Sect. 4.1.3), domain pinning field [95] or temperature [81].

2.4 | Exchange bias (ExB)

Field-free CIMS requires breaking the spatial symmetry in the considered systems. Several concepts have been developed, such as placing the nanodevice very close to the magnetic dot [78, 96], breaking the lateral symmetry in the magnetic structure by introducing layer thickness gradients to induce an out-of-plane FM torque [97] or a tilted anisotropy [98, 99], or using an AFM layer that provides an in-plane ExB [100–102].

ExB is a phenomenon that occurs when a FM material is in contact with an AFM material, such as NiO. The AFM has a fixed magnetic direction that influences the FM and shifts its hysteresis loop. This results in a nonzero magnetization at zero applied field called the ExB field (H_{exb}) [103].

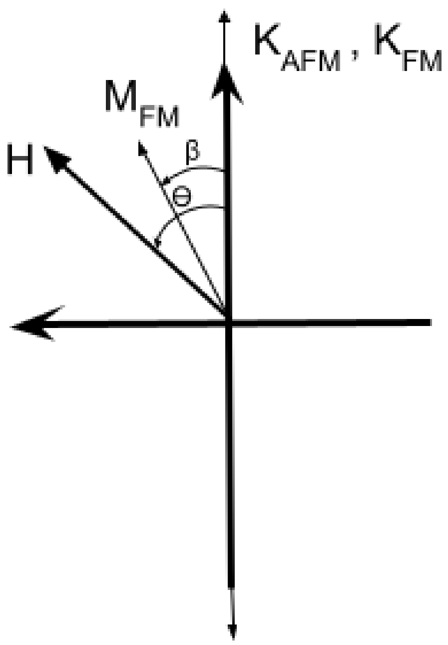

Figure 2.3: Schematic view of angles and vectors in M-B [104] model. β is an angle between M_{FM} and the anisotropy axis of the FM layer. Adapted from [105]

.

The uncompensated spins at the interface between the ferromagnet and the antiferromagnet then experience a net exchange field, which induces a unidirectional shift in the magnetic hysteresis loop of the ferromagnet. H_{exb} can range from a few to a few thousand Oersteds [106–108]. The magnitude and direction of H_{exb} depend on various factors, such as the thickness of the AFM layer, the strength of the exchange interaction between the ferromagnet and antiferromagnet, and the angle between the magnetizations of the ferromagnet and the antiferromagnet. The ExB effect can also depend on the method of interface preparation and the temperature at which the FM layer is cooled [109–111]. For example, in a NiO/NiFe/NiO trilayer structure, a positive H_{exb} was observed when the NiO layer was 40 nm thick, but a negative H_{exb} when the NiO layer was thicker than 40 nm [112].

To describe the ExB phenomenon, the macro-spin Meiklejohn-Bean model (M-B model) [96, 104, 113] was used, which assumes, for instance, that both FM and AFM are in a single domain state and FM / AFM are atomically smooth, as well as spins in AF are completely uncompensated at the interface. The Stoner-Wohlfarth model was used to [114] describe the coherent rotation of magnetization. A schematic diagram of the angles and vectors used in the M-B model is shown in Fig.2.3.

Starting from the equation for energies per unit area assuming coherent rotation of magnetization, applying field parallel to the anisotropy direction (θ= 0) and AFM spins orientation parallel to the anisotropy axis [105]:

$$E_A = -\mu_0 H M_S t_{\mathrm{FM}} \cos(\theta - \beta) + K_{\mathrm{FM}} t_{\mathrm{FM}} \sin^2(\beta) - J_{\mathrm{eb}} \cos(\beta) \tag{2.25}$$

where: J_{eb} is the interfacial exchange energy (includes all interactions within the range of exchange coupling and expressed as $E_{\mathrm{int}} = \sum_{\mathrm{ij}} J_{\mathrm{ij}} S_i^{\mathrm{AFM}} S_j^{\mathrm{FM}}$) [115] per unit area, M_{S} - saturation magnetization of the ferromagnetic layer, K_{FM} - volume anisotropy constant of ferromagnet and β is a magnetization orientation.
The stability condition $\partial E_{\mathrm{A}} / \partial \theta$ = 0 has two types of solutions:

$$\beta = \cos^{-1}[(J_{\mathrm{eb}} - \mu_0 H M_{\mathrm{S}} t_{\mathrm{FM}})/2K_{\mathrm{FM}}] \tag{2.26}$$

for $\mu_0 H M_{\mathrm{S}} t_{\mathrm{FM}} - J_{\mathrm{eb}} \leq 2K_{\mathrm{FM}}$, and

$$\beta = 0, \pi \tag{2.27}$$

for $\mu_0 H M_{\mathrm{S}} t_{\mathrm{FM}} - J_{\mathrm{eb}} \geq 2K_{\mathrm{FM}}$ which are the positive and negative saturation, respectively.
Coercive fields H_{c1} and H_{c2} for $\beta = 0, \pi$:

$$H_{\mathrm{c1}} = -\frac{2K_{\mathrm{FM}} t_{\mathrm{FM}} + J_{\mathrm{eb}}}{\mu_0 M_{\mathrm{S}} t_{\mathrm{FM}}}, \tag{2.28}$$

$$H_{c2} = \frac{2K_{FM}t_{FM} - J_{eb}}{\mu_0 M_S t_{FM}} \tag{2.29}$$

The H_{exb} can be expressed as follows:

$$H_{exb} = \frac{H_{c1} + H_{c2}}{2} \tag{2.30}$$

which gives:

$$H_{exb} = -\frac{J_{eb}}{\mu_0 M_S t_{FM}} \tag{2.31}$$

The obtained solution represents the ideal case, particularly the linear dependence on the interfacial energy J_{eb} and the inverse dependence on FM thickness. Of course, there are other models, such as the domain state model [116], the spin-flop model [117], and the uncompensated spin model [118], which more accurately describe the ExB involving more phenomena and degrees of freedom. The difference between ExB in-plane and perpendicular at the interface of the FM and AFM layers is related to the direction of magnetization of the FM layer and the H_{exb}. In-plane ExB occurs when the magnetization of the FM layer lies in the plane of the film, parallel to the interface, in this case, in-plane exchange bias field ($H_{exb}^{(x)}$) component occurs. The perpendicular ExB appears when the magnetization of the FM layer is perpendicular to the plane of the thin film, and the perpendicular exchange bias field ($H_{exb}^{(z)}$) component is present. The magnitude and sign of H_{exb} can vary depending on the measurement direction. For example, in a Pt/Co/IrMn trilayer system, both in-plane and perpendicular H_{exb} can be observed, but they have opposite signs and different temperature dependences. This indicates that other mechanisms generate the ExB effect in different directions [119].

3

Experimental Methods

3.1 | Samples deposition

The most of thin film systems analyzed in this dissertation were deposited in the Department of Thin Films of the Institute of Molecular Physics of the Polish Academy of Sciences in Poznań [120].

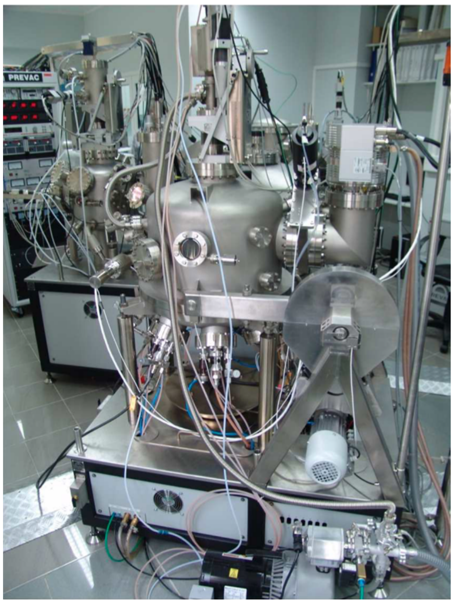

Figure 3.1: Picture showing the system for thin film deposition. In the foreground, there is the magnetron sputtering deposition chamber equipped with six targets. On the right side behind it, the chamber for pulsed laser deposition (PLD) is shown [121].

The magnetron sputtering method [121, 122] was used to deposit metallic layers, while the insulating nickel oxide (NiO_2) layer was deposited by PLD [123]. Thermally oxidized Si/SiO_2 silicon substrate (the amorphous SiO_2 layer was approximately 1000 nm; due to this reason, the seed and buffer layers grew up without transferring the Si wafer orientation) was used to ensure complete electrical isolation from the substrate. The magnetron sputtering system in Fig.3.1 has six different targets with a size of 2 inches each, allowing multilayer structures to be applied during a single application session [121]. A unique feature of the sputtering system was the ability to deposition wedge-shaped as well as oxide layers byPLD in a separate chamber, without breaking ultra-high vacuum (UHV) conditions of less than 5×10^{-8} mbar.

A shutter was used to apply the samples where the wedge layer occurred. It is assumed that the thickness of the applied layer depends on the sputtering time at a constant sputtering power. Moving the sample under the shutter with a constant velocity gradient gives a layer with a linear dependence of the thickness on the position on the substrate, as presented in Fig.3.2. Typically, wedge samples were applied to 20x20 mm^2 substrates. Because the wedge typically spreads over a length of 20 mm, its change gradient is small, which makes the variation in the thickness of the wedge layer negligibly small in a single device (order of approximately 0.01 nm for the width of the device = 10 ¯m).

Of course, this method requires calibration deposition rates separately for each type of material. Calibration was performed using two independent techniques: quartz balance during deposition and post-deposition by x-ray reflectivity (XRR). In the case of

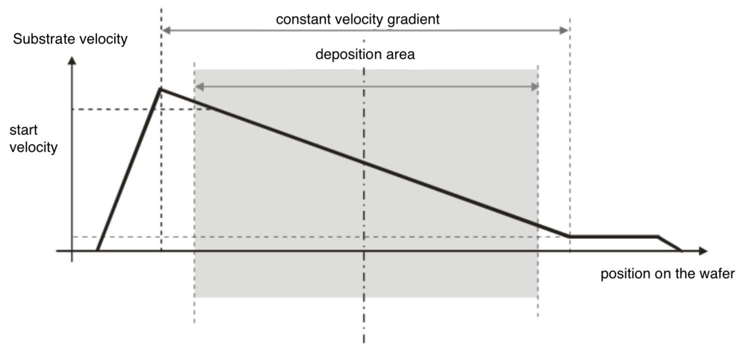

Figure 3.2: Graph demonstrating the dependence of the speed of substrate movement during deposition on the position of the silicon wafer. As can be seen, the deposition area is in the range of a constant movement velocity gradient, guaranteeing a constant thickness change of the deposition layer. Graph from [121].

the W layer, a low direct current (DC) power of 4W was used and a distance of 6 cm between the substrate and the target, giving a slow deposition rate of 0.01 nm/s that guaranteed a high SHA of the high resistive cubic β-W layer. Regarding Pt, the most common power used was 8 W (0.029 nm/s), and Co and CoFeB were applied at 15 W with deposition rates of 0.045nm/s and 0.030nm/s, respectively. During the deposition of hybrid HM (W, Pt)/Co/NiO systems, an external magnetic field of 1.1 kOe was applied, directed perpendicularly to the sample plane to induce a perpendicular ExB field between Co and NiO layers [106, 124–126]. NiO was deposited in a controlled O_2 atmosphere with a partial pressure of 1.5×10^{-5} mbar. A rotation of the sample holder at a frequency of 2 Hz was used to obtain a NiO layer of constant thickness [124].

3.2 | Kerr effects microscopy (MOKE)

After deposition, the p-MOKE technique was used to measure the local hysteresis loop M(H) in the wedge-shaped layer. This method involves the rotation of the polarization plane of linearly polarized light reflected from the surface of a magnetic material. Moreover, in the case of polar measurement (sensitive to magnetization perpendicular to the sample plane), there is a change in the polarization direction from linear to elliptical.

Measured quantities for the change in polarization of the reflected beam compared to the incident beam are the Kerr angle (θ_{k}) and the Kerr ellipticity (ϵ_{k} and η_{k}), which are then converted to light intensity by the analyzer and recorded by a computer.

Most often, magneto-optical measurements are performed in the presence of an external magnetic field (to obtain M(H) loop) that can be applied at any angle (θ) to the normal of the sample plane. In the case of our wedge-shaped systems, changing the value of the magnetic field applied perpendicular to the sample plane ($\theta = 0^o$) while mapping the sample surface allows studies of the local orientation of the magnetization as a function of the external field M(H) [P3,P5] (Fig.3.3(a)), and estimate the value of the $H_{\mathrm{exb}}^{(z)}$ field (Fig.3.3(b)) [P2].

The incredible advantage of this measurement technique is the ability to combine it with microscopic techniques, which opens up enormous possibilities for observing magnetization changes at the local level, such as the motion of domain walls [127], determining the direction of DMI interactions [128], or observing skyrmions [129]. We used Kerr microscopy to image the domain structure of the Pt/Co system with DMI (see Sect.4.1.3) and Co/Pt/Co trilayer during the CIMS experiment (see Sect.4.2.3).

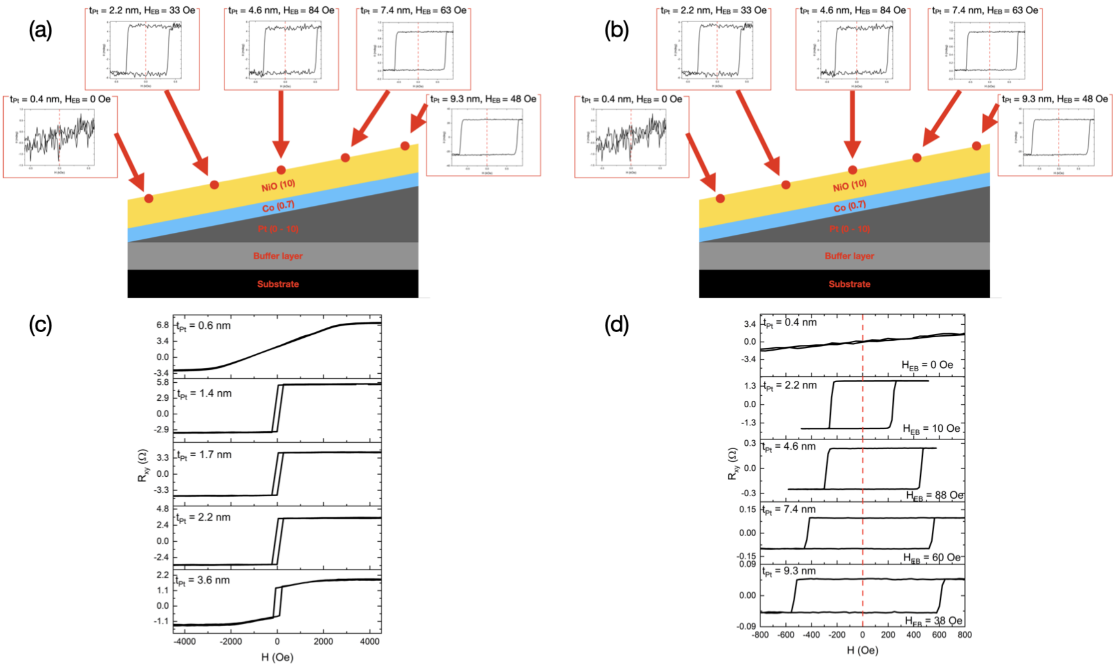

Figure 3.3: Schematic diagram of the studied Ti(2)/Co(1)/Pt(0-4)/Co(1)/MgO(2)/Ti(2) (a), and Pt(0-10)/Co(0.7)/NiO(10) (b) thin film systems (thickness in nm). In the figures, red dots indicate examples of p-MOKE loop measurement locations to determine the Pt thickness region where perpendicular magnetic anisotropy (PMA) and ExB occur. Figs. (c,d) show the results of AHE magnetization hysteresis loops on elements with Pt layer thickness corresponding to MOKE loops for both systems. It can be seen that the results obtained by both methods are in complete agreement.

3.3 | X-ray Absorption Spectroscopy (XAS)

The techniques of magnetic dichroism in the x-ray range, such as X-ray magnetic circular dichroism (XMCD) [130] and X-ray magnetic linear dichroism (XMLD) [131–133] have been used to determine the spin order of Co and NiO layers, in particular at the Co/NiO interface in the studied HM/FM/AFM structures (the results are presented in the supplementary materials to the [P2] paper). Both measurement techniques are available at the PIRX beamline using soft x-rays from the Solaris National Synchrotron Radiation Center in Krakow [134].

The magnetic properties of transition metals (TM), which include the materials studied in this dissertation, depend mainly on the electrons of the 3d valence subshell. The properties of electrons from this subshell are best studied by absorption at the L-edge, the transition from the 2p to the 3d subshell. The L-edge is characterized by two main peaks of about 15 eV in TM and TM-oxides. The intensity of the measured peaks is pro-

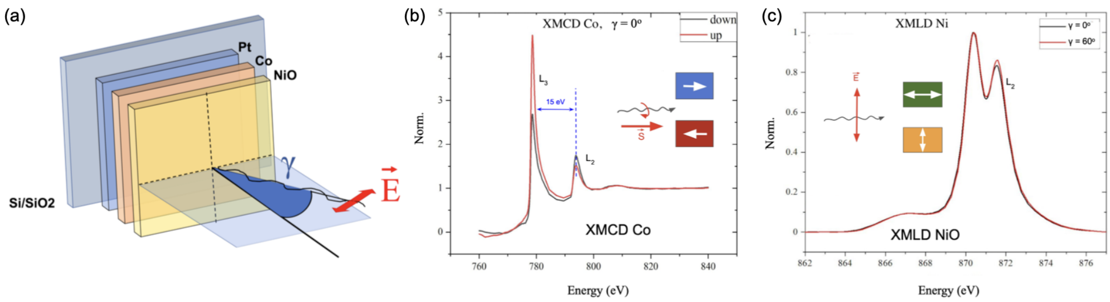

Figure 3.4: (a) Schematic illustration of incident synchrotron radiation on the sample surface. (b) Example of XMCD spectrum of Co with incident synchrotron radiation perpendicular to the plane of the sample measured at RT. (c) XMLD spectrum of Ni at RT for two angles of incidence of synchrotron radiation perpendicular to the plane of the sample ($\gamma = 0^o$) and $\gamma = 60^o$ to normal to investigate the direction of spin axes in antiferromagnetic NiO.

portional to the number of free states on the d subshell. In oxides, a multiplet structure can be seen here, originating from the SOC of the ground states of the electrons.

The XMCD spectroscopy technique is used mainly to measure the magnetic properties of ferromagnets. In our case, it was used to study the spin orientation of the ferromagnetic Co layer at the interface of FM and AFM. The unequal occupation of d-subshell states by electrons with spin down and spin up (depicted by the difference in the intensity of the black and red lines) leads to a nonzero spin moment. The magnitude of the dichroism effect scales with $\cos(\theta)$, where θ is the angle between the photon's spin and the direction of magnetization. The most significant effect is obtained when the spin and magnetization vector are parallel or antiparallel, as shown in Fig.3.4(b).

The second method used is the XMLD technique, which is sensitive only to the direction of the spin axis and cannot be used to determine the direction of the spin, which makes it ideal for studying AFM layers [135]. It is based on decoupling the electric field vector **E** of linearly polarized x-rays with the charges in the atom. The maximum of XMLD is given by the difference in the signal for $\mathbf{E}_{\parallel}$ and $\mathbf{E}_{\perp}$ with respect to the direction of the spin axis. XMLD shows a $\cos^2(\theta)$ dependence on the angle between **E** and the spin axis. The sizeable signals may be seen in materials with multiplet splitting (such as AFM oxides). Fig.3.4(c) showed example XMLD spectra on the Ni L_2 line when the synchrotron radiation was incident at 0^o to the normal (gray line) and at 60^o to the normal (red line). The difference in peak height indicates a slight ordering of the AFM spin axis perpendicular to the film plane (parallel to [100]).

3.4 | Structural characterization

The multilayer crystal structure investigations were carried out on an X-Pert MPD diffractometer with a Cu anode. The following x-ray diffraction methods were used: goniometric (θ - 2θ), XRR, grazing incidence x-ray diffraction (GIXD), rocking curve, and polar figures. They are used to determine the thickness of individual layers by XRR, the phase analysis by θ - 2θ, and the predominant polycrystalline texture by rocking curve and polar figures. Example results of measurements with the above methods on samples W(5)/Co(1)/NiO(10) and Si/SiO_2/Pt(0-10) are shown in Fig.3.5.

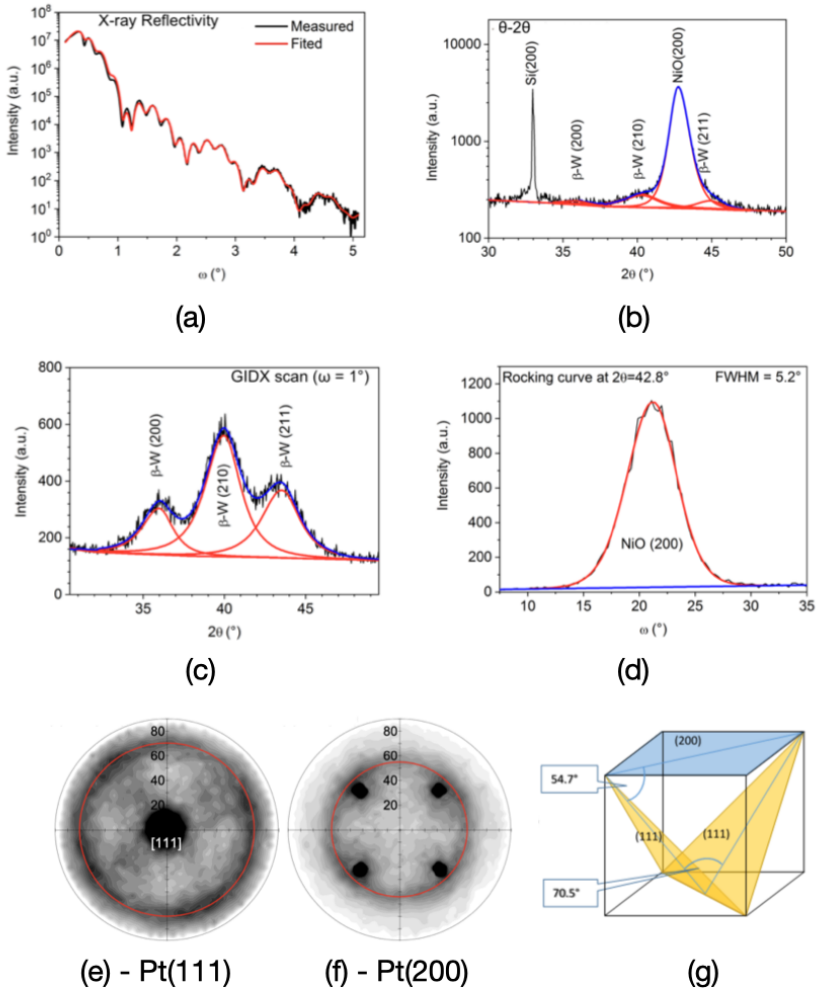

Figure 3.5: Examples of x-ray diffraction measurements: (a) XRR; (b) θ - 2θ goniometric measurement; (c) GIXD (ω = 1^o); (d) rocking curve of of W(5)/Co(0.7)/NiO(10) system. Figures (e) and (f) show pole figures at the Pt(111) and Pt(200) positions in the cubic cell (f) of Si/SiO2/Pt(0–10) system measured at the middle position of Pt wedge.

It was possible to identify the structure and crystalline phase of the multilayer sample (Fig.3.5(b,c)), as well as the predominant texture of NiO (200) (Fig.3.5(d)). The surface-sensitive low-angle method of XRR-reflectometry curves allows the determination of the actual layer thicknesses and their morphologies (roughness and mixing interfaces) [136, 137] and [P1]. Measurements are made near the critical angle using a focusing mirror (Fig.3.5(a)). The radiation reflected from the surface of the layer and the interfaces are recorded as a function of the angle of incidence.

The GIXD method allows recording of diffraction spectra at small angles (in our case, $\omega = 1^o$). This enables precise control of the penetration depth of the radiation and allows minimizing the influence of the substrate and buffer layers on diffraction spectra on top layers (Fig.3.5(c) and Fig.S1(a,b) in Supplementary Material to [P1]).

When small angles tilt the sample in the rocking curve method, we get a rocking curve at a specified Bragg reflection. Based on the width of the resulting peak, the degree of the texture of the layer can be easily assessed (Fig.3.5(d)). In turn, the measurement of the polar figures (Figs.3.5(e,f) makes it possible to determine the spatial distribution of the crystallographic directions (Fig.3.5(g).

3.5 | Device fabrication

After structural and magnetic characterization of the continuous layers, the samples were patterned as Hall bars in the Micro- and Nanofabrication Laboratory of the AGH Academic Center for Materials and Nanotechnology [138]. The clean room compartment includes two rooms with a cleanliness class of ISO5 and ISO7, respectively. The dust content in the air is a critical factor for the success of micro- and nanofabrication processes.

A two-step lithography method was used to pattern the studied systems, consisting of the double application and development of photoresist. The lithography process starts in the ISO7 clean room. On an Arias process bench used for application, annealing, and resist removal, the multilayer sample is pretreated by thoroughly cleaning it in an ultrasonic washer in ethanol for several minutes. After that, a thin layer of AR-N 4340 negative photoresist [139] is applied to the surface of the sample. The appropriate thickness of the photosensitive layer was obtained by centrifuging excess photoresist in a spin coater at 6000 rpm for 30 seconds. Adequate photoresist crosslinking was achieved by heating the sample on a heating plate at 90ºC for 1 min. The next step involves exposing the matrix of the active elements of the system. Each time, both the arrangement of the elements on the mask and their shapes and sizes are designed specifically for the methods and measuring equipment that will be applied subsequently, thus ensuring the maximum degree of yield. The mask used in the lithography process was created in the KLayout software [140]. An example is presented in Fig.3.6. Durham DMO DLP baby 3+ projection lithography, which has a 365 nm LED light source, was used for exposure. A digital light processor (DLP) chip with 1 million moving cantilever reflectors illuminates the mask image on the substrate. The device has two lenses with varying achievable resolutions of 5 μm or 1 μm. The sample was positioned using a four-point method using unique markers in the mask. A resolution of 1 μm and an energy of 140 mJ/cm^2 and a dose of 3 were used to expose the studied systems. The dose and energy have been optimized to achieve the sharpest edges of the device. After the exposure process,

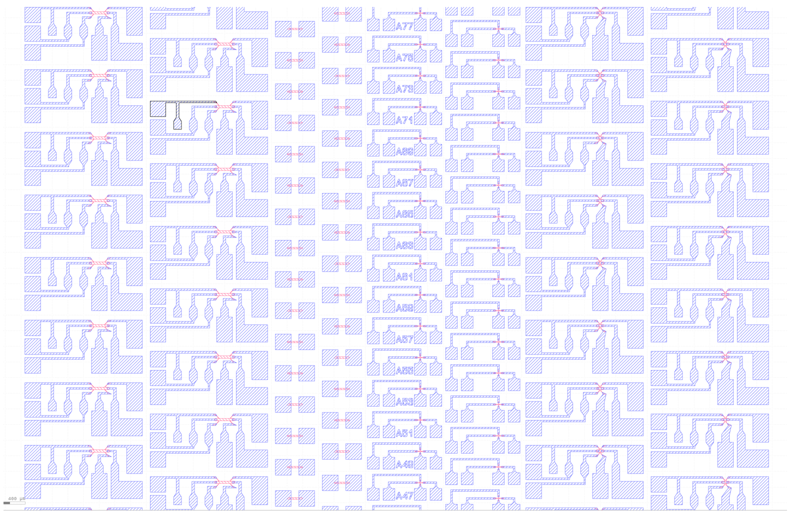

Figure 3.6: An example of a lithographic mask used for DLP lithography to nanostructure devices in studied samples. The first two rows of devices on the left are designed for precision 4-point resistance measurements, the next two rows for magnetization dynamics measurements using the SD-FMR method, the next two rows for magnetoresistance and Hall measurements, and finally, the last two on the right are optimized for magnetization current switching measurements.

the samples were additionally annealed at 95^{o}C for 2 min, after which the unexposed areas of the sample were developed in AR 300-475 developer [141] for 30 s. After visual inspection of the correctness of the exposure process under a Nikon optical polarizing microscope, the sample was moved to the second ISO5 cleanroom, where there is the Microsystems IonSys 500 ion etching and thin film deposition device. The system has an Ar$^+$ ion gun and a mass spectrometer detector, allowing atomic resolution etching depth control and three magnetron sputtering sources (Al, Au, Ti). The etching was carried out at a gun power of 250 W with a gas flow of 8 sccm. A mass spectrometer acts as the endpoint detector, which enables a precise etching stop at the required depth. The remaining photoresist was removed in 1-methyl-2-pyrrolidinone in an ultrasonic cleaner at 70^{o}C for 15 minutes. This process is called *lift-off*. After the photoresist was removed, the chips were inspected in detail under an optical microscope.

The second lithography step began with applying AR-P 3740 positive photoresist [142] and heating the sample on a hot plate at 100^{o}C for 1 min. The exposure process was carried out with a dose of 0.5. Then, using the AR 300-47 developer [143], the photoresist was removed for 10 seconds. The second etching step lasted about 25 seconds. The magnetron sputtering method was then used to deposit electrode material, respectively, Ti at an Ar flow rate of 50 sccm and magnetron power of 50 W for 4 min and then Au at an Ar flow rate of 69 sccm and power of 40 W for 8 min. The final step is lift-off in an ultrasonic cleaner for about 20 min, clean in ethanol, and dry in a stream of nitrogen. The finished systems were visually inspected again under an optical microscope.

3.6 | Electrical detection

3.6.1 | Static electrical methods

Resistance, longitudinal and transversal magnetoresistance, and Hall effect measurements were performed mainly in a rotating probe station, allowing any angular position in an external magnetic field. This probe station was designed and made especially for our laboratory.

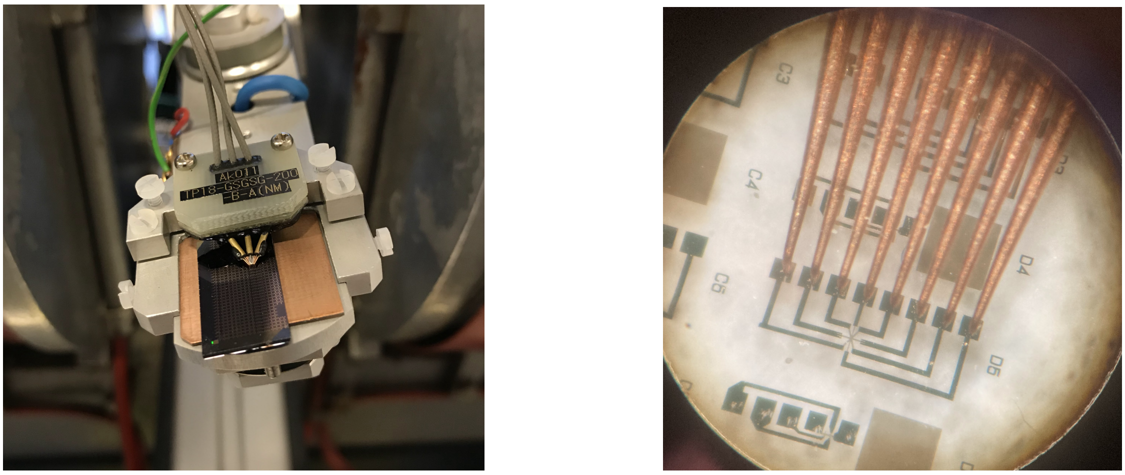

(a) (b)

Figure 3.7: The figure shows an example of a probe used for electrical measurements (a), with a connection of 8-fingers to the micro/nanodevice (b).

The main element of this measurement station is an automatic rotating arm equipped with a sample holder. The maximum angular range of sample rotation to the magnetic field is from -220^o to $+110^o$ degrees in the horizontal plane and -225^o to $+45^o$ degrees in the vertical plane. The electromagnet allows for a maximum field of about 1.8 T. Time-stable electrical contact with the sample is provided by an own designed different types of multifinger measuring probes (presented in Fig.3.7), which can be used for both RF and DC measurements, like, e.g., highly accurate resistance measurements of the investigated sample using a 4-point method with a Keithley 2636. Fig.3.8 presents

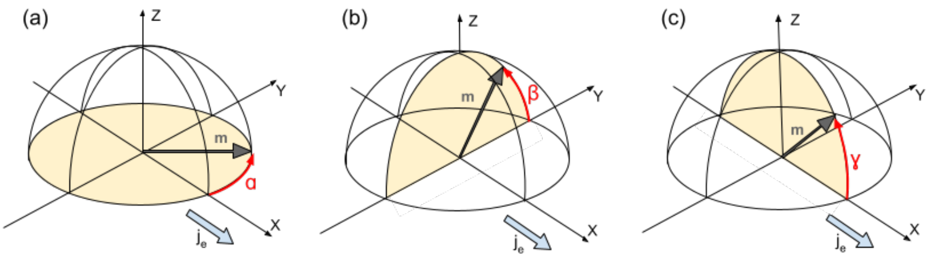

Figure 3.8: Schematic illustration of three possible rotations concerning an applied external magnetic field: (a) in the x-y plane (α rotation), (a) in the y-z plane (β rotation), and (c) in x-z plane (γ rotation).

the most common measurement configurations, where the sample was rotated in relation to the external magnetic field in the x-y plane (α angle), the x-z plane (γ angle), and the y-z plane (β angle). Moreover, the sample is stabilized in the holder by vacuum suction. Measurement of voltage and resistance in longitudinal and transversal orientation without rewiring the device is possible using four measurement channels and a specially customized contact electrode array. Another advantage of this type of setup is that it is not bonded to the contact pads, and thus the testing element can be quickly switched to another matrix device on the sample.

3.6.2 | Harmonics methods

3.6.2.1 | Magnetic field harmonics method

For analyzing spin-orbit interactions in HM/FM thin-film systems, Hayashi [144] applied harmonic methods, which are now one of the most popular techniques reported in the literature [145–150]. In the shortest summary, the method consists of analyzing by lock-in the first (V_ω) and second ($V_{2\omega}$) harmonic signals of the voltage response of the system to a low frequency (284 Hz) alternating current (AC). Measurements are usually made in Hall geometry while current is applied along the long axis of the Hall bar (x direction). The output voltage (V_{xy}) is measured on the transverse electrodes in the y direction (V_{xy}). During measurement, an external magnetic field is applied in-plane perpendicular (H_y) and parallel (H_x) to the current (Fig.3.9). The current flowing through

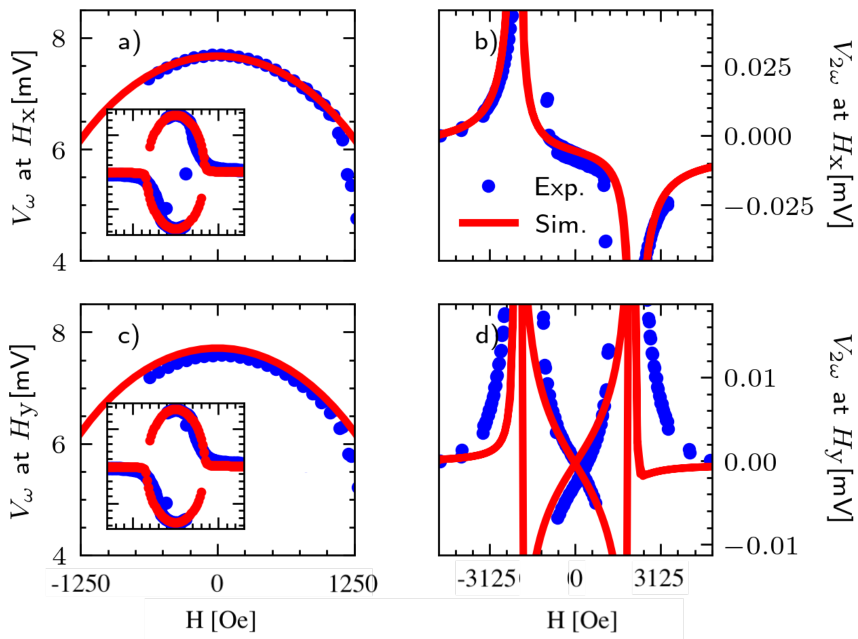

Figure 3.9: An example of the experimental data and simulation results of the harmonic field measurements in the Ta(5)/CoFeB(1.45)/MgO(2)/Ta(1) system: (a) and (b) the first and second harmonic responses measured in the H_x field with $\theta = 90^o$, respectively, (c) and (d) the first and second harmonic responses measured in the H_y field with $\theta = 90^o$. Inset shows the total view of the first harmonic response in the field in the $\pm$ 5 kOe range. Figure from [P6].

the device generates effective fields dumping-like (H_{DL}), field-like (H_{FL}), and Oersted field components. These fields drive the magnetization vector out of equilibrium. Following Hayashi et al. [144] we can define the transverse voltage V_{xy} as:

$$V_{xy} = V_0 + V_\omega \sin \omega t + V_{2\omega} \cos 2\omega t. \tag{3.1}$$

Making several assumptions [144] such as neglecting the influence of ordinary Hall effect and small value of tilt angle of magnetization from the z-axis i.e., $\cos\theta \ll 1$, the following expressions for the each harmonics were obtained:

$$V_\omega \approx \pm\frac{1}{2}\Delta R_{AHE}\left[1 - \frac{1}{2}\left(\frac{H\sin\theta_H}{H_K \pm H\cos\theta_H}\right)^2\right]\Delta I$$

$$V_{2\omega} \approx -\frac{1}{4}[\mp\Delta R_{\mathrm{AHE}}(\Delta H_{\mathrm{x}}\cos\varphi_{\mathrm{H}} + \Delta H_{\mathrm{y}}\sin\varphi_{\mathrm{H}})+$$
$$+2\Delta R_{\mathrm{PHE}}(-\Delta H_{\mathrm{x}}\sin\varphi_{\mathrm{H}} + \Delta H_{\mathrm{y}}\cos\varphi_{\mathrm{H}})\cos 2\varphi_{\mathrm{H}}]\times$$
$$\times\frac{H\sin\theta_{\mathrm{H}}}{(H_{\mathrm{K}} \pm H\cos\theta_{\mathrm{H}})^2}]\Delta I$$

where: R_{AHE} and R_{PHE} are AHE and PHE resistances, respectively; H - external magnetic field applied at the polar θ_{H} and azimuthal φ_{H} angles; H_{K} -perpendicular anisotropy field, H_{x}, and H_{y} are an in-plane component of the external field H directed along one of the Cartesian coordinate axes (along x or y-axis due to considerably simplifying many of the expressions) and ΔI - current flowing through the system.

The following expressions are given for the ratio of the derivatives of the measured signals for systems with out-of-plane magnetization.

$$B \equiv \left(\frac{\partial V_{2\omega}}{\partial H} / \frac{\partial^2 V_{\omega}}{\partial H^2}\right) =$$
$$= \frac{1}{2}\left[(\Delta H_{\mathrm{x}} \mp 2\frac{\Delta R_{\mathrm{PHE}}}{\Delta R_{\mathrm{AHE}}}\cos 2\varphi_{\mathrm{H}}\Delta H_{\mathrm{y}})\cos\varphi_{\mathrm{H}} + (\Delta H_{\mathrm{y}} \pm 2\frac{\Delta R_{\mathrm{PHE}}}{\Delta R_{\mathrm{AHE}}}\cos 2\varphi_{\mathrm{H}}\Delta H_{\mathrm{x}})\sin\varphi_{\mathrm{H}}\right] \tag{3.2}$$

Defining the components $B_{\mathrm{x}} \equiv (\frac{\partial V_{2\omega}}{\partial H})|_{\vec{H}||\hat{x}}$ and $B_{\mathrm{y}} \equiv (\frac{\partial V_{2\omega}}{\partial H})|_{\vec{H}||\hat{y}}$ and the coefficient $r \equiv \frac{\Delta R_{\mathrm{PHE}}}{R_{\mathrm{AHE}}}$, which is the ratio of PHE to AHE, the final expression for the components of the effective SOT field is obtained:

$$\Delta H_{\mathrm{x}} = -2\frac{(B_{\mathrm{x}} \pm 2rB_{\mathrm{y}})}{1-4r^2} \tag{3.3}$$

$$\Delta H_{\mathrm{y}} = -2\frac{(B_{\mathrm{y}} \pm 2rB_{\mathrm{x}})}{1-4r^2} \tag{3.4}$$

where ΔH_{x} is proportional to DL field, ΔH_{y} is proportional to FL field and the sign of $\pm$ corresponds to the direction of the magnetization vector along the +z or -z axis, respectively.

The determined DL and FL effective fields, after applying the following equation, allow the calculation of the spin Hall efficiency:

$$\xi_{\mathrm{FL(DL)}} = (2|e|/\hbar)(\mu_0 M_{\mathrm{s}} t_{\mathrm{FM}}/J_{\mathrm{HM}})\Delta H_{\mathrm{y(x)}} \tag{3.5}$$

where: t_{FM} - thickness of FM layer and J_{HM} - current density in HM.

3.6.2.2 | Angular harmonics method

The above-mentioned method does not apply to systems with in-plane magnetic anisotropy (IMA). Avci [151] was the first to implement the angular harmonic method for samples with IMA. This method uses first harmonics (V_ω) and second ($V_{2\omega}$) harmonics of the voltage response of the system to a low-frequency current as a function of the angle φ_H in the $x-y$ plane (assumed polar angle $\theta_H = \frac{\pi}{2}$) in the presence of an external magnetic field, respectively.

The in-phase first and out-of-phase second harmonics of the transverse voltage can be written as:

$$V_\omega = V_{\rm PHE} \sin 2\varphi_{\rm H} \tag{3.6}$$

$$V_{2\omega} = \frac{V_{\rm PHE}(H_{\rm FL} + H_{\rm Oe})}{H} \cos\varphi_{\rm H} \cos 2\varphi_{\rm H} - \left(\frac{V_{\rm AHE} H_{\rm DL}}{2H_{\rm eff}} - V_{\rm ANE}\right) \cos\varphi_{\rm H} \tag{3.7}$$

where φ_H is the azimuthal angle of the magnetization vector, H - external magnetic field, and $H_{\rm eff} = H + H_{\rm dem} - H_{\rm ani}$, $V_{\rm AHE}$, and $V_{\rm PHE}$ are anomalous and planar Hall voltages, respectively, $V_{\rm ANE}$ is the parasitic contribution arising from (anomalous Nernst effect (ANE)). The advantage of this method is the ability to separate FL -SOT from the

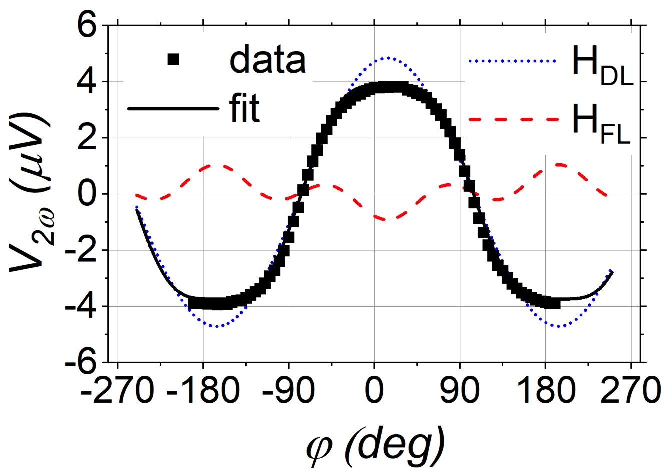

Figure 3.10: An example of the angular dependence of the second harmonic response in the Pt($t_{\rm Pt}$)/CoFeB(2)/Ta(2) system and the determined values of damping- and field-like SOT efficiencies versus Pt thickness. Figure from [P9].

influence of the anti-damping spin-orbit torque (AD-SOT)+ANE effects (see Fig.3.10) since the different components of the second harmonic signal are differently proportioned to the constant magnetic field acting on magnetization. As shown in Eq.3.7, the

FL term disappears as $1/H$ approximately, the DL disappears as $1/H_{\text{eff}}$. The ANE contribution is independent of the magnetic field strength (see Figs.4(e,f) in [P2] and Fig.10 in [P3]):

$$V_{2\omega,\text{FL}} \sim \frac{1}{H}$$
$$V_{2\omega,\text{AD}} \sim \frac{1}{H + H_{\text{dem}} - H_{\text{ani}}}$$
$$V_{2\omega,\nabla\text{T}} \sim const.$$

This allows one to calculate AD and FL effective field components induced by current flow as:

$$H_{\text{AD}} = \left[V_{2\omega,\text{AD}} / \left(\cos\varphi_{\text{H}} \frac{dV_{\omega}}{d\theta_{\text{H}}} \right) \right] H \tag{3.8}$$

$$H_{\text{FL}} + H_{\text{Oe}} = \left[V_{2\omega,\text{FL}} / \left(\cos\varphi_{\text{H}} \frac{dV_{\omega}}{d\varphi_{\text{H}}} \right) \right] H. \tag{3.9}$$

3.6.3 | Current-induced magnetization switching (CIMS)

CIMS experiments performed on all systems studied were carried out using Hall-bar devices with four electrical contact pads that allowed simultaneous current flow through the system and measurement of the transverse Hall voltage (V_{xy}). The length (L) and width (w) of the Hall bar were selected in each case so that a relatively small voltage could be used to cause a high current density to flow through HM, allowing the critical current (I_{c}) value to be exceeded.

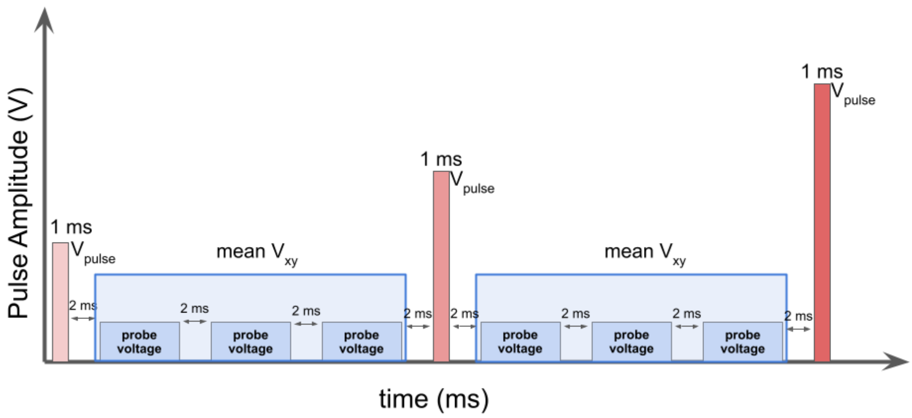

Figure 3.11: An example of the pulse scheme given during the CIMS experiment. The length of the pulse, its amplitude, the interval between pulses, and the number of probing pulses were changed as required.

As in all electrical measurements, stable contact was ensured by a multi-finger probe to whose pads of the device were connected. In any case, before the experiment began, the external magnetic field perpendicular to the sample plane (H_z) was applied to bring the resistance R_{xy} to the maximum resistance R_{xy} of AHE. Current pulses with a duration of typically 1 ms were generated using a Keithley 2636 current source. Each pulse was followed by a 2 ms gap, and several measurements of R_{xy} were carried out using an Agilent 34410 multimeter with low sampling voltage. The measured value of R_{xy} was then averaged. Transport measurement software carried out the entire experiment, including data acquisition, ensuring proper synchronization of the subsequent measurement steps. An example of the most commonly implemented and executed pulse pattern is shown in Fig.3.11.

It is worth mentioning that the scheme shown above was modified based on the system and the requirements of the experiments. The in-plane magnetic field was applied to the device parallel to the direction of the charge current (H_x) flowing through the system. The precise alignment of the device to H_x was made possible by a rotating probe station. During a single measurement cycle, the amplitude of the voltage pulses

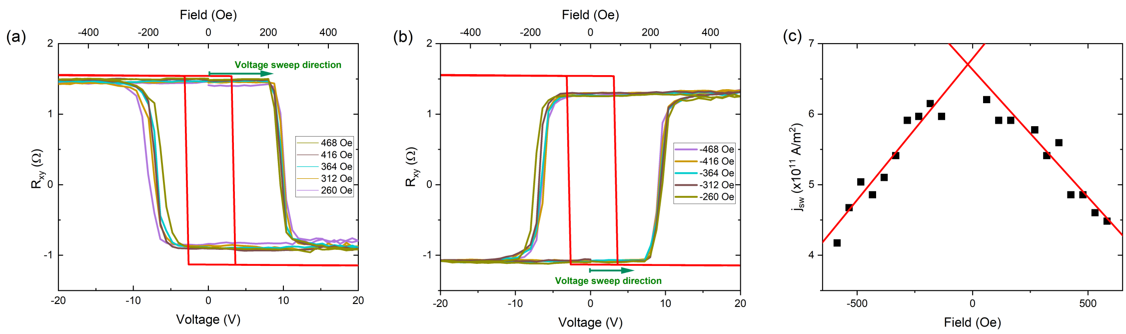

Figure 3.12: Measured loops for the Pt(4)/Co(1)/MgO system for representative values of the positive (a) and negative (b) external magnetic field. The red line indicates the AHE loops. The non-reaching of the CIMS loops to the full amplitude of the AHE loop and their non-ideally rectangular shape suggest the domain nature of the switching. (c) Densities of critical switching currents as a function of the external magnetic field. The red lines indicate the fit of Eq. 2.24

was varied from 0 V to a maximum positive value (+V_{max}), then to a maximum fixed negative value (-V_{max}), and finally to 0 V. This scheme made it possible to obtain a complete current switching loop characterized by two stable high (R_{high}) and low (R_{low}) resistance states, as shown in Fig.3.12(a,b).

Measurement of a series of switching loops for different values of the H_x field was necessary to determine numerous dependencies, such as critical switching currents as a function of the external magnetic field and the value of ExB in systems with antiferromagnets. For this purpose, after each CIMS loop was obtained, the magnetic field value was changed from a maximum positive value to a maximum negative value. Fig.3.12(a,b) presents a series of CIMS loops for different negative and positive values of the external magnetic field. The number of measurement points for each loop is the same and is selected in such a way as to be able to accurately determine the value of the voltage for which switching takes place. The value of this voltage was then converted to the current density flowing in the HM called the critical switching current j_{sw} (Fig.3.12(c)). From the slope of the $j_{sw}(H_x)$ relation it is possible to determine, e.g., SHA (θ_{SH}). For a detailed analysis, see Sect.4.3.2.

4

Results & Discussion

This chapter was divided into three subsections concerning three types of hybrid layers: HM/FM, FM/HM/FM, and HM/FM/AFM systems whose spin-orbit properties can be exploited in modern SOT-RAMs. First, we present the results of the study of several basic HM/FM bilayer systems with both in-plane magnetic anisotropy (IMA) and PMA where W, Pt, and Au were HM while Co and CoFeB were FM layer. The second of these treats the FM/HM/FM coupled system with the example of the Co/Pt/Co trilayer system. The last section describes the study of HM/FM/AFM systems with antiferromagnetic nickel oxide (NiO) applied to the top of the HM/FM bilayer system of Pt/Co/NiO and W/Co/NiO. In all of these systems mentioned above, we studied AMR, SMR, SHE, CIMS, and magnetization dynamics.

4.1 | Heavy metal/ferromagnet (HM/FM) system

The SMR effect, the theoretical basis of which is presented in Sect.2.1.1, was studied in a spectrum of ten different HM/FM thin film systems, differing in both the heavy metal layer and the ferromagnetic layer, characterized by different crystal structures. The magnetoresistance results of the investigated systems and the comparison between them and their properties are analyzed in the [P1]. The following subsection involves the study of the efficiency of spin current generation using the low-frequency angular harmonic method in systems with variable thicknesses of Pt and variable interfaces of the Pt-Ti superlattice. This part is based on the work of paper [P2]. The last subsection describes CIMS studies and analysis of magnetization switching loops based on a phenomenological model that considers Dzyaloshinskii–Moriya interaction (DMI).

4.1.1 | Spin Hall Magnetoresistance and Anisotropic Magnetoresistance

The study of the SMR effect in the HM/FM systems was carried out on a series of patterned bilayers in the form of Hall bar devices in which W, Pt and Au were HM layer, at the same time, Co and CoFeB were FM in different combinations: W/CoFeB, CoFeB/Pt, Au/CoFeB, W/Co, and Co/Pt heterostructures. The wedge thickness has the HM (t_{HM}) as well as FM layer (t_{FM}) that allows the fabrication of a matrix of devices. We measured magnetoresistance (MR = $\Delta R/R_0$) as a function of $t_{\mathrm{HM(FM)}}$ (see Figs.1 and 2 in [P1]). Due to the different crystallinity nature of the FM layer (while Co is crystalline (see Fig.S1 in the Supplementary Materials to [P1]), and CoFeB amorphous). In turn, changes in the thickness of the W layer (Fig.S1(b)) caused a transition from a disoriented crystalline β-W phase to an amorphous phase. This, in turn, caused an increase in resistance of the W layer, resulting in various interfacial properties and significant differences in the mutual contributions of AMR to SMR depending on the thickness of FM and HM.

A theoretical spin drift-diffusion model of SMR including the contribution AMR in metallic bilayers (for details see *Theory* section in [P1]) was fitted to the $\Delta R/R_0(t_{\mathrm{HM(FM)}})$ dependencies (see Fig.S3 in the Supplementary Materials to [P1]). This model allowed for the separation and estimation of the contributions of SMR and AMR to the total magnetoresistance signal. The more significant contribution of SMR was confirmed when HM was W (Fig.1(a) in [P1]) than in the case of Pt (Fig.1(b) in [P1]) or Au (Fig.1(c) in [P1]) due to the much higher SHA (θ_{SH}) in W (Tab. 1 in [P1]). The Au(t_{Au})/CoFeB showed a more outstanding contribution SMR to magnetoresistance than the CoFeB/Pt (t_{Pt}), even though Pt (Fig.1(b) in [P1]) has higher SHA than Au (Fig.1(c)). Due to the much lower resistivity of Au in relation to CoFeB than is the case in the system with Pt (see Tab. 1 in [P1]). In this case, more current flows through the HM, which increases the spin Hall response. Similarly, when the thickness of CoFeB is changed (Fig.1(e,f) in [P1]), the contribution of SMR dominates only in the W-based device (Fig.1(d) in [P1]), almost the whole range of FM thickness. In contrast, AMR dominates in systems with Pt (Fig.1(e) in [P1]) and Au (Fig.1(f) in [P1]), however, only for $t_{\mathrm{CoFeB}} > 4$ nm and $t_{\mathrm{CoFeB}} > 3$ nm, respectively. In smaller thicknesses, SMR contribution dominates over AMR.

We observed the opposite behavior in crystalline Co-based systems. Here, bilayers with varying thicknesses of W and Pt (Fig.2(a,b) in [P1]), with almost all contributions to magnetoresistance, come from AMR. This component (AMR) also dominates when t_{FM} is changed (Fig.2(c,d) in P1). This is due to the significant difference in the resistivities of the individual layers, especially in the wedge-shaped Co layer. It causes most of the charge current to flow through Co, leading to errors in determining SHA and negligibly small SMR values. Another reason for the inaccuracy of SMR determination is that W is structurally disoriented and highly resistive. At the same time, Co is crystalline, which affects the spin transport properties at the interface through differences in the crystal structure.

In summary, a theoretical spin-diffusion model for Co and CoFeB allowed determining the contribution of SMR and AMR to the total magnetoresistance. Comparing the results between systems will allow future optimization of spintronic devices to maximize the SMR effect, which is essential in systems based on the SOT effect.

www.nature.com/scientificreports

SCIENTIFIC REPORTS
natureresearch

Check for updates

OPEN

Optimization of spin Hall magnetoresistance in heavy-metal/ferromagnetic-metal bilayers

Łukasz Karwacki[1,2✉], Krzysztof Grochot[2,3✉], Stanisław Łazarski[2], Witold Skowroński[2], Jarosław Kanak[2], Wiesław Powroźnik[2], Józef Barnaś[1,4], Feliks Stobiecki[1] & Tomasz Stobiecki[2,3]

We present experimental data and their theoretical description on spin Hall magnetoresistance (SMR) in bilayers consisting of a heavy metal (H) coupled to in-plane magnetized ferromagnetic metal (F), and determine contributions to the magnetoresistance due to SMR and anisotropic magnetoresistance (AMR) in five different bilayer systems: W/$Co_{20}Fe_{60}B_{20}$, $Co_{20}Fe_{60}B_{20}$/Pt, Au/$Co_{20}Fe_{60}B_{20}$, W/Co, and Co/Pt. The devices used for experiments have different interfacial properties due to either amorphous or crystalline structures of constitutent layers. To determine magnetoresistance contributions and to allow for optimization, the AMR is explicitly included in the diffusion transport equations in the ferromagnets. The results allow determination of different contributions to the magnetoresistance, which can play an important role in optimizing prospective magnetic stray field sensors. They also may be useful in the determination of spin transport properties of metallic magnetic heterostructures in other experiments based on magnetoresistance measurements.

Spin Hall magnetoresistance (SMR) is a phenomenon that consists in resistance dependence on the relative orientation of magnetization and spin accumulation at the interface of ferromagnet and strong spin-orbit material (such as 5*d* metals[1–8], topological insulators[9], or some 2D systems [10]). In transition metals such as W and Pt, the spin accumulation results from spin current driven by the spin Hall effect (SHE)[11–14]. The spin current diffuses then into the ferromagnet or exerts a torque on the magnetization while being backscattered. Due to the inverse spin Hall effect (ISHE), the backscattered spin current is converted into a charge current that flows parallel to the bare charge current driven by external electric field, which effectively reduces the resistance[3,4]. One of the most important advantages of driving spin currents by SHE is that the spin currents can be induced by a charge current flowing in the plane of the sample[15]. This may remedy some obstacles on the road to further miniaturization of prospective electronic components, which have been encountered in spin-valves and magnetic tunnel junctions when the electric field is applied perpendicularly to interfaces. One of the drawbacks, however, is that the strength and effectiveness of such subtle effects depend strongly on the quality and spin properties of interfaces[16–23].

Although early SMR experiments were performed on heavy-metal/ferromagnetic-insulator bilayers[1], recent efforts are focused on the bilayers with ferromagnetic metallic layers, such as Co or $Co_{20}Fe_{60}B_{20}$ ones[5,7], which are currently more relevant for applications. When the magnetization is parallel to the spin accumulation, the spin current from the heavy-metal can easily diffuse into the ferromagnetic metal (influencing its spin transport properties and spin accumulation on the ferromagnetic metal side)[5,24–30]. This is especially important when an additional spin sink (another heavy-metal layer or an antiferromagnet) is on the other side of the ferromagnetic layer, where effects such as spin current interference might take place[6].

Moreover, as charge current flows in plane of the sample, additional phenomena may occur, such as anisotropic magnetoresistance (AMR) or anomalous Hall effect (AHE)[31–36]. These effects can obscure determination of spin transport parameters and make evaluation of the SMR contribution to the measured magnetoresistance more difficult. Since the determination of such transport properties as the spin Hall angle (which parameterizes

[1]Institute of Molecular Physics, Polish Academy of Sciences, ul. M. Smoluchowskiego 17, 60-179 Poznań, Poland. [2]Department of Electronics, AGH University of Science and Technology, Al. Mickiewicza 30, 30-059 Kraków, Poland. [3]Faculty of Physics and Applied Computer Science, AGH University of Science and Technology, al. Mickiewicza 30, 30-059 Kraków, Poland. [4]Faculty of Physics, Adam Mickiewicz University, ul. Uniwersytetu Poznańskiego 2, 61-614 Poznań, Poland. ✉email: karwacki@ifmpan.poznan.pl; grochot@agh.edu.pl

No.	Sample	ρ_0^{H} ($\mu\Omega$cm)	ρ_0^{F} ($\mu\Omega$cm)	$\lvert\theta_{\mathrm{SH}}\rvert$ (%)	θ_{AMR} (%)	λ_{H} (nm)	λ_{F} (nm)
W1	$\mathrm{W(5)/Co_{20}Fe_{60}B_{20}}(t_F)\mathrm{/Ta(1)}$	185	144	22.5 ± 0.4	0.19 ± 0.03	1.3^a	5^c
W2	$\mathrm{W}(t_H)\mathrm{/Co_{20}Fe_{60}B_{20}(5)/Ta(1)}$	166	144	21 ± 1	0.07 ± 0.08	1.3^a	5^c
W3	$\mathrm{W(5)/Co}(t_F)\mathrm{/Ta(1)}$	120	22	≈ 0	1.1 ± 0.3	1.3^a	7^c
W4	$\mathrm{W}(t_H)\mathrm{/Co(5)/Ta(1)}$	120	30	23 ± 2	0.69 ± 0.02	1.3^a	7^c
P1	$\mathrm{Co_{20}Fe_{60}B_{20}}(t_F)\mathrm{/Pt(3)}$	95	102	16.0 ± 0.2	0.38 ± 0.01	2.2^a	5^c
P2	$\mathrm{Co_{20}Fe_{60}B_{20}(5)/Pt}(t_H)$	151	161	6 ± 2	0.36 ± 0.03	2.2^a	5^c
P3	$\mathrm{Co}(t_F)\mathrm{/Pt(4)}$	55	18	≈ 0	0.5 ± 0.1	2.2^a	7^b
P4	$\mathrm{Co(5)/Pt}(t_H)$	24	57	9 ± 1	1.5 ± 0.1	2.2^a	7^b
A1	$\mathrm{Ti(2)/Au(5)/Co_{20}Fe_{60}B_{20}}(t_F)\mathrm{/Ti(1.5)}$	24	96	3.3 ± 0.1	0.210 ± 0.008	1.6^a	5^c
A2	$\mathrm{Ti(2)/Au}(t_H)\mathrm{/CoFeB(5)/Ti(1.5)}$	15	96	5 ± 1	0.33 ± 0.05	1.6^a	5^c

Table 1. Composition of samples, and resistivities of heavy metal and ferromagnetic layers. Numbers in parentheses next to material symbol denote thickness (in nm) of the corresponding layer; parameters used for fitting the model to experimental data. [a]Ref. 38, [b]Ref. 39, [c]Ref. 40.

strength of the spin Hall effect) and spin diffusion length in different experimental schemes, for instance in spin-orbit torque ferromagnetic resonance (SOT-FMR)[37,38], relies heavily on the magnetoresistive properties of a system, it is important to properly determine all the contributions to magnetoresistance.

Here, we revisit the theory of spin Hall magnetoresistance in metallic bilayers by explicitly including the contribution from AMR into the spin drift-diffusion theory for the ferromagnetic metal layer. The expressions for magnetoresistance are then fitted to the data obtained from resistance measurements on heavy-metal (H)/ferromagnet (F) bilayers, where H: W, Pt, Au, while F: Co, $\mathrm{Co_{20}Fe_{60}B_{20}}$. This allows us to determine more accurately contributions from various magnetotransport phenomena occurring in metallic bilayers where the spin Hall effect is the driving source. Such analysis may also be useful in the efforts to optimize prospective devices for information technology.

Results

This section is divided into two sections depending on the ferromagnetic material used in the bilayer. As $\mathrm{Co_{20}Fe_{60}B_{20}}$ is amorphous and Co is crystalline, they present differently in magnetoresistance experiments and can influence the estimation of spin transport properties, especially when the thickness of ferromagnetic material is varied while thickness of heavy metal remains constant.

The spin Hall angles obtained from fitting for W, Pt, and Au, shown in Table 1, agree quite well with spin Hall angles for thick heavy metals obtained in spin-orbit torque ferromagnetic resonance experiments used in our previous papers[38,41]. Larger spin Hall angle for Pt-based bilayer P1, where the thickness of ferromagnetic metal varies, can be attributed to, f.i., changes in spin-mixing conductivity[17], which, as described above, we do not take into account in current approach.

$\mathrm{Co_{20}Fe_{60}B_{20}}$-based bilayers. Figure 1 shows relative magnetoresistance as a function of heavy metal (Fig. 1a–c) and ferromagnetic metal (Fig. 1d–f) layer thicknesses for $\mathrm{H/Co_{20}Fe_{60}B_{20}}$ bilayers where H: W, Pt, Au.

Dependence of magnetoresistance on heavy-metal thickness, with fixed $t_{\mathrm{F}} = 5$ nm, shown in Fig. 1a–c indcates, as expected, that SMR is the largest contribution to magnetoresistance in heterostructure with W as a heavy metal layer due to larger spin Hall angle of W, $|\theta_{\mathrm{SH}}| \approx 21\%$, compared to Pt, $|\theta_{\mathrm{SH}}| \approx 6\%$, and to Au, $|\theta_{\mathrm{SH}}| \approx 4\%$. Consequently, in Pt and Au bilayers AMR dominates over SMR.

The dependence of magnetoresistance on ferromagnetic layer thickness is shown in Fig. 1d–f. For 5 nm–thick W as heavy metal layer, shown in Fig. 1d SMR is still the dominating contribution to the total magnetoresistance in the studied thickness range. For device with 3 nm–thick Pt, the SMR for $t_{\mathrm{F}} \gtrsim 2$ nm is smaller than AMR. Note that for both W- and Pt-based bilayers the model fit and theoretical prediction do not describe the behavior of MR for $t_{\mathrm{F}} \lesssim 2$ nm, which can be attributed to strong dependence of the interfacial parameters such as spin-mixing conductance on thickness. Due to small spin Hall angle, SMR in Au-based is rather small and MR is dominated by AMR.

Co-based bilayers. Magnetoresistance and relative magnetoresistance in H/Co bilayers (H: W, Pt) are shown in Fig. 2 as a function of heavy metal (Fig. 2a,b) and ferromagnetic metal (Fig. 2c,d) layer thicknesses.

For W and Pt bilayers with varying heavy metal thickness and $t_{\mathrm{F}} = 5$ nm, shown in Fig. 2, the total magnetoresistance is mostly due to AMR, in contrast to $\mathrm{Co_{20}Fe_{60}B_{20}}$–based bilayers described in the previous subsection.

For bilayers with varying ferromagnetic metal (Co) thickness, shown in Fig. 2c,d, the total magnetoresistance is also largely dominated by AMR.

Due to existence of a magnetic dead layer, disoriented crystalline structure of Co, and due to the fact that magnetization of Co does not lie completely in-plane of the sample for small thicknesses we introduced the magnetically effective thickness, $t_{\mathrm{F,eff}}$, of Co layer. More details on some of these aspects can be found in Supplementary Information. Since the thickness of heavy-metal is fixed and the thickness of the ferromagnetic metal

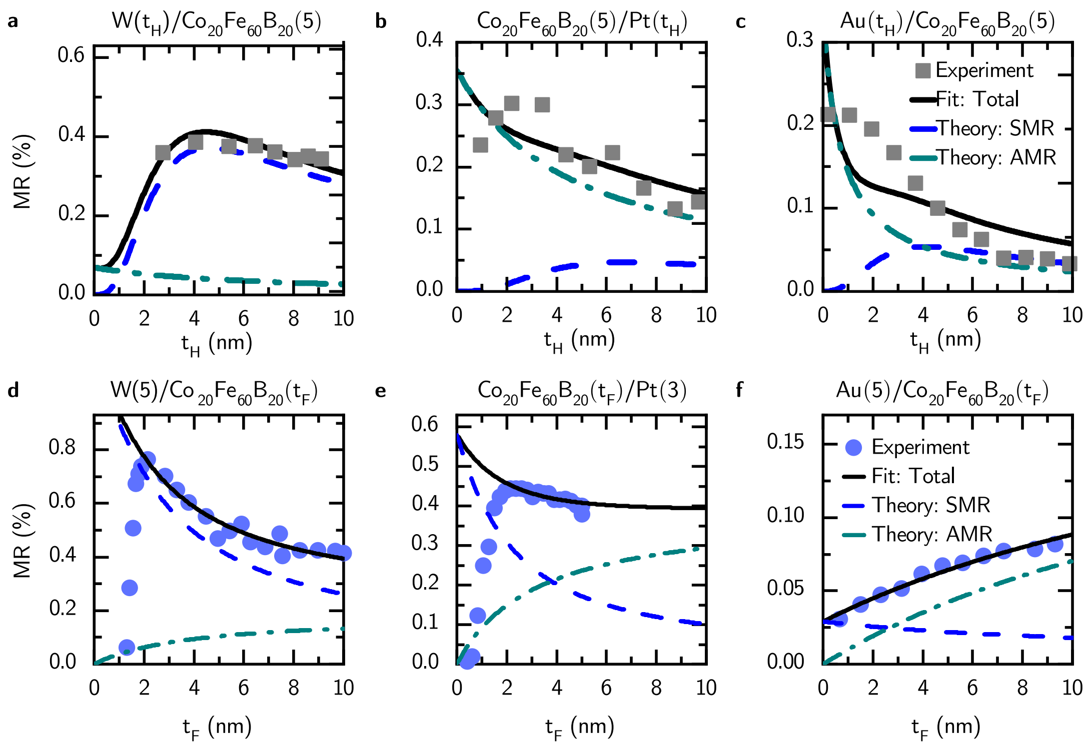

Fig. 1. Relative magnetoresistance, *MR*, as a function of heavy metal's thickness, t_H, for: **a**, W/$Co_{20}Fe_{60}B_{20}$, **b**, $Co_{20}Fe_{60}B_{20}$/Pt, and **c**, Au/$Co_{20}Fe_{60}B_{20}$ bilayers, and as a function of ferromagnetic metal's thickness, t_F, for: **d**, W(5)/$Co_{20}Fe_{60}B_{20}$, **e**, $Co_{20}Fe_{60}B_{20}$/Pt(3), and **f**, Au(5)/$Co_{20}Fe_{60}B_{20}$ bilayers. Parameters used for theoretical curves are gathered in Table 1.

increases, the large differences in resistivities result in larger portion of charge current flowing into Co leading to negligible SMR—thus preventing proper estimation of spin Hall angle of both W and Pt.

Discussion

Our systematic analysis of magnetoresistance in in-plane magnetized heavy-metal/ferromagnetic-metal bilayers with crystalline Co and amorphous $Co_{20}Fe_{60}B_{20}$ has shown that proper choice of ferromagnetic-metal is crucial to the optimization of spin Hall magnetoresistance.

As shown in previous section, although W has larger spin Hall angle than Pt and Au, the magnetoresistance of W/$Co_{20}Fe_{60}B_{20}$ and even W/Co (for thin W) bilayers can be lower than that of Co/Pt bilayer due to high AMR contribution in the latter. This also leads to possible underestimation of SMR contribution which is lower in W/Co than in W/$Co_{20}Fe_{60}B_{20}$ bilayers, one of the main reasons for which is quite large difference in resistivities of both layers (see Table 1), due to the fact that here β-W phase is disoriented (amorphous-like) resulting in more current flowing through Co than W and on average smaller spin Hall effect (see Supplementary Information). Moreover, due to the fact that here W is mostly amorphous and Co crystalline, a different interface properties between these materials than between crystalline-crystalline or amorphous-amorphous bilayers can influence spin transport as well.

For materials with stronger spin-orbit coupling (W and Pt) and comparable resistivities to $Co_{20}Fe_{60}B_{20}$, one obtains higher magnetoresistance response with thinner ferromagnet. In the case of Au-based bilayer, whose resistivity is smaller than that of $Co_{20}Fe_{60}B_{20}$, one obtains higher magnetoresistance with thicker ferromagnet. The predicted SMR contribution for Au/$Co_{20}Fe_{60}B_{20}$ can be higher than the SMR contribution for $Co_{20}Fe_{60}B_{20}$/Pt due to the fact that larger current density flows through Au than through Pt, thus increasing the spin Hall response.

The estimation of SMR in the case of metallic bilayers is hindered by large differences in resistivity of the constituent metallic layers. Since in this case AMR is strongly dominating, the total MR increases with increasing effective thickness of Co.

In conclusion, we have developed an extended model of magnetoresistance for magnetic metallic bilayers with in-plane magnetized ferromagnets, which explicitly includes SMR and AMR contributions. The model was then fitted to experimental data on magnetoresistance in: W/$Co_{20}Fe_{60}B_{20}$, $Co_{20}Fe_{60}B_{20}$/Pt, Au/$Co_{20}Fe_{60}B_{20}$, W/Co,

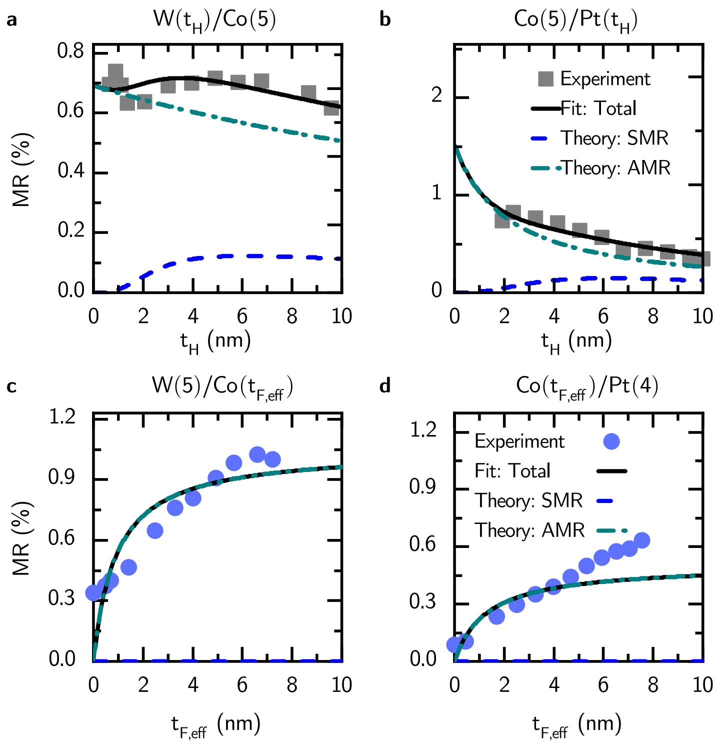

Fig. 2. Relative magnetoresistance, *MR*, as a function of heavy metal's thickness, t_H, for: **a**, W(t_H)/Co(5), **b**, Co(5)/Pt(t_H) bilayers, and as a function of ferromagnetic metal's effective thickness, $t_{F,eff}$, for: **c**, W(5)/Co($t_{F,eff}$), **d**, Co($t_{F,eff}$)/Pt(4) bilayers. Parameters used for theoretical curves are gathered in Table 1.

Co/Pt heterostructures, to estimate the strength of SMR and AMR effects. In particular, we have compared the influence of amorphous ferromagnet ($Co_{20}Fe_{60}B_{20}$) and crystalline ferromagnet (Co) on total magnetoresistance and analyzed the dependence of magnetoresistance on ferromagnet's thickness, which allows for better optimization of magnetic bilayers.

These results allow for a more accurate estimation of different contributions to magnetoresistance in magnetic metallic systems, which is important for applications in, e. g., spintronic SOT-devices[42] or in other experimental schemes that rely on magnetoresistance measurements in evaluation of the spin transport properties.

Methods

Experiment. Table 1 shows the multilayer systems that were produced for SMR studies. The magnetron sputtering technique was used to deposit multilayers on the Si/SiO_2 thermally oxidized substrates. Thickness of wedged layers were precisely calibrated by X-ray reflectivity (XRR) measurements. The details of sputtering deposition parameters as well as structural phase analysis of highly resistive W and Pt layers can be found in our recent papers[38,41]. Au in Au/$Co_{20}Fe_{60}B_{20}$ bilayers is (111) fcc textured similarly as Pt in $Co_{20}Fe_{60}B_{20}$/Pt bilayer[38]. In turn, structure analysis of the hcp-Co crystal phases grown on disoriented β-W can be found in the Supplementary Information.

After deposition, multilayered systems were nanostructured using either electron-beam lithography or optical lithography, ion etching and lift-off. The result was a matrix of Hall bars and strip nanodevices for further electrical measurements. The sizes of produced structures were: 100 μm x 10 μm or 100 μm x 20 μm. In order to ensure good electrical contact with the Hall bars and strips, Al(20)/Au(30) contact pads with dimensions of 100 μm x 100 μm were deposited. Appropriate placement of the pads allows rotation of the investigated sample and its examination at any angle with respect to the external magnetic field in a dedicated rotating probe station using a four-points probe. The constant magnetic field, controlled by a gaussmeter exceeded magnetization saturation in plane of the sample and the sample was rotated in an azimuthal plane from $-120°$ to $+100°$.

The resistance of the system was measured with a two- and four-point technique using Keithley 2400 sourcemeters and Agilent 34401A multimeter. As shown in Supplementary Information, resistances of bilayers with amorphous ferromagnet $Co_{20}Fe_{60}B_{20}$ are about one order higher than these with polycrystalline Co. The same results were obtained using both methods. The thickness-dependent resistivity of individual layers was determined by method described in Ref. 7, and by a parallel resistors model. For more details on resistivity measurements we refer the reader to Supplementary Information.

Theory. To properly assess all contributions to magnetoresistance one should find first the average current density flowing through the whole heterostructure. This approach, in contrast to the one described in Ref. 5 allows one to properly describe magnetoresistance in more complicated heterostructures, where *ad hoc* addition of consitutent terms might lead to oversimplification and improper determination of different components in the magnetoresistance. Moreover, calculating average current density allows for a phenomenological description of how various magnetoresistance effects depend on thicknesses of the constituent layers. The drawback, however, is the necessary simplification of fitting parameters, which we discuss in more detail in the next subsection devoted to fitting procedure.

Only the component flowing along the normal to interfaces is relevant and will be taken into account in the following, i.e.

$$\mathbf{j}_s^{\mathrm{H}}(z) = -\frac{\theta_{\mathrm{SH}}}{\rho_0^{\mathrm{H}}}\hat{\mathbf{e}}_z \times \mathbf{E} + \frac{1}{2e\rho_0^{\mathrm{H}}}\frac{\partial \boldsymbol{\mu}_s^{\mathrm{H}}(z)}{\partial z}\,. \tag{1}$$

Here θ_{SH} is the spin Hall angle, ρ_0^{H} is the bare resistivity of the heavy metal, and $\boldsymbol{\mu}_s^{\mathrm{H}}(z)$ is the spin accumulation that is generally z-dependent.

The charge current density in the heavy-metal (H) layer, in turn, can be written in the form

$$\mathbf{j}_c^{\mathrm{H}}(z) = \frac{1}{\rho_0^{\mathrm{H}}}\mathbf{E} + \frac{\theta_{\mathrm{SH}}}{2e\rho_0^{\mathrm{H}}}\hat{\mathbf{e}}_z \times \frac{\partial \boldsymbol{\mu}_s^{\mathrm{H}}(z)}{\partial z}\,, \tag{2}$$

and contains the bare charge current density and the current due to inverse spin Hall effect. Note, that the spin current in general can induce charge current also flowing along the axes x and y. However, due to lateral dimensions of the samples much larger than the layer thicknesses and spin diffusion lengths, those additional components can be neglected.

Thus, one can write[28,29]:

$$\mathbf{j}_s^{F}(z) = \frac{1}{2e\rho_0^{\mathrm{F}}}\nabla\mu_s^{\mathrm{F}}(z) + \frac{\beta}{2e\rho_0^{\mathrm{F}}}\nabla\mu_c^{\mathrm{F}}(\mathbf{r}) - \frac{\theta_{\mathrm{AMR}}}{2e\rho_0^{\mathrm{F}}}\hat{\mathbf{m}}\left[\hat{\mathbf{m}}\cdot\nabla\mu_s^{\mathrm{F}}(z)\right], \tag{3}$$

in which θ_{AMR} is the AMR angle, defined as $\theta_{\mathrm{AMR}} = \sigma_{\mathrm{AMR}}\rho_0^{\mathrm{F}}$, while $\mu_c^{\mathrm{F}}(\mathbf{r}) = 2e\mathbf{E}\cdot\mathbf{r} + \mu_c^{F}(z)$ is the electrochemical potential.

Charge current density in the ferromagnetic layer (F) can be written as[28,29],

$$\mathbf{j}_c^{F}(z) = \frac{1}{2e\rho_0^{\mathrm{F}}}\nabla\mu_c^{\mathrm{F}}(\mathbf{r}) + \frac{\beta}{2e\rho_0^{\mathrm{F}}}\nabla\mu_s^{\mathrm{F}}(z) - \frac{\theta_{\mathrm{AMR}}}{2e\rho_0^{\mathrm{F}}}\hat{\mathbf{m}}\left[\hat{\mathbf{m}}\cdot\nabla\mu_c^{\mathrm{F}}(\mathbf{r})\right]. \tag{4}$$

Note, in the above equations the current densities in both H and F layers we assumed as linear response to electric field, i.e. we neglected the so-called unidirectional spin Hall magnetoresistance effect[24–27].

The spin current $\mathbf{j}_s^{\mathrm{HF}}$ flowing through the heavy-metal/ferromagnet interface is given by the following expression [43]:

$$\mathbf{j}_s^{\mathrm{HF}} = G_F\left[\left(\boldsymbol{\mu}_s^{\mathrm{F}}(0) - \boldsymbol{\mu}_s^{\mathrm{H}}(0)\right)\cdot\hat{\mathbf{m}}\right]\hat{\mathbf{m}} + G_r\hat{\mathbf{m}}\times\hat{\mathbf{m}}\times\boldsymbol{\mu}_s^{\mathrm{H}}(0)\,. \tag{5}$$

Here $G_F = (1-\gamma^2)(G_\uparrow + G_\downarrow)/2$ with γ defined as $\gamma = (G_\uparrow - G_\downarrow)/(G_\uparrow + G_\downarrow)$ and $G_\uparrow$ and $G_\downarrow$ denoting the interface conductance for spin-$\uparrow$ and spin-$\downarrow$. Furthermore, $G_r \equiv \mathrm{Re}G_{\mathrm{mix}}$ and $G_i \equiv \mathrm{Im}G_{\mathrm{mix}}$, where G_{mix} is the so-called spin-mixing conductance. Note, that we neglect explicitly a contribution from the interfacial Rashba-Edelstein spin polarization[38]. A strong interfacial spin-orbit contribution which induces spin-flip processes can also be combined with the interfacial spin conductance G_F as a spin-conductance reducing parameter $1-\eta$, with $\eta = 0$ for no interfacial spin-orbit coupling, and $\eta = 1$ for maximal spin-orbit coupling. Note, that this reduction could also be attributed to the magnetic proximity effect, especially in the case of Pt-based heterostructures[13], however recent studies suggest its irrelevance for spin-orbit-torque–related experiments[22]. In the following discussion we assume $\eta = 0$ and treat G_F as an effective parameter.

To find charge and spin currents we need to find first the spin accumulation at the H/F interface and also at external surface/interfaces. This can be found from the following boundary conditions:

$$\mathbf{j}_s^{\mathrm{H}}(z = -t_H) = 0\,, \tag{6a}$$

$$\mathbf{j}_s^{\mathrm{F}}(z = t_F) = 0\,, \tag{6b}$$

$$\mathbf{j}_s^{\mathrm{H}}(z = 0) = \mathbf{j}_s^{\mathrm{HF}}\,, \tag{6c}$$

$$j_{s,z}^{\mathrm{F}}(z = 0) = \mathbf{j}_s^{\mathrm{HF}}\cdot\hat{\mathbf{m}}\,. \tag{6d}$$

Having found electrochemical potential and spin accumulation from general solution

$$\mu_s^{F,H}(z) = \mathbf{A}_{F,H}e^{-z/\lambda_{F,H}} + \mathbf{B}_{F,H}e^{z/\lambda_{F,H}}\,, \tag{7}$$

where $\mathbf{A}_{F,H}$ and $\mathbf{B}_{F,H}$ are coefficients to be determined and $\lambda_{F,H}$ is the spin diffusion length in ferromagnet or heavy metal, one can find the longitudinal in-plane components of the averaged charge current $\mathbf{j}(\hat{\mathbf{m}})$ from the formula:

$$j_{xx}(\hat{\mathbf{m}}) = \frac{1}{t_H + t_F}\left[\int_{t_H} dz\hat{\mathbf{e}}_x \cdot \mathbf{j}_c^{\mathrm{H}}(z) + \int_{t_F} dz\hat{\mathbf{e}}_x \cdot \mathbf{j}_c^{\mathrm{F}}(z)\right]. \tag{8}$$

The total longitudinal charge current can be written down in the Ohm's-law form,

$$j_{xx}(\hat{\mathbf{m}}) = \frac{1}{\rho_{xx}(\hat{\mathbf{m}})} E_x\,, \tag{9}$$

where the longitudinal resistivity is defined as follows:

$$\frac{1}{\rho_{xx}(\hat{\mathbf{m}})} = \sigma_0 + \sigma_x m_x^2 + \sigma_y m_y^2 \tag{10}$$

with

$$\sigma_0 \approx \frac{\rho_0^{\mathrm{F}} t_H + \rho_0^{\mathrm{H}} t_F}{\rho_0^{\mathrm{F}}\rho_0^{\mathrm{H}} t_F + \rho_0^{\mathrm{F}}\rho_0^{\mathrm{H}} t_H} \tag{11}$$

$$\begin{aligned}\sigma_x &= \frac{\theta_{\mathrm{SH}}^2}{\rho_0^{\mathrm{H}}}\frac{g_{\mathrm{DL}}\lambda_{\mathrm{H}}}{t_F + t_H}\tanh\left(\frac{t_H}{2\lambda_{\mathrm{H}}}\right) - \frac{\theta_{\mathrm{AMR}}}{\rho_0^{\mathrm{F}}}\frac{t_F}{t_F + t_H}\,,\\ &= \sigma_x^{\mathrm{SH}} + \sigma_x^{\mathrm{AMR}}\,,\end{aligned} \tag{12}$$

$$\sigma_y = \frac{\theta_{\mathrm{SH}}^2}{\rho_0^{\mathrm{H}}}\frac{g_H^{\mathrm{F}}\lambda_{\mathrm{H}}}{t_F + t_H}\tanh\left(\frac{t_H}{2\lambda_{\mathrm{H}}}\right). \tag{13}$$

In the above expressions the following dimensionless coefficients have been introduced to simplify the notation:

$$g_{\mathrm{DL}} = \left[1 - \mathrm{sech}\left(\frac{t_H}{\lambda_{\mathrm{H}}}\right)\right]\frac{g_r(1+g_r) + g_i^2}{(1+g_r)^2 + g_i^2}\,, \tag{14}$$

$$g_{r,i} = 2G_{r,i}\rho_0^{\mathrm{H}}\lambda_{\mathrm{H}}\coth\left(\frac{t_H}{\lambda_{\mathrm{H}}}\right), \tag{15}$$

$$g_H^{\mathrm{F}} = \left[1 - \mathrm{sech}\left(\frac{t_H}{\lambda_{\mathrm{H}}}\right)\right]\frac{1}{1 + \left(\frac{1}{2G_F\lambda_{\mathrm{H}}\rho_0^{\mathrm{H}}} + \gamma_H^{\mathrm{F}}\right)\tanh\left(\frac{t_H}{\lambda_{\mathrm{H}}}\right)}\,, \tag{16}$$

$$\gamma_H^{\mathrm{F}} = \frac{\lambda_{\mathrm{F}}\rho_0^{\mathrm{F}}}{\lambda_{\mathrm{H}}\rho_0^{\mathrm{H}}(1-\beta^2)}\coth\left(\frac{t_F}{\lambda_{\mathrm{F}}}\right). \tag{17}$$

With the resistivity defined in Eq. (10) we can now define magnetoresistance,

$$MR = \frac{\rho_{xx}(\hat{\mathbf{m}} \parallel \hat{\mathbf{e}}_x) - \rho_{xx}(\hat{\mathbf{m}} \parallel \hat{\mathbf{e}}_y)}{\rho_{xx}(\hat{\mathbf{m}} \parallel \hat{\mathbf{e}}_x)}\,, \tag{18}$$

Taking into account Eqs. (11)-(13), the above formula can be written as,

$$MR \approx \frac{\sigma_y - \sigma_x}{\sigma_0}\,. \tag{19}$$

In order to compare the models with and without AMR, we define SMR as:

$$SMR = MR\Big|_{\theta_{\mathrm{AMR}}\to 0} = \frac{\sigma_y^{\mathrm{SH}} - \sigma_x^{\mathrm{SH}}}{\sigma_0}\,, \tag{20}$$

which simplifies our model to that introduced by Kim et al. 5. We also define AMR coefficient

$$AMR = MR\Big|_{\theta_{\mathrm{SH}}\to 0} = -\frac{\sigma_x^{\mathrm{AMR}}}{\sigma_0}\,. \tag{21}$$

Fitting procedure. In order to analyze the experimental data in light of our extended model, we fit Eq. (19) to the data on relative magnetoresistance. We have assumed some constant values according to literature and our previous works: spin polarization at Fermi level of both Co and $Co_{20}Fe_{60}B_{20}$ are taken as $\beta = 0.3$. Note that this value can range in $Co_{20}Fe_{60}B_{20}$ from 0.1 to 0.6[40] and can influence the fit of the model to the data. We have assumed spin diffusion lengths in Pt and W from our previous papers[38,41] to be 2.2 nm and 1.3 nm, respectively. For $Co_{20}Fe_{60}B_{20}$ we assumed constant room-temperature value of $\lambda_F \approx 5$ nm [40] and for Co $\lambda_F \approx 7$ nm[39]. Note, that we have assumed constant effective spin diffusion lengths for the constituent layers obtained from our previous analyses [38,41]. In general, however, these parameters can depend on temperature or thickness of the layers[44,45]. This fact can lead to underestimation of spin diffusion lengths and overestimation of the spin Hall angles. One of the remedies might be to use effective thickness-dependent parameters[45]. However, such approaches are still mostly empirical and not based on proper theoretical grounding and as such have their own limitations.

Moreover we have assumed transparent contacts for spin transport, i.e. $G_F \to \infty$ and $G_r \to \infty$, and also assumed G_i to be negligible. These assumptions are mostly valid for metallic interfaces. However, these parameters can also strongly depend on type of interface, i.e. they can differ in amorphous/crystalline (f.i. $Co_{20}Fe_{60}B_{20}$/Pt), crystalline/crystalline (Co/Pt), and amorphous-like/amorphous (f.i. W/$Co_{20}Fe_{60}B_{20}$) heterostructures.

We have assumed spin Hall angle θ_{SH} and AMR coefficient θ_{AMR} as fitting parameters and the results of fitting the model to the experimental data on magnetoresistance are gathered in Table 1. Morevoer, we have assumed anomalous Hall effect to be negligible in the in-plane magnetized systems considered in the paper. This effect might play an important role for ferromagnets with stronger spin-orbit coupling or ferromagnets tilted out of plane[28–30].

Received: 7 February 2020; Accepted: 8 June 2020
Published online: 01 July 2020

References

1. Althammer, M. et al. Quantitative study of the spin Hall magnetoresistance in ferromagnetic insulator/normal metal hybrids. Phys. Rev. B 87, 224401 (2013).
2. Nakayama, H. et al. Spin Hall magnetoresistance induced by a nonequilibrium proximity effect. Phys. Rev. Lett. 110, 206601 (2013).
3. Chen, Y.-T. et al. Theory of spin Hall magnetoresistance. Phys. Rev. B 87, 144411 (2013).
4. Chen, Y.-T. *et al.* Theory of spin Hall magnetoresistance (SMR) and related phenomena. *J. Phys. Condens. Matt.***28**, 103004 (2016).
5. Kim, J., Sheng, P., Takahashi, S., Mitani, S. & Hayashi, M. Spin Hall magnetoresistance in metallic bilayers. Phys. Rev. Lett. 116, 097201 (2016).
6. Choi, J.-G., Lee, J. W. & Park, B.-G. Spin Hall magnetoresistance in heavy-metal/metallic-ferromagnet multilayer structures. Phys. Rev. B 96, 174412 (2017).
7. Kawaguchi, M., Towa, D., Lau, Y. C., Takahashi, S. & Hayashi, M. Anomalous spin Hall magnetoresistance in Pt/Co bilayers. Appl. Phys. Lett. 112, 202405 (2018).
8. Avci, C. O., Beach, G. S. D. & Gambardella, P. Effects of transition metal spacers on spin-orbit torques, spin hall magnetoresistance, and magnetic anisotropy of pt/co bilayers. *Phys. Rev. B***100**, (2019).
9. Lv, Y. et al. Unidirectional spin-Hall and Rashba-Edelstein magnetoresistance in topological insulator-ferromagnet layer heterostructures. Nat. Commun. 9, 111 (2018).
10. Narayanapillai, K. et al. Interfacial Rashba magnetoresistance of the two-dimensional electron gas at the LaAlO3 / SrTiO3 interface. Phys. Rev. B 96, 064401 (2017).
11. Hirsch, J. E. Spin Hall effect. Phys. Rev. Lett. 83, 1834–1837 (1999).
12. Dyakonov, M. I. Magnetoresistance due to edge spin accumulation. Phys. Rev. Lett. 99, 126601 (2007).
13. Huang, S. Y. et al. Transport magnetic proximity effects in platinum. Phys. Rev. Lett. 109, 107204 (2012).
14. Sinova, J., Valenzuela, S. O., Wunderlich, J., Back, C. H. & Jungwirth, T. Spin Hall effects. Rev. Mod. Phys. 87, 1213 (2015).
15. Liu, Y., Zhou, B. & Zhu, J.-G. Field-free magnetization switching by utilizing the spin Hall effect and interlayer exchange coupling of iridium. Sci. Rep. 9, 325 (2019).
16. Kobs, A. et al. Anisotropic interface magnetoresistance in Pt/Co/Pt sandwiches. Phys. Rev. Lett. 106, 217207 (2011).
17. Pai, C.-F., Ou, Y., Vilela-Leão, L. H., Ralph, D. C. & Buhrman, R. A. Dependence of the efficiency of spin Hall torque on the transparency of Pt/ferromagnetic layer interfaces. Phys. Rev. B 92, 064426 (2015).
18. Zhang, W., Han, W., Jiang, X., Yang, S.-H. & Parkin, S. S. P. Role of transparency of platinum–ferromagnet interfaces in determining the intrinsic magnitude of the spin Hall effect. Nat. Phys. 11, 496–502 (2015).
19. Zhang, S. S.-L., Vignale, G. & Zhang, S. Anisotropic magnetoresistance driven by surface spin-orbit scattering. Phys. Rev. B 92, 024412 (2015).
20. Tokaç, M. et al. Interfacial contribution to thickness dependent in-plane anisotropic magnetoresistance. AIP Advances 5, 127108 (2015).
21. Tokaç, M. et al. Interfacial structure dependent spin mixing conductance in cobalt thin films. Phys. Rev. Lett. 115, 056601 (2015).
22. Zhu, L. J., Ralph, D. C. & Buhrman, R. A. Irrelevance of magnetic proximity effect to spin-orbit torques in heavy-metal/ferromagnet bilayers. Phys. Rev. B 98, 134406 (2018).
23. Amin, V. P., Zemen, J. & Stiles, M. D. Interface-generated spin currents. Phys. Rev. Lett. 121, 136805 (2018).
24. Avci, C. O. et al. Unidirectional spin Hall magnetoresistance in ferromagnet/normal metal bilayers. Nat. Phys. 11, 570–575 (2015).
25. Avci, C. O. et al. Magnetoresistance of heavy and light metal/ferromagnet bilayers. Appl. Phys. Lett. 107, 192405 (2015).
26. Zhang, S. S.-L. & Vignale, G. Theory of unidirectional spin Hall magnetoresistance in heavy-metal/ferromagnetic-metal bilayers. Phys. Rev. B 94, 140411(R) (2016).
27. Avci, C. O., Mendil, J., Beach, G. S. D. & Gambardella, P. Origins of the unidirectional spin Hall magnetoresistance in metallic bilayers. Phys. Rev. Lett. 121, 087207 (2018).
28. Taniguchi, T., Grollier, J. & Stiles, M. D. Spin-transfer torques generated by the anomalous Hall effect and anisotropic magnetoresistance. Phys. Rev. Appl. 3, 044001 (2015).
29. Taniguchi, T. Magnetoresistance generated from charge-spin conversion by anomalous Hall effect in metallic ferromagnetic/nonmagnetic bilayers. Phys. Rev. B 94, 174440 (2016).
30. Yang, Y. et al. Anomalous Hall magnetoresistance in a ferromagnet. Nat. Commun. 9, 2255 (2018).
31. Jan, J.-P. Galvamomagnetic and thermomagnetic effects in metals. In *Solid State Physics*, 1–96 (Elsevier, 1957).
32. McGuire, T. & Potter, R. Anisotropic magnetoresistance in ferromagnetic 3d alloys. IEEE Trans. Magn. 11, 1018–1038 (1975).
33. Bass, J. & Pratt, W. P. Spin-diffusion lengths in metals and alloys, and spin-flipping at metal/metal interfaces: an experimentalist's critical review. *J. Phys. Condens. Mat.***19**, 183201 (2007).

34. Bechthold, P. S. Galvanomagnetic transport: from Hall effect to AMR. In Blügel, S., Bürgler, D., Morgenstern, M., Schneider, C. M. & Waser, R. (eds.) Spintronics - From GMR to Quantum Information. Institute of Solid State Research, Forschungszentrum Jülich (Forschungszentrum Jülich GmbH, Jülich, 2009).
35. Nagaosa, N., Sinova, J., Onoda, S., MacDonald, A. H. & Ong, N. P. Anomalous Hall effect. Rev. Mod. Phys. 82, 1539 (2010).
36. Iihama, S. et al. Spin-transfer torque induced by the spin anomalous Hall effect. Nat. Electron. 1, 120–123 (2018).
37. Liu, L., Moriyama, T., Ralph, D. C., & Buhrman, R. A. Spin-torque ferromagnetic resonance induced by the spin Hall effect. Phys. Rev. Lett. 106, 036601 (2011).
38. Skowroński, W. et al. Determination of spin Hall angle in heavy-metal/Co-Fe-B-based heterostructures with interfacial spin-orbit fields. Phys. Rev. Appl. 11, 024039 (2019).
39. Zahnd, G. et al. Spin diffusion length and polarization of ferromagnetic metals measured by the spin-absorption technique in lateral spin valves. Phys. Rev. B 98, 174414 (2018).
40. Ahn, C., Shin, K. H. & Pratt, W. P. Magnetotransport properties of CoFeB and Co/Ru interfaces in the current-perpendicular-to-plane geometry. Appl. Phys. Lett. 92, 102509 (2008).
41. Łazarski, S. et al. Field-free spin-orbit-torque switching in Co/Pt/Co multilayer with mixed magnetic anisotropies. Phys. Rev. Appl. 12, 014006 (2019).
42. Manchon, A. *et al.* Current-induced spin-orbit torques in ferromagnetic and antiferromagnetic systems. *Rev. Mod. Phys.***91**, (2019).
43. Brataas, A., Bauer, G. & Kelly, P. Non-collinear magnetoelectronics. Phys. Rep. 427, 157–255 (2006).
44. Cecot, M. et al. Influence of intermixing at the Ta/CoFeB interface on spin hall angle in Ta/CoFeB/MgO heterostructures. Sci. Rep. 7, 968 (2017).
45. Swindells, C., Hindmarch, A. T., Gallant, A. J. & Atkinson, D. Spin transport across the interface in ferromagnetic/nonmagnetic systems. Phys. Rev. B 99, 064406 (2019).

Acknowledgements

This work is supported by the National Science Centre in Poland Grant UMO-2016/23/B/ST3/01430 (SPINORBITRONICS). WS acknowledges National Science Centre in Poland Grant No. 2015/17/D/ST3/00500. JK and WP acknowledge National Science Centre in Poland Grant No. 2012/05/E/ST7/00240. The nanofabrication process was performed at the Academic Centre for Materials and Nanotechnology (ACMiN) of AGH University of Science and Technology. The authors thank M. Schmidt for technical support.

Author contributions

KG, SŁ, and WS fabricated Hall-bars in the clean-room and carried out electrical measurements, FS provided the samples, JK and WP, performed and analyzed XRD and XRR data. ŁK and JB developed the theory, ŁK, TS and JB, analyzed the results. All authors reviewed the manuscript.

Competing interests

The authors declare no competing interests.

Additional information

Supplementary information is available for this paper at https://doi.org/10.1038/s41598-020-67450-3.

Correspondence and requests for materials should be addressed to Ł.K. or K.G.

Reprints and permissions information is available at www.nature.com/reprints.

Publisher's note Springer Nature remains neutral with regard to jurisdictional claims in published maps and institutional affiliations.

Supplementary Information for

Optimization of Spin Hall Magnetoresistance in Heavy-metal/Ferromagnetic-metal Bilayers

Łukasz Karwacki [1,2], Krzysztof Grochot [2,3], Stanisław Łazarski [2], Witold Skowroński [2], Jarosław Kanak [2], Wiesław Powroźnik [2], Józef Barnaś [4,1], Feliks Stobiecki [1] and Tomasz Stobiecki [2,3]

[1] Institute of Molecular Physics, Polish Academy of Sciences, ul. Smoluchowskiego 17, 60-179 Poznań, Poland

[2] AGH University of Science and Technology, Department of Electronics, Al. Mickiewicza 30, 30-059 Kraków, Poland

[3] Faculty of Physics and Applied Computer Science, AGH University of Science and Technology, 30-059 Kraków, Poland

[4] Faculty of Physics, Adam Mickiewicz University, ul. Uniwersytetu Poznańskiego 2, 61-614 Poznań, Poland

Structural characterization

The samples studied in this paper were deposited using magnetron-sputtering technique. The details on deposition parameters as well as structural phase analysis for W/CoFeB, CoFeB/Pt, and Co/Pt bilayers were described in our recent papers [S1, S2]. In these publications we have shown that the tungsten layer grows in the disoriented β-W phase, CoFeB is amorphous, while Co and Pt are strongly textured in direction fcc (111). However, the growth of Co on disoriented β-W underlayer is quite unexpected. The grazing incidence X-ray diffraction (GIXD) profiles at incidence angle $\omega=1^{o}$ (this method was used in order to minimized the influence of W underlayer on top Co layer) show very weak hcp-Co peaks (Fig. S1). In the sample W3 (Fig. S1 (a)) we measured overlapping by β-W (210) hcp-Co(100) and decreasing reflection intensity of hcp-Co (101) with decreasing of Co thickness. Weak diffraction non-textured polycrystalline hcp-Co is due to growing hcp-Co on strongly disoriented β-W underlayer. A diffraction peak of hcp-Co(101) also appears in sample W4 (Fig. S1 (b)). In addition, as a result from GIXD measurements below 4 nm, W layers grow in the amorphous-like structure (Fig. S1 (b)).

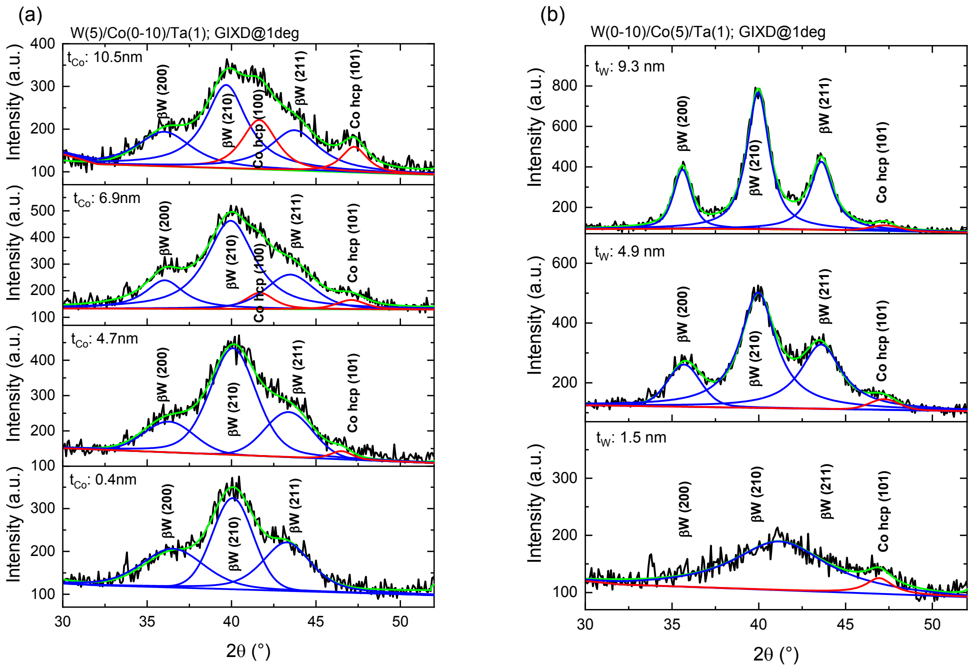

Fig. S1 GIXD profiles at incidence angle ω =1^o : (a) sample W3: W(5)/Co(0-10)/Ta(1) (b) sample W4: W(0-10)/Co(5)/Ta(1).

Resistivity measurements

The resistivity of each material is determined from the measured sheet conductance G = L/(w·R) of each microstrip as a function of the thickness of heavy metals and ferromagnets according to the procedure described in Ref. [S3]. As shown in Fig. S2 sheet conductance of all investigated samples decreases linearly with thickness decreasing in the range of 10 nm to about 2 nm. For the majority of studied systems below 2 nm the deviation from linearity of G(t) dependence is due to transition from polycrystalline to amorphous-like structure. For example, below 2 nm, hcp-Co in the sample W3 and β-W in the sample W4 transformed to amorphous phase (Fig. S2(a)). Intersection of G(t) dependencies at 5 nm, for samples W3 and W4, shows complementary behavior in W/Co system. G(t) dependencies of the samples W1 and W2 are similar, due to high resistivities of β-W and amorphous CoFeB. However, sheet conductances for samples P1 and P2 with amorphous ferromagnet CoFeB are smaller than for samples P3 and P4 with polycrystalline fcc-Co (Fig. S2(b)). Table I contains resistivities for all studied systems obtained from sheet conductance measurements and calculated using parallel resistors model. To determine the resistivity in the W1, W2, W3 and W4 samples, the capping Ta layer was not taken into account because for a thickness of 2 nm Ta is oxidized and does not conduct. In the case of samples A1 and A2 Ti buffer and capping layers were also oxidized.

(a) (b)

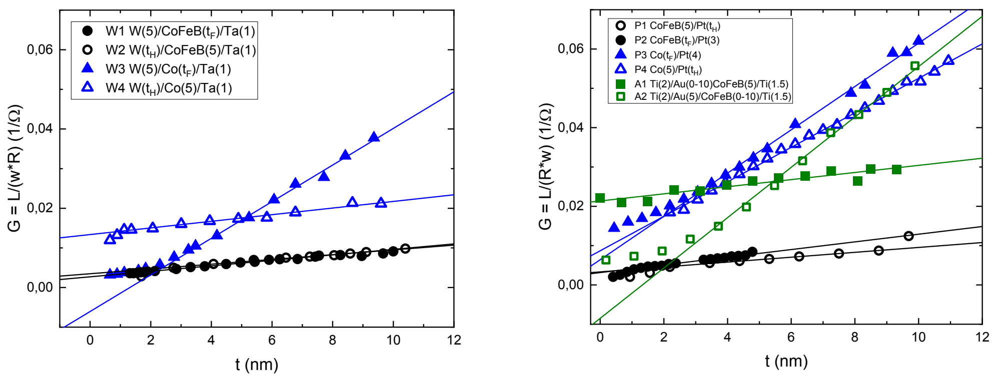

Fig. S2 Sheet conductance G as a function of heavy metal (W, Pt, Au) and ferromagnet (CoFeB, Co) thickness t for: (a) W/CoFeB and W/Co bilayers, (b) CoFeB/Pt, Co/Pt and Au/CoFeB bilayers.

Table I. Resistivities of heavy metal and ferromagnetic layers obtained from measurements of sheet conductance. Resistivity values have been rounded up to integers and the measurement error is smaller than 1 μΩcm.

No.	**Sample**	**ρ_0^H (μΩcm)**	**ρ_0^F (μΩcm)**
W1	W(5)/CoFeB(t_F)/Ta(1)	185	144
W2	W(t_H)/CoFeB(5)/Ta(1)	166	144
W3	W(5)/Co(t_F)/Ta(1)	120	22
W4	W(t_H)/Co(5)/Ta(1)	120	30
P1	CoFeB(t_F)/Pt(3)	95	102
P2	CoFeB(5)/Pt(t_H)	151	161
P3	Co(t_F)/Pt(4)	51	18
P4	Co(5)/Pt(t_H)	24	57
A1	Ti(2)/Au(t_H)CoFeB(5)/Ti(1.5)	15	96
A2	Ti(2)/Au(5)/CoFeB(t_F)/Ti(1.5)	24	96

Afterwards, an in-plane magnetic field of 2 kOe, which was sufficient to achieve magnetization saturation was applied and the angular measurement of resistance as a function of azimuthal angle of magnetization was measured. Figures S3 and S4 show examples of the rotational magnetoresistance curves for investigated systems. Maximal changes of magnetoresistance ratio (MR= $(R_{max}-R_{min})/R_{min}$) as a function of the heavy metal and ferromagnet thickness were determined from in-plane angular measurements of MR curves and are collected in Figs.3-6 in the main part of this work.

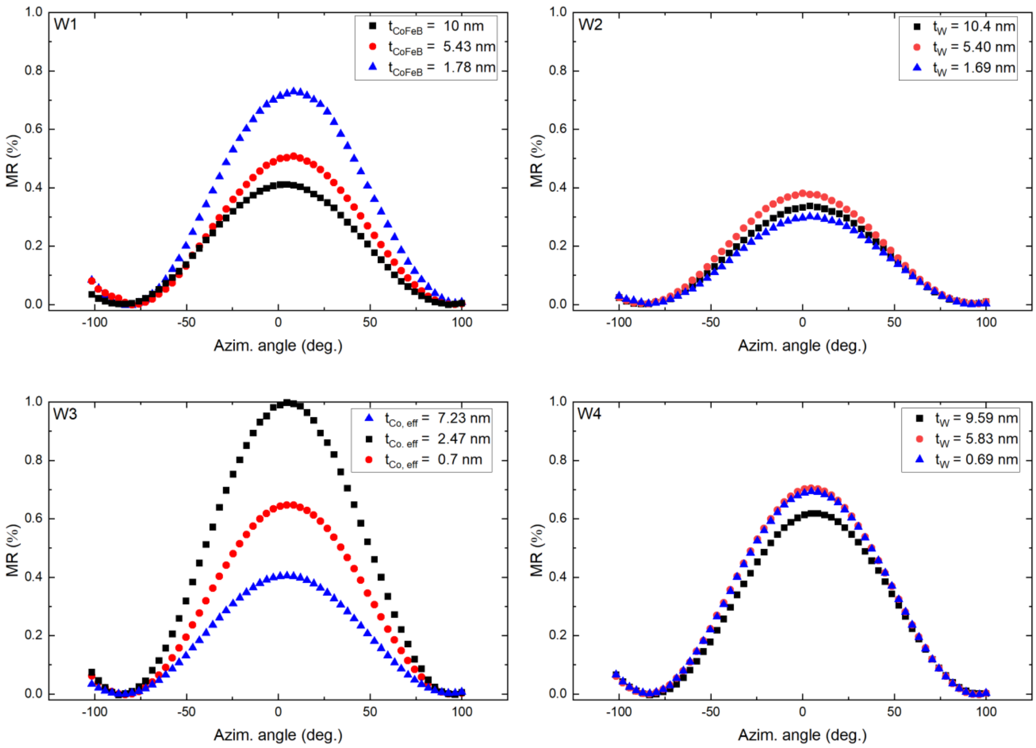

Fig. S3 The rotational magnetoresistance curves at H=2 kOe for W/CoFeB and W/Co bilayers.

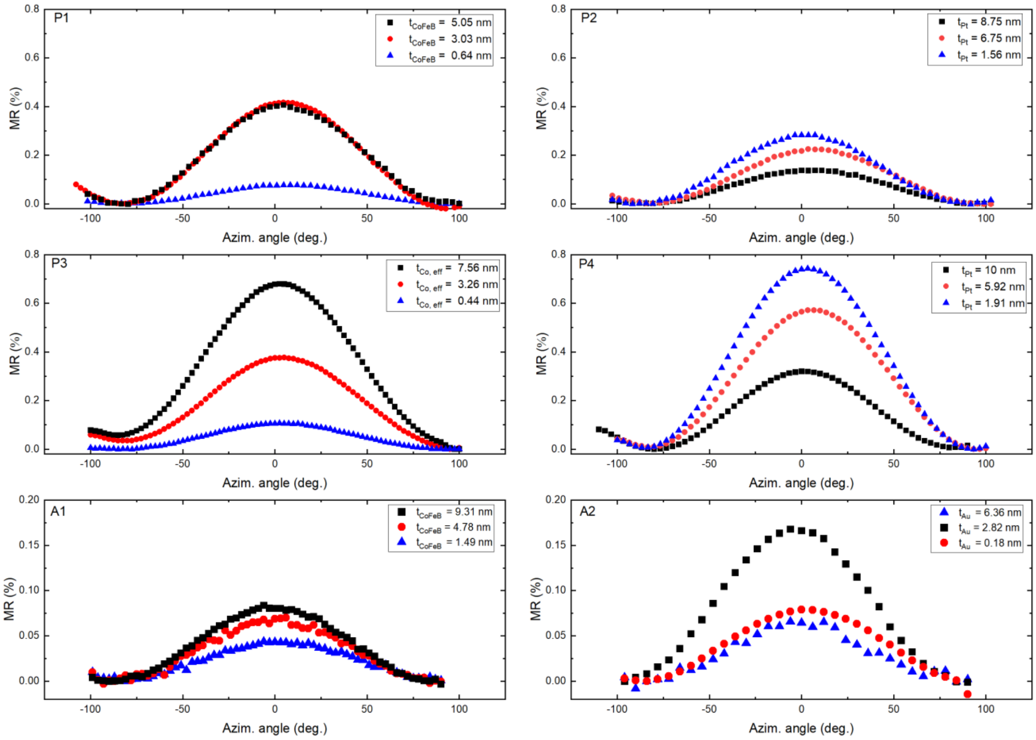

Fig. S4 The rotational magnetoresistance curves at H=2kOe for CoFeB/Pt, Co/Pt and Au/CoFeB bilayers.

References:

[S1] W. Skowroński, Ł. Karwacki, S. Ziętek, J. Kanak,S. Łazarski, K. Grochot, T. Stobiecki, P. Kuswik, F. Stobiecki, and J. Barnaś, Determination of spin Hall angle in heavy-metal/Co-Fe-B-based heterostructures with interfacial spin-orbit fields, Phys. Rev. Appl. **11**, 024039 (2019)

[S2] S. Łazarski, W. Skowroński, J. Kanak, L. Karwacki, S. Ziętek, K. Grochot, T. Stobiecki, and F. Stobiecki, Field-free spin-orbit-torque switching in Co/Pt/Co multilayer with mixed magnetic anisotropies, Phys. Rev. Appl. **12**, 014006 (2019)

[S3] M. Kawaguchi, D. Towa, Y. C. Lau, S. Takahashi, and M. Hayashi, Anomalous spin Hall magnetoresistance in Pt/Co bilayers, Appl. Phys. Lett. **112**, 202405 (2018)

4.1.2 | Spin Hall Effect and magnetization dynamics

Pt is one of the most popular materials used in modern spintronics as a spin current source. The authors of the work [152] showed that increasing the number of interfaces can lead to an enhanced SHA in systems with Pt. Concerning this, we present the results of systematic measurements SHA in the Ta(1)/Pt(t_{Pt})/CoFeB(2)/Ta(2) system with t_{Pt} varying from 4 to 16 nm and Ta(1) / [Pt(d)/Ti(0.2)]m / Pt(d) / CoFeB(2) / Ta(2) system, where (m+1) $\times$ d = 6 nm for m = 3, 5, 7 interlayers using angular harmonic voltage methods (described in Sect. 3.6.2.2). The subsection is based on the results published in the [P2] paper.

Analyzing the first (Fig.4(a) in P2) and second (Fig.4(b) in P2) harmonics of the Hall voltage signal, we obtained the dependencies of the spin Hall efficiencies ξ_{DL} and ξ_{FL} on t_{Pt} shown in Fig.5(f) in [P2]. As shown, the Pt-Ti system was characterized by an almost constant and high value of the intrinsic SHA (θ_{SH}, more than 30%) based on the relation: $\theta_{SH} = \xi_{DL}/T$ (Eq.(5) in [P2]) regardless of the number of interfaces (m). On the contrary, in the system containing only the Pt layer, SHA decreased significantly with its thickness. Furthermore, both systems were characterized by high values of spin Hall conductivity (SHC) (σ_{SH}), which reach a maximum value of 3.3×10^5 S/m for the 5.6-nm thick Pt underlayer, which is among the highest values reported for Pt. This value is essential in practical applications, since systems with high σ_{SH} generate much less Joule heat during current flow. Note that in these considerations, we have neglected the component related to thermoelectric effects (ANE). The summary parameters obtained from the experiments are listed in Tab.II in [P2].

Comparisons between Pt and Pt-Ti conducted studies suggest that Pt-Ti superlattice may be an attractive material for SOT applications in spintronics devices. We also carried out measurements of magnetization dynamics by ferromagnetic resonance (FMR) method using the spin-diode effect for different excitation frequencies (Fig.3(c) in [P2]). It should be noted that the low effective damping α, especially for the Pt-Ti buffer, where the effective α decreased with an increasing number of interfaces (m) (Fig.3(f) in [P2]) is useful for practical applications.

Angular Harmonic Hall Voltage and Magnetoresistance Measurements of Pt/FeCoB and Pt-Ti/FeCoB Bilayers for Spin Hall Conductivity Determination

Witold Skowroński, Krzysztof Grochot, Piotr Rzeszut, Stanisław Łazarski, Grzegorz Gajoch, Cezary Worek, Jarosław Kanak, Tomasz Stobiecki, Jürgen Langer, Berthold Ocker, *Member, IEEE*, and Mehran Vafaee

***Abstract*—Materials with significant spin-orbit coupling enable efficient spin-to-charge interconversion, which can be utilized in novel spin electronic devices. A number of elements, mainly heavy metals (HMs), have been identified to produce a sizable spin current (j_s), while supplied with a charge current (j), detected mainly in the neighboring ferromagnetic (FM) layer. Apart from the spin Hall angle $\theta_{SH} = j_s/j$, spin Hall conductivity (σ_{SH}) is an important parameter, which takes also the resistivity of the material into account. In this work, we present a measurement protocol of the HM/FM bilayers, which enables for a precise σ_{SH} determination. Static transport measurements, including resistivity and magnetization measurements, are accompanied by the angular harmonic Hall voltage analysis in a dedicated low-noise rotating probe station. Dynamic characterization includes effective magnetization and magnetization damping measurement, which enable HM/FM interface absorption calculation. We validate the measurement protocol in Pt and Pt-Ti underlayers in contact with FeCoB and present σ_{SH} of up to 3.3 × 10^5 S/m, which exceeds the values typically measured in other HM, such as W or Ta.**

***Index Terms*—Anisotropic magnetoresistance (AMR), ferromagnetic resonance (FMR), magnetic thin films, spin Hall effect, spin Hall magnetoresistance (SMR), spintronics.**

Manuscript received May 31, 2021; revised August 16, 2021 and September 30, 2021; accepted October 18, 2021. Date of publication November 2, 2021; date of current version December 1, 2021. The work of Krzysztof Grochot, Stanisław Łazarski, and Tomasz Stobiecki was supported by the National Science Centre, Poland, under Grant UMO-2016/23/B/ST3/01430. This work was supported by the National Science Centre, Poland, under Grant UMO-2015/17/D/ST3/00500. The review of this article was arranged by Editor L. Ge. *(Corresponding author: Witold Skowroński.)*

Witold Skowroński, Piotr Rzeszut, Stanisław Łazarski, Grzegorz Gajoch, Cezary Worek, and Jarosław Kanak are with the Institute of Electronics, AGH University of Science and Technology, 30-059 Kraków, Poland (e-mail: skowron@agh.edu.pl).

Krzysztof Grochot and Tomasz Stobiecki are with the Institute of Electronics, and the Faculty of Physics and Applied Computer Science, AGH University of Science and Technology, 30-059 Kraków, Poland.

Jürgen Langer, Berthold Ocker, and Mehran Vafaee are with Singulus Technologies AG, 63796 Kahl am Main, Germany (e-mail: mehran.khanjani@singulus.de).

Color versions of one or more figures in this article are available at https://doi.org/10.1109/TED.2021.3122999.

Digital Object Identifier 10.1109/TED.2021.3122999

I. Introduction

UTILIZING spin of the electron in addition to its charge opens up the way for the design of novel electronic devices [1]. The magnetic material, whose properties can be controlled using the spin current, is utilized widely in magnetic field sensors, data storage devices [2], radio-frequency (RF) electronics [3], and, more recently, in hardware implementation of biomimetic circuits [4]. It has been recently proposed that non-magnetic elements with high spin-orbit coupling can act as a source of the spin current [5]. In such spin-orbit torque (SOT) effect, the spin current (j_s) is generated as result of the charge current (j), with electron current, spin current, and spin vectors being orthogonal to each other [6]. Since its discovery, there have been multiple studies on SOT in different materials exhibiting spin-orbit coupling and the effect is now quantified using the so-called spin Hall angle (θ_{SH}) = j_s/j [7], [8]. Several methods of determination of θ_{SH} were proposed, such as ferromagnetic resonance (FMR) line-shape analysis [9], harmonic Hall voltage measurement [10], Kerr-effect-based optical determination [11], spin Hall magnetoresistance (SMR) [12], and threshold current magnetization switching [13]. All these methods require slightly different multilayer structure, or different ferromagnetic detecting layer's anisotropy axis and post-analysis, which enables quantitative investigation of material parameters.

In this article, we present an experimental protocol for the detailed measurement of spin Hall efficiency based on static and dynamic electrical measurements. We select a conventional system composed of a Pt/FeCoB bilayer together with a recently proposed [14] Pt-Ti/FeCoB system for the protocol verification. The presented protocol does not require special conditions, as opposed to perpendicular magnetic anisotropy of the FM for in-plane harmonic Hall voltage determination or negligible field-like torque for FMR line-shape analysis. Pt was chosen as one of the most reliable materials with well-established parameters, especially in terms of θ_{SH}, crystal structure, and conductivity [15], while FeCoB has been shown to exhibit the highest tunneling magnetoresistance effect [16] together with the MgO barrier [17]. It has been recently shown that creating additional interfaces [18], for example, by using Pt-Ti multilayer, θ_{SH} can be enhanced at the cost of the resistivity. Utilizing a simple two-step lithography procedure, the Hall-bar matrix of different thickness of Pt or Pt-Ti interface number was fabricated, which enables determination of the magnetization saturation, resistivity, magnetization damping, and spin Hall efficiency. Magnetotransport properties measurement protocol include both high-frequency dynamic characterization and low-frequency resistance and harmonic Hall voltage measurements characterized by an ultra-low noise. Investigation within the two frequency regimes allows us to determine all mentioned magnetotransport properties in a single device. For this, a multi-probe RF rotating probe station was designed, which is controlled by a linear driver, enabling detailed measurement with an nV resolution. Using the presented protocol, we investigate both Pt/FeCoB and Pt-Ti/FeCoB bilayer properties that are the most relevant for device applications.

II. Experiment

A. Deposition and Microlithography

Multilayer stacks were deposited using magnetron sputtering on thermally oxidized 4-in Si wafer, with a wedged-shaped Pt layer in a Singulus Timaris cluster tool system. The following structure with Pt: Ta(1)/Pt(t_{Pt})/$Fe_{60}Co_{20}B_{20}$(2)/Ta(2) (thickness in nm) with t_{Pt} varying from 4 to 16 nm and Pt-Ti: Ta(1)/[Pt(d)/Ti(0.2)]$_m$/Pt(d)/$Fe_{60}Co_{20}B_{20}$(2)/Ta(2), where $(m + 1) \times d = 6$ nm for $m = 3$, 5, and 7 interlayers, were deposited and annealed at 310 °C in ultra-high vacuum chamber. The annealing step is required for a crystallization of the CoFeB along with the MgO tunnel barrier of the magnetic tunnel junction for further applications. The slope of the Pt-wedge is 1.2 nm/cm. The top Ta layer oxidizes after exposing to the atmospheric condition, forming a protective layer, while the bottom Ta layer serves as a buffer. After the deposition process, the multilayers were patterned into 200 μm $\times$ 30 μm stripes for resistance measurements and 30 μm $\times$ 10 μm Hall-bars for static and dynamics transport characterization, using optical lithography, lift-off, and ion-beam etching processes. The long axis of the stripes is perpendicular to the wedge direction, resulting in a negligible variation of the Pt thickness in a single device. Ti(5)/Au(50) contact electrodes were fabricated in a second lithography step. Devices enable resistance measurement using the four-point method, harmonic Hall voltage measurements, and FMR using the so-called spin-diode effect [19].

B. Transport Measurement

The Hall voltage signal was measured using low-frequency (2387 Hz) stimuli of 1 V in both out-of-plane and in-plane magnetic field. Depending on the sample resistance, the current (current density) ranged from 2.2 to 10 mA (5.2–7.2 MA/cm^2). FMR was measured using amplitude-modulated RF signal of $P = 16$ dBm applied to the long axis of the stripe and measurement of the mixing voltage (V_{mix}) using short-axis electrodes with a lock-in amplifier synchronized with the modulating signal. Harmonic Hall voltage measurements were performed in a fixed magnetic field with a rotating sample stage with an RF-multiprobe from T-plus attached. The mechanical rotation of the stage was controlled with a stepper motor driven by the dedicated linear controller.

C. Rotating Probe Station

Detailed investigation of the spin Hall effect requires measurement in a magnetic field applied at various angles with respect to the Hall-bar axis. Specifically, anisotropy field H_k is determined from anomalous Hall effect (AHE) measured in a perpendicular magnetic field, while harmonic Hall voltage investigation requires rotation of the in-plane magnetic field vector. Dedicated mechanical setup was designed and fabricated by MeasLine Ltd., Skawina, Poland, which enabled rotation of the sample at an arbitrary polar and azimuth angle with respect to the magnetic field produced by the dipole electromagnet. To reduce the noise, a dedicated stepper driver controller was designed.

A standard stepper motor driver incorporates pulse width modulation (PWM) signal to tune and stabilize coil current of the motors. This current must be applied to the motor even when stationary, to hold the position while using microstepping (i.e., ability to move motor more precise than its full step resolution). While PWM signal allows to reduce size of the driver unit and increase its power efficiency, it also generates a switching noise. This causes generation of dynamic electromagnetic fields around the motors and cabling, which significantly disrupts precise measurements performed in the rotating setup due to radio frequency interference (RFI). The spectra of this interference are broad, as it originates from a square-shape PWM waveform. In order to eliminate it, a specialized driver was designed, which uses a linear (i.e., non-switching) voltage sources for the motors with negligible RFI. Additionally, a dedicated printed circuit board was designed to minimize the electromagnetic interference from the board itself.

The stepper motor driver was built using multiple high-current digitally controlled voltage sources. Instead of using a PWM signal, digital to analog converters (DACs)—dual-channel 14-b AD5643R—provide a voltage corresponding to the requested motor's phase current. Operational amplifiers—OPA548T—uses 0–2.5-V voltage from DAC and convert it to bipolar $\pm$9 V. Each coil of the motor has its own DAC and the driver, in addition to the total of four drivers [Fig. 1(b)]. A 32-b ARM microcontroller STM32F103C8T6 is responsible for receiving commands from the measurement software using FT230XQ USB interface, creating trapezoidal motion profiles (to smoothly start and end the movement) and controlling DACs by generating required voltages for each motor phase. Maximum voltages per phase, parameters of trapezoidal motion profiles, and microstepping factors can be adjusted by sending configuration commands. Whole system is powered using an external linear laboratory power supply, which is also controlled by a designed unit. Additionally, the USB interface is completely opto-isolated from the system,

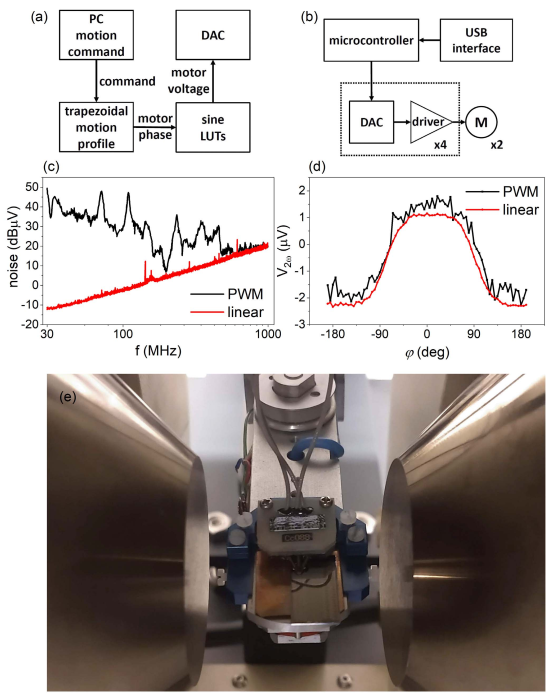

Fig. 1. Microwave rotating probe station design: (a) software flow, (b) driver's hardware block-diagram, (c) comparison of the switching and linear driver performance in terms of the electromagnetic radiation, and (d) second harmonic Hall measurements. (e) Photograph of the rotating probe station.

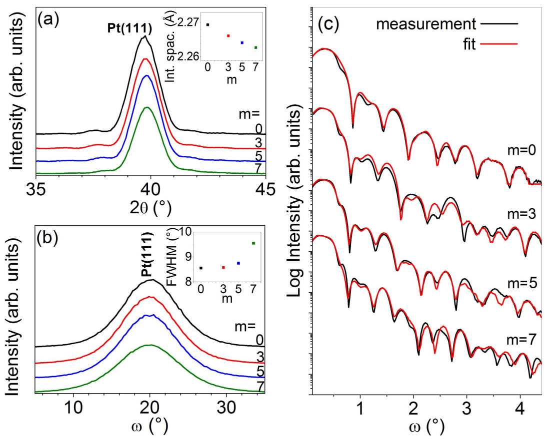

Fig. 2. X-ray diffraction (XRD) and X-ray reflectivity (XRR) measurements of the investigated multilayers. (a) Intensity of the Pt(111) peak decreases with increasing Ti interfaces. In addition, the peak position shifts to higher angles with higher *m*, which is interpreted as a decrease in interplanar distances of Pt (inset). (b) Rocking curves are resulting in an increase of FWHM with *m* (inset). (c) XRR for all multilayers together with corresponding fits. The fitting parameters are collected in Table I.

which protects the PC in the case of mains power issues. A software flow is shown in Fig. 1(a).

Fig. 1(c) presents the comparison of the measured radiation emissions correlated to 10-m open area test site (OATS) for both PWM (based on Leadshine EM402 driver) and the presented linear driver. Measurements were performed using a GHz transverse electromagnetic (GTEM) chamber, calculated and correlated according to electromagnetic interference standards [20]. To verify the operation of the driver, the angular measurement of the second harmonics Hall voltage dependence on the in-plane magnetic field was determined [Fig. 1(d)], which shows an improvement with respect to the PWM-based driver in terms of the measurement noise. An image of the entire probe station is presented in Fig. 1(e). Specifically, both in-plane and out-of-plane magnetic field characteristics as well as angular dependence using the four-point technique can be measured upon contacting the device under test, which is an advancement to the previously published setup [21], [22].

III. Results and Discussion

A. X-Ray Diffraction, Resistivity, and Anomalous Hall Effect

X-ray diffraction (XRD) patterns for both Pt- and Pt-Ti-based multilayers are presented in Fig. 2(a). The intensities of θ–2θ XRD peaks decrease together with increasing the number m of the Pt-Ti multilayers. The lattice plane spacing calculated from the position of Pt (111) decreases similarly to [14] (Fig. 2(a), inset). For both Pt- and Pt-Ti-based samples, the grain size in the direction perpendicular to the layers, calculated from the Scherrer equation, are comparable to the Pt and Pt-Ti thickness. Fig. 2(b) shows the XRD rocking curve patterns of Pt(111) for investigated structures. From fitting of the rocking curve peaks, a full-width at half-maximum (FWHM) parameter was determined [Fig. 2(b), inset]. The highest FWHM was calculated for the sample with the greatest number of Ti layers, which means that the Ti atoms diffused into Pt grains [23] after the deposition and annealing process. X-ray reflectivity (XRR) measurements and the corresponding fits for the Pt-Ti-based multilayers are shown in Fig. 2(c). Fitting parameters for samples with different number of Ti monolayers are collected in Table I. The fits were made by replacing the Pt-Ti superlattice with a single Pt layer with total $[\mathrm{Pt}(d)/\mathrm{Ti}(0.2)]_m/\mathrm{Pt}(d)$ thickness and reduced density (compared to the Pt density of 21.45 g/cm^3) as a result of dissolving Ti in Pt. This assumption was supported by a strong mixing enthalpy for Ti in Pt (−290 kJ/mole of atoms) and Pt in Ti (−290 kJ/mole of atoms) [24].

Around 100 devices with different t_{Pt} were used for resistivity (ρ) determination. For each device, the resistance (R) was transformed into sheet conductance $G_S = l/wR$, with l and w being the length and the width of the stripe, respectively. The resistivity of Pt was then calculated as $\rho_{\mathrm{Pt}} = t_{\mathrm{Pt}}/(G_S - G_0)$, where $G_0 = 0.0011$ S is the sheet conductance of the multilayer without Pt buffer. Similarly, the resistivity of the Pt-Ti $\rho_{\mathrm{Pt-Ti}}$ was calculated for different number of Pt-Ti interfaces. The results are presented in Fig. 3, together with a

TABLE I

XRR FITTING PARAMETERS—DENSITY (g/cm^3), THICKNESS (nm), ROUGHNESS (nm)—FOR Pt- AND Pt-Ti-BASED MULTILAYERS

	Pt			[Pt-Ti]$_3$			[Pt-Ti]$_5$			[Pt-Ti]$_7$		
	density	t	roughness	density	t	roughness	density	t	roughness	density	t	roughness
Si	2.33	-	0.27	2.33	-	0.26	2.32	-	0.31	2.33	-	0.26
SiO	2.64	100	0.31	2.64	100	0.29	2.64	100	0.34	2.64	100	0.26
Ta	16.6	1.10	0.46	13.3	0.86	0.24	14.1	0.99	0.21	13.6	0.98	0.35
Pt	21.4	5.97	0.47	16.9	6.69	0.44	17.4	7.05	0.48	17.0	7.44	0.43
FeCoB	8.13	1.89	0.36	8.31	1.88	0.42	8.29	1.87	0.37	8.38	1.76	0.44
Ta	15.9	0.36	0.50	13.3	1.36	0.36	13.5	1.26	0.34	13.0	1.35	0.36
Ta_2O_5	5.14	3.46	0.37	5.86	3.27	0.36	6.64	3.49	0.41	5.57	3.31	0.37

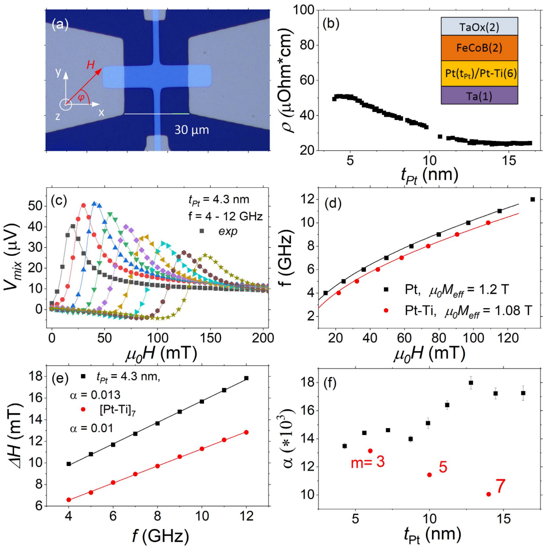

Fig. 3. (a) Micrograph of the Hall-bar, (b) resistivity versus Pt thickness dependence, (c) example of the FMR measured using spin-diode effect for different excitation frequency for the Hall-bar with $t_{Pt} = 4.3$ nm, (d) resonance frequency versus in-plane magnetic field for Pt ($t_{Pt} = 4.3$ nm) and Pt-Ti ($m = 7$) underlayers modeled using Kittel formula, (e) FMR linewidth (ΔH) versus frequency dependence, together with a line fit, enabling damping constant calculation, and (f) damping dependence on t_{Pt} and number of Pt-Ti interfaces.

micrograph of the Hall-bar. ρ_{Pt} versus t_{Pt} behavior resembles similar dependence measured in Pt/Co/MgO multilayers [25].

B. Saturation Magnetization and Damping

Saturation magnetization (M_S) for each underlayer was measured using a vibrating sample magnetometer, while the effective magnetization (M_{eff}) and magnetization damping (α) were determined from the FMR. To do so, the V_{mix} versus in-plane magnetic field (H) was measured for different input frequencies (f) spanning from 4 to 12 GHz. As a result, the family of Lorentz-shape curves were obtained, which were fitted using the formula

$$V_{\text{mix}} = V_S \frac{\Delta H^2}{\Delta H^2 + (H - H_0)^2} + V_{\text{AS}} \frac{\Delta H (H - H_0)}{\Delta H^2 + (H - H_0)^2} \quad (1)$$

where V_S and V_{AS} are the magnitude of symmetric and antisymmetric Lorentz curves, respectively, ΔH is the linewidth, and H_0 is the resonance field. f versus H_0 dependence was fitted using the Kittel formula [26], and the fitting parameters are presented in Table II. The dependence of damping on Pt thickness and Pt-Ti interfaces is depicted in Fig. 3(f). We note that for Pt-Ti buffer, the effective damping decreases with increasing number of interfaces (m), which may be useful for applications, as the critical current density needed to switch the ferromagnet depends linearly on the effective damping [27].

C. Spin Hall Angle

The spin Hall efficiency was determined from the harmonic Hall voltage measurements performed in the rotating in-plane magnetic field [28]. Fig. 4 presents angular dependence of the first (V_ω) and second ($V_{2\omega}$) harmonic Hall voltage versus azimuth angle φ between the magnetic field vector and long axis of the Hall-bar [as denoted in Fig. 4(a)]. Both dependencies were modeled using the following equation:

$$\begin{aligned} V_\omega &= V_P \sin 2\varphi \\ V_{2\omega} &= -\frac{V_P (H_{\text{FL}} + H_{\text{Oe}})}{H} \cos\varphi \cos 2\varphi \\ &\quad + -\left(\frac{V_A H_{\text{DL}}}{2H_{\text{eff}}} - V_{\text{ANE}}\right) \cos\varphi \end{aligned} \quad (2)$$

where V_P and V_A are the planar and anomalous Hall voltages, H_{FL}, H_{Oe}, and H_{DL} are the field-like, Oersted field, and damping-like field components, respectively, and $H_{\text{eff}} = H + H_k$ is the effective field, which is the sum of the external magnetic field and anisotropy field, determined from the AHE measurement in the perpendicular orientation (H along the z-axis). V_{ANE} is the additional contribution from the anomalous Nernst effect, which was found negligible in the investigated bilayers. The spin Hall efficiency ξ_{DL} was calculated using the formula

$$\xi_{\text{DL}} = \frac{\mu_0 M_S t_{\text{FeCoB}} H_{\text{DL}}}{j\hbar/2e}. \quad (3)$$

As a result of the calculation, the dependence of the spin Hall efficiencies was obtained as a function of t_{Pt}. Similar to [25] and [29], ξ_{DL} reaches its maximum for $t_{\text{Pt}} = 5$ nm and decreases with increasing thickness of HM. To account for the Oersted field, we used an analytical expression $H_{\text{Oe}} = J t_{\text{Pt}}/2$. The calculated values dominate the field-like contribution, which means that both H_{FL} and H_{Oe} are comparable in amplitude but of opposite sign. Nonetheless, ξ_{FL} is an order of magnitude smaller than ξ_{DL} for the thinnest Pt but increases with increasing t_{Pt}. The results of the effective field values

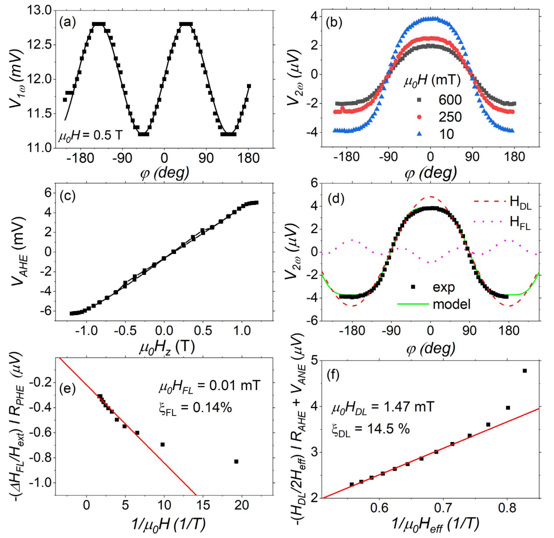

Fig. 4. Hall voltage measurements of the (a) first and (b) second harmonic components versus in-plane magnetic field angle of the Hall bar with $t_{\mathrm{Pt}} = 4.3$ nm. (c) Anomalous Hall voltage measurement in the perpendicular field, that is, along z-axis enables anisotropy field determination. (d) Second harmonic Hall voltage was modeled using (2) enabling separation of the damping-like (H_{DL}) and field-like (H_{FL}) effective field components. (e) Dependence of the H_{FL} versus inverse of the applied magnetic field and (f) H_{DL} versus inverse of the effective magnetic field enables calculation of the spin Hall efficiencies.

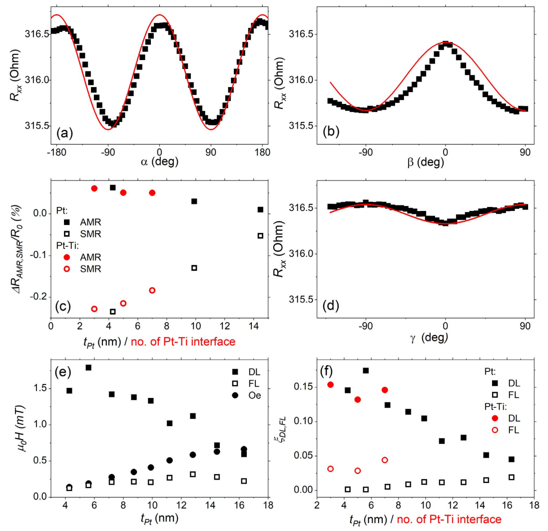

Fig. 5. (a)–(c) Example of the longitudinal resistance (R_{xx}) in different azimuth (α) and polar (β and γ) angles for $t_{\mathrm{Pt}} = 4.3$ nm, enabling separation of the AMR and SMR contribution to the total magnetoresistance. (b) and (d) Measurements were performed in a magnetic field $H = 1.8$ T, which exceeds the anisotropy field, but is unable to saturate the FeCoB magnetization at polar angles $0 < \theta < 90$, hence a small deviation from the cosine dependence. (d) AMR and SMR values determined for different t_{Pt} and number of Pt-Ti interfaces. (e) Calculated effective fields in Pt-based elements. (f) As a result, the spin Hall efficiencies for all devices.

are presented in Fig. 5. In order to calculate the intrinsic θ_{SH}, one has to take into account the interface transparency. To do so, we first calculate the absorption of the spin current on the Pt/FeCoB interface using the following formula:

$$g_{\mathrm{eff}}^{\uparrow\downarrow} = \frac{4\pi M_S t_{\mathrm{FeCoB}}}{g\mu_B}(\alpha_{\mathrm{eff}} - \alpha_0) \tag{4}$$

where g is the Lande factor, μ_B is the Bohr magneton, and $\alpha_0 = 0.004$ is intrinsic damping of FeCoB. $g_{\mathrm{eff}}^{\uparrow\downarrow}$ for different Pt thickness and Pt-Ti underlayer were calculated and presented in Fig. 5. In general, $g_{\mathrm{eff}}^{\uparrow\downarrow}$ increases (decreases) with the thickness of Pt (with a number of Pt-Ti interfaces) as a result of increasing (decreasing) damping constant. Next, the interface transparency T is calculated as

$$T = \frac{g_{\mathrm{eff}}^{\uparrow\downarrow}\tanh\dfrac{t_{\mathrm{Pt}}}{2\lambda_{\mathrm{Pt}}}}{g_{\mathrm{eff}}^{\uparrow\downarrow}\coth\dfrac{t_{\mathrm{Pt}}}{\lambda_{\mathrm{Pt}}} + \dfrac{h}{\rho_{\mathrm{Pt}}\lambda_{\mathrm{Pt}}2e^2}} \tag{5}$$

where $\lambda_{\mathrm{Pt}} = 2$ nm is the spin diffusion length [30] in Pt, h is the Planck constant, and e is the electron charge. The calculated transparency, which varies slightly between 0.42 and 0.5 for Pt/FeCoB and Pt-Ti/FeCoB interfaces, were included in Table II. Finally, $\theta_{\mathrm{SH}} = \xi_{\mathrm{DL}}/T$ and spin Hall conductivity $\sigma_{\mathrm{SH}} = \xi_{\mathrm{SH}}/\rho_{\mathrm{HM}}$ were calculated. We note that we took into account the transparency of the HM/FM interface to calculate the intrinsic spin Hall angle [15]. The spin Hall efficiency ranges between 0.17 and 0.05 depending on the thickness of Pt. Similar values were obtained using a line-shape analysis of the SOT-FMR signal, based on [31], SMR, and the current-assisted magnetic-field switching experiments [30]. Nevertheless, the intrinsic spin Hall angle is a function of the interface transparency determination, which depends on spin diffusion length and spin mixing conductance. In the presented analysis, the interface transparency ranges between 0.5 and 0.4, which results in θ_{SH} between 0.35 and 0.12. Smaller interface transparency would translate into even higher intrinsic θ_{SH}, which were recently reported in [14] and [32].

D. Magnetoresistance

To complete the spin-dependent transport analysis, the angular measurements of the magnetoresistance in x–y (α-rotation), y–z (β-rotation), and x–z (γ-rotation) planes were conducted [33]. Fig. 5 presents angular resistance dependence in Pt/FeCoB with $t_{\mathrm{Pt}} = 4.3$ nm. Using the formulas from [34], SMR and anisotropic magnetoresistance (AMR) were derived [Fig. 5(c)]. The dependence of SMR on t_{Pt} and a number of Pt-Ti interfaces coincides with the dependence of the spin Hall conductivity, however, it does not match the dependence of the resistivity—for Pt underlayer, the highest SMR was determined in the bilayer with the thinnest Pt, whereas for Pt-Ti, the highest SMR was reported for the smallest number of Pt-Ti interfaces. The AMR contribution decreases with increasing t_{Pt} due to shunting effect from Pt [35].

TABLE II
SUMMARY OF THE SPIN TRANSPORT PARAMETERS DETERMINED IN Pt-BASED (DIFFERENT THICKNESS) AND Pt-Ti-BASED (DIFFERENT NUMBER OF INTERFACES) DEVICES

t_{Pt}/ Pt-Ti intf.	Pt 5.6	10	14	Pt-Ti 3	5	7	units nm/no.
ρ_{HM}	52	34	24	54	60	95	$\mu\Omega$cm
$\mu_0 M_{\mathrm{S}}$	1.51	1.42	1.4	1.38	1.38	1.38	T
α	14	15	17	13	11	10	10^{-3}
$g_{\mathrm{eff}}^{\uparrow\downarrow}$	16.3	16.8	19.6	13.4	10.4	8.9	10^{18}/m^2
T	0.5	0.46	0.42	0.48	0.44	0.51	
θ_{SH}	0.35	0.23	0.12	0.36	0.34	0.32	
σ_{SH}	3.3	3.07	2.13	3.2	2.6	1.75	$10^5/(\Omega m)$

There are a few materials reported with higher intrinsic spin Hall angle, including HMs: W [36], [37], Ta [9], and topological insulators: BiSe [38], however, at the cost of increased resistivity of the material. Similar tendency is maintained by alloying HMs with good conductors: AuPt [39] and AuTa [40]. Surprisingly, σ_{SH} for Pt reaches a maximum value of 3.3×10^5 S/m for 5.6-nm-thick underlayer, which is among one of the highest values reported for Pt [41]–[43], Pt-based multilayers [18] and alloys [44], exceeding other HM and their compounds [45], mainly due to small resistivity of the Pt. Even higher intrinsic spin Hall angle has been measured recently in an all-epitaxial ferrite/Pt system [32]. This finding, together with well-established deposition technique, crystal properties, and endurance, leads to the conclusion that Pt is one of the most optimal materials for SOT applications in line with potential spin-logic circuits [46].

IV. SUMMARY

In summary, the measurement protocol of the spin orbit torque efficiency based on low-frequency harmonic Hall voltage measurement and RF ferromagnetic resonance analysis was presented. The design of the setup including a rotating probe station and a dedicated linear driver together with microfabricated Hall bar bilayers based on FeCoB with different underlayer materials was shown, which enables a thorough analysis of the spin-dependent phenomena in HM/FM bilayer system. The protocol was verified in Pt- and Pt-Ti-based devices, resulting in an intrinsic spin Hall angle of up to 0.35 and spin Hall conductivity reaching 3.3×10^5 S/m, which is among the highest values reported. Our findings indicate that Pt remains one of the most attractive material for spintronics.

ACKNOWLEDGMENT

Nanofabrication was performed at the Academic Centre for Materials and Nanotechnology, AGH University of Science and Technology, Kraków, Poland.

REFERENCES

[1] A. Hirohata *et al.*, "Review on spintronics: Principles and device applications," *J. Magn. Magn. Mater.*, vol. 509, Sep. 2020, Art. no. 166711.
[2] R. Andrawis, A. Jaiswal, and K. Roy, "Design and comparative analysis of spintronic memories based on current and voltage driven switching," *IEEE Trans. Electron Devices*, vol. 65, no. 7, pp. 2682–2693, Jul. 2018.
[3] B. Dieny *et al.*, "Opportunities and challenges for spintronics in the microelectronics industry," *Nature Electron.*, vol. 3, no. 8, pp. 446–459, Aug. 2020.
[4] J. Grollier, D. Querlioz, and M. D. Stiles, "Spintronic nanodevices for bioinspired computing," *Proc. IEEE*, vol. 104, no. 10, pp. 2024–2039, Oct. 2016.
[5] J. E. Hirsch, "Spin Hall effect," *Phys. Rev. Lett*, vol. 83, no. 9, pp. 1834–1837, Aug. 1999.
[6] A. Hoffmann, "Spin Hall effects in metals," *IEEE Trans. Magn.*, vol. 49, no. 10, pp. 5172–5193, Oct. 2013.
[7] I. M. Miron *et al.*, "Perpendicular switching of a single ferromagnetic layer induced by in-plane current injection," *Nature*, vol. 476, no. 7359, pp. 189–193, Aug. 2011.
[8] L. Liu, C.-F. Pai, Y. Li, H. W. Tseng, D. C. Ralph, and R. A. Buhrman, "Spin-torque switching with the giant spin Hall effect of tantalum," *Science*, vol. 336, no. 6081, pp. 555–558, 2012.
[9] L. Liu, T. Moriyama, D. C. Ralph, and R. A. Buhrman, "Spin-torque ferromagnetic resonance induced by the spin Hall effect," *Phys. Rev. Lett.*, vol. 106, no. 3, 2011, Art. no. 036601.
[10] J. Kim *et al.*, "Layer thickness dependence of the current-induced effective field vector in Ta|CoFeB|MgO," *Nature Mater.*, vol. 12, pp. 240–245, Dec. 2013.
[11] C. Stamm *et al.*, "Magneto-optical detection of the spin Hall effect in Pt and W thin films," *Phys. Rev. Lett.*, vol. 119, no. 8, Aug. 2017, Art. no. 087203.
[12] H. Nakayama *et al.*, "Spin Hall magnetoresistance induced by a nonequilibrium proximity effect," *Phys. Rev. Lett.*, vol. 110, no. 20, May 2013, Art. no. 206601.
[13] Q. Hao and G. Xiao, "Giant spin Hall effect and switching induced by spin-transfer torque in a W/$Co_{40}Fe_{40}B_{20}$/MgO structure with perpendicular magnetic anisotropy," *Phys. Rev. Appl.*, vol. 3, no. 3, Mar. 2015, Art. no. 034009.
[14] L. Zhu and R. A. Buhrman, "Maximizing spin-orbit-torque efficiency of Pt/Ti multilayers: Trade-off between intrinsic spin Hall conductivity and carrier lifetime," *Phys. Rev. Appl.*, vol. 12, no. 5, Nov. 2019, Art. no. 051002.
[15] G. D. H. Wong *et al.*, "Strain-mediated spin–orbit torque enhancement in Pt/Co on flexible substrate," *ACS Nano*, vol. 15, pp. 8319–8327, May 2021.
[16] S. Ikeda *et al.*, "Tunnel magnetoresistance of 604% at 300 K by suppression of Ta diffusion in CoFeB/MgO/CoFeB pseudo-spin-valves annealed at high temperature," *Appl. Phys. Lett.*, vol. 93, no. 8, 2008, Art. no. 082508.
[17] S. Yuasa, T. Nagahama, A. Fukushima, Y. Suzuki, and K. Ando, "Giant room-temperature magnetoresistance in single-crystal Fe/MgO/Fe magnetic tunnel junctions," *Nature Mater.*, vol. 3, no. 12, pp. 868–871, 2004.
[18] L. Zhu, D. C. Ralph, and R. A. Buhrman, "Spin-orbit torques in heavy-metal–ferromagnet bilayers with varying strengths of interfacial spin-orbit coupling," *Phys. Rev. Lett.*, vol. 122, no. 7, Feb. 2019, Art. no. 077201.
[19] A. A. Tulapurkar *et al.*, "Spin-torque diode effect in magnetic tunnel junctions," *Nature*, vol. 438, no. 7066, pp. 339–342, Nov. 2005.
[20] R. Guirado, R. del Rio, J. Carpio, F. Garnacho, A. Valladolid, and M. Valcarcel, "Comparison between GTEM and OATS radiated field emission measurements," in *Proc. Int. Symp. Electromagn. Compat.*, 1995, pp. 338–342.
[21] S. He, Z. Meng, L. Huang, L. K. Yap, T. Zhou, and C. Panagopoulos, "A versatile rotary-stage high frequency probe station for studying magnetic films and devices," *Rev. Sci. Instrum.*, vol. 87, no. 7, Jul. 2016, Art. no. 074704.
[22] S. Tamaru *et al.*, "Bias field angle dependence of the self-oscillation of spin torque oscillators having a perpendicularly magnetized free layer and in-plane magnetized reference layer," *Appl. Phys. Exp.*, vol. 7, no. 6, May 2014, Art. no. 063005.
[23] M. Kopcewicz, T. Stobiecki, M. Czapkiewicz, and A. Grabias, "Microstructure and magnetic properties of Fe/Ti multilayers," *J. Phys., Condens. Matter*, vol. 9, no. 1, pp. 103–115, Jan. 1997.
[24] F. D. Boer, W. C. M. Mattens, R. Boom, A. R. Miedema, and A. K. Niessen, *Cohesion in Metals*. Amsterdam, The Netherlands: North Holland, 1988.
[25] M.-H. Nguyen, D. C. Ralph, and R. A. Buhrman, "Spin torque study of the spin Hall conductivity and spin diffusion length in platinum thin films with varying resistivity," *Phys. Rev. Lett.*, vol. 116, no. 12, Mar. 2016, Art. no. 126601.
[26] C. Kittel, "On the theory of ferromagnetic resonance absorption," *Phys. Rev.*, vol. 73, no. 2, pp. 155–161, Jan. 1948.
[27] E. B. Myers, D. C. Ralph, J. A. Katine, R. N. Louie, and R. A. Buhrman, "Current-induced switching of domains in magnetic multilayer devices," *Science*, vol. 285, no. 5429, pp. 867–870, 1999.

[28] C. O. Avci *et al.*, "Interplay of spin-orbit torque and thermoelectric effects in ferromagnet/normal-metal bilayers," *Phys. Rev. B, Condens. Matter*, vol. 90, no. 22, Dec. 2014, Art. no. 224427.

[29] C. F. Pai, Y. Ou, H. L. Vilela-Leão, D. C. Ralph, and R. A. Buhrman, "Dependence of the efficiency of spin Hall torque on the transparency of Pt/ferromagnetic layer interfaces," *Phys. Rev. B, Condens. Matter*, vol. 92, no. 6, 2015, Art. no. 064426.

[30] A. Magni *et al.*, "Spin Hall magnetoresistance and spin orbit torque efficiency in Pt/FeCoB bilayers," *IEEE Trans. Magn.*, early access, May 28, 2021, doi: 10.1109/TMAG.2021.3084866.

[31] D. MacNeill, G. M. Stiehl, M. H. D. Guimaraes, R. A. Buhrman, J. Park, and D. C. Ralph, "Control of spin–orbit torques through crystal symmetry in WTe_2/ferromagnet bilayers," *Nature Phys.*, vol. 13, no. 3, pp. 300–305, Mar. 2017.

[32] P. Li *et al.*, "Charge-spin interconversion in epitaxial Pt probed by spin-orbit torques in a magnetic insulator," *Phys. Rev. Mater.*, vol. 5, no. 6, Jun. 2021, Art. no. 064404.

[33] S. Cho, S.-H. C. Baek, K.-D. Lee, Y. Jo, and B.-G. Park, "Large spin Hall magnetoresistance and its correlation to the spin-orbit torque in W/CoFeB/MgO structures," *Sci. Rep.*, vol. 5, Oct. 2015, Art. no. 14668.

[34] J. Kim, P. Sheng, S. Takahashi, S. Mitani, and M. Hayashi, "Spin Hall magnetoresistance in metallic bilayers," *Phys. Rev. Lett.*, vol. 116, Feb. 2016, Art. no. 097201.

[35] Ł. Karwacki *et al.*, "Optimization of spin Hall magnetoresistance in heavy-metal/ferromagnetic-metal bilayers," *Sci. Rep.*, vol. 10, no. 1, p. 10767, Jul. 2020.

[36] C.-F. Pai, L. Liu, Y. Li, H. W. Tseng, D. C. Ralph, and R. A. Buhrman, "Spin transfer torque devices utilizing the giant spin Hall effect of tungsten," *Appl. Phys. Lett.*, vol. 101, no. 12, 2012, Art. no. 122404.

[37] W. Skowroński *et al.*, "Temperature dependence of spin-orbit torques in W/CoFeB bilayers," *Appl. Phys. Lett.*, vol. 109, no. 6, 2016, Art. no. 062407.

[38] D. C. Mahendra *et al.*, "Room-temperature high spin–orbit torque due to quantum confinement in sputtered $Bi_xSe_{(1-x)}$ films," *Nature Mater.*, vol. 17, no. 9, pp. 800–807, Sep. 2018.

[39] L. Zhu, L. Zhu, S. Shi, D. C. Ralph, and R. A. Buhrman, "Energy-efficient ultrafast SOT-MRAMs based on low-resistivity spin Hall metal $Au_{0.25}Pt_{0.75}$," *Adv. Electron. Mater.*, vol. 6, no. 2, 2020, Art. no. 1901131.

[40] P. Laczkowski *et al.*, "Large enhancement of the spin Hall effect in Au by side-jump scattering on Ta impurities," *Phys. Rev. B, Condens. Matter*, vol. 96, no. 14, Oct. 2017, Art. no. 140405.

[41] W. S. Torres, J. F. Sierra, L. A. Benítez, F. Bonell, M. V. Costache, and S. O. Valenzuela, "Spin precession and spin Hall effect in monolayer graphene/Pt nanostructures," *2D Mater.*, vol. 4, no. 4, Sep. 2017, Art. no. 041008.

[42] W. Yan, E. Sagasta, M. Ribeiro, Y. Niimi, L. E. Hueso, and F. Casanova, "Large room temperature spin-to-charge conversion signals in a few-layer graphene/Pt lateral heterostructure," *Nature Commun.*, vol. 8, no. 1, p. 661, Sep. 2017.

[43] V. T. Pham *et al.*, "Ferromagnetic/nonmagnetic nanostructures for the electrical measurement of the spin Hall effect," *Nano Lett.*, vol. 16, pp. 6755–6760, Nov. 2016.

[44] L. Zhu, D. C. Ralph, and R. A. Buhrman, "Highly efficient spin-current generation by the spin Hall effect in $Au_{1-x}Pt_x$," *Phys. Rev. Appl.*, vol. 10, no. 3, Sep. 2018, Art. no. 031001.

[45] J.-Y. Kim *et al.*, "Enhancement of spin Hall conductivity in W–Ta alloy," *Appl. Phys. Lett.*, vol. 117, no. 14, Oct. 2020, Art. no. 142403.

[46] V. T. Pham *et al.*, "Spin–orbit magnetic state readout in scaled ferromagnetic/heavy metal nanostructures," *Nature Electron.*, vol. 3, no. 6, pp. 309–315, Jun. 2020.

4.1.3 | CIMS supported by Dzyaloshinskii–Moriya interaction (DMI)

In this subsection on current-induced magnetization switching CIMS in HM/FM bilayers, we examine the evolution of the domain wall and CIMS of the perpendicular magnetized Pt(4)/Co(1)/MgO(2) system. A single bubble-shaped domain was generated in the devices where CIMS experiments were carried out. For this purpose, a saturating field H_z = -4500 Oe was applied perpendicular to the nanodevice. Then, at a slight angle relative to the sample plane, the device was exposed to a series of magnetic field pulses ($\Delta t = 0.1$ s) in the direction parallel to the Hall bar axis. Changing the angle caused a change in the values of the components H_x and H_z of the external field applied. As a result, the domain wall was moved under magnetic field pulses via the expansion of the bubble.

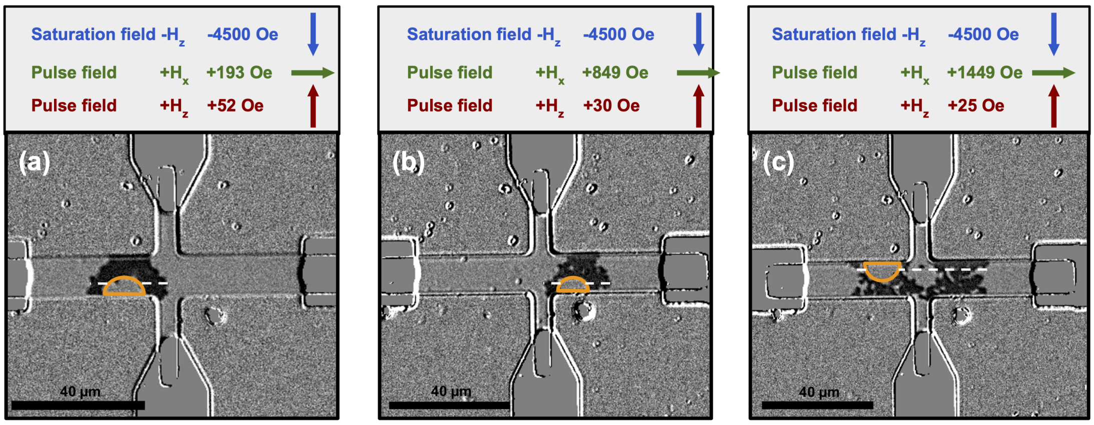

Figure 4.1: Differential p-MOKE images of the growth of the bubble domain with applied (a) in-plane H_x = +193 Oe and perpendicular H_z = +52 Oe field; (b) H_x = +849 Oe and H_z = +30 Oe; (c) H_x = +1449 Oe and H_z = +25 Oe for Pt(4)/Co(1)/MgO. The orange semicircle indicates the initial position of the bubble domain.

As seen in the series of images (Figs. 4.1), a field with a small perpendicular component H_z causes asymmetric growth of the domain wall, preferring the direction following the H_x field. The asymmetry finding shows the presence of DMI, and analysis of this asymmetry indicates the counterclockwise (CCW) chirality of Néel-type DWs [153–155]. Moreover, increasing the H_x component generates an increasingly finer domain structure, evident in Fig.4.1(c). A similar fine-grained domain structure was also observed in the Co/Pt/Co trilayer. The results are presented in Sect.4.2.3.

Next, a CIMS experiment was carried out to study the impact of DMI on this process. The obtained CIMS loops differ in shape depending on the value of the component H_x.

As a result, switching loops were obtained whose shape differed with increasing external magnetic field H_x. For this reason, the loops were divided into three groups, as presented in Fig.4.2: Loops obtained in a high field $|H_x| > 1000$ Oe, a medium field 1000 Oe $> |H_x| > 400$ Oe, and a small field $|H_x| < 400$ Oe. It is worth noting that the resistance value R_{xy} not reached by a single CIMS loop the value equal to the upper or lower state of the AHE loop indicates incomplete switching of the FM layer due to the domain structure.

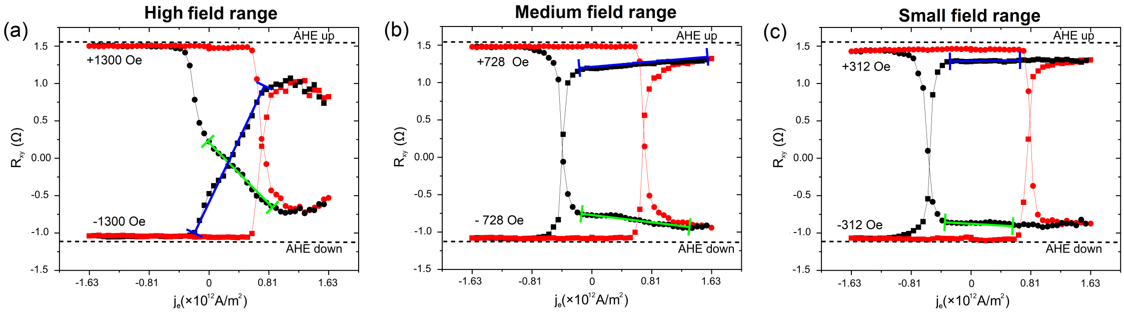

Figure 4.2: Examples of CIMS loops measured at three ranges of the external magnetic field H_x: CIMS loop for the high field (a), medium field (b), and small field (c). The red and black points indicate the directions of the current sweep: from $-j_e \rightarrow +j_e$ (red points) and $+j_e \rightarrow -j_e$ (black points). Slopes of green and blue lines indicate the influence of the magnetic domains on the shape of CIMS loops. As it is easy to notice in j_e=0, the most remagnetization occurs in case (a) and is confirmed by the domain image in Fig.4.1(c).

The most significant differences in the shape of the CIMS loops for positive and negative H_x fields are observed for high fields, as shown in Fig.4.2(a). The shape of both loops deviates significantly from the classic rectangular shape that we expected and is implemented by the macrospin SOT mechanism of the CIMS model [93]. The green and blue lines indicate the parts of the loops that deviate from the rectangular shape of the CIMS loops. As can be seen, the slope of the marked fragment decreases as the field H_x decreases. Finally, in the small field range, the green line becomes almost horizontal, and the CIMS loop assumes an almost rectangular shape (Fig.4.2(c)). There is also an asymmetry in the length of the oblique part of the loop relative to the direction of the magnetic field. In each case, the negative field is characterized by an oblique part (blue line) longer than the positive field (green line). This suggests the presence of an internal H_{DMI} field, which, depending on the direction of the external field H_x, in the first case, adds to it, making the device "feel" a larger magnetic field than is applied. In the other case, it subtracts, reducing the total field that acts on the position of the magnetization vector. Therefore, the applied H_x under which the Néel DWs become stationary can be defined as a compensating or stopping field for which no motion is expected via SOT.

The 1D of the domain wall velocity from [156–158] was used to estimate the H_{DMI} field and explain the effects described above. The existence of a compensating field H_{x}^{*} of opposite sign to H_{DMI} but of the same strength, and the recovery of the Néel-DW configuration, for which no motion is expected over SHE-SOT (Eq.4.1) can be written after [156]:

$$H_{\mathrm{x}}^{*} = H_{\mathrm{DMI}} + \mathrm{sgn}(\theta_{\mathrm{SH}}) \frac{\hbar |j_e|}{2\mu_0 |e| M_s t_{\mathrm{FM}}} \cos(\theta) \tag{4.1}$$

where θ_{SH} is the SHA, j_{e} is the charge current density, t_{FM} the thickness of the FM, and θ internal in-plane DW angle, which is the angle of projection of magnetization in the x-y plane. By analyzing a series of CIMS loops for different H_{x} fields, we found

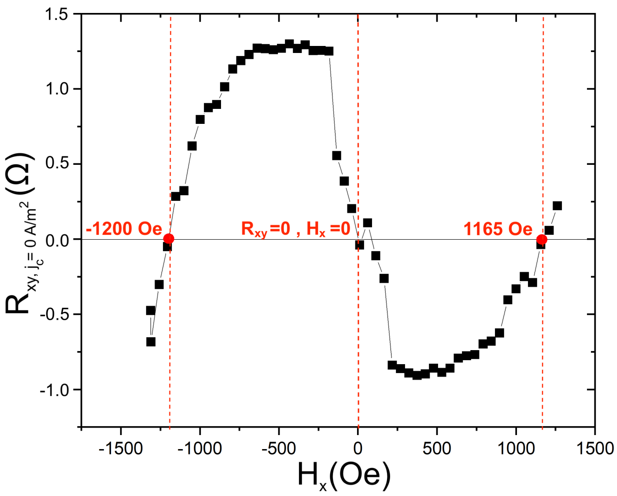

Figure 4.3: The transverse resistance R_{xy} for zero voltage applied as a function of the external magnetic field H_{x}. The red points at the intersection of the experimental data with the zero R_{xy} line give the values of the compensating field $|H_{\mathrm{x}}^{*}| = -H_{\mathrm{DMI}}$

.

a R_{xy} when the zero current density $j_{\mathrm{e}} = 0$ is applied to the Hall bar. This made it possible to null the second term of the formula in Eq.4.1 and obtain the simple relation $H_{\mathrm{x}}^{*} = H_{\mathrm{DMI}}$ (Fig.4.3). The resulting value is $H_{\mathrm{DMI}} \approx 1200$ Oe. Relatively high H_{DMI} in Pt/Co systems have been studied by many [155, 158–160]. The inconsistency of the results for positive and negative fields is within the range of measurement uncertainty. Furthermore, the obtained value of H_{DMI} was used to estimate the DMI energy density (D_{eff}) in the studied system. Using the following formula [156]:

$$D_{\mathrm{eff}} = \frac{\mu_0 M_{\mathrm{S}} \Delta}{H_{\mathrm{DMI}}}$$

where: M_S = 1.35 T is saturation magnetization [155], Δ = 8.3 nm [161] is the width parameter of DW. Using the parameters given above, the value of D_{eff} = 1.1 mJ/m^2 was obtained. The result is very close to a similar Pt(4)/Co(1)/AlO_x sample, where D_{eff} = 1.2 mJ/m^2.

To explain the CIMS loops shape, we developed diagrams that illustrate the behavior of the magnetization vector at successive points in the CIMS loops (marked with numbers 1-6) measured for high fields of H_x = 1300 Oe and -1300 Oe, where the braking or assisting effects are strongest (Fig.4.4).

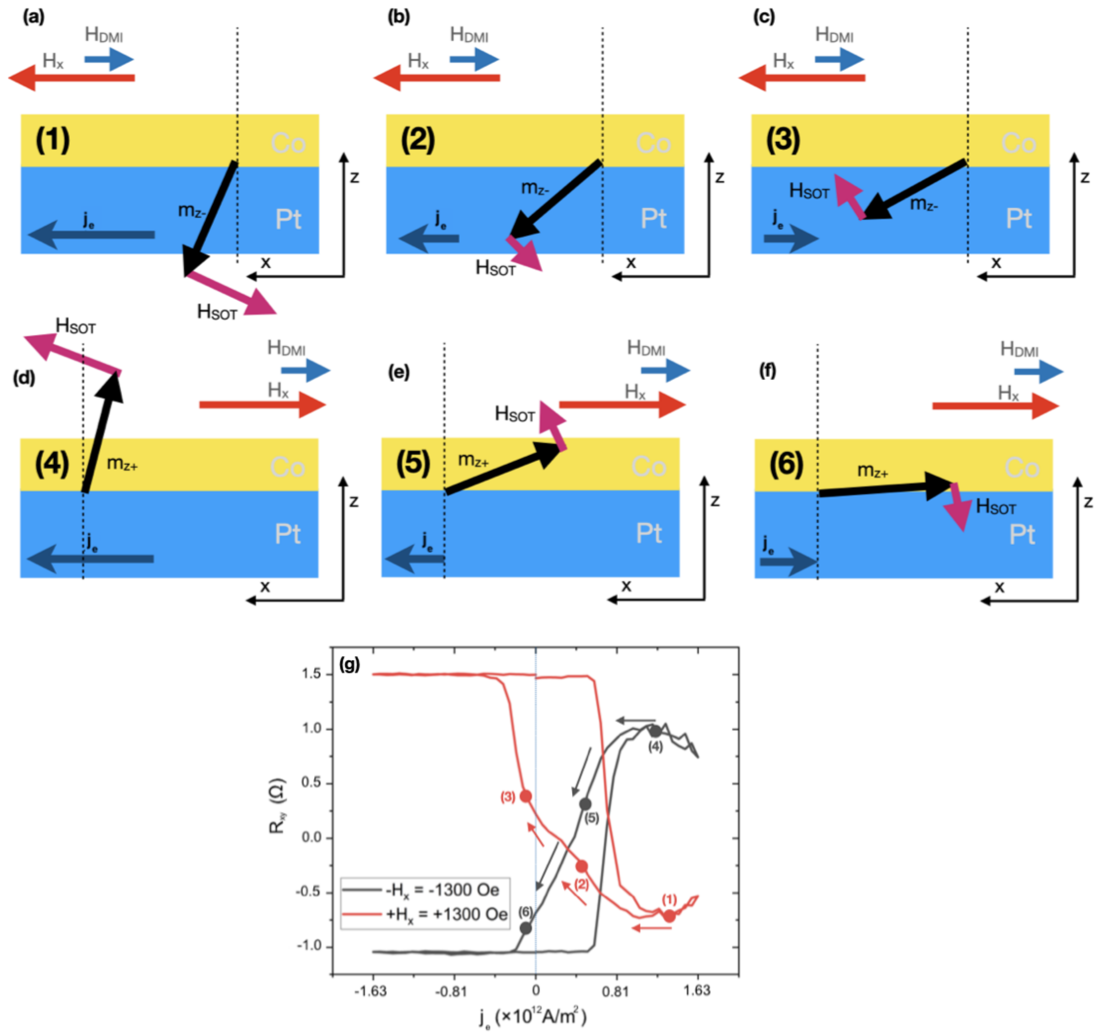

Figure 4.4: A schematic representation of the phenomenological macrospin model of the simultaneous interaction of the external field H_x, the DMI field H_{DMI} and the SOT field (H_{SOT}) at several points on the current switching loops.

At first, the system is in a stable state corresponding to the position of the magnetization vector, respectively, collinear to +z for the CIMS loop corresponding to the +1300 Oe field (red loop) and collinear to -z for the loop corresponding to the -1300 Oe field (gray loop). As is easy to see, the H_{DMI} field is antiparallel to the H_{x} (Fig.4.4 a(1), b(2) and c(3)) and parallel to the -H_{x} field (Fig.4.4 d(4), e(5) and f(6)), so in the first case it sums up with the external field, and in the second it subtracts.

At points 1 and 4 (Fig.4.4), respectively, the effective field component z of H_{SOT} affects the magnetization vector to align it perpendicular to the sample plane. After reaching a maximum current density of $+1.63 \times 10^{12}$ A/m^2, its value gradually decreases, which simultaneously leads to a decrease in the value of H_{SOT} so that a constant sum field H_{x} + H_{DMI} or a difference H_{x} - H_{DMI}, respectively, increasingly pulls the magnetization vector in one direction in-plane, which manifests itself in a gradual increase of R_{xy} (points 2 and 5). The length of the sloped section depends on the magnitude of the total field that affects the magnetization vector. After changing the polarity (points 3 and 6) of the applied voltage and further increasing its value, the magnetization of the system is switched to the maximum R_{xy} due to the effect of H_{SOT}.

In conclusion, analysis of switching loop shapes, together with imaging of the domain structure using the MOKE microscope and the phenomenological model, allowed us to qualitatively study the impact of DMI on the CIMS loop shapes in the bilayer system Pt(4)/Co(1)/NiO. The results are in preparation for publication.

Section summary

In summary, in this section, we have analyzed the results of our study on the SMR and SOT effects in metallic bilayers consisting of a HM layer and a FM metal layer. We have investigated the influence of different factors, such as the thickness and material of the HM and FM layers, the interface morphology and the DMI, on the phenomena mentioned above.

We have used a theoretical spin drift-diffusion model to separate and estimate the contributions of SMR and AMR to the total magnetoresistance signal. We have found that SMR dominates over AMR in systems with W as the HM layer and amorphous CoFeB and crystalline Co as the FM layer due to the high SHA of W. However, in systems with Pt or Au as the HM layer and Co as the FM layer, AMR dominates over SMR due to the large difference in the resistivities of the layers and the different crystallinity of the Co and W layer.

We have also measured the SHA (θ_{SH}) and the SHC (σ_{SH}) of Pt and Pt-Ti systems with different interface structures. We have shown that inserting thin Ti layers between Pt can enhance the SHA of the system by increasing the number of interfaces. We have also observed high values of SHC σ_{SH} in these systems, which are beneficial in reducing Joule heating.

Finally, we performed CIMS experiments in Pt/Co/MgO systems with perpendicular magnetic anisotropy. We have analyzed the shape of the CIMS loops and the domain wall evolution under different external magnetic fields. We have found that DMI affects the CIMS process by creating an internal field that either assists or opposes the external field, depending on its direction. We have estimated the DMI field and effective DMI energy from our CIMS data. We have also developed a phenomenological model based on a one-dimensional domain wall velocity equation to qualitatively explain the CIMS loop shapes.

We have demonstrated that SMR and SOT effects in metallic bilayers are sensitive to various parameters and can be tuned by engineering the interface properties. Our results provide useful insights for optimizing spintronics devices based on these effects.

4.2 | Ferromagnet/heavy metal/ferromagnet (FM/HM/FM) system

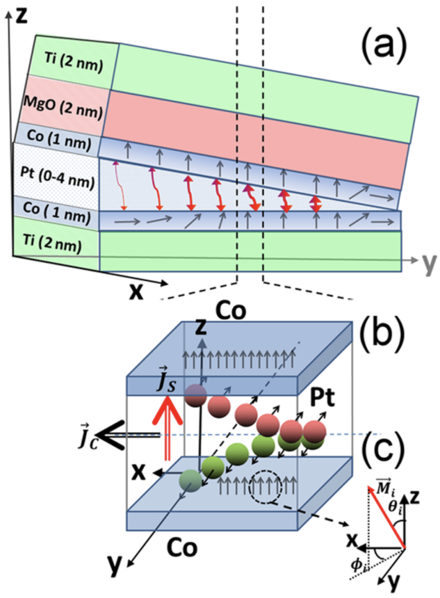

Figure 4.5: (a) Sketch of the investigated three-layer system with a wedge-shaped Pt layer. The gray arrows show the direction of Co layers magnetization as a function of the thickness of the Pt spacer, and the red arrows of varying thickness indicate the value of the IEC coupling. (b) The figure shows the device with a specified Pt thickness. The black arrow indicates the direction of the charge current, while the red arrow indicates the SHE-generated spin current. The gray arrows indicate the direction of magnetization of the two Co layers. (c) Polar and azimuthal angles describe the direction of magnetization in the Co layers. Figure from [P3].

After analyzing the thin-film bilayer system, it was decided to focus on the Co(1)/Pt(0-4)/Co(1) trilayer (a diagram of the layer structure which includes the Ti(2) seed and MgO(2)/Ti(2) capping layers is shown in Fig.4.5), in which the Pt spacer plays the role of both HM in generating spin current and a nonmagnetic interlayer whose variable thickness enables the magnitude of the ferromagnetic IEC to be effectively tuned. The experimental and simulation results presented in this section are based on two publications [P3] and [P4]. First, they describe detailed studies of the system in terms of the influence of coupling on magnetization dynamics and spin transport effects by magnetoresistance and SOT-FMR methods, as well as experimental measurements of interface SOT fields supported by relevant micromagnetic and macrospin simulations and spin diffusion model. [P4] describe studies of CIMS and multilevel switching as a function of Pt thickness.

4.2.1 | Spin Hall Magnetoresistance and Anisotropic Magnetoresistance

Continuing the problem of the dependence of SMR and AMR on Pt thickness, a spin diffusion model was developed for the Co/Pt/Co trilayer taking into account the relative orientations of the magnetizations $\mathbf{m_1}$ and $\mathbf{m_2}$ as a result of IEC coupling. Magnetoresistance dependencies were determined by measuring R_{xx} as a function of the external magnetic field applied in the x, y, and z directions (see Fig.6 in [P3]). A spin diffusion model defined by Eq.7 in [P3] describing the average longitudinal resistance as a function of the orientation of the magnetization of both Co layers was fitted to the magnetoresistance curves (see Fig.7 in [P3]). A detailed discussion of the model and parameters used to fit dependencies of AMR and SMR can be found in Sect.3.2 of the [P3].

It is worth mentioning that the fitting of the macrospin model was further supported by micromagnetic simulations performed with the MUMAX3 software [162]. They confirmed that the parameters obtained are reasonable since the magnetoresistance loops are fully in agreement with those of the macrospin model (Fig.6 in [P3]). Details can be found in Section 4.2 in [P3].

Consequently, the dependence of the SMR (Fig.7(a) in [P3]) and the AMR (Fig.7(b) in [P3]) were determined as a function of the Pt layer thicknesses. The maximum value of $\mathrm{SMR}_{\mathrm{max}}$ = 3.2 Ω is determined from the model for region II (t_{Pt}=1.5 nm Fig.7(a) in [P3]) which is compared to the Co (5) / Pt (t_{Pt}) bilayer system (see Fig.2(b) in [P1]) for which $\mathrm{SMR}_{\mathrm{max}}$ occurs for $t_{\mathrm{Pt}} \approx 6$ nm, is shifted to smaller Pt thicknesses. As can be seen, spin accumulation and spin currents affect the magnetoresistance of the sample through an inverse SHE. Thus, it can be concluded that the highest spin accumulation at Pt interfaces occurs for the area where both layers of Co are magnetized perpendicularly and then decreases for larger Pt thicknesses as a result of spin decoherence, which affects the spin current and reduces the effective spin accumulation at the Co/Pt interface. Determining the absolute relative value of $|\mathrm{SMR}/\mathrm{R}_0|$ of 0.45% and 0.80% for the trilayer and Pt/Co bilayers, respectively, we can see a significant decrease in $\mathrm{SMR}/\mathrm{R}_0$ for the trilayer system. This is because experimentally determined SMR is the sum of the SMRs from the top and bottom Co layers. The spin currents generated by SHE have opposite polarizations at the Co/Pt and Pt/Co interfaces. On the contrary, the positive value of the AMR rapidly (for the region I t_{Pt}<1 nm) and next monotonically decreases with Pt thickness (Fig.7(b) in [P3]) since the average charge current density flowing into the

FM layer decreases for the thicker Pt layer. This, in turn, causes the AMR to decrease according to Eq. 9 in [P3]. The misalignment between the experimental and theoretical results of SMR and AMR (Fig.7 in [P3]), especially for the thin Pt layer (region I), is due to the strong mixing and alloying at the interfaces, as demonstrated in Fig.3 in [P3]).

4.2.2 | Spin Hall Effect and magnetization dynamics

Another aim of the research was to determine SHA (θ_{SH}) in a wide range of Pt thickness considering PMA and IMA in both FM layers. For this, devices where both Co layers have PMA (regions II (1 nm > t_{Pt} > 1.9 nm) and III (1.9 nm > t_{Pt} > 2.9 nm)) were analyzed by field dependence of the harmonic voltage method (described in Sect.3.6.2.1). Example results for devices with PMA ($t_{\mathrm{Pt}} = 1.74$ nm region II and $t_{\mathrm{Pt}} = 2.64$ nm region III) measurements of the first (V_{ω}) and second ($V_{2\omega}$) field harmonic voltages are shown in Fig.8 in [P3]. In contrast, for devices where both Co layers were IMA (region I ($t_{\mathrm{Pt}} < 1$ nm) or one layer, due to poor coupling, is IMA, and the other is PMA (region IV $t_{\mathrm{Pt}} > 2.9$ nm) the angular dependence of the harmonic Hall voltage was used (see Sect.3.6.2.2). An example of angular curves of $V_{2\omega}$ representative samples from regions I ($t_{\mathrm{Pt}} = 0.52$ nm) and IV ($t_{\mathrm{Pt}} = 3.76$ nm) are shown in Fig.9(a,b) in [P3]. Using the equations Eq.3.3 and Eq.3.4, the effective fields H_{DL} and H_{FL} were determined (marked as red and blue points Fig.11(a) in [P3]).

For small t_{Pt}, both effective fields are close to zero, while in region II, both components increase. In region III, the DL field slightly exceeds the FL component. At the boundary between regions III and IV, the field H_{DL} increases rapidly and begins to dominate significantly over H_{FL}. In region IV, the values of the DL field are saturated, while the FL field falls back to small values.

In devices where both ferromagnets have the same direction of anisotropy (in-plane in region I and perpendicular in regions II-III) (Figs.5(a,b) in [P3]), the determined values H_{DL} and H_{FL} are the sums of the SOT fields acting on the top and bottom Co layers $H_{\mathrm{DL}} = H_{\mathrm{DL,1}} + (-H_{\mathrm{DL,2}})$ and $H_{\mathrm{FL}} = -H_{\mathrm{FL,1}} + H_{\mathrm{FL,2}}$. Opposite signs of the components come from the opposite signs of the spin current at the Co/Pt and Pt/Co interfaces. The values of the $H_{\mathrm{DL,1(2)}}$ and $H_{\mathrm{FL,1(2)}}$ components at each interface are derived from the different real parts of the mixture conductance $G_{\mathrm{r}}^{(1)}$ and $G_{\mathrm{r}}^{(2)}$. To support the analysis, we calculated the effective fields using the spin diffusion model (for details, see Subsection 3.2 in [P3]). In the case of H_{FL} (blue line in Fig.11(a) in [P3]), the theoretical curve deviates significantly from the experimental curve. Only taking into account the Oersted field (H_{Oe}) (red dashed line in Fig.11(a) in [P3]) originating from the charge current and the spin-orbital field ($H_{\mathrm{S-O}}$) (black dashed line in Fig.11(a) in [P3]) satisfactorily reproduced experimental dependence (green line in Fig.11(a) in [P3]).

The calculated SHA increases in the II region, where the thickness of Pt is already sufficient to generate a significant spin current (Fig.11(b) in [P3]). After reaching a maximum value of approximately 14% for t_{Pt} = 3.24 nm, it decreases slightly in region IV. The theoretical curve of the diffusion model differs significantly from the experimental points of effective SHA ($\theta_{SH,eff}$). This is because the theoretical value of pure SHE efficiency is a material parameter within the very thick HM limit.

In our analysis, we also estimate the contribution of ANE to the total harmonic response. By fitting a linear function that interception with the y axis indicates ANE contribution, we found that for devices with $t_{Pt} = 0.52$ nm and $t_{Pt} = 3.76$ nm, the ANE-related electric field were $|E_{ANE}| \approx -0.03$ V/m and $|E_{ANE}| = -0.015$ V/m, respectively. These values are much lower than those reported in the literature $|E_{ANE}| = -0.21$ V/m for Pt(1)/Co(2.5) and $|E_{ANE}|$ = -0.08 V/m for Pt(2)/Co(2.5) systems [151]. This allowed us to neglect this contribution in our consideration.

In this section, we also considered the magnetization dynamics of Co/Pt/Co trilayer by the FMR spin diode method [163] in a wide range of Pt thicknesses. In the results, we measured and analyzed dispersion relations [164, 165] for all Pt thickness regions depicted in Fig.4 in [P3]. The macrospin model based on numerical calculations of the resonance frequencies from the Landau-Lifshitz-Gilbert-Slonczewski (LLGS) equation allows for dispersion relations, which, in turn, were used to determine ferromagnetic interlayer exchange coupling (IEC) between two Co layers separated by the variable thickness of Pt.

As can be easily seen in Fig.4, the number and shape of experimentally detectable dispersion branches strongly depend on the coupling. Note that the macrospin simulations indicate all resonance mods, even those that are not available by measurement methods, because the model predicts all possible stationary states of the mods. The additional mods, especially in regions III and IV (Fig.4(e-g) in [P3]), may come from the independent dynamics of each magnetization, where the high-amplitude oscillations come from the in-plane layer and the rest from the perpendicular magnetized Co layer. By fitting a theoretical resonance model, we could estimate the magnetic parameters of the system, such as the anisotropy of each layer (the top Co and the bottom Co) (Fig.5(a,b) in [P3]), saturation magnetization (Fig.5(c) in [P3]), and IEC coupling as a function of Pt thickness (Fig.5(d) in [P3]). In the thin Pt region, where $t_{Pt} < 1.36$ nm, the IEC value cannot be determined unambiguously because high-frequency optical mods (oscillations of magnetization in opposite phase) are detectable at frequencies >30 GHz, but not experimentally observable due to losses in microwave power applied to the device. All obtained parameters were used in all the studies described above.

ACS APPLIED MATERIALS & INTERFACES

www.acsami.org Research Article

Study of Spin−Orbit Interactions and Interlayer Ferromagnetic Coupling in Co/Pt/Co Trilayers in a Wide Range of Heavy-Metal Thickness

Piotr Ogrodnik,* Krzysztof Grochot, Łukasz Karwacki, Jarosław Kanak, Michał Prokop, Jakub Chęciński, Witold Skowroński, Sławomir Ziętek, and Tomasz Stobiecki

Cite This: *ACS Appl. Mater. Interfaces* 2021, 13, 47019−47032 Read Online

ACCESS | Metrics & More | Article Recommendations | Supporting Information

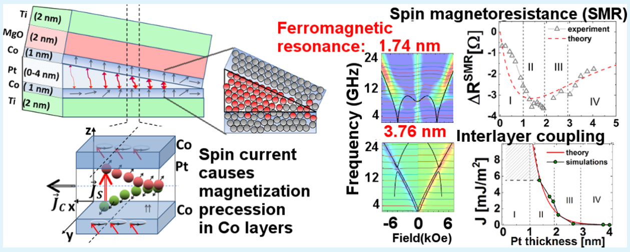

ABSTRACT: The spin−orbit torque, a torque induced by a charge current flowing through the heavy-metal-conducting layer with strong spin−orbit interactions, provides an efficient way to control the magnetization direction in heavy-metal/ferromagnet nanostructures, required for applications in the emergent magnetic technologies like random access memories, high-frequency nano-oscillators, or bioinspired neuromorphic computations. We study the interface properties, magnetization dynamics, magnetostatic features, and spin−orbit interactions within the multilayer system Ti(2)/Co(1)/Pt(0−4)/Co(1)/MgO(2)/Ti(2) (thicknesses in nanometers) patterned by optical lithography on micrometer-sized bars. In the investigated devices, Pt is used as a source of the spin current and as a nonmagnetic spacer with variable thickness, which enables the magnitude of the interlayer ferromagnetic exchange coupling to be effectively tuned. We also find the Pt thickness-dependent changes in magnetic anisotropies, magnetoresistances, effective Hall angles, and, eventually, spin−orbit torque fields at interfaces. The experimental findings are supported by the relevant interface structure-related simulations, micromagnetic, macrospin, as well as the spin drift-diffusion models. Finally, the contribution of the spin−orbital Edelstein−Rashba interfacial fields is also briefly discussed in the analysis.

KEYWORDS: *ferromagnetic resonance, spin Hall effect, magnetoresistance, spin−orbit torques, Rashba−Edelstein effect*

1. INTRODUCTION

The magnetic multilayer structures consisting of thin ferromagnetic (F) layers and nonmagnetic spacers are known to exhibit plenty of phenomena, among which one can find those extensively studied for the last decades like anisotropic, giant and tunneling magnetoresistance or spin-transfer torque effect (STT),[1,2] and recently, current-driven spin−orbit torque (SOT) magnetization switching.[3] These effects are widely exploited in the spintronic devices, magnetic random access memories (MRAM) like STT-MRAM and SOT-MRAM,[4−7] as well as may be exploited in magnetic sensors (including magnetic nanoparticles) and nano-oscillators.[8,9] Such devices include nonmagnetic layers that are crucial for their features and performance. These layers may be both insulating (e.g., MgO in magnetic tunnel junctions) and metallic (e.g., Cu, Au in GMR devices).[9] Recently, the nonmagnetic layers made of heavy metallic (HM) elements (W, Ta, Pt, and their alloys[10−12]) are extensively studied because of their large spin−orbit coupling (SOC).[13] Such layers combined with ferromagnetic ones (typically Co, CoFeB) are expected to have new spin transport properties related to the SOC, e.g., spin Hall effect (SHE) and Rashba−Edelstein effect (REE).[14,15] Although the SHE occurs in a single HM layer,[16] it is detectable in heterostructures with ferromagnets only, such as F/HM bi-[17] and F/HM/F trilayers.[18,19] In these structures, the spin-polarized electrons can accumulate at the HM/F interfaces and then may be efficiently injected into the F

Received: June 22, 2021
Accepted: September 14, 2021
Published: September 24, 2021

https://doi.org/10.1021/acsami.1c11675
ACS Appl. Mater. Interfaces 2021, 13, 47019−47032

layer exerting the spin−orbit torque (SOT) on its magnetic moment. This effect has been predicted theoretically[20−22] and reported in many experimental works on SOT-induced magnetic dynamics[23] and magnetic switching.[19,24−26] Especially for the F layers with a magnetic perpendicular anisotropy, the SOT enables a promising way to design efficient, ultralow power consumption spintronic devices. Apart from the SHE and related spin accumulation, the other pure interfacial effects, like charge-spin conversion REE at interfaces, contribute to the SOT.[27−29] Particularly, in multilayer systems with the symmetry-breaking axis along the direction of the current flow, the REE enables field-free magnetization switching.[30,31] Similar effect was also found in the magnetic multilayers in the presence of spin current gradients.[32,33] Therefore, interface engineering and quantifying the REE become significant for the optimization of SOT-based devices.[34−36] The spin currents injected into the F layer and SOTs may be examined by electric measurements through its magnetoresistance[37−39] and the anomalous Hall effect (AHE).[40] The change of the resistance of the hybrid structure caused by the above effects is referred to as spin Hall magnetoresistance (SMR).[41] Up to date, the specific multilayer structures (bi- and trilayers) were studied in detail. Among them, we find CoFeB-based structures like W/i-CoFeB/Pt[42] and p-CoFeB/Ta, as well as the Co-based multilayers like[43] p-Co/Pt/i-Co,[19] p-Co/Pt,[44−46] i-Co/Ta,[46] Ta/i-Co/Pt,[47] Ru/p-Co/Ru, and Ru/p-Co/Ru/W,[48] where p(i) stands for perpendicular(in-plane) anisotropy. Also, the recent studies on Pt/Co/Ru/Co/Pt showed that the RKKY interlayer exchange coupling (IEC) could tailor the properties of the multilayers.[49]

In this paper, we present the detailed studies of the Co/Pt/Co system with the use of the electrically detected FMR (ferromagnetic resonance), as well as low-frequency harmonic Hall voltage and static magnetotransport measurements. Here, the Pt layer plays a double role in the considered structure, first as a source of substantial spin currents and second as an essential element of the exchange ferromagnetic coupling mechanism. Therefore, the Pt thickness can be varied to control the spin currents and interlayer coupling, both essential for designing SOT-MRAM and high-frequency spintronic devices. We provide the results on the resonance frequencies and the SOT effective fields depending on the Pt thickness. Also, we analyze the magnetic parameters of the system like anisotropies, saturation magnetizations, and the IEC. We show that anisotropies and the IEC strongly depend on the Pt thickness, particularly for Pt layer thicknesses less than 2 nm. For such a thin Pt, the transition from the effective in-plane Co anisotropy to the perpendicular one may occur. We account for the features by providing reliable theoretical macrospin models of magnetization dynamics, magnetoresistance, and the effective spin Hall effect angle.

2. EXPERIMENTAL SECTION

2.1. Multilayer Stack. Multilayers are deposited on thermally oxidized Si substrates using magnetron sputtering at room temperature. We study the Co/Pt/Co trilayer within the Ti(2)/Co(1)/Pt(0−4)/Co(1)/MgO(2)/Ti(2) structure shown in Figure 1 (the numbers in parentheses indicate the nominal thickness of the individual layers in nanometers). The Co/Pt/Co trilayer was designed so that it allows us to study the influence of the Pt thickness on the magnetic anisotropy of bottom and top Co layers, the IEC between Co layers through the Pt spacer, magnetization dynamics, and SHE-driven SOT acting on the F layers. For this purpose, both bottom and top thin Co layers should have small anisotropy (differing by interfaces Ti/Co and Co/MgO), with values close to the transition from in-plane to perpendicular. The Ti underlayer improves subsequent layers' adhesion and smoothens the substrate surface. Moreover, as shown in ref 50, the Ti/Co interface is alloyed due to mixing during magnetron deposition, while the Co/MgO interface is sharp.[51] Therefore, the top Co layer is characterized by a higher interface perpendicular anisotropy.

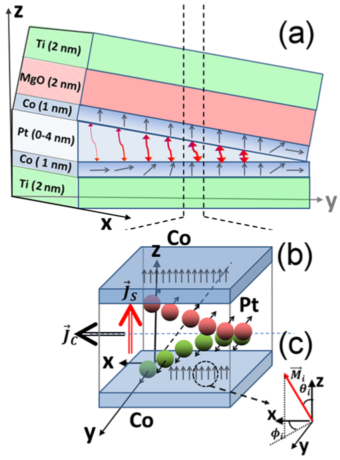

Figure 1. (a) Experimental multilayer stack with a wedge of Pt. The red thick (thin) wavy arrows indicate strong (weak) IEC, whereas the gray arrows show the change in the magnetization alignment with the Pt thickness; (b) the patterned device for a certain thickness of Pt—the arrows indicate the direction of the current flow ($\vec{j}_c$) and associated spin current ($\vec{j}_s$) due to SHE. The short arrows depicted in the Co layers denote their magnetization vectors for a given Pt thickness at remanence; and (c) the polar and azimuthal angles describing the magnetization direction within the Co layers.

2.2. Structural Characterization. High-resolution X'Pert−MPD diffractometer with a Cu anode was used for X-ray diffraction (XRD) characterization. Figure 2 shows the XRD $\theta-2\theta$ profiles of the Si/SiO_2/Ti/Co(1)/Pt(0−4)/Co(1)/MgO/Ti multilayer measured at different positions of the Pt wedge. The $\theta-2\theta$ measurements show the preferred growth of the Pt/Co in the [111] direction of the fcc structure. The peak of the Co layers is invisible because of their tiny thicknesses ($t_{Co} \approx 1$ nm). The arrows indicate the Co (111) peak position present in the thick Co layer case (see the Supplemental

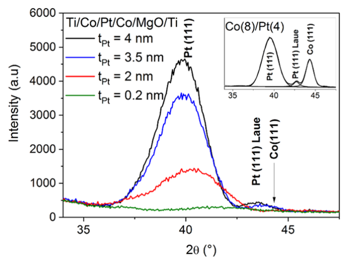

Figure 2. XRD $\theta-2\theta$ profiles of a Si/SiO_2/Ti/Co(1)/Pt(0−4)/Co/MgO/Ti measured at different positions of the Pt wedge. The arrow indicates the 2θ position of the structural Co (111) peak visible in the reference sample with 8 nm of Co and 4 nm of the Pt layer thickness (inset).

https://doi.org/10.1021/acsami.1c11675
ACS Appl. Mater. Interfaces 2021, 13, 47019−47032

Material in refs 19, 52). The peak on the right side of the Pt(111) is a Laue satellite[19] that confirms the asymmetry in top Pt/Co and bottom Co/Pt interfaces. The intensity of the profiles depends on the number of Pt atoms. Therefore, in the case of very thin (0.2 nm) Pt layers, the Laue peaks are out of detection of the experimental method. However, one can see that the Pt peak slightly shifts to the right for thin Pt layers. It suggests that most of the Pt layer becomes mixed with Co atoms, making a rather Co−Pt compound than a well-separated layer.

Figure 3a shows the profile measured for the Si/SiO_2/Ti(2)/Co(1)/Pt(4)/Co(1)/MgO(2)/Ti(2) at a Pt thickness of ≈ 4 nm,

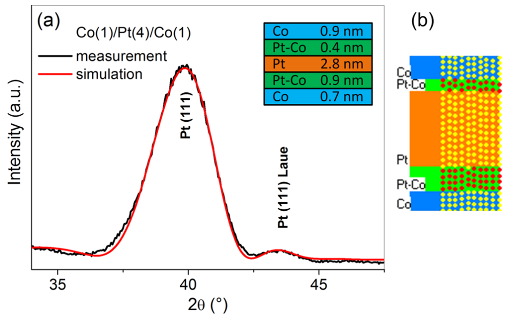

Figure 3. Measured and calculated XRD $\theta - 2\theta$ profiles (a). The assumed thicknesses of the Pt and Co layers and transition area with the Pt−Co mixed interfaces (inset). A snapshot of the Monte Carlo simulation of the interface structure in Co/Pt/Co (b).

together with the profile calculated using the simulated[52] structure (Figure 3b). An excellent agreement between the experimental and theoretical profiles is achieved. The structure was simulated with the assumption of Pt and Co mixing at the interfaces. The simulations represent the columnar grains in the Pt and Co layers and a transition area with the Pt−Co mixed interface. Mixing of the Pt and Co atoms at the interface causes decreasing Pt lattice plane spacing compared to that of pure Pt.

The simulation assumes more significant mixing at the bottom side of the Pt than at the top one. In the former case, the heavy Pt atoms can penetrate the Co layer more easily than in the latter case. Moreover, for Pt within Co, the interfacial enthalpy is −33 kJ/(mole of atoms), whereas, for Co in Pt, the interfacial enthalpy is −26 kJ/(mole of atoms). Higher negative enthalpy results in easier mixing at the bottom Co/Pt interface.

3. THEORY

3.1. Resonance Model. This subsection presents the macrospin model that allows us to calculate resonance frequencies of the considered Co/Pt/Co structure. Since the Co layers may be either coupled or uncoupled, we employ the approach that has been already presented in detail and successfully applied in our previous work.[53] We describe magnetic moments of each layer by spherical angles (polar θ_i and azimuthal ϕ_i)

$$\boldsymbol{M_i} = M_{S,i}[\sin\theta_i\cos\phi_i,\ \sin\theta_i\sin\phi_i,\ \cos\theta_i] \tag{1}$$

where $i = 1(2)$ is referred to as the top(bottom) cobalt layer. The magnetization dynamics of the system is described by two coupled Landau−Lifshitz−Gilbert (LLG) equations

$$\frac{d\boldsymbol{M_i}}{dt} = -\gamma_e \boldsymbol{M_i} \times \boldsymbol{H}_{\text{eff},i} + \frac{\alpha_g}{M_{S,i}}\boldsymbol{M_i} \times \frac{d\boldsymbol{M_i}}{dt} + \gamma_e(\boldsymbol{\tau}_{DL,i} + \boldsymbol{\tau}_{FL,i}) \tag{2}$$

where $\gamma_e \approx 1.760859644 \times 10^{11}\ \frac{\text{rad}}{\text{sT}}$ is the gyromagnetic ratio, and α_g is the Gilbert damping parameter for each layer.

The terms $\tau_{DL} = H_{DL}(\boldsymbol{m}_i \times \boldsymbol{m}_i \times \hat{\boldsymbol{e}}_y)$ and $\tau_{FL} = H_{FL}(\boldsymbol{m}_i \times \hat{\boldsymbol{e}}_y)$ stand for SOT damping-like (DL) and field-like(FL) components with the unit vector $\boldsymbol{m}_{1(2)} = \frac{\mathbf{M}_{1(2)}}{M_{S,1(2)}}$ and the amplitudes H_{DL} and H_{FL}, respectively.

The effective field (H_{eff}) can be expressed as a functional derivative of the following total magnetic energy of the system

$$\begin{aligned} U = \sum_{i=1}^{2} K_{\perp,i} t_{Co_i}[(\cos\beta_i \sin\theta_i \sin\phi_i - \sin\beta_i \cos\theta_i)^2 + \\ +(\cos\delta_i(\cos\theta_i \cos\beta_i + \sin\theta_i \sin\phi_i \sin\beta_i) - \\ -\cos\phi_i \sin\theta_i \sin\delta_i)^2] + K_{\parallel,i}(\cos^2\theta_i + \sin^2\theta_i \sin^2\phi_i) - \\ -t_{Co_i}\boldsymbol{M_i}\cdot\boldsymbol{H}_{\text{ext}} - t_{Co_i}\boldsymbol{M_i}\cdot\boldsymbol{H}_{dem,i} - J\boldsymbol{M_i}\cdot\boldsymbol{M_j} \end{aligned} \tag{3}$$

The complex expression for the anisotropies originates from the rotation of the easy axes around x and y directions with the use of the relevant Euler rotation matrices. The angles β and δ have been introduced to account for a small deviation of the perpendicular anisotropies ($K_{\perp,i}$) from the perpendicular (z) direction (δ, $\beta \ll \pi/2$). The perpendicular anisotropy terms simplify into a well-known form $K_{\perp,i} \sin^2\theta_i$ when δ_i, $\beta_i = 0$. Also, we have added a small in-plane contribution $K_\parallel \ll K_\perp$ along the y direction. As long as they are small, they slightly improve the fitting of the macrospin model to the experimental data. In eq 3, $t_{\text{Co},i}$, $\boldsymbol{H}_{\text{ext}}$, $\boldsymbol{H}_{\text{dem},i}$, and J stand for magnetic layer thickness, external magnetic field, demagnetizing field, and IEC, respectively.

The LLG equation (eq 2) in polar coordinates can be written in the general form

$$\dot{\boldsymbol{\alpha}} = \boldsymbol{v}(\theta_i, \phi_i)^T \tag{4}$$

where $\dot{\alpha}$ and $\boldsymbol{v}$ are the vectors containing the spherical angles ($\theta_{1,2}$, $\phi_{1,2}$), time-derivatives, and the right-hand side (RHS) of the LLG equation, respectively. After linearization of $\boldsymbol{v}$ with respect to small deviations in θ_i and ϕ_i from their stationary values, one can write eq 4 in the form

$$\dot{\boldsymbol{\alpha}} = \hat{X}\boldsymbol{\Gamma}(t) \tag{5}$$

where $\hat{X}$ is a 4 × 4 matrix consisting of the derivatives of the RHS of eq 4 with respect to the angles θ_i, ϕ_i (i.e., $X_{kj} \equiv \frac{\partial v_k}{\partial \alpha_j}$), while $\Gamma(t) = (\delta\alpha_1(t), ..., \delta\,\alpha_4(t))^T$ is a vector containing time-dependent angle differentials, i.e., $\delta\alpha_1(t) \equiv \delta\,\theta_1(t)$, $\delta\alpha_2(t) \equiv \delta\,\phi_1(t)$, etc. When small oscillations are assumed and in the absence of the external driving force (i.e., SOT or Oersted field), eq 5 can be rewritten as an eigenvalue problem of the matrix $\hat{X}$

$$|\hat{X} - \omega\hat{I}| = 0 \tag{6}$$

The solution of the problem provides the complex eigenvalues ω_i determining two distinct natural resonance angular frequencies of the system, $\omega_{R,i} = \text{Re}\ \omega_i$.

https://doi.org/10.1021/acsami.1c11675
ACS Appl. Mater. Interfaces 2021, 13, 47019−47032

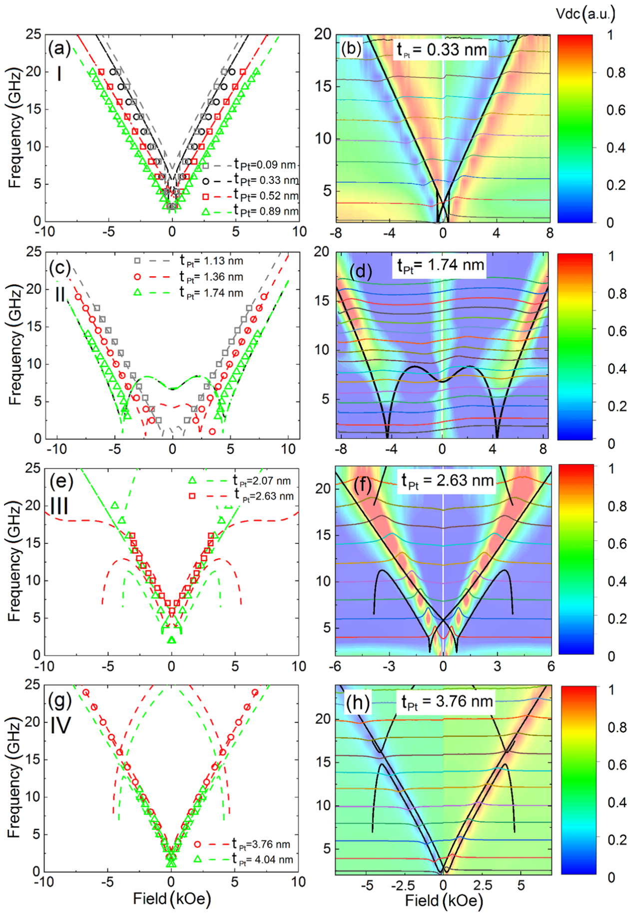

Figure 4. Experimental versus theoretical relations of dispersion for samples from regions I (a, b), II (c, d), III (e, f), and IV (g, h). Left column: the sets of theoretical (lines) and experimental (points) dependencies for each region. Right column: the experimental V_{DC} spectra shown as color map (color is the magnitude of the SD signal) and the source raw spectra measured at the frequency ranging from 2 to 20 GHz (light color lines), with the corresponding theoretical $f(H)$ dependencies (solid black lines). The macrospin simulation magnetic parameters are the same as presented in Figure 5a−d.

3.2. Diffusive Model of the Magnetoresistance. The average longitudinal resistance of our trilayer stack is, in general, dependent on the orientation of magnetizations $\boldsymbol{m}_{1(2)}$ in both ferromagnetic layers and reads

$$R_{xx}(\boldsymbol{m}_{1(2)}) = \frac{L}{w}\left[\frac{1}{E_x}\frac{1}{\sum_\chi t_\chi}\sum_\chi \int_\chi dz j^\chi_{c,x}(z, \boldsymbol{m}_{1(2)})\right]^{-1} \quad (7)$$

where E_x is the electric field in the x direction, L is the length, w is the width, and t_χ is the thickness of layer $\chi = HM$, F1, F2, and $\int_\chi$ denotes the integral with limits corresponding to the position of layer χ in the stack. For Pt, i.e., for $\chi = HM$, the charge current density reads

$$j^{HM}_{c,x}(z, \boldsymbol{m}_{1(2)}) = \frac{1}{\rho_{HM}}E_x - \frac{\theta_{SH}}{2e\rho_{HM}}\frac{\partial\mu^{HM}_{s,y}(z, \boldsymbol{m}_{1(2)})}{\partial z} \quad (8)$$

where ρ_{HM} is the resistivity of the Pt layer, θ_{SH} is the spin Hall angle defined as the charge-to-spin current conversion efficiency at a very thick HM layer limit, and $\mu^{HM}_{s,y}(z, \boldsymbol{m}_{1(2)})$ is the spin accumulation, while for the ferromagnetic layers, i.e., χ = F1 (χ = F2)

$$j^{F1(F2)}_{c,x}(z, \boldsymbol{m}_{1(2)}) = \frac{[1 - \theta_{AMR}(\boldsymbol{m}_{1(2)}\cdot\hat{\boldsymbol{x}})^2]}{\rho_{F1(F2)}}E_x \quad (9)$$

where $\rho_{F1(F2)}$ is the resistivity of the corresponding ferromagnetic layer, θ_{AMR} is the AMR in the thick ferromagnetic limit (assumed for simplicity the same in both ferromagnetic layers). For more details, see, e.g., ref 37.

To obtain spin accumulation in the Pt layer, we consider the spin current density flowing in Pt

https://doi.org/10.1021/acsami.1c11675
ACS Appl. Mater. Interfaces 2021, 13, 47019−47032

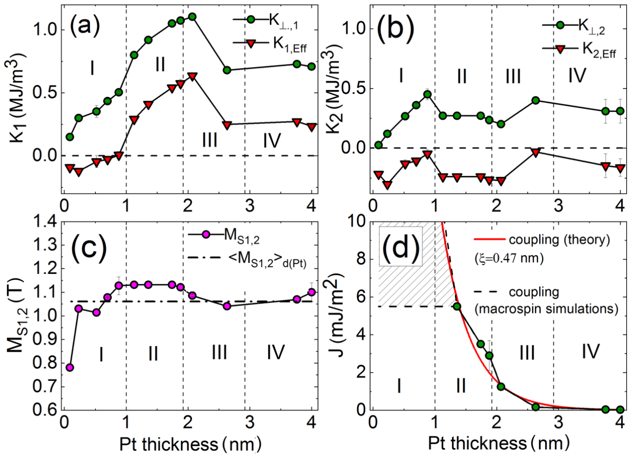

Figure 5. Magnetic parameters of the Co layers as a function of the Pt layer thickness derived from the macrospin simulations of the spin diode FMR spectra: perpendicular and effective anisotropies (a, b), magnetization saturation (c), and interlayer coupling (d).

$$\mathbf{j}_s^{HM}(z, \boldsymbol{m}_{\mathbf{1(2)}}) = -\theta_{SH}\frac{1}{\rho_{HM}}E_x\hat{\boldsymbol{y}} + \frac{1}{2e\rho_{HM}}\frac{\partial \boldsymbol{\mu}_s^{HM}(z, \boldsymbol{m}_{\mathbf{1(2)}})}{\partial z} \quad (10)$$

along with the boundary conditions

$$\mathbf{j}_s^{HM}(-t_H, \boldsymbol{m}_\mathbf{1}) = \mathbf{q}_1(\boldsymbol{m}_\mathbf{1}) \quad (11a)$$

$$\mathbf{j}_s^{HM}(0, \boldsymbol{m}_\mathbf{2}) = -\mathbf{q}_2(\boldsymbol{m}_\mathbf{2}) \quad (11b)$$

$$j_s^{F1}(-t_{HM} - t_{F1}) = 0 \quad (11c)$$

$$j_s^{F1}(-t_{HM}) = \mathbf{m}_1\cdot\mathbf{q}_1(\boldsymbol{m}_\mathbf{1}) \quad (11d)$$

$$j_s^{F2}(0) = \mathbf{m}_2\cdot\mathbf{q}_2(\boldsymbol{m}_\mathbf{2}) \quad (11e)$$

$$j_s^{F2}(t_{F2}) = 0 \quad (11f)$$

where the spin current in ferromagnetic metals assumes the following form

$$j_s^{F1(F2)}(z) = \frac{(1 - \beta_{F1(F2)}^2)}{2e\rho_{F1(F2)}}\frac{\partial \mu_s^{F1(F2)}(z)}{\partial z} \quad (12)$$

and the interfacial spin currents

$$\begin{aligned}\boldsymbol{q}_1(\boldsymbol{m}_\mathbf{1}) &= G_s^{(1)}[\mu_s^{F1}(-t_{HM}) - \boldsymbol{m}_\mathbf{1}\cdot\boldsymbol{\mu}_s^{HM}(-t_{HM}, \boldsymbol{m}_{\mathbf{1(2)}})]\boldsymbol{m}_\mathbf{1}\\ &+G_r^{(1)}\boldsymbol{m}_\mathbf{1} \times \mathbf{m}_1 \times \boldsymbol{\mu}_s^{HM}(-t_{HM}, \boldsymbol{m}_{\mathbf{1(2)}})\\ &+G_i^{(1)}\boldsymbol{m}_\mathbf{1} \times \boldsymbol{\mu}_s^{HM}(-t_{HM}, \boldsymbol{m}_{\mathbf{1(2)}})\end{aligned} \quad (13a)$$

$$\begin{aligned}\boldsymbol{q}_2(\boldsymbol{m}_\mathbf{2}) &= G_s^{(2)}[\mu_s^{F2}(0) - \boldsymbol{m}_\mathbf{2}\cdot\boldsymbol{\mu}_s^{HM}(0, \boldsymbol{m}_{\mathbf{1(2)}})]\boldsymbol{m}_\mathbf{2}\\ &+G_r^{(2)}\boldsymbol{m}_\mathbf{2} \times \boldsymbol{m}_\mathbf{2} \times \boldsymbol{\mu}_s^{HM}(0, \boldsymbol{m}_{\mathbf{1(2)}})\\ &+G_i^{(2)}\boldsymbol{m}_\mathbf{2} \times \boldsymbol{\mu}_s^{HM}(0, \boldsymbol{m}_{\mathbf{1(2)}})\end{aligned} \quad (13b)$$

where $G_s^{(1)}$ and $G_s^{(2)}$ are spin conductances and $G_{r(i)}{}^{(1)}$ and $G_{r(i)}{}^{(2)}$ are the real (imaginary) parts of spin-mixing conductances for interfaces 1 (F1/HM) and 2 (HM/F2), respectively. Moreover, the effective fields, H_{DL} and H_{FL} (cf. Section 3.1), due to SHE and spin accumulation at the interfaces can be expressed as follows

$$H_{DL}^{1(2)} = -\frac{\hbar}{2e^2}\frac{1}{\mu_0 M_{S,1(2)}t_{F1(F2)}}\mathbf{x}\cdot(\mathbf{m}_{1(2)}\times\mathbf{q}_{1(2)}) \quad (14)$$

and

$$H_{FL}^{1(2)} = -\frac{\hbar}{2e^2}\frac{1}{\mu_0 M_{S,1(2)}t_{F1(F2)}}\mathbf{y}\cdot(\mathbf{m}_{1(2)}\times\mathbf{q}_{1(2)}) \quad (15)$$

To fit the appropriate magnetoresistance relations obtained from eq 7, we use the following parameters:[37,54−56] ρ_{HM} = 59 $\mu\Omega$ cm, $\rho_{F1(F2)}$ = 72.5 $\mu\Omega$ cm, λ_{HM} = 1.8 nm, $\lambda_{F1} = \lambda_{F2}$ = 7 nm, θ_{SH} = 8%, θ_{AMR} = 0.15%, $\beta_1 = \beta_2$ = 0.3, $G_s^{(1)} = G_s^{(2)} = G_r^{(1)} = G_i^{(1)} = 10^{15}\ \Omega^{-1}\ \mathrm{m}^{-2}$, and $G_r^{(2)} = G_i^{(2)} = 0.4\ G_r^{(1)}$. The parameters were also used to calculate SOT effective fields that turn out to be pivotal in the interpretation of the experimental data presented in Section 4.3.

4. RESULTS

4.1. FMR and Interlayer Coupling. First, we measured the magnetization dynamics of the Co/Pt/Co sample in a wide range of Pt thickness from strong through moderate coupling to completely decoupled Co layers. The dynamics was investigated using the electrically detected FMR through the spin diode effect,[57] as described in Section 6.3. We observed the dispersion relations changing once the Pt thickness reaches boundary values. Thus, we could point out the distinct regions where the system behaves differently. This feature is illustrated in Figure 4. On the right panel of Figure 4, one can see the color FMR spectral line shapes. On the left panel, points correspond to the experimental resonance frequencies. On both sides of this figure, we show that for thin Pt spacer (below 1 nm), the dispersion relations are typical Kittel-like dependencies and move toward lower frequencies when the

https://doi.org/10.1021/acsami.1c11675
ACS Appl. Mater. Interfaces 2021, 13, 47019−47032

t_{Pt} is growing. Next, for $t_{Pt} > 1$ *nm*, the $f(H_r)$ changes their slopes. Also, their branches part from each other, especially at low frequencies when a sort of resonance mode gaps in experimental data occurs. The increase of the Pt thickness ($t_{Pt} > 2$ nm) provides the Kittel-like dependencies again. However, for thick Pt ($t_{Pt} > 3$ nm), the experimental $f(H_r)$ practically does not change anymore with the Pt thickness.

To understand the $f(H_r)$ dependence on the Pt thickness, we performed the macrospin simulations and a vast number of fittings for the whole range of the Pt thickness, i.e., from 0.09 to 4.04 nm (Figure 4). Varying the anisotropies ($K_{\perp(\|),1(2)}$), perpendicular easy-axis deviation angles ($\beta_{1(2)}$,$\delta_{1(2)}$), magnetization saturations ($M_{S1(2)}$), and the interlayer coupling strength (J) from eq 3, we reproduced the difference in the dynamical behavior of the structure and were able to identify the boundaries between different regions of Pt thickness where these behaviors occur, namely, regions I (thin Pt), II (medium Pt), III (intermediate Pt), and IV (thick Pt). Despite the similarity of $f(H_r)$ in regions III and IV, we refer to the former as the intermediate since the differences occur in magnetoresistance results discussed in the further part of the paper. The presence of the additional modes (especially in regions III and IV) that were not registered in the experiment can be explained in a couple of ways. First, the theoretical results based on the model presented in Section 3.1 come from the solution of the eigenvalue problem, i.e., the model predicts all possible steady-state modes, regardless of the source of their excitations. On the other hand, the different way of forcing the excitation (by SOTs or Oersted field) is inherent. The resonance modes are not always excited, depending on the force amplitude and its origin. Second, these additional modes are related to the independent dynamics of two magnetizations of F1 and F2 layers due to weak interlayer coupling in regions III and IV. In contrast to regions I and II, there are no collective oscillations and therefore the mode with the large amplitude originates from the in-plane, whereas all other modes come from the perpendicular magnetization dynamics. However, the magnetization oscillations in the latter case do not contribute to the SD signal because of the significant effective damping caused by spin-pumping.[58]

The macrospin parameters are summarized in Figure 5. The vertical dashed lines indicate the boundaries between regions I, II, III, and IV. Figure 5a−d presents perpendicular anisotropies $K_{\perp,1,2}$, saturation magnetization $M_{S,1,2}$, as well as the strength of the interlayer coupling. We also depicted the effective anisotropies $K_{eff,1,2} \equiv K_{\perp,1,2} - \frac{\mu_0}{2}M_{S,1,2}^2$. The in-plane anisotropies (see the Supporting Information) have small values that have the importance in reproducing subtle R_{xx} (H_z) dependencies for the thinnest Pt layers only (e.g., see in Figure 6a). On the other hand, the anisotropy deviation angles (less than 30°) had to be introduced so that we could find a set of magnetic parameters reproducing both the static (magnetoresistance, AHE) and dynamic (FMR) characteristics simultaneously. One can see that the Co layer (indexed as 1) covered by the MgO layer exhibits a larger perpendicular anisotropy than that adjacent to the Ti layer (indexed as 2), similarly as in the system Si/SiO2/Ti(2)/Co(3)/Pt(t_{Pt})/Co(1)/MgO(2)/Ti(2) examined in our previous work.[19] Moreover, on the basis of magnetization measurements in an external perpendicular field, using vibrating sample magnetometer (VSM), we showed that the sample Pt(4)/Co(1)/MgO(2)/Ti(2) has a smaller effective anisotropy field ($H_{K,eff}$ = 1.3 kOe) than Ti(2)/Co(1)/Pt(4) ($H_{K,eff}$ = 1.65 kOe). In Figure 5a,b, we show that the effective anisotropy $K_{eff,1}$ changes its sign, while the $K_{eff,2}$ is negative for all Pt thicknesses. The change in the sign of the effective anisotropy is related to the boundary between regions I and II. Furthermore, one can see that $K_{\perp,1}$ increases with the Pt thickness up to t_{Pt} = 2 nm, whereas the value of $K_{\perp,2}$ is growing just up to 1 nm. Above this thickness, $K_{\perp,2}$ is rather

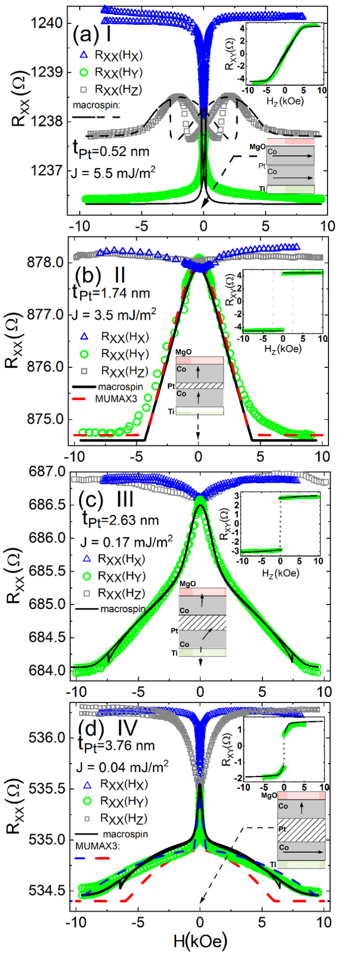

Figure 6. Magnetoresistances R_{xx} and R_{xy} (inset) as a function of the magnetic field in the samples with Pt thickness: (a) 0.52 nm as an example from region I, (b) 1.74 nm from region II, (c) 2.63 nm from region III, and (d) 3.76 nm from region IV: R_{xx} experimental data measured at the magnetic field applied in x (blue triangles), y (green circles), and z (gray squares) directions. The depicted diagrams for all regions indicate the direction of magnetizations of magnetic layers at remanence. The macrospin (black solid and dashed lines) and micromagnetic (dashed red and blue lines) simulations of $R_{xx}(H_y)$. Micromagnetic simulations for t_{Pt} = 3.76 nm were performed using the same parameters (cf. Figure 5) as derived from the macrospin model (red-dashed line), as well as for a K_1 anisotropy increased by 0.17 MJ/m^3 (blue dashed line).

https://doi.org/10.1021/acsami.1c11675
ACS Appl. Mater. Interfaces 2021, 13, 47019−47032

stable, and its values are more or less 0.2 MJ/m^3. The $K_{\perp,1}$ reaches its highest value at $t_{Pt} \approx 2$ nm when it drops to the level of about 0.75 MJ/m^3. We relate the different values of $K_{\perp,1}$ than those of $K_{\perp,2}$ to the much more efficient perpendicular anisotropy at Co/MgO than at the Co/Ti interface. On the other hand, the mean value magnetization saturation averaged over the whole range of the Pt thickness is about 1.07 T for both Co layers. The actual value for a given t_{Pt} differs by ± 10 %. The abrupt decrease in M_S for the very thin Pt layer (0.09 nm) is caused by the quality of the interfaces and related intermixing of Pt and Co atoms.

The last but not least, the parameter derived from the macrospin is the interlayer coupling energy J. The polarization of the Pt is the mechanism of the interaction between two magnetic moments in Co layers. Such an interaction is ferromagnetic by its very nature,[59] whereas the dipolar coupling (neglected here) is antiferromagnetic. The indirect way to probe the coupling (and the polarization of the Pt) by electrical detection is to measure FMR by rectification of radiofrequency current.[60−62] We derived the coupling (J) from the macrospin simulations, similarly to magnetizations and anisotropies. The coupling dependence on Pt thickness is shown in Figure 5d. However, we could estimate J down to a Pt thickness of 1.36 nm, at which J = 5.5 mJ/m^2. Below this thickness, the coupling has no effect on the resonance fields at frequencies experimentally accessible (<25 GHz). The strong coupling causes both Co layers to rotate in the same manner, and they can be treated as one layer rather than two separate layers. In addition, two magnetizations of Co layers oscillate in phase (acoustic mode). It is seen in the experiment as the observed low-frequency mode.[53] On the contrary, the magnetization oscillations with opposite phases correspond to the high-frequency optical mode (>30 GHz), not achievable in the experimental method due to large losses in the power of the microwave current injected into the sample.[62] For this reason, although the exact value of J is undeterminable for $t_{Pt} <$ 1.36 *nm*, we just kept the value J = 5.5 mJ/m^2 for simulations. This J magnitude is marked as a horizontal dashed line in Figure 5d. Its real value may reach any point from the hatched region, and particularly, it may follow the exponential dependence, as predicted in ref 59 and shown in Figure 5d too. For the thicker Pt ($t_{Pt} \geq 1.36$ nm), the fitting procedure to the Pt polarization model returned the Pt polarization depth parameter $\xi \approx 0.47$ nm, which is 1.5 times greater than ξ reported for the Py/Pt/Py structure.[59]

Summarizing, we emphasize that the coupling strength correlates with the regions from I to IV. The constant value of J within region I corresponds to large and undetectable coupling, whereas in region II, J is still significant and measurable. The intermediate region III is characterized by weak coupling, while samples within region IV are practically decoupled.

Having the magnetic parameters derived from the macrospin simulations of the spin diode FMR dynamics, we calculated longitudinal static magnetoresistance (R_{xx}) dependencies on the external magnetic field in H_x, H_y, and H_z directions. We also modeled the anomalous Hall resistance (R_{xy}) when the external magnetic field is applied in the z direction.

4.2. Magnetoresistance and Anomalous Hall Effect.

The Pt-based magnetic multilayers are expected to exhibit a large spin magnetoresistance due to substantial spin−orbit interaction within the HM layer. These interactions cause the relatively large spin currents to be generated and injected into the ferromagnetic layers. The spin currents and spin accumulations at the Co/Pt interfaces influence the magnetoresistance of the sample, as predicted by the theoretical model presented in Section 3.2. Here, we focus on the spin−orbit interactions that are reflected in SMR. The SMR is defined as the difference in the longitudinal resistance measured in the saturated magnetization of Co layers under the external magnetic field applied in the y and z directions, i.e., SMR = $R_{xx}(H_y) - R_{xx}(H_z)$, while the AMR is defined similarly as in Section 3.2 as AMR = $R_{xx}(H_x) - R_{xx}(H_z)$.[41] Also, we measured the AHE configuration (R_{xy}) in the field applied in the z direction. All magnetoresistance and AHE measurements were performed by the DC current method sweeping the external magnetic field up to 10 kOe.

Then, we modeled the magnetoresistance dependencies with the use of the macrospin model. We used the parameters derived previously by fitting the model to the FMR experimental results (shown in Figure 5). For the sake of simplicity, we treat the considered sample as doubled bilayers: Co/Pt and Pt/Co. It allows us to calculate the resistance of the Co/Pt/Co structure as the equivalent resistance of layers connected in parallel: $R_{xx} = \frac{R_1 \cdot R_2}{R_1 + R_2}$ where composite layer resistances are described by $R_{xx1(2)} = R_{0,1(2)} + \Delta R_{AMR} m_{x1(2)}{}^2 + \Delta R_{SMR} m_{y1(2)}{}^2$.[41] The AHE-related resistances are given by $R_{xy} = \Delta R_{\mathrm{AHE}} m_{z1(2)}$.[41] In Figure 6, we show the typical MR curves for samples from regions I to IV.

For t_{Pt} = 0.52 nm, the macrospin qualitatively reproduces a narrow peak in MR. It also accounts for a more complicated dependence of $R_{xx}(H_z)$ (see Figure 6a). The AHE curve does not exhibit a hysteresis and its shape is typical for the hard-axis rotation of both Co layers magnetized in-plane in the remanent state. The hysteresis in $R_{xx}(H_z)$ is due to a competition between different anisotropies: in-plane and perpendicular that affect how the magnetizations rotate. Moreover, as one can see in Figure 7b, the AMR effect dominates in region I with the thinnest Pt layers.

On the contrary, in region II, the SMR is the highest as predicted by the spin-diffusive model and macrospin simulations (cf. Figure 7a). The representative sample from region II (t_{Pt} = 1.74 nm) exhibits a parabolic-like $R(H_y)$ dependence. It means that two Co layers are magnetized perpendicularly to the sample plane in the remanent state. Therefore, the AHE reveals a clear switching-like shape (see the inset in Figure 6b). Both, simulation and experimental results, show negligible contribution of the AMR.

For the sample from region III (t_{Pt} = 2.63 nm), the $R(H_y)$ is rather convex-shaped than parabolic. On the other hand, the AHE curve still exhibits a switching-like behavior. It suggests that the magnetization of layer 2 is tilted away from the perpendicular toward the in-plane direction.

For the thickest Pt layer (e.g., t_{pt} = 3.76 nm in Figure 6d) when the Co layers are weakly coupled (region IV), one can see $R_{xx}(H_y)$ having a parabolic-like shape in high magnetic fields. This part of the curve is due to the rotation of the perpendicularly magnetized Co layer from the z to y direction. On the contrary, at low fields, there is a characteristic sharp peak related to the rotation of the in-plane magnetized Co layer from its remanent state direction to the y direction. The dependence was well reproduced by the macrospin model (black solid line in Figure 6d). The same macrospin parameters provide the satisfactory agreement of AHE magnetoresistance with experimental points (see the inset in

https://doi.org/10.1021/acsami.1c11675
ACS Appl. Mater. Interfaces 2021, 13, 47019−47032

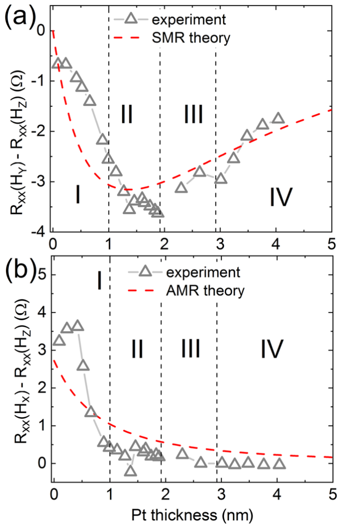

Figure 7. (a) SMR and (b) AMR amplitudes derived directly from the measurements (empty gray triangles) and calculated within the diffusive model (red-dashed lines) as a function of the Pt thickness.

the same figure). The AHE curve exhibits a smooth-edged shape hysteresis, characteristic for the simultaneous rotation of the bottom Co layer magnetization ($\vec{M}_2$) in its hard direction and switching of the top Co layer between two states: $\pm\vec{M}_{1,z}$.

We supported the macrospin model with micromagnetic simulations in the case of the almost decoupled Co layers. The relevant calculations were performed with MUMAX3,[63] where the LLG equation was integrated numerically for each simulation cell. Due to memory and time usage limits, the simulated area was nominally restricted to 5 × 20 μm^2. However, we also utilized periodic boundary conditions along the x direction to produce a demagnetization tensor matching the actual experimental conditions. To optimize simulation performance, the cell size was chosen as 4.88 × 4.88 × 0.87 nm^3 for t_{Pt} = 1.74 nm and as 4.88 × 4.88 × 0.94 nm^3 for t_{Pt} = 3.76 nm. In both cases, the external magnetic field H_y was increased with a 500 Oe step, and the magnetization of Co layers was allowed to relax fully before moving to the next step. Then, the averaged magnetization vector for each layer was registered and used as an input for further resistance calculations. The micromagnetics revealed the same shapes of R_{xx} curves as the macrospin model, for the same parameters (or very close), as shown in Figure 5 (see the caption of Figure 6 for details). The agreement between macrospin and micromagnetic simulations confirmed that the macrospin parameters are reliable.

For the sake of completeness, in Figure 7, we show the ΔR_{AMR} and ΔR_{SMR} that were derived in the whole range of the Pt thickness from experiment and predicted by the spin-diffusive model described in Section 3.2. The obtained amplitudes agree to a satisfactory extent. As one can see from eqs 8 and 9, the SMR and AMR depend on the charge current flowing in HM and F layers, respectively. However, the currents in the HM layer are also influenced by spin accumulation at interfaces of this layer due to inverse SHE. The spin accumulation is mainly determined by the mean spin diffusion length (λ_{HM}) and spin Hall angle (θ_{SH}). The negative value of the SMR reaches its maximum at $t_{Pt} \approx$ 1.5 nm and decreases for thicker Pt layers, for which the spin decoherence affects the spin current, which, in turn, reduces the effective spin accumulation at the F/HM interface. On the contrary, the positive value of the AMR rapidly and monotonically decreases with HM thickness since the average charge current density flowing into the F layer decreases for the thicker Pt layer.

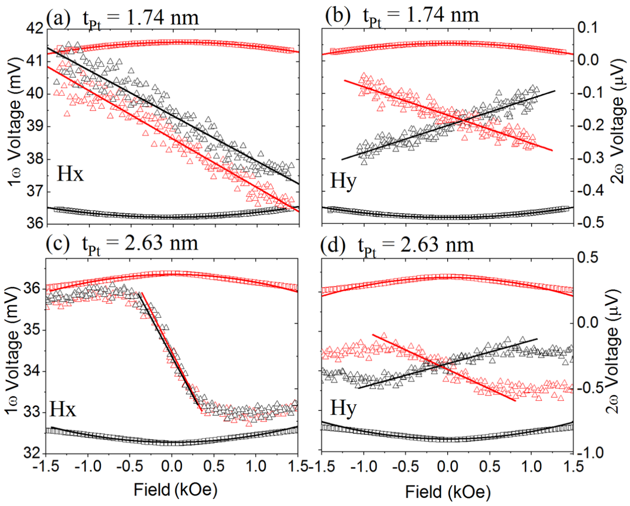

Figure 8. Experimental harmonic voltages V_ω and $V_{2\omega}$ for the representative samples from regions (a, b) II (t_{Pt} = 1.74 nm) and (c, d) III (t_{Pt} = 2.63 nm), both measured at the in-plane magnetic fields (H_x and H_y) swept from −1.5 to +1.5 kOe (cf. eq 16). The fitted linear and quadric functions correspond to the field-sweeping method (see ref 65).

https://doi.org/10.1021/acsami.1c11675
ACS Appl. Mater. Interfaces 2021, 13, 47019−47032

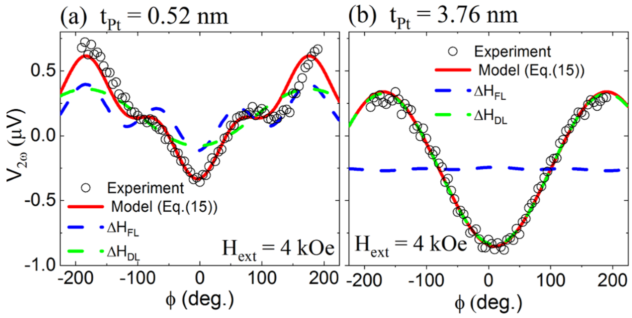

Figure 9. Experimental harmonic voltages $V_{2\omega}$ for the representative samples from regions (a) I (t_{Pt} = 0.52 nm) and (b) IV (t_{Pt} = 3.76 nm), both measured using the angular harmonic voltage method (cf. eq 17). The fitted trigonometric functions follow eq 17.

Discrepancies between the experimental and theoretical MR dependencies in region I result from strongly mixed and alloyed interfaces for small thicknesses of Pt.

4.3. Spin Hall Angle and Spin–Orbit Torques. To quantitatively characterize the spin–orbit interactions in the Co/Pt/Co trilayers, we performed the harmonic measurements briefly described in Section 6.4. For the samples for which both or one of the Co layers is magnetized in-plane (regions I and IV) in the remanent state, we applied the angular harmonic voltage measurement method.[11,64] On the contrary, in the case of the Co layers that magnetizations are perpendicularly oriented (regions II and III), we measured the field dependence of the relevant harmonic voltages.[65] In the latter method, the damping-like (DL) and field-like (FL) components of SOT fields are determined using the following formula

$$\Delta H_{DL(FL)} = -2\frac{B_{x(y)} \pm 2\xi B_{y(x)}}{1 - 4\xi^2} \tag{16}$$

where $B_{x(y)} \equiv \frac{\partial V_{2\omega}}{\partial H_{x(y)}} / \frac{\partial^2 V_{\omega}}{\partial H_{x(y)}^2}$ and $H_{x(y)}$ stands for the in-plane external magnetic field applied in the $x(y)$ direction (cf. Figure 1). The parameter $\xi = \frac{\Delta R_{PHE}}{\Delta R_{AHE}}$ is planar to the anomalous Hall effect ratio. The first and second harmonic voltages (V_{ω} and $V_{2\omega}$) measured as a function of the applied magnetic fields (H_x and H_y) are plotted in Figure 8. The results shown in Figure 8 are representative of the samples from regions II (t_{Pt} = 1.74 nm) and III (t_{Pt} = 2.63 nm). Next, we could use eq 16 and follow the method described in ref 65 to calculate SOT effective fields $\Delta H_{DL(FL)}$ in samples from regions II and III. Nevertheless, the above method turns out to be ineffective in the case of samples with one or both layers magnetized in-plane. In this case, to determine $\Delta H_{DL(FL)}$, we measured the angular dependence of $V_{2\omega}$ on the magnetic field applied in the sample plane. Such a dependence may be expressed as follows[11,64]

$$V_{2\omega} = \left(-\frac{\Delta H_{FL}}{H_{ext}} R_{PHE} \cos 2\phi_H - \frac{1}{2}\frac{\Delta H_{DL}}{H_{eff}} R_{AHE} + \alpha_0\right) I \cos \phi_H \tag{17}$$

where ϕ_H stands for the in-plane angle of the magnetic field. The term α_0 is the anomalous Nernst effect (ANE) coefficient due to thermal gradients within the samples induced by the Joule heating.[64] The experimental angular dependencies $V_{2\omega}(\phi_H)$ for the samples with t_{Pt} = 0.52 nm (region I) and t_{Pt} = 3.76 nm (region IV) are shown in Figure 9a,b. As one can see, the damping-like SOT effective field (ΔH_{DL}) is proportional to the $\cos\phi_H$, whereas the field-like one (ΔH_{FL}) is proportional to the $\cos\phi_H \cos 2\phi_H$. Moreover, the $H_{eff} = H_{ext} - \frac{2K_{eff}}{M_S}$, where K_{eff} (defined as in Section 4.1) and M_S are the parameters of the Co layers magnetized in-plane. As long as we knew the magnetic parameters (summarized in Figure 5) of the layers, we could fit eq 17 to the experimental data and consequently determine both field-like and damping-like SOT components.

In addition, by plotting the terms proportional to ΔH_{DL} as a function of $1/H_{ext}$, we could estimate the contribution of the ANE. One should note that the offset of linear fit (at $1/H_{ext}$ = 0) visible in Figure 10a,b is the ANE contribution $\alpha_0 I_0$. We

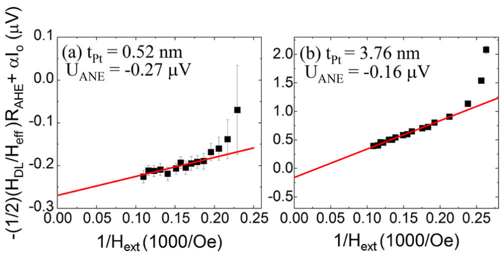

Figure 10. Amplitude of eq 17 plotted as a function of the magnetic field $1/H_{ext}$ measured in the samples with Pt thicknesses 0.52 nm (a) and 3.76 nm (b) at angle ϕ_H = 45°. The interceptions with the y axis indicate the ANE contribution.

show the relevant plots for two samples (t_{Pt} = 0.52 and 3.76 nm). The small offsets of fitted lines ($\approx -0.3\mu V$) and ($\approx -0.15\mu V$) corresponding to the ANE-related electric fields $E_{ANE} \approx -0.03 V/m$ and $E_{ANE} \approx -0.015 V/m$, respectively, are much smaller than the values in the Co/Pt systems present in the literature, e.g., in ref 64. Therefore, it suggests that the ANE contribution is negligible in our devices with thin and thick Pt layers. It is worthy to notice that the dependencies shown in Figure 10 can be used to examine the applicability of eq 17. At low magnetic fields, the dependencies deviate from

https://doi.org/10.1021/acsami.1c11675
ACS Appl. Mater. Interfaces 2021, 13, 47019–47032

the linear and eq 17 is not fulfilled. On the other hand, according to the model, the dependencies are linear at high fields.

We summarize the results for the samples from all regions (I−IV) in Figure 11a. For very thin Pt (region I), both field-like and damping-like components are small, although the former contributes slightly more than the latter one. In regions II and III, both components increase in their magnitudes; however, in region III, the DL component (filled red points), due to intermixing and alloying Co and Pt, surpasses the FL component's (blue-filled points) magnitude. The most intriguing is region IV, where the damping-like component dominates over the field-like, especially for $t_{Pt} > 3$ nm. For such a thick Pt layer, the H_{DL} saturates, while the H_{FL} drops again toward small values. Similarly, the effective spin Hall angle defined by $\theta_{SH,eff} = \frac{2e}{\hbar}\frac{H_{DL}M_{S}t_{Co}}{j_{Pt}}$ starts to increase in region II where the Pt thickness is sufficient to generate significant spin currents and consequently the H_{DL} SOT field. The $\theta_{SH,eff}$ continues increasing in region III and then reaches its maximum value c.a. 14% at t_{Pt} = 3.24 nm. Next, it slightly decreases with the Pt thickness in region IV.

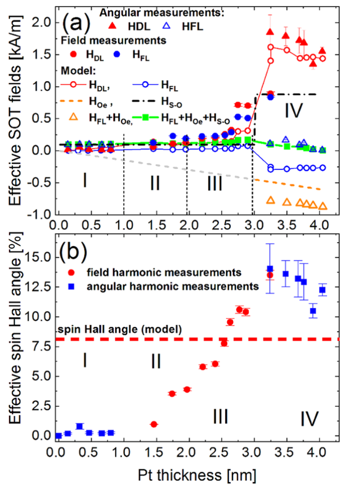

Figure 11. (a) Experimental SOT effective fields: damping-like and field-like components obtained with macrospin magnetic parameters from Figure 5 (blue- and red-filled points and blue empty triangles), the effective theoretical sum of SOT fields: H_{FL} (blue empty points), and separately H_{DL} (red empty points) acting on two Co layers. The amplitude of the Oersted field (H_{Oe}) (orange and gray dashed lines) and the Rashba−Edelstein spin−orbital field (H_{S-O}) (black dash-dotted line). The resultant field-like SOT (filled green squares) including the H_{S-O} field in regions I−IV and, additionally, the Oersted field in region IV. Orange triangles correspond to the case when the Oersted field only is added to the H_{FL}. (b) The effective spin Hall angle is determined from field (red circles) and angular (blue squares) harmonics measurements, with the H_{DL} amplitudes from panel (a). The red-dashed line indicates the theoretical value of the spin Hall angle fitted to the experimental MR dependencies (cf. Figure 7).

One should note that $\theta_{SH,eff}$ accounts for the spin accumulation effect at interfaces in the trilayer system. For this reason, the experimental value of $\theta_{SH,eff}$ may substantially differ from the theoretical one (θ_{SH} in Section 3.2), introduced as a material parameter of pure SHE efficiency at a very thick HM thickness limit. More precisely, the effective spin Hall angle is smaller than the theoretical one (θ_{SH}) for $t_{Pt} < 2.6$ nm. For thicker Pt layers, $\theta_{SH,eff}$ increases and becomes higher than the theoretical value. It is correlated with the change of magnetization direction from perpendicular to the in-plane for the thick Pt layer, particularly in region IV. To shed light on the $\theta_{SH,eff}$ dependence on Pt thickness, one needs to go back to Figure 11a based on which the $\theta_{SH,eff}$ was determined. The two modes of the experimental harmonics method allow the measurement of the effective SOT fields acting on the Co layers magnetized only in the plane (angular method) or perpendicular to the plane (field method). This limitation arises from very high fields required to saturate the layers magnetized in-plane (perpendicularly) at remanence into the perpendicular (in-plane) direction. Therefore, the data recorded with the experimental harmonic method accounts for both magnetic layers when magnetized in the same direction. That is the case of samples from regions I−III. On the contrary, only one magnetic layer can be sensed by the measurement setup in region IV, where both magnetizations are orthogonal. Therefore, the experimental conditions differ in regions I−IV. As a consequence, the experimentally determined H_{DL} and H_{FL} fields in regions I−III are the sums of the related SOT fields acting on F1(top) and F2(bottom) magnetic layers. Since the spin currents generated by the SHE have opposite polarizations at F/HM and HM/F interfaces, the SOT effective fields also have the opposite signs. The residual fields, defined as $H_{DL} = H_{DL,1} + (-H_{DL,2})$ and $H_{FL} = -H_{FL1} + H_{FL2}$, come from the different interface properties, included in real parts of mixing conductances $G_r^{(1)}$ and $G_r^{(2)}$ of the diffusive model (cf. Section 3.2). To support our analysis, we calculated the SHE-induced SOT effective fields using the formulas (eqs 14 and 15) and magnetic parameters from Figure 5. Next, we plotted the difference of $H_{DL,1}$ and $H_{DL,2}$ in regions from I to III at the experimental thicknesses of Pt. Nevertheless, considering the experimental conditions discussed above, we plotted the $H_{DL,2}$ field only in region IV. The results are shown in Figure 11a as red empty circles and agree with the experimental ones (red-filled points, triangles, and circles) to a satisfactory extent.

On the contrary, a similar procedure is insufficient to reproduce the experimental H_{FL} field. The theoretical H_{FL} (empty blue circles) depends differently on the HM thickness than the experimental one (blue-filled circles and empty blue triangles). However, the diffusive model does not account for an Oersted field (H_{Oe}) coming from the charge current, as well as a spin−orbital field (H_{S-O}) at interfaces, arising from the REE. Both fields have the same direction as SHE-induced H_{FL}. Thus, the additional terms have to be included in the analysis of the effective field-like field. We assumed that the Oersted field linearly increases with the Pt thickness (gray and orange dashed lines in Figure 11a), whereas the H_{S-O} (black dash-dotted line) is independent of the HM thickness.[19,42] Since the Oersted field has the same amplitude with opposite signs in both F layers, its impact on the resultant H_{FL} cancels out and does not affect the field-like SOT in I−III regions. For the same reason, as discussed above, the H_{Oe} adds to H_{FL} in region IV (see the full orange triangles in Figure 11a). Conversely, the H_{S-O} fields do not cancel out due to the difference in F/HM and HM/F interfaces. Therefore, their difference contributes

https://doi.org/10.1021/acsami.1c11675
ACS Appl. Mater. Interfaces 2021, 13, 47019−47032

to the total H_{FL} term in regions I−III. In region IV, the amplitude H_{S-O} significantly increases because the perpendicularly magnetized Co layer is out of the experimental detection. Thus, the estimated magnitude generated at the Co/Pt interface was 0.86 kA/m. One should note that such a substantial value of the SOT field due to REE is much higher than its FL counterpart coming from the SHE. Moreover, it is of the order of the charge-current-induced effective Oersted field. However, all fields of SHE-related H_{FL}, H_{Oe}, and H_{S-O} must be considered in the total FL SOT component to achieve a satisfactory agreement with experimental data in the F/HM/F trilayer system (see the solid green line in Figure 11a). The discrepancies at the border between regions III and IV are due to the unreliability of the experimental methods (field and angular harmonics) applicable only when magnetic layers are magnetized fully in the plane or fully perpendicularly to the plane. This requirement is not fulfilled in the intermediate case, especially at t_{Pt} = 2.87 nm. It has its consequence in the spin Hall angle value that slightly drops at this Pt thickness. On the other hand, at t_{Pt} = 3.24 nm, the SOT fields determined from the field and angular harmonics methods differ. In this case, the field harmonics method detects the magnetic layer magnetized perpendicularly. Therefore, as discussed earlier, the SOT fields at the Pt/Co interface are different from those at the Co/Pt interface. However, the spin Hall angle (Figure 11b) treated as the HM material parameter is the same for both experimental methods. For thicker Pt, the detection signal in the field harmonics measurement was too weak to properly determine the H_{DL} and H_{FL} effective fields.

5. CONCLUSIONS

The paper presents the detailed results on structural, static, and dynamic properties of the Co/Pt/Co trilayer in which the Pt features a double role of the source of spin currents and interlayer exchange coupling in a wide range of the Pt layer thickness. First, we showed the Co/Pt and Pt/Co inherent interface asymmetries that resulted in different interfacial spin−orbit-related properties of ferromagnetic layers, magnetic anisotropies, and the effective spin−orbit torque fields due to SHE and REE. The difference in anisotropies makes the Co layer with stronger perpendicular anisotropy be a primary layer that determines the magnetization direction of the secondary Co layer through the interlayer exchange coupling. Therefore, we were able to determine four ranges of Pt thickness where the trilayer reveals different static and dynamic behaviors correlated with the strength of coupling: region I (two Co magnetizations are in-plane), region II (Co magnetizations are both perpendicular to the plane), region III (one of the Co magnetizations is tilted from the perpendicular direction), and, finally, region IV (one Co magnetization is in-plane, whereas the second one is perpendicular). We showed that the experimental relation of dispersions and magnetoresistances differs in each region. This difference is accounted for by the macrospin models that we used, and therefore, both the experimental magnetoresistance and SOT−FMR relations of dispersion were reproduced by theoretical calculations to a satisfactory extent. Moreover, we made a detailed analysis of the SOT effective fields determined using harmonics measurements. We showed that the experimental method applied to trilayers with two Co magnetizations aligned both in-plane or both out-of-plane allows measuring a difference of the effective SOT fields coming from two F/HM and HM/F interfaces. However, when two magnetizations are orthogonal, the experimental technique enables measuring SOT fields from the single F layer. The experimental results revealed this feature and were successfully parameterized with the magnitudes of damping-like and field-like SOT obtained from the diffusive model. Finally, both experimental and theoretical data allowed us to determine the contribution of Oersted (H_{Oe}) and spin−orbital (H_{S-O}) fields to the resultant experimental field-like SOT. We showed that the latter contribution due to REE might be comparable to the effective Oersted field and more significant than the field-like SOT caused by the SHE.

6. EXPERIMENTAL METHODS

6.1. Sample Preparation. The base pressure in the deposition chamber was 4.5 × 10^{-8} mbar. The substrate temperature was at room temperature (RT). The Ar pressure during the deposition process was 8.53 × 10^{-3} mbar, except for the deposition of the MgO layer when it was 8.52 × 10^{-3} mbar. A fixed direct current (DC) power of 8 W for Pt and 15 W for Co and an alternating (RF) power of 75 W for MgO and 50 W for Ti were used. The Pt layer was deposited in a wedge-shaped form with thickness varying from 0 to 4 nm along a 20 mm long sample edge (x coordinate). The resulting thickness gradient (0.0002 nm/μm) was achieved by the controlled movement of a shutter. Thicknesses of all layers were determined from the deposition growth rate of particular materials calibrated using X-ray reflectivity measurements. Before patterning to the form of bar devices, all as-deposited samples were characterized by X-ray diffraction $\theta-2\theta$ (XRD) and grazing incidence diffraction (GIXD) and also examined by the polar Kerr magnetometer (p-MOKE) and time-resolved TR-MOKE to determine the static and dynamic magnetization parameters, which studies have been described in detail in a separate work.[66] After basic characterization of continuous samples, multilayers were patterned using optical direct imaging lithography and ion etching to create a matrix of Hall- and resistance-bar devices, with different thicknesses of Pt for subsequent electrical measurements. The sizes of prepared structures were 100 μm × 20 μm for magnetoresistance and spin diode effect measurements, whereas they were 100 μm × 10 μm for the AHE and harmonics measurements. The sizes of the devices assure that the structure symmetry is broken in the direction perpendicular to the layer plane only, and therefore the effects of REE-related fields and spin current gradients can be neglected.

Al(20)/Au(30) electrical leads of 100 μm × 100 μm were deposited in a second lithography step followed by the lift-off process.

6.2. Resistance Measurements. Specific locations of pads near the Hall bars were designed for measurement in a custom-made rotating probe station, allowing a 2- or 4-point measurement of electrical transport properties in the presence of the magnetic field applied at an arbitrary azimuthal and polar angle with respect to the Hall bar axis. The scheme of the experimental setup for longitudinal (R_{xx}) and Hall (R_{xy}) resistance measurements is shown in Figure S1. The resistance was measured using a four-point method,[67] and resistivities of Pt and Co layers were determined using a parallel resistor model and the method described by Kawaguchi et al.[68] The Pt and Co resistivity analyses yielded 59 $\mu\Omega$ cm and 72.5 $\mu\Omega$ cm, respectively.

6.3. Spin Diode Effect Measurements. The magnetic dynamics of the patterned samples was electrically detected with the FMR measurements through the spin diode effect.[57] The scheme of the measurement setup is shown in Figure S2. The effect occurs when the rf current flows through the magnetoresistive element that in the case of our samples exhibits the anisotropic magnetoresistance (AMR) and SMR. Then, the current-related effective magnetic fields (as Oersted, H_{Oe}, or SOT fields) force the sample magnetization to oscillate. The magnetization oscillations, in turn, result in the time-dependent resistance of the sample, which mixes up with the rf current.

Therefore, the measured output voltage may be expressed as $V_{out} = I_0 \cos(\omega t) \cdot R(\omega t + \Phi)$, where the Φ is the phase shift between the

https://doi.org/10.1021/acsami.1c11675
ACS Appl. Mater. Interfaces 2021, 13, 47019−47032

current and resistance. One notes that V_{out} includes ac and dc contributions, namely, $V_{out} = V_{dc} + V_{ac} = I_0\,\delta R\cos\Phi + I_0\,\delta R(2\,\omega\,t + \Phi)$. The dc output voltage depends on the angular frequency, external magnetic field, and parameters of the sample.

The spin diode FMR measurements are performed with an amplitude-modulated radiofrequency (rf) current with a corresponding power of P = 16 dBm and frequencies ranging from 1 to 25 GHz. The mixing voltage (V_{out}) is measured using a lock-in amplifier synchronized to the rf signal. The in-plane magnetic field (H_{ext}) is applied at $\phi = 45$ deg with respect to the microstrip long axis and was swept from 0 up to 9 kOe.

6.4. Harmonic Hall Voltage Measurements. To determine spin−orbit torque fields (damping- and field-like components), as well as the spin Hall angle, we used the methods based on the harmonic measurements.[11,64,69] For these measurements, we apply a low-frequency constant-amplitude sinusoidal voltage to the Hall bar device with current density from j= 3.12×10^{10} A/m^2 to $j = 3.29 \times 10^{10}$ A/m^2 depending on the Pt layer thickness. Using two lock-in amplifiers, we measure simultaneously the in-phase first harmonic (V_ω) and the out-of-phase second harmonic Hall voltages ($V_{2\omega}$) as a function of an external magnetic field H_{ext}. The sample is rotated within the x−y plane, making an azimuthal angle ϕ_H with the x-axis, as depicted in Figure S3. The measurements were conducted in two configurations: the first one is referred to as field measurements and the samples were probed with the different magnitudes of the external magnetic field applied along both the x and y directions,[65] while the second configuration is the angular measurements. The sample is rotated in the x−y plane while the $V_{\omega,2\omega}$ is recorded[64,65] for fixed magnitudes of the external magnetic field. The field measurements are relevant in the case of samples with out-of-plane effective anisotropies. On the contrary, the angular measurements allow us to detect harmonic signals in samples with in-plane effective anisotropy.

ASSOCIATED CONTENT

Supporting Information

The Supporting Information is available free of charge at https://pubs.acs.org/doi/10.1021/acsami.1c11675.

Experimental setups for electrical measurements, the in-plane anisotropy magnitudes, and the perpendicular anisotropy easy-axis deviation angles (PDF)

AUTHOR INFORMATION

Corresponding Author

Piotr Ogrodnik − *Institute of Electronics, AGH University of Science and Technology, 30-059 Kraków, Poland; Faculty of Physics, Warsaw University of Technology, 00-662 Warsaw, Poland;* orcid.org/0000-0002-4907-3409; Email: piotr.ogrodnik@pw.edu.pl

Authors

Krzysztof Grochot − *Institute of Electronics, AGH University of Science and Technology, 30-059 Kraków, Poland; Faculty of Physics and Applied Computer Science, AGH University of Science and Technology, 30-059 Kraków, Poland;* orcid.org/0000-0002-5796-7963

Łukasz Karwacki − *Institute for Theoretical Physics, Utrecht University, 3584 CC Utrecht, The Netherlands; Institute of Molecular Physics, Polish Academy of Sciences, 60-179 Poznań, Poland;* orcid.org/0000-0002-8329-0474

Jarosław Kanak − *Institute of Electronics, AGH University of Science and Technology, 30-059 Kraków, Poland*

Michał Prokop − *Catalan Institute of Nanoscience and Nanotechnology (ICN2), CSIC and BIST, 08193 Barcelona, Spain;* orcid.org/0000-0003-2358-7599

Jakub Chęciński − *Institute of Electronics, AGH University of Science and Technology, 30-059 Kraków, Poland;* orcid.org/0000-0002-3106-298X

Witold Skowroński − *Institute of Electronics, AGH University of Science and Technology, 30-059 Kraków, Poland;* orcid.org/0000-0002-4568-2688

Sławomir Ziętek − *Institute of Electronics, AGH University of Science and Technology, 30-059 Kraków, Poland;* orcid.org/0000-0001-6699-7155

Tomasz Stobiecki − *Institute of Electronics, AGH University of Science and Technology, 30-059 Kraków, Poland; Faculty of Physics and Applied Computer Science, AGH University of Science and Technology, 30-059 Kraków, Poland;* orcid.org/0000-0001-7380-2897

Complete contact information is available at: https://pubs.acs.org/10.1021/acsami.1c11675

Notes

The authors declare no competing financial interest.

ACKNOWLEDGMENTS

This work was supported by the National Science Centre, Poland, Grant No. 2016/23/B/ST3/01430 (SPINORBITRONICS). Numerical calculations were supported by PL-GRID infrastructure. As part of cooperation, the multilayer systems were deposited in the Institute of Molecular Physics Polish Academy of Sciences and nanofabrication was performed at the Academic Centre for Materials and Nanotechnology of the AGH University of Science and Technology. The authors would like to express their gratitude to Prof. F. Stobiecki for helpful discussions on data analysis. The authors also thank Jakub Mojsiejuk for his help with preparing numerical calculations. W.S. acknowledges National Science Centre Grant No. UMO-2015/17/D/ST3/00500, Poland.

REFERENCES

(1) Ralph, D.; Stiles, M. Spin transfer torques. *J. Magn. Magn. Mater.* **2008**, *320*, 1190−1216.

(2) Brataas, A.; Kent, A. D.; Ohno, H. Current-induced torques in magnetic materials. *Nat. Mater.* **2012**, *11*, 372−381.

(3) Manchon, A.; Železný, J.; Miron, I. M.; Jungwirth, T.; Sinova, J.; Thiaville, A.; Garello, K.; Gambardella, P. Current-induced spin-orbit torques in ferromagnetic and antiferromagnetic systems. *Rev. Mod. Phys.* **2019**, *91*, No. 035004.

(4) Zhang, C.; Takeuchi, Y.; Fukami, S.; Ohno, H. Field-free and sub-ns magnetization switching of magnetic tunnel junctions by combining spin-transfer torque and spin−orbit torque. *Appl. Phys. Lett.* **2021**, *118*, No. 092406.

(5) Garello, K.; Yasin, F.; Kar, G. S. In *Spin-Orbit Torque MRAM for Ultrafast Embedded Memories: From Fundamentals to Large Scale Technology Integration*. IEEE 11th International Memory Workshop (IMW), 2019; pp 1−4.

(6) Bhatti, S.; Sbiaa, R.; Hirohata, A.; Ohno, H.; Fukami, S.; Piramanayagam, S. Spintronics based random access memory: a review. *Mater. Today* **2017**, *20*, 530−548.

(7) Ikegawa, S.; Mancoff, F. B.; Janesky, J.; Aggarwal, S. Magnetoresistive random access memory: Present and future. *IEEE Trans. Electron Dev.* **2020**, *67*, 1407−1419.

(8) Dieny, B.; Prejbeanu, I. L.; Garello, K.; Gambardella, P.; Freitas, P.; Lehndorff, R.; Raberg, W.; Ebels, U.; Demokritov, S. O.; Akerman, J.; et al. Opportunities and challenges for spintronics in the microelectronics industry. *Nat. Electron.* **2020**, *3*, 446−459.

(9) Hirohata, A.; Yamada, K.; Nakatani, Y.; Prejbeanu, I.-L.; Diény, B.; Pirro, P.; Hillebrands, B. Review on spintronics: Principles and device applications. *J. Magn. Magn. Mater.* **2020**, *509*, No. 166711.

(10) Obstbaum, M.; Decker, M.; Greitner, A. K.; Haertinger, M.; Meier, T. N. G.; Kronseder, M.; Chadova, K.; Wimmer, S.; Ködderitzsch, D.; Ebert, H.; Back, C. H. Tuning Spin Hall Angles by Alloying. *Phys. Rev. Lett.* **2016**, *117*, No. 167204.

(11) Fritz, K.; Wimmer, S.; Ebert, H.; Meinert, M. Large spin Hall effect in an amorphous binary alloy. *Phys. Rev. B* **2018**, *98*, No. 094433.

(12) Wang, T.; Xiao, J. Q.; Fan, X. Spin−Orbit Torques in Metallic Magnetic Multilayers: Challenges and New Opportunities. *Spin* **2017**, *7*, No. 1740013.

(13) Song, C.; Zhang, R.; Liao, L.; Zhou, Y.; Zhou, X.; Chen, R.; You, Y.; Chen, X.; Pan, F. Spin-orbit torques: Materials, mechanisms, performances, and potential applications. *Prog. Mater. Sci.* **2021**, *118*, No. 100761.

(14) Sinova, J.; Valenzuela, S. O.; Wunderlich, J.; Back, C.; Jungwirth, T. Spin Hall effects. *Rev. Mod. Phys.* **2015**, *87*, No. 1213.

(15) Edelstein, V. M. Spin polarization of conduction electrons induced by electric current in two-dimensional asymmetric electron systems. *Solid State Commun.* **1990**, *73*, 233−235.

(16) Hirsch, J. E. Spin Hall Effect. *Phys. Rev. Lett.* **1999**, *83*, 1834−1837.

(17) Mihajlović, G.; Mosendz, O.; Wan, L.; Smith, N.; Choi, Y.; Wang, Y.; Katine, J. Pt thickness dependence of spin Hall effect switching of in-plane magnetized CoFeB free layers studied by differential planar Hall effect. *Appl. Phys. Lett.* **2016**, *109*, No. 192404.

(18) Lim, G. J.; Gan, W.; Lew, W. S. Effect of seed and interlayer Pt thickness on spin-orbit torque efficiency in Co/Pt multilayer with perpendicular magnetic anisotropy. *J. Phys. D: Appl. Phys.* **2020**, *53*, No. 505002.

(19) Łazarski, S.; Skowroński, W.; Kanak, J.; Karwacki, L.; Ziętek, S.; Grochot, K.; Stobiecki, T.; Stobiecki, F. Field-Free Spin-Orbit-Torque Switching in Co/Pt/Co Multilayer with Mixed Magnetic Anisotropies. *Phys. Rev. Appl.* **2019**, *12*, No. 014006.

(20) Chen, Y.-T.; Takahashi, S.; Nakayama, H.; Althammer, M.; Goennenwein, S. T. B.; Saitoh, E.; Bauer, G. E. W. Theory of spin Hall magnetoresistance. *Phys. Rev. B* **2013**, *87*, No. 144411.

(21) Choi, J.-G.; Lee, J. W.; Park, B.-G. Spin Hall magnetoresistance in heavy-metal/metallic-ferromagnet multilayer structures. *Phys. Rev. B* **2017**, *96*, No. 174412.

(22) Hals, K. M.; Brataas, A. Phenomenology of current-induced spin-orbit torques. *Phys. Rev. B* **2013**, *88*, No. 085423.

(23) Liu, L.; Moriyama, T.; Ralph, D. C.; Buhrman, R. A. Spin-Torque Ferromagnetic Resonance Induced by the Spin Hall Effect. *Phys. Rev. Lett.* **2011**, *106*, No. 036601.

(24) Zhang, C.; Fukami, S.; Sato, H.; Matsukura, F.; Ohno, H. Spin-orbit torque induced magnetization switching in nano-scale Ta/CoFeB/MgO. *Appl. Phys. Lett.* **2015**, *107*, No. 012401.

(25) Garello, K.; Avci, C. O.; Miron, I. M.; Baumgartner, M.; Ghosh, A.; Auffret, S.; Boulle, O.; Gaudin, G.; Gambardella, P. Ultrafast magnetization switching by spin-orbit torques. *Appl. Phys. Lett.* **2014**, *105*, No. 212402.

(26) Lau, Y.-C.; Betto, D.; Rode, K.; Coey, J.; Stamenov, P. Spin−orbit torque switching without an external field using interlayer exchange coupling. *Nat. Nanotechnol.* **2016**, *11*, 758−762.

(27) Du, Y.; Gamou, H.; Takahashi, S.; Karube, S.; Kohda, M.; Nitta, J. Disentanglement of Spin-Orbit Torques in Pt/Co Bilayers with the Presence of Spin Hall Effect and Rashba-Edelstein Effect. *Phys. Rev. Appl.* **2020**, *13*, No. 054014.

(28) Fan, X.; Celik, H.; Wu, J.; Ni, C.; Lee, K.-J.; Lorenz, V. O.; Xiao, J. Q. Quantifying interface and bulk contributions to spin−orbit torque in magnetic bilayers. *Nat. Commun.* **2014**, *5*, No. 3042.

(29) Cui, B.; Wu, H.; Li, D.; Razavi, S. A.; Wu, D.; Wong, K. L.; Chang, M.; Gao, M.; Zuo, Y.; Xi, L.; Wang, K. L. Field-Free Spin-Orbit Torque Switching of Perpendicular Magnetization by the Rashba Interface. *ACS Appl. Mater. Interfaces* **2019**, *11*, 39369−39375.

(30) Yu, G.; Upadhyaya, P.; Fan, Y.; Alzate, J. G.; Jiang, W.; Wong, K. L.; Takei, S.; Bender, S. A.; Chang, L.-T.; Jiang, Y.; et al. Switching of perpendicular magnetization by spin−orbit torques in the absence of external magnetic fields. *Nat. Nanotechnol.* **2014**, *9*, 548−554.

(31) Cao, Y.; Sheng, Y.; Edmonds, K. W.; Ji, Y.; Zheng, H.; Wang, K. Deterministic magnetization switching using lateral spin−orbit torque. *Adv. Mater.* **2020**, *32*, No. 1907929.

(32) Cai, K.; Yang, M.; Ju, H.; Wang, S.; Ji, Y.; Li, B.; Edmonds, K. W.; Sheng, Y.; Zhang, B.; Zhang, N.; et al. Electric field control of deterministic current-induced magnetization switching in a hybrid ferromagnetic/ferroelectric structure. *Nat. Mater.* **2017**, *16*, 712−716.

(33) Yang, M.; Deng, Y.; Cai, K.; Ju, H.; Liu, S.; Li, B.; Wang, K. Deterministic magnetic switching of perpendicular magnets by gradient current density. *J. Magn. Magn. Mater.* **2019**, *489*, No. 165474.

(34) Lee, H.-Y.; Kim, S.; Park, J.-Y.; Oh, Y.-W.; Park, S.-Y.; Ham, W.; Kotani, Y.; Nakamura, T.; Suzuki, M.; Ono, T.; Lee, K.-J.; Park, B.-G. Enhanced spin−orbit torque via interface engineering in Pt/CoFeB/MgO heterostructures. *APL Mater.* **2019**, *7*, No. 031110.

(35) Avci, C. O.; Beach, G. S. D.; Gambardella, P. Effects of transition metal spacers on spin-orbit torques, spin Hall magnetoresistance, and magnetic anisotropy of Pt/Co bilayers. *Phys. Rev. B* **2019**, *100*, No. 235454.

(36) Zhu, L.; Zhu, L.; Shi, S.; Sui, M.; Ralph, D.; Buhrman, R. Enhancing Spin-Orbit Torque by Strong Interfacial Scattering From Ultrathin Insertion Layers. *Phys. Rev. Appl.* **2019**, *11*, No. 061004.

(37) Karwacki, Ł.; Grochot, K.; Łazarski, S.; Skowroński, W.; Kanak, J.; Powroźnik, W.; Barnaś, J.; Stobiecki, F.; Stobiecki, T. Optimization of spin Hall magnetoresistance in heavy-metal/ferromagnetic-metal bilayers. *Sci. Rep.* **2020**, *10*, No. 10767.

(38) Skowroński, W.; Cecot, M.; Kanak, J.; Ziętek, S.; Stobiecki, T.; Yao, L.; Van Dijken, S.; Nozaki, T.; Yakushiji, K.; Yuasa, S. Temperature dependence of spin-orbit torques in W/CoFeB bilayers. *Appl. Phys. Lett.* **2016**, *109*, No. 062407.

(39) Cecot, M.; Karwacki, Ł.; Skowroński, W.; Kanak, J.; Wrona, J.; Żywczak, A.; Yao, L.; van Dijken, S.; Barnaś, J.; Stobiecki, T. Influence of intermixing at the Ta/CoFeB interface on spin Hall angle in Ta/CoFeB/MgO heterostructures. *Sci. Rep.* **2017**, *7*, No. 968.

(40) Yamaguchi, A.; Motoi, K.; Hirohata, A.; Miyajima, H. Anomalous Hall voltage rectification and quantized spin-wave excitation induced by simultaneous application of dc and rf currents in a single-layered $Ni_{81}Fe_{19}$ nanoscale wire. *Phys. Rev. B* **2009**, *79*, No. 224409.

(41) Kim, J.; Sheng, P.; Takahashi, S.; Mitani, S.; Hayashi, M. Spin Hall Magnetoresistance in Metallic Bilayers. *Phys. Rev. Lett.* **2016**, *116*, No. 097201.

(42) Skowroński, W.; Karwacki, L.; Ziętek, S.; Kanak, J.; Łazarski, S.; Grochot, K.; Stobiecki, T.; Kuświk, P.; Stobiecki, F.; Barnaś, J. Determination of Spin Hall Angle in Heavy-Metal/Co−Fe−B-Based Heterostructures with Interfacial Spin-Orbit Fields. *Phys. Rev. Appl.* **2019**, *11*, No. 024039.

(43) Liu, L.; Pai, C.-F.; Li, Y.; Tseng, H. W.; Ralph, D. C.; Buhrman, R. A. Spin-Torque Switching with the Giant Spin Hall Effect of Tantalum. *Science* **2012**, *336*, 555−558.

(44) Ryu, J.; Avci, C. O.; Karube, S.; Kohda, M.; Beach, G. S. D.; Nitta, J. Crystal orientation dependence of spin-orbit torques in Co/Pt bilayers. *Appl. Phys. Lett.* **2019**, *114*, No. 142402.

(45) Hayashi, H.; Musha, A.; Sakimura, H.; Ando, K. Spin-orbit torques originating from the bulk and interface in Pt-based structures. *Phys. Rev. Res.* **2021**, *3*, No. 013042.

(46) Avci, C. O.; Garello, K.; Ghosh, A.; Gabureac, M.; Alvarado, S. F.; Gambardella, P. Unidirectional spin Hall magnetoresistance in ferromagnet/normal metal bilayers. *Nat. Phys.* **2015**, *11*, 570−575.

(47) Luo, F.; Wong, Q. Y.; Li, S.; Tan, F.; Lim, G. J.; Wang, X.; Lew, W. S. Dependence of spin-orbit torque effective fields on magnetization uniformity in Ta/Co/Pt structure. *Sci. Rep.* **2019**, *9*, No. 10776.

(48) Stebliy, M. E.; Kolesnikov, A. G.; Ognev, A. V.; Davydenko, A. V.; Stebliy, E. V.; Wang, X.; Han, X.; Samardak, A. S. Advanced

Method for the Reliable Estimation of Spin-Orbit-Torque Efficiency in Low-Coercivity Ferromagnetic Multilayers. *Phys. Rev. Appl.* **2019**, *11*, No. 054047.
(49) Dai, Z.; Liu, W.; Zhao, X.; Liu, L.; Zhang, Z. Controllable Spin−Orbit Torque Efficiency in Pt/Co/Ru/Co/Pt Multilayers with Interlayer Exchange Couplings. *ACS Appl. Electron. Mater.* **2021**, *3*, 611−618.
(50) Süle, P.; Kotis, L.; Toth, L.; Menyhard, M.; Egelhoff, W., Jr Asymmetric intermixing in Co/Ti bilayer. *Nucl. Instrum. Methods Phys. Res., Sect. B* **2008**, *266*, 904−910.
(51) Gweon, H. K.; Yun, S. J.; Lim, S. H. A very large perpendicular magnetic anisotropy in Pt/Co/MgO trilayers fabricated by controlling the MgO sputtering power and its thickness. *Sci. Rep.* **2018**, *8*, No. 1266.
(52) Kanak, J.; Wiśniowski, P.; Stobiecki, T.; Zaleski, A.; Powroźnik, W.; Cardoso, S.; Freitas, P. X-ray diffraction analysis and Monte Carlo simulations of CoFeB-MgO based magnetic tunnel junctions. *J. Appl. Phys.* **2013**, *113*, No. 023915.
(53) Ogrodnik, P.; Kanak, J.; Czapkiewicz, M.; Ziętek, S.; Pietruczik, A.; Morawiec, K.; Dłużewski, P.; Dybko, K.; Wawro, A.; Stobiecki, T. Structural, magnetostatic, and magnetodynamic studies of Co/Mo-based uncompensated synthetic antiferromagnets. *Phys. Rev. Mater.* **2019**, *3*, No. 124401.
(54) Chen, W.; Sigrist, M.; Sinova, J.; Manske, D. Minimal model of spin-transfer torque and spin pumping caused by the spin Hall effect. *Phys. Rev. Lett.* **2015**, *115*, No. 217203.
(55) Nan, T.; Emori, S.; Boone, C. T.; Wang, X.; Oxholm, T. M.; Jones, J. G.; Howe, B. M.; Brown, G. J.; Sun, N. X. Comparison of spin-orbit torques and spin pumping across NiFe/Pt and NiFe/Cu/Pt interfaces. *Phys. Rev. B* **2015**, *91*, No. 214416.
(56) Dubowik, J.; Graczyk, P.; Krysztofik, A.; Głowiński, H.; Coy, E.; Załęski, K.; Gościańska, I. Non-Negligible Imaginary Part of the Spin-Mixing Conductance and its Impact on Magnetization Dynamics in Heavy-Metal−Ferromagnet Bilayers. *Phys. Rev. Appl.* **2020**, *13*, No. 054011.
(57) Tulapurkar, A.; Suzuki, Y.; Fukushima, A.; Kubota, H.; Maehara, H.; Tsunekawa, K.; Djayaprawira, D.; Watanabe, N.; Yuasa, S. Spin-torque diode effect in magnetic tunnel junctions. *Nature* **2005**, *438*, 339−342.
(58) Wei, J.; He, C.; Wang, X.; Xu, H.; Liu, Y.; Guang, Y.; Wan, C.; Feng, J.; Yu, G.; Han, X. Characterization of spin-orbit torque efficiency in magnetic heterostructures with perpendicular magnetic anisotropy via spin-torque ferromagnetic resonance. *Phys. Rev. Appl.* **2020**, *13*, No. 034041.
(59) Omelchenko, P.; Heinrich, B.; Girt, E. Measurements of interlayer exchange coupling of Pt in Py|Pt|Py system. *Appl. Phys. Lett.* **2018**, *113*, No. 142401.
(60) Harder, M.; Cao, Z. X.; Gui, Y. S.; Fan, X. L.; Hu, C.-M. Analysis of the line shape of electrically detected ferromagnetic resonance. *Phys. Rev. B* **2011**, *84*, No. 054423.
(61) Ziętek, S.; Ogrodnik, P.; Frankowski, M.; Chęciński, J.; Wiśniowski, P.; Skowroński, W.; Wrona, J.; Stobiecki, T.; Żywczak, A.; Barnaś, J. Rectification of radio-frequency current in a giant-magnetoresistance spin valve. *Phys. Rev. B* **2015**, *91*, No. 014430.
(62) Ziętek, S.; Ogrodnik, P.; Skowroński, W.; Wiśniowski, P.; Czapkiewicz, M.; Stobiecki, T.; Barnaś, J. The influence of interlayer exchange coupling in giant-magnetoresistive devices on spin diode effect in wide frequency range. *Appl. Phys. Lett.* **2015**, *107*, No. 122410.
(63) Vansteenkiste, A.; Leliaert, J.; Dvornik, M.; Helsen, M.; Garcia-Sanchez, F.; Van Waeyenberge, B. The design and verification of MuMax3. *AIP Adv.* **2014**, *4*, No. 107133.
(64) Avci, C. O.; Garello, K.; Gabureac, M.; Ghosh, A.; Fuhrer, A.; Alvarado, S. F.; Gambardella, P. Interplay of spin-orbit torque and thermoelectric effects in ferromagnet/normal-metal bilayers. *Phys. Rev. B* **2014**, *90*, No. 224427.
(65) Hayashi, M.; Kim, J.; Yamanouchi, M.; Ohno, H. Quantitative characterization of the spin-orbit torque using harmonic Hall voltage measurements. *Phys. Rev. B* **2014**, *89*, No. 144425.
(66) Bonda, A.; Uba, S.; Uba, L.; Skowronski, W.; Stobiecki, T.; Stobiecki, F. Laser-induced magnetization precession parameters dependence on Pt spacer layer thickness in mixed magnetic anisotropies Co/Pt/Co trilayer. *J. Magn. Magn. Mater.* **2020**, *505*, No. 166702.
(67) Smits, F. M. Measurement of Sheet Resistivities with the Four-Point Probe. *Bell Syst. Tech. J.* **1958**, *37*, 711−718.
(68) Kawaguchi, M.; Towa, D.; Lau, Y.-C.; Takahashi, S.; Hayashi, M. Anomalous spin Hall magnetoresistance in Pt/Co bilayers. *Appl. Phys. Lett.* **2018**, *112*, No. 202405.
(69) Lau, Y.-C.; Hayashi, M. Spin torque efficiency of Ta, W, and Pt in metallic bilayers evaluated by harmonic Hall and spin Hall magnetoresistance measurements. *Jpn. J. Appl. Phys.* **2017**, *56*, No. 0802B5.

https://doi.org/10.1021/acsami.1c11675
ACS Appl. Mater. Interfaces 2021, 13, 47019−47032

Supporting Information for "Study of Spin-Orbit Interactions and Interlayer Ferromagnetic Coupling in Co/Pt/Co Trilayers in Wide Range of Heavy Metal Thickness"

Piotr Ogrodnik,[*,†,§] Krzysztof Grochot,[†,‖] Łukasz Karwacki,[‡,⊥] Jarosław Kanak,[†] Michał Prokop,[¶] Jakub Chęciński,[†] Witold Skowroński,[†] Sławomir Ziętek,[†] and Tomasz Stobiecki[†,‖]

†*Institute of Electronics, AGH University of Science and Technology, 30-059 Kraków, Poland*

‡*Institute for Theoretical Physics, Utrecht University, Princetonplein 5, 3584 CC Utrecht, Netherlands*

¶*Catalan Institute of Nanoscience and Nanotechnology (ICN2), CSIC and BIST, Campus UAB, Bellaterra, 08193 Barcelona, Spain*

§*Faculty of Physics, Warsaw University of Technology, 00-662 Warsaw, Poland*

‖*Faculty of Physics and Applied Computer Science, AGH University of Science and Technology, 30-059 Kraków, Poland*

⊥*Institute of Molecular Physics, Polish Academy of Sciences, ul. M.Smoluchowskiego 17, 60-179 Poznań, Poland*

E-mail: piotr.ogrodnik@pw.edu.pl

1 Experimental setups for electrical measurements

Below we present the experimental setups used for the transport measurements (MR, AHE) as well as the electrically detected spin-diode SOT-FMR.

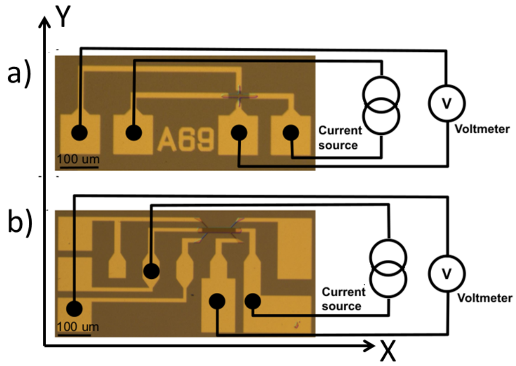

Fig. S1: The Hall resistance (R_{xy}) (a) and 4-points longitudinal magnetoresistance (b) measurement setups depicted on micrographs of the devices.

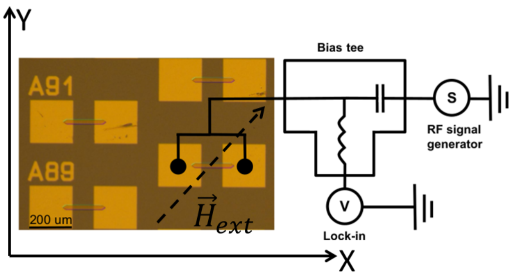

Fig. S2: The resistance-bar attached to the spin-diode FMR measurement setup (see main text for details) depicted on the set of four patterned devices photomicrography. The dashed arrow indicates the direction of the external magnetic field $\vec{H}_{ext}$.

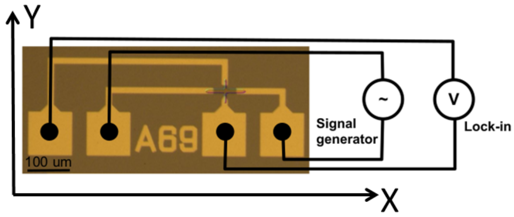

Fig. S3: The Hall-bar and the experimental setup for harmonic Hall voltage ($V_{\omega,2\omega}$) measurements.

2 Anisotropies

In fitting procedure we used a relatively small in-plane anisotropies with the maximum value of 0.025 MJ/m3. The in-plane anisotrpoy improves the MR fitting, especially in the region I.

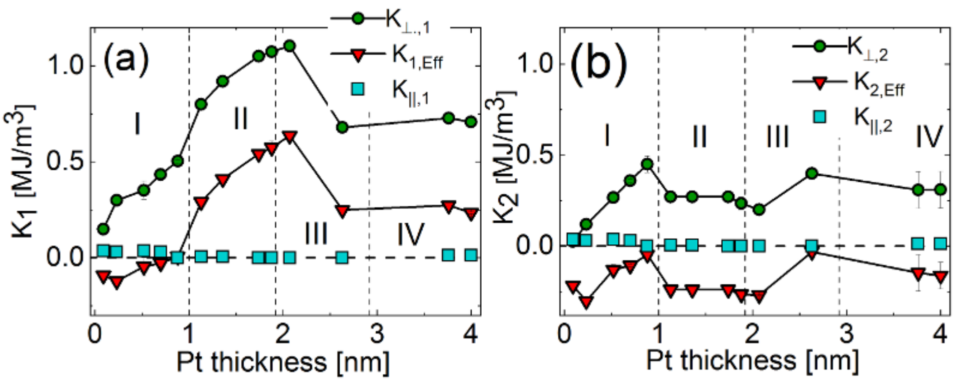

Fig. S4: The in-plane anisotropies ($K_{\|,1,2}$) compared to the perpendicular ones. The anisotropies are estimated from the fitting macrospin model to the experimental data

The perpendicular anisotropy easy axes were deviated from the z direction by a maximum angle of 30 deg. For the definition of the anisotropy deviation angles see Figure below.

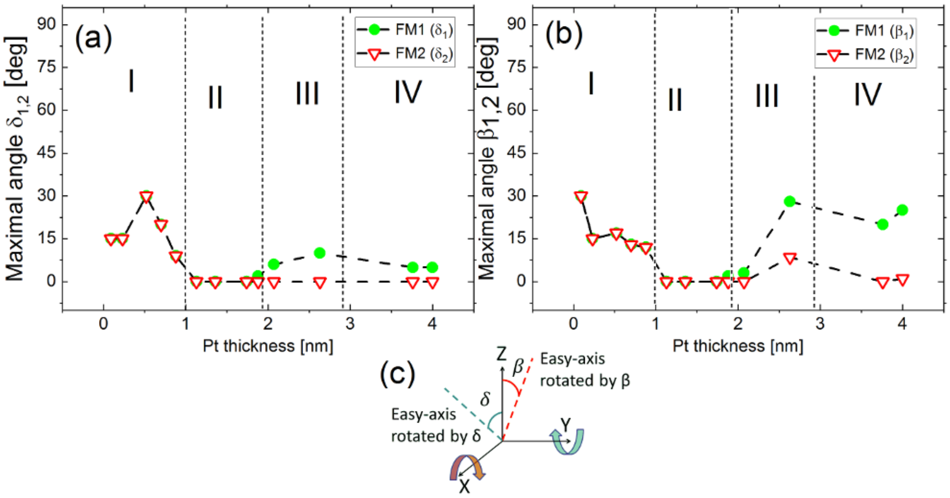

Fig. S5: The perpendicular anisotropy easy-axis deviation angles (a) δ and (b) β dependencies on the Pt thickness. (c) the rotation of easy-axis around x and y axes.

4.2.3 | Multilevel CIMS

This subsection aimed to study the impact of the IEC change resulting in the CIMS process in the Co/Pt/Co trilayer. We show a four-state CIMS due to the collective action of interface asymmetry and coupling.

Nanodevices in which at least one Co layer is characterized by PMA were selected for CIMS experiments. As a result, a series of CIMS loops were obtained for different values of the external magnetic field. Example loops for four elements that differ t_{Pt} are shown in Fig.4(a-d) in [P4]. The CIMS loops measured at two different polarizations of the external magnetic field on devices from regions I and II are separated and spaced by a gap (see Fig.9 in [P4]). As a result, the system possesses four stable resistance states (two in the top loop and two in the bottom loop). When the magnetic field changes polarity, there is a smooth transition between the top and bottom loops. The size of the gap decreases as t_{Pt} increases, and for an element of t_{Pt} = 3.57 nm, it completely disappears, creating a system in which there are only two stable resistance states. Analysis of the

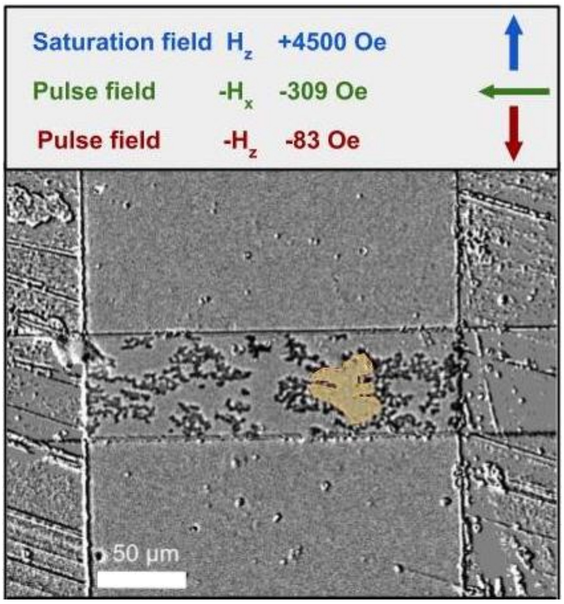

Figure 4.6: Differential p-MOKE images of the fine-grained domain structure in a strongly coupled Co(1)/Pt(1.27)/Co(1) trilayer system. The orange shape indicates the position of the initial domain.

densities of critical switching current ($j_{\mathrm{c,Pt}}$) showed its linear nature as a function of H_{x} [93] for all studied devices (Fig.5(a) in [P4]). The amplitude value for the selected field H_{x} = 800 Oe as a function of t_{Pt} linearly decreased with increasing thickness of the Pt layer in the range from 1.6 to 3 nm (Fig.5(b) in [P4]). This decrease is due to the higher

SOT efficiency for the thicker Pt layer in region III/IV (Fig.11 in [P3]). However, for the thinnest Pt from region II (1.3 nm) and the thickest from region IV (3.57 nm), the value of $j_{c,\mathrm{Pt}}$ decreased. In the thin Pt layer, this is caused by the existence of a strong IEC, which, combined with the different values of the Co anisotropy fields ($H_{k,\mathrm{eff}}$ (top) > H_k (bottom)), makes the Co layers magnetically stiffened and behaves as a single layer with effective anisotropy: H_k (top) > $H_{k,\mathrm{eff}}$ < H_k (bottom). In the thick layer of Pt, where IEC is neglected, only the top Co layer with higher anisotropy (H_k (top)) is switched, increasing $j_{c,\mathrm{Pt}}$. To observe the mechanism of domain switching in the system during CIMS, we selected each region of thickness of the Pt layer and imaged it with p-MOKE while applying the H_x field. For the Hall bar with $t_{\mathrm{Pt}} = 1.36$ nm (region II), a very fine-grained domain structure was observed, as seen in Fig.6(A-D) in [P4], which changes to the single domain for the decoupled Co layers t_{Pt} =3.57 nm (region IV) (Fig.6(E-H) in [P4]. Similarly, a fine-grained domain structure was also obtained for a strongly coupled device with t_{Pt} = 1.23 nm (region II) when successive pulses of an external field with H_x = -309 Oe and H_z = -83 Oe components were applied to a domain (highlighted in the orange area) previously generated with a H_z saturating field. Fig.4.6 shows the domain structure after a series of such six pulses.

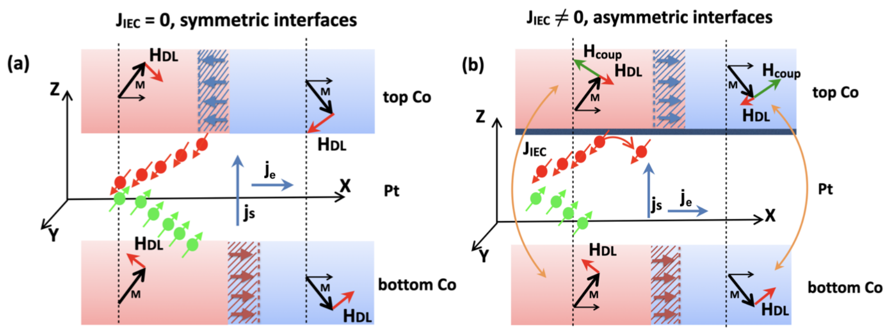

Figure 4.7: Mechanisms of SOT-CIMS effect for the case of symmetric Pt/Co and Co/Pt interfaces and no IEC coupling (a) and for the case of strong coupling and asymmetric interfaces (less transparency of top interface marked as a solid blue layer) (b). Areas of magnetic domains with average magnetization $+m_z$($-m_z$) are marked in red and blue, while the dashed border area indicates the change in domain size under the effect of H_{DL}-SOT (thick red arrows) and the ferromagnetic coupling field (H_{coup}) (thick green arrows). The spin current (j_s) is depicted as red(green) bold points with arrows.

The phenomenological model can explain the current multistate switching. Effective fields that act on a fully symmetric and decoupled trilayer are shown in Fig.4.7(a). In this type of system, when the charge current flowing through the device reaches a critical value, the increase $+m_z$ in one layer is compensated by increasing $-m_z$ in the other, resulting in no change in the total resistance of the system. However, the system with a thin Pt layer discussed in this section is far from a fully symmetrical example. In this case, the IEC ferromagnetic coupling is very strong, and the anisotropies and interfaces of the two Co layers are different. Consequently, the H_{DL} effective field acting on each Co layer differs. For this reason, switching the bottom Co layer also results, through IEC, in switching the top Co layer (Fig.4.7(b)). This results in higher system resistance when more domains are pointed in the $+z$ direction than in the $-z$ direction in both layers.

PCCP

ARTICLE TYPE

Cite this: DOI: 00.0000/xxxxxxxxxx

Multilevel switching due to spin-orbit torques in Co/Pt/Co

Krzysztof Grochot,[*a,b] Piotr Ogrodnik,[c] Jakub Mojsiejuk,[a] Piotr Mazalski,[d,e] Witold Skowroński,[a] and Tomasz Stobiecki[a,b]

Received Date
Accepted Date

DOI: 00.0000/xxxxxxxxxx

Spin-orbit torque current-induced magnetization switching provides an energy-efficient way of manipulating the magnetization in the ferromagnetic layers. Here, we present a detailed study of multilevel magnetization switching via spin-orbit torque in the Co/Pt/Co heterostructure with varied Pt thickness. Hence, the Pt layer plays the role of a spacer, providing the ability to control interlayer exchange coupling. As a result of the asymmetry between the top Pt/Co and bottom Co/Pt interfaces, and the coupling between the Co layers, four separate resistance states emerge when the external magnetic field is applied in the direction of the charge current. We reproduce the multilevel current switching mechanism using a numerical macro-spin model using the Landau-Lifshitz-Gilbert-Slonczewski equation. Finally, we propose an explanation of the accompanying multi-domain behavior, supported by measurements from polar-magnetooptical Kerr microscopy. Based on our findings, multilevel switching may have a potential application in energy-efficient high-density memory cells.

1 Introduction

Among magnetization switching methods, spin-orbit torque current-induced magnetization switching (SOT-CIMS) in metallic multilayers offers a very short switching time (less than 1 ns) with no breakdown risk of the tunnel barrier used in typical spin-transfer torque (STT)-based memory cells.[1–5] Up to now, the SOT-CIMS was observed in a variety of heavy metal (HM)-based layered systems, such as simple FM/ferromagnet (FM) bilayers[1,6,7], or HM/FM/antiferromagnet (AFM)[8–12] and FM/HM/FM trilayers.[13–22] The HM plays the role of a spin current source due to the presence of substantial spin-orbit interactions, which gives rise to the spin current generation due to charge current flow, as predicted in 23–26. Spin current may be injected into the FM layer due to the gradient of spin accumulation at the interface and exerts the effective SOT fields, field-like (H_{FL}) and damping-like (H_{DL}), that can switch the magnetization of the FM layer.[27–33] In systems where the FM layer is characterized by perpendicular magnetic anisotropy, the magnetization dynamics is also driven, in addition to the SHE, by a Rashba-Edelstein effect originating from the inversion symmetry breaking at the HM/FM interfaces.[26,34–37]

In a bilayer HM/FM system, only two stable resistance states are possible during CIMS. The spin current generated in the HM accumulates at both HM interfaces; however, it can act on one FM layer only, causing the reversal of its magnetization. In contrast, in trilayer FM/HM/FM systems, the spin current has a different polarization at both interfaces. Thus, its effect on the magnetizations of both FMs may be more sophisticated than in bilayers. The energy efficiency of the magnetization reversal in such trilayer systems is supposed to be slightly higher than in the bilayer ones. However, the advantage of trilayers is that they provide the possibility of four stable resistance states. This feature makes them attractive for potential use in low-power consumption and high-density memory design and in the simulation of synapses for neuromorphic computation.[16,38]

In this work, we present a detailed study of multilevel switching via SOT-CIMS in the Co/Pt/Co system as a function of variable Pt thickness. As shown in our previous work[39], the thickness of Pt varies along the wedge shape of the sample, controlling the efficiency of spin current generation and the interlayer exchange coupling (IEC). We demonstrated that the effective magnetic anisotropy of the two layers is different and strongly depends on the Pt thickness. For a thin Pt layer between 1 and 2 nm of Pt, a transition of the effective anisotropy was observed, from in-plane to perpendicular. We also showed a significant difference in the atomic structure of the lower Co/Pt and upper Pt/Co interfaces, which consequently affects the amount of spin cur-

* *E-mail: grochot@agh.edu.pl*
[a] *Institute of Electronics, AGH University of Science and Technology.*
[b] *Faculty of Physics and Computer Science, AGH University of Science and Technology.*
[c] *Faculty of Physics, Warsaw University of Technology, Warsaw, Poland.*
[d] *Jerzy Haber Institute of Catalysis and Surface Chemistry of the Polish Academy of Sciences, Cracow, Poland.*
[e] *Faculty of Physics, University of Bialystok, Bialystok, Poland.*

rent flowing into both Co layers and, thereby, switching of their magnetizations. Here, the above results are combined with the multi-level magnetization switching. We support our findings with polar-magnetooptical Kerr microscopy (p-MOKE) measurements and macro-spin modeling of the magnetization dynamics. We also provide a qualitative explanation for the magnetization switching mechanism in investigated trilayers. Finally, we show the dependence of the critical switching current on the magnitude of the IEC.

2 Experimental

2.1 Device fabrication

The continuous, wedge-shaped FM/HM/FM heterostructure was deposited using a magnetron sputtering technique on the 20 × 20 mm^2 Si/SiO$_2$ substrate at room temperature and under the same conditions as in Ref.39. The sample cross-section scheme and the coordinate system used are shown in Fig.1. The layers are ordered as follows: Si/SiO$_2$/Ti(2)/Co(1)/Pt(0-4)/Co(1)/MgO(2)/Ti(2)(thicknesses listed in parentheses are in nanometers). Both the bottom and the top Ti layers perform the function of buffer and protection layer. They do not contribute to the studied phenomena due to their partial oxidation and small spin-orbit coupling.[40–42] After the deposition process, the sample was characterized by X-ray diffraction. We detected the presence of a face-centered cubic fcc(111) texture at the Pt/Co and Co/Pt interfaces and confirmed the existence of an asymmetry between these two interfaces. Details of the structural analysis of the studied samples are described in Ref.39.

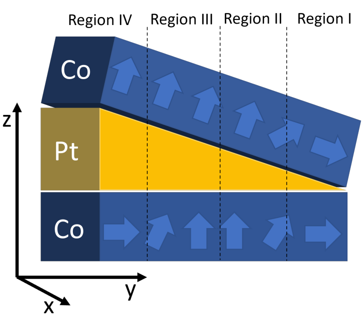

Fig. 1 Cross-section through the studied heterostructure. The blue arrows depict the direction of magnetization vectors in both ferromagnetic Co layers in specified Pt thickness regions. The dashed lines indicate the border of each region.

We performed X-ray reflectivity measurements to precisely calibrate the thickness of each layer as a function of the position on the sample wedge. In doing so, we were able to precisely determine the thickness of the layers located at a specific position on the wedge of Pt. The thickness variation of the Pt layers in the device was less than 0.006 nm, so that the Pt thickness is constant throughout the device. The sample was microstructures by optical laser lithography, ion etching, and lift-off to an array matrix of different sizes of Hall bar devices, which were optimized for the measurement techniques used. We used Hall bars of size 80 x 10 μm^2 for current-induced magnetization switching (CIMS) measurements, while resistance and magnetoresistance measurements were performed on 140×20 μm^2 devices using the 4-probe method. Prior X-ray measurement ensured the thickness variation of the Pt layers throughout each device was constant (less than 0.006 nm).

2.2 Anomalous Hall effect and effective anisotropies

In the next step, we measured the anomalous Hall effect (AHE) for all elements along the Pt wedge. As a result, we obtained a set of AHE resistance loops as a function of the external magnetic field applied along the z direction (H_z). By analyzing their shapes, we could distinguish four regions of Pt thickness (marked regions I-IV) in which the AHE loops exhibit a similar shape (Fig. 2). As shown in our previous work[39], in region I, the magnetizations of both Co layers are in-plane ($K_{\text{eff}}<0$) and, as a consequence, AHE depends linearly on the magnetic field H_z. Therefore, it is not possible to distinguish resistance states with AHE during CIMS in this region. Regions II and III were characterized by two Co layers magnetized perpendicularly to the sample plane in the remanent state and strong IEC (both Co layers switch simultaneously), and as a result, the AHE hysteresis loops become rectangular, as demonstrated in Fig.2(b),(c). Moving from region III to IV, the interlayer exchange coupling (IEC) decreases substantially as the Pt spacing layer thickness.[39] Consequently, the top Co remains magnetized perpendicularly, whereas the bottom layer tends to be magnetized in the plane again.

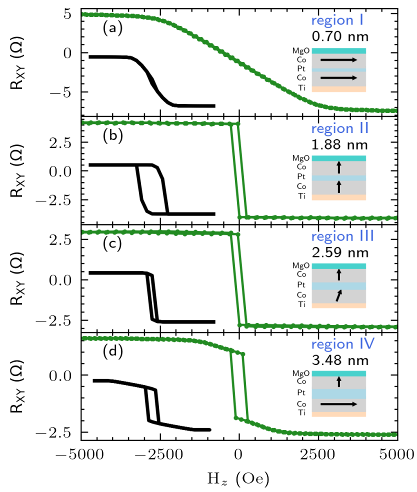

Fig. 2 AHE loops for Hall-bar devices with different thicknesses of the Pt spacing layer. The solid black lines in the inset denote the simulated AHE loops using the model described in Sect.4. The depicted diagrams of multilayer cross sections for all regions indicate the direction of magnetizations of magnetic layers at remanence.

3 Results and discussion

3.1 Current-induced magnetization switching

We measured the AHE to observe magnetization switching between two stable high- and low-resistance states of the AHE loop. CIMS takes place in regions II-IV only, where at least one layer is perpendicularly magnetized in the remanent state.

In order to achieve magnetization saturation, the samples were subjected to a large magnetic field in the $-z$ direction. Then, to drive magnetization switching, we applied a sequence of 1 ms current pulses, with a pulse spacing of 2 ms in the x direction. The voltage was swept from 0 V to a maximum negative value ($-V_{\mathrm{max}}$), then to the maximum positive value ($+V_{\mathrm{max}}$), and then back to 0 V. Simultaneously, we measured the transverse voltage (V_{xy}) in the presence of an in-plane magnetic field H_{x}, which is co-linear to the current direction. The measurement setup is presented schematically in Fig.3. The in-plane magnetic field H_{x} was

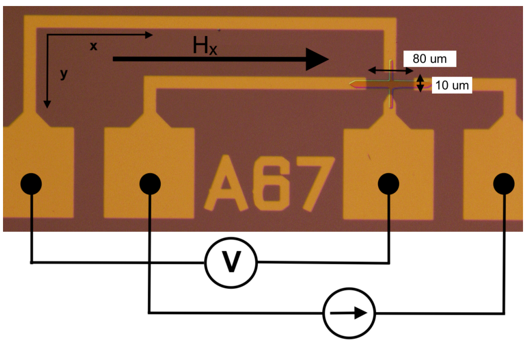

Fig. 3 Device used for CIMS measurements.

changed sequentially after each CIMS loop in the wide range of $\pm$ 7 kOe. As a result, we obtained a set of CIMS loops in different H_{x} for representative Pt thicknesses from regions II to IV and examples are plotted in Fig.4.

As shown in Fig.4(a) and (b), experimentally obtained CIMS loops measured at positive and negative magnetic fields are clearly separated in regions I and II. Both stable resistance states of the CIMS loops have a higher resistance for $+H_{\mathrm{x}}$ (blue loop) than those measured for $-H_{\mathrm{x}}$ (orange loop). When the direction of the magnetic field changes from +x to -x, we observed a smooth transition from the high-resistance loop to the low-resistance loop (follow the green loop), as indicated by the red arrows in Fig. 4(a),(b). For the thicker Pt spacer in Fig.4(c) ($t_{\mathrm{Pt}} = 1.64$ nm) separation gap becomes smaller compared to the sample of Pt = 1.36 nm thick (Fig.4(a). In region III ($t_{\mathrm{Pt}} = 2.16$ nm)(Fig.4(c), however, the four resistance states can still be observed. In the case of the thickest Pt ($t_{\mathrm{Pt}} = 3.57$ nm), for which only one Co layer exhibits perpendicular anisotropy, the separation gap disappears. Regardless of the direction of H_{x} only two resistance states exist, as in the case of the HM/FM bilayer (not shown here).[1,6,7,43]

Subsequently, we performed an analysis of the critical current densities ($j_{\mathrm{c,Pt}}$) required to switch magnetization. For this pur-

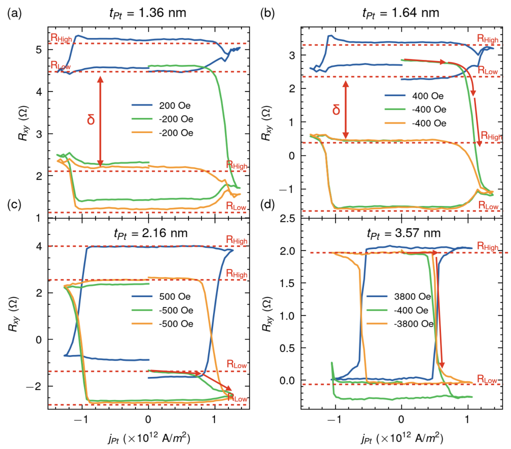

Fig. 4 CIMS loops for devices from regions: (a)-(b) II, (c) III, and (d) IV. Red dashed lines indicate the resistance levels of the bottom and top Co layers, respectively, while the red solid arrows show a transition from the high to low resistance loop. The blue and orange solid lines indicate CIMS loops for positive and negative magnetic fields, respectively. The green line corresponds to the resistance curve after reversal of the direction of the applied magnetic field to the opposite. In accordance with the macrospin model, we denoted the gap between loops by δ.

pose, the dependence of $j_{\mathrm{c,Pt}}$ through the Pt was plotted as a function of the applied external magnetic field (H_{x}). As demonstrated in Fig.5(a) for $H_{\mathrm{x}} \ll H_{\mathrm{k,eff}}$, the experimental dependencies measured in all devices are linear, which stays consistent with Ref.44.

In Fig.5(b) we show the $j_{\mathrm{c,Pt}}$ dependence on the Pt layer thickness. The critical $j_{\mathrm{c,Pt}}$ linearly decreases in a wide range of Pt thickness, from 1.6 to 3 nm, when it reaches its lowest value. However, for the thinnest and the thickest Pt layer, $j_{\mathrm{c,Pt}}$ deviates from the linear dependence by slightly dropping and rising, respectively.

The highest values of the critical current amplitude required for switching are found for elements with a small thickness of Pt and then slightly decreases linearly to a value of approximately 0.5×10^{12} A/m^2 for the element with $t_{\mathrm{Pt}} = 2.92$ nm (Fig.5(b)).

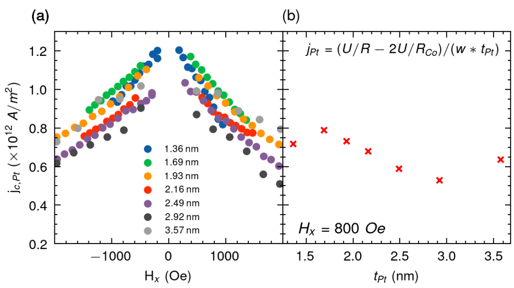

Fig. 5 Critical switching current density as a function of the external magnetic field (H_{x}) for samples from region II and III (a), critical current density ($j_{\mathrm{c,Pt}}$) as a function of Pt thickness (b). Changes in $j_{\mathrm{c,Pt}}$ are explained in detail in Sec 3.2.

3.2 Domain mechanism of multilevel switching

We qualitatively explain the observed CIMS loops in terms of magnetic domains in microstrips of the Hall-bar devices. For this purpose, selected Hall-bars from each region of Pt thickness were imaged with p-MOKE while the H_x field was applied. It enabled us to relate the change of magnetic domain structure with the resistance level measured during CIMS. Firstly, the magnetization of each Hall bar was saturated with H_z field to the lowest resistance state, indicated by A and E in Figs.6(a) and (b), respectively. Therefore, it was possible to assign images of the domain structure to the corresponding resistances on the current switching loops, as shown in Figs.6(a) and (b).

We also repeated this procedure for the perpendicular field H_z and in this case the magnetization reversal was performed by a single-domain wall motion.

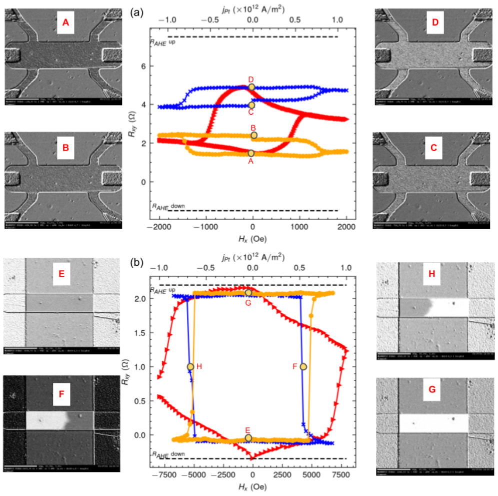

Fig. 6 CIMS loops for (a) $t_{Pt} = 1.36$ nm thick element (region II) and (b) $t_{Pt} = 3.57$ nm thick element (region IV). The CIMS loops (blue and orange) were obtained in fields H_x of $+0.8$ kOe and -0.8 kOe in (a) and $+3.8$ kOe and -3.8 kOe in (b), respectively. The red triangles indicates the R_{xy} loops measured in the H_x field. The letters (A-H) in figures (a) and (b) indicate the relevant p-MOKE images labeled with the same letter.

We observed a very fine-grained domain structure (Fig.6(a) A-D) for the Hall bar with thickness $t_{Pt} = 1.36$ nm (region II) at $H=0$ ($j=0$). When current-induced SOT switches the magnetization, a number of domains change their state to the opposite. The new distribution of magnetic domains results in an intermediate state (yellow dots B and C) placed between the two extremes marked in Fig.6(a) with letters A and D. This transition of magnetic domains can be observed as a change in the gray color level of elements marked A and B (or C and D) in Fig.6(a). The smooth shape of the CIMS loops in this region confirms the fine-grained magnetic domain switching mechanism.

The opposite behavior occurs in the region IV element with a Pt thickness of 3.57 nm, where we observed a complete magnetization reversal driven by a current-induced domain-wall motion. Such behavior demonstrates itself as a perfectly rectangular shape of the CIMS loops with only two stable resistance states for both directions of the magnetic field ($+H_x$ and $-H_x$) (Fig.6b)

The generation of the fine domain structure visible in Fig.6a was achieved by, first, saturating the sample with a perpendicular field (H_z), then applying a field H_x of about 10 kOe, and then gradually reducing its value to about 1 kOe. As a result, the field-free resistance of the system is not equal to the high-resistance state of the AHE loop due to the uneven distribution of the m_z components of the magnetic domains in both Co layers. This condition is presented in Fig.6(a), where there is a predominance of domains with a $+m_z$ component at remanence. Reapplying a small H_x field generates a m_x component parallel to the direction of the magnetic field in both Co layers, the existence of which is necessary for symmetry breaking and switching magnetization by the spin-polarized current.

The following scenario is proposed to explain the CIMS behaviour: in the top Co layer, the current-induced SOT damping-like effective field ($\mathbf{H}_{DL} \sim \mathbf{m} \times \mathbf{e}_y$) acts oppositely on domains with $+m_z$ and $-m_z$ components, i.e., for positive currents, $+H_{DL}$ forces $+m_z$ domains to switch, while $-H_{DL}$ pushes $-m_z$ domains back to the perpendicular direction. On the other hand, the spin current flowing into the bottom Co layer has the opposite sign. Therefore, SOT stabilizes the $+m_z$ domains while switching the $-m_z$ domains in this layer (Fig. 7(a). The SOT field effect on an uncoupled and fully symmetric trilayer is depicted in Fig.7(a). When the current pulse reaches a critical amplitude value, each of the Co layers can switch only partially. However, we note that in a fully symmetric and uncoupled case, the SOT would not result in resistance change. Then, the increase of $-m_z$ in one layer would be balanced by the increase of $+m_z$ in the second layer, which is illustrated in Fig.7(a) with horizontal arrows pointing in opposite directions. However, thin Pt devices (region II) are far from the symmetric case(Ref.39). The top and bottom interfaces differ, and therefore the magnitudes of effective H_{DL} fields acting on each Co are not equal. Moreover, the magnetic anisotropies in both layers are different and a large ferromagnetic IEC is present in this region.[39] For this reason, when the lower Co layer switches, the ferromagnetic coupling forces the magnetization of the upper Co layer to switch as well. The mechanism is illustrated in Fig.7(b).

The switching process results in a higher resistance related to a larger number of domains with magnetization pointing in the +z, rather than the -z direction, in both Co layers.

The described mechanism is consistent with the dependence of the critical current density ($j_{c,Pt}$) on the thickness of Pt presented in Fig.5. The $j_{c,Pt}$ decreases for the Pt thickness, ranging from 1.7 to 3.0 nm (regions II and III). This decrease is due to a more efficient SOT for the thicker Pt layer.[45] However, for the thinnest Pt in region II (1.3 nm), $j_{c,Pt}$ drops by about $\Delta j_c = 0.10 \times 10^{-12} A/m^2$). Similarly, for the thickest Pt in region IV (3.6 nm), the critical current abruptly increases approximately ($\Delta j_c = 0.17 \times 10^{-12} A/m^2$). The deviations from the linear dependence are correlated with very strong coupling (for the thinnest Pt) and negligible coupling (for the thickest Pt). The switching in the thin Pt case relies on the magnetization reversal in both Co layers. These two layers have different anisotropy fields (H_k (top) > 0, H_k (bot-

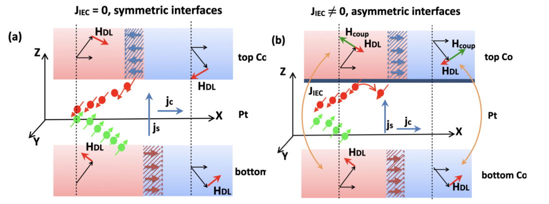

Fig. 7 Mechanism of SOT-CIMS in two cases: With no coupling (J_{IEC}=0) and symmetric Co/Pt – Pt/Co interfaces (a) and in the presence of strong coupling and asymmetric interfaces (top interface with less transparency is marked as solid navy blue layer) (b). The red(blue) areas represent magnetic domains with average $+m_z$($-m_z$) components. The dashed ares together with horizontal arrows indicate the change in domain size under the H_{DL} SOT components (thick red arrows) and ferromagnetic coupling H_{coup} field (thick green arrows, solid orange arrows show the coupling between Co layers). The spin current with polarization $+\mathbf{e}_y$($-\mathbf{e}_y$) is depicted as red(green) bold points with arrows.

tom)<0).[39] It means that the bottom layer is more susceptible to the torque from the SOT effect. Therefore, when the IEC field is strong enough, it easily overcomes H_k in the top layer, allowing it to switch at a lower current (SOT). Then, both Co layers are magnetically stiff and behave somewhat like one layer with the effective anisotropy: H_k(top)>$H_{k_{eff}}$> H_k(bottom).

For the intermediate IEC (border of regions II and III), the bottom layer is still more switchable, but the coupling does not provide the top layer with enough torque to switch. Both layers become less magnetically stiff, so more current (more SOT) is needed to switch both of them.

The bottom layer magnetization is in-plane when the coupling becomes negligible (region IV). It means that the SOT only switches the top layer with higher anisotropy (H_k(top)). Therefore, the critical current rises despite the thick Pt and a large SOT.

3.3 Multilevel magnetization switching

One of the most important components of the current-induced magnetization switching process is the difference between high and low resistance levels of the current switching loop, denoted $\Delta R = R_{high} - R_{low}$. The larger ΔR, the wider the practical application of the device in spintronics due to the low probability of spontaneous switching to the opposite state when detecting the state of a memory cell with small voltage. In the case of the studied devices, the amplitude ΔR depends on the thickness of the Pt spacer and, therefore, on the magnitude of the IEC. Elements with a thin Pt layer (region II and III) and, thus, with strong coupling, exhibit small values of ΔR, reaching a $\Delta R/\Delta R_{AHE}$ value of 0.8 (Fig.8(a). The fact that the amplitude ratio does not reach the maximum value ($\Delta R/\Delta R_{AHE} < 1$) indicates a domain-specific origin of switching and therefore the magnetic domains persist in remanence. Elements in region IV, where the coupling is negligible (Fig.8(b), show $\Delta R/\Delta R_{AHE}$ values close to 1, suggesting that the switching is practically single-domain and only Co layer with perpendicular anisotropy switches.

For t_{Pt} = 1.55 nm (region I), we chose two values (+0.5 kOe and −0.5 kOe) of the external magnetic field for which both loops

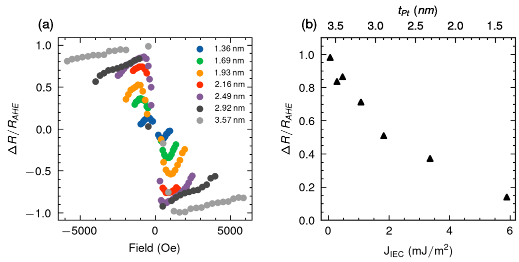

Fig. 8 (a) $\Delta R/R_{AHE}$ ratio as a function of the external magnetic field for elements with different Pt layer thicknesses. (b) The maximum values of $\Delta R/R_{AHE}$ ratio as a function of IEC.

show significant amplitude (ΔR) and are completely separated. As shown in Fig.9(a), the four different resistance states are present. Next, based on the switching loops, we determined the critical currents ($I_{c,Pt}$) of +32 and -32 mA needed to switch the magnetization at ±0.5 kOe. Then, to switch the resistance between four well-separated levels, we applied both current pulses of $\pm I_c$ amplitude and the magnetic field of magnitude of ±500 Oe (Fig. 9(a).

By carefully choosing the combination of signs H_x (Fig.9(b) and I_c(Fig.9(c), we obtained a ladder-shaped waveform of the resistance of the system (Fig.9(d). The procedure of tuning the switching pulse duration and its amplitude for an arbitrary field allows the system to be set in a single well-defined resistance state and, therefore, to store considerably more information in a single memory cell.

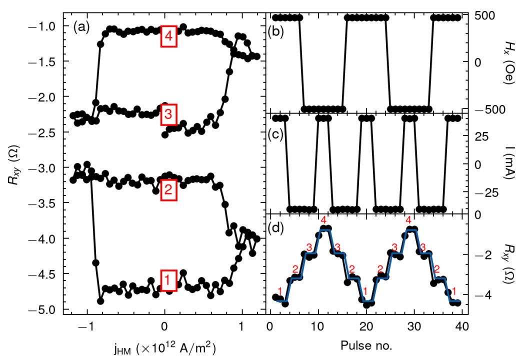

Fig. 9 Four stable resistance states for the sample from region I (t_{Pt} = 1.55 nm (a), obtained by manipulating the magnitude of the current pulse (b) and the external magnetic field (c). Resistance levels in (a) correspond to the levels of current switching loops in (d).

4 Macrospin model for multilevel switching

We support the explanation of the multilevel switching phenomenon using the numerical macrospin model. The model is based on Landau-Lifshitz-Gilbert-Slonczewski (LLGS) of the following form[46–48]:

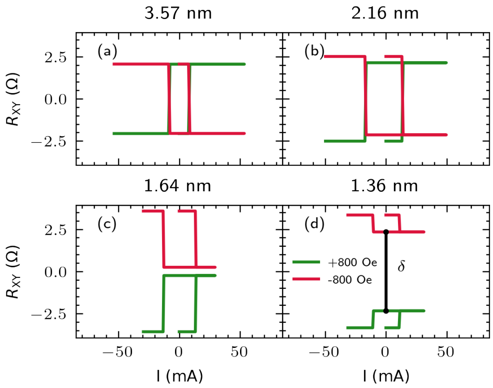

Fig. 10 (a-d) Multilevel switching for a range of thicknesses. The external field was the same for all simulations with $H_x = \pm 0.8$ kOe. An example of δ separation was marked in (d).

$$\frac{\mathrm{d}\mathbf{m}}{\mathrm{d}t} = -\gamma_0 \mathbf{m} \times \mathbf{H}_{\text{eff}} + \alpha_G \mathbf{m} \times \frac{\mathrm{d}\mathbf{m}}{\mathrm{d}t} - \gamma_0 H_{\text{FL}} (\mathbf{m} \times \mathbf{e}_y) - \gamma_0 \eta H_{\text{FL}} (\mathbf{m} \times \mathbf{m} \times \mathbf{e}_y) \tag{1}$$

where $\mathbf{m} = \frac{\mathbf{M}}{M_s}$ is the normalized magnetization vector, with M_s as magnetization saturation, α_G is the dimensionless Gilbert damping coefficient, γ_0 is the gyromagnetic ratio, $H_{\text{DL}} = \eta H_{\text{FL}}$ and H_{FL} are damping-like and field-like torque amplitudes respectively, and $\mathbf{e}_y$ is the spin polarization vector in y direction. The $\mathbf{H}_{\text{eff}}$ is the effective field vector that includes contributions from anisotropy, IEC, and demagnetization energy. For the reproduction of the experimental results, we used the open source CMTJ package[49], taking simulation parameters from Ref.39. We note that a small anisotropy polar angle ($\theta_{K1} = 5°$, measured from the $+z$ axis) is sufficient to facilitate loop separation for samples from region II. Similarly, small in-plane components of anisotropy are necessary to break the symmetry under an external field H_x. In all simulations, we take the Gilbert damping of $\alpha_G = 0.05$.[39]

To account for the interfacial asymmetry in our macrospin model, we adapted and modified the resistance model for R_{xy} from Kim et al.[50] First, we neglected $\Delta R_{\text{SMR}_{xy}}$ and $\Delta R_{\text{AMR}_{xy}}$ due to their small values in the investigated samples (the maximum values were $\frac{\Delta R_{\text{SMR}_{xy}}}{R_0}$(max) = -0.42% and $\frac{\Delta R_{\text{AMR}_{xy}}}{R_0}$(max) = 0.24%, respectively). Second, we introduced the symmetry parameter β in the following way:

$$R_{xy} = R^{(1)}_{xy0} + R^{(2)}_{xy0} + \frac{1}{2}\kappa \Delta R_{\text{AHE}} (m_z^{(1)} + \beta m_z^{(2)}) \tag{2}$$

where the superscript refers to the top (1) or the bottom layer (2). The β parameter ranges from 0 exclusive (asymmetric interfaces) to 1 inclusive for entirely symmetric interfaces. Furthermore, the dimensionless κ parameter effectively corrects the R_{xy} amplitude for the multidomain behavior in regions II through III, which is necessary due to limitations of the macrospin model. We show the different stages of multilevel switching in Fig.10.

5 Conclusions

In conclusion, we demonstrated a four-level current-induced magnetization switching in the Co/Pt/Co heterostructure. We showed that the interface asymmetry and the interlayer coupling together make it possible to achieve four separate states of resistance at the external magnetic field applied in the charge current direction. Moreover, we explained the multilevel switching in terms of a fine-grain domain structure and its partial change under the current-induced SOT. This effect disappears as the coupling weakens and the thickness of the Pt spacer increases. At that moment, we observe only two resistance states, and the transition between them is realized by generating and moving a single domain wall. We showed that the critical switching current exhibits weakly linear dependence on the Pt thickness for a wide range of thicknesses, t_{Pt} (1.5 nm - 3.0 nm). In contrast, it deviates from linearity for the thinnest and thickest Pt layer due to large and negligible IEC respectively. Furthermore, we demonstrated that the resistance state separation ΔR, resistance loop separation δ and $\Delta R/\Delta R_{AHE}$ ratio can be easily tailored by changing the HM thickness. Our findings have promising potential for the development of low-power consumption and high-density SOT devices. For example, in neuromorphic computing, multilevel switched elements can function as synapses, thus proving useful in applications such as spintronics-based artificial intelligence or on-the-fly learning.[51]

Author Contributions

Krzysztof Grochot: Carried out microstructurization, conducted the electrical conductivity, spin Hall and anomalous Hall experiments. Performed data analysis, visualization, writing-reviewing and editing contents of the paper.
Piotr Ogrodnik: Performed formal analysis and visualization. Writing-reviewing and editing contents of the paper.
Piotr Mazalski: Conducted magnetic domain imaging using p-MOKE microscopy measurement. Writing-reviewing and editing contents of the paper.
Jakub Mojsiejuk: Software developer of modelling software. Conducted formal analysis and visualization. Writing-reviewing and editing contents of the paper.
Witold Skowroński: Microstructurization, design and programming of measurement methods
Tomasz Stobiecki: Supervised the experimental and theoretical modeling aspects of the project. Writing-reviewing and editing contents of the paper.

Conflicts of interest

There are no conflicts to declare.

Acknowledgements

This work was supported by the National Science Centre in Poland under SPINORBITRONICS (2016/23/B/ST3/01430) and Beethoven 2 (UMO-2016/23/G/ST3/04196) projects.

Notes and references

1 I. M. Miron, K. Garello, G. Gaudin, P.-J. Zermatten, M. V. Costache, S. Auffret, S. Bandiera, B. Rodmacq, A. Schuhl and P. Gambardella, *Nature*, 2011, **476**, 189–193.

2 A. Brataas and K. M. D. Hals, *Nature Nanotechnology*, 2014, **9**, 86–88.

3 T. Wang, J. Q. Xiao and X. Fan, *SPIN*, 2017, **07**, 1740013.

4 B. Dieny, I. L. Prejbeanu, K. Garello, P. Gambardella, P. Freitas, R. Lehndorff, W. Raberg, U. Ebels, S. O. Demokritov, J. Akerman, A. Deac, P. Pirro, C. Adelmann, A. Anane, A. V. Chumak, A. Hirohata, S. Mangin, S. O. Valenzuela, M. C. Onbaşlı, M. d'Aquino, G. Prenat, G. Finocchio, L. Lopez-Diaz, R. Chantrell, O. Chubykalo-Fesenko and P. Bortolotti, *Nature Electronics*, 2020, **3**, 446–459.

5 K. Garello, C. O. Avci, I. M. Miron, M. Baumgartner, A. Ghosh, S. Auffret, O. Boulle, G. Gaudin and P. Gambardella, *Applied Physics Letters*, 2014, **105**, 212402.

6 G. Yu, P. Upadhyaya, Y. Fan, J. G. Alzate, W. Jiang, K. L. Wong, S. Takei, S. A. Bender, L.-T. Chang, Y. Jiang, M. Lang, J. Tang, Y. Wang, Y. Tserkovnyak, P. K. Amiri and K. L. Wang, *Nature Nanotechnology*, 2014, **9**, 548–554.

7 L. Liu, O. J. Lee, T. J. Gudmundsen, D. C. Ralph and R. A. Buhrman, *Physical Review Letters*, 2012, **109**, 096602.

8 K. Grochot, L. Karwacki, S. Łazarski, W. Skowroński, J. Kanak, W. Powroźnik, P. Kuświk, M. Kowacz, F. Stobiecki and T. Stobiecki, *Physical Review Applied*, 2021, **15**, 014017.

9 S. Maat, K. Takano, S. S. P. Parkin and E. E. Fullerton, *Physical Review Letters*, 2001, **87**, 087202.

10 Y.-W. Oh, S.-h. Chris Baek, Y. M. Kim, H. Y. Lee, K.-D. Lee, C.-G. Yang, E.-S. Park, K.-S. Lee, K.-W. Kim, G. Go, J.-R. Jeong, B.-C. Min, H.-W. Lee, K.-J. Lee and B.-G. Park, *Nature Nanotechnology*, 2016, **11**, 878–884.

11 S. Fukami, C. Zhang, S. DuttaGupta, A. Kurenkov and H. Ohno, *Nature Materials*, 2016, **15**, 535–541.

12 A. van den Brink, G. Vermijs, A. Solignac, J. Koo, J. T. Kohlhepp, H. J. M. Swagten and B. Koopmans, *Nature Communications*, 2016, **7**, 10854.

13 Y. Sheng, Y. C. Li, X. Q. Ma and K. Y. Wang, *Applied Physics Letters*, 2018, **113**, 112406.

14 C. O. Avci, M. Mann, A. J. Tan, P. Gambardella and G. S. D. Beach, *Applied Physics Letters*, 2017, **110**, 203506.

15 P. Gospodarič, E. Młyńczak, I. Soldatov, A. Kákay, D. E. Bürgler, L. Plucinski, R. Schäfer, J. Fassbender and C. M. Schneider, *Physical Review Research*, 2021, **3**, 023089.

16 D. Li, B. Cui, X. Guo, Z. Xiao, W. Zhang, X. Jia, J. Duan, X. Liu, J. Chen, Z. Quan, G. Yu and X. Xu, *APL Materials*, 2021, **9**, 071108.

17 G. J. Lim, W. L. Gan, W. C. Law, C. Murapaka and W. S. Lew, *Journal of Magnetism and Magnetic Materials*, 2020, **514**, 167201.

18 Y. Wang, T. Taniguchi, P.-H. Lin, D. Zicchino, A. Nickl, J. Sahliger, C.-H. Lai, C. Song, H. Wu, Q. Dai and C. Back, *Time-Resolved Detection of Multilevel Switching of the Magnetization and Exchange Bias Driven by Spin-Orbit Torques*, In review preprint, 2021.

19 Y. Yang, H. Xie, Y. Xu, Z. Luo and Y. Wu, *Physical Review Applied*, 2020, **13**, 034072.

20 J. Yun, Q. Bai, Z. Yan, M. Chang, J. Mao, Y. Zuo, D. Yang, L. Xi and D. Xue, *Advanced Functional Materials*, 2020, **30**, 1909092.

21 S. Zhang, Y. Su, X. Li, R. Li, W. Tian, J. Hong and L. You, *Applied Physics Letters*, 2019, **114**, 042401.

22 L. Zhu, X. Xu, M. Wang, K. Meng, Y. Wu, J. Chen, J. Miao and Y. Jiang, *Applied Physics Letters*, 2020, **117**, 112401.

23 M. Dyakonov and V. Perel, *Physics Letters A*, 1971, **35**, 459–460.

24 J. E. Hirsch, *Phys. Rev. Lett.*, 1999, **83**, 1834–1837.

25 S. Zhang, *Physical Review Letters*, 2000, **85**, 393–396.

26 J. Sinova, S. O. Valenzuela, J. Wunderlich, C. Back and T. Jungwirth, *Reviews of Modern Physics*, 2015, **87**, 1213–1260.

27 S. Emori, U. Bauer, S. Woo and G. S. D. Beach, *Applied Physics Letters*, 2014, **105**, 222401.

28 M. Yang, K. Cai, H. Ju, K. W. Edmonds, G. Yang, S. Liu, B. Li, B. Zhang, Y. Sheng, S. Wang, Y. Ji and K. Wang, *Scientific Reports*, 2016, **6**, 20778.

29 S. Łazarski, W. Skowroński, J. Kanak, L. Karwacki, S. Ziętek, K. Grochot, T. Stobiecki and F. Stobiecki, *Physical Review Applied*, 2019, **12**, 014006.

30 K. M. D. Hals and A. Brataas, *Physical Review B*, 2013, **88**, 085423.

31 L. Liu, T. Moriyama, D. C. Ralph and R. A. Buhrman, *Physical Review Letters*, 2011, **106**, 036601.

32 C. Zhang, S. Fukami, H. Sato, F. Matsukura and H. Ohno, *Applied Physics Letters*, 2015, **107**, 012401.

33 Y.-C. Lau, D. Betto, K. Rode, J. M. D. Coey and P. Stamenov, *Nature Nanotechnology*, 2016, **11**, 758–762.

34 V. M. Edelstein, *Solid State Communications*, 1990, **73**, 233–235.

35 Y. Cao, Y. Sheng, K. W. Edmonds, Y. Ji, H. Zheng and K. Wang, *Advanced Materials*, 2020, **32**, 1907929.

36 B. Cui, H. Wu, D. Li, S. A. Razavi, D. Wu, K. L. Wong, M. Chang, M. Gao, Y. Zuo, L. Xi and K. L. Wang, *ACS Applied Materials & Interfaces*, 2019, **11**, 39369–39375.

37 X. Fan, H. Celik, J. Wu, C. Ni, K.-J. Lee, V. O. Lorenz and J. Q. Xiao, *Nature Communications*, 2014, **5**, 3042.

38 X. Lan, Y. Cao, X. Liu, K. Xu, C. Liu, H. Zheng and K. Wang, *Advanced Intelligent Systems*, 2021, **3**, 2000182.

39 P. Ogrodnik, K. Grochot, L. Karwacki, J. Kanak, M. Prokop, J. Chęciński, W. Skowroński, S. Zietek and T. Stobiecki, *ACS Applied Materials & Interfaces*, 2021, **13**, 47019–47032.

40 P. Süle, L. Kotis, L. Toth, M. Menyhard and W. F. Egelhoff, *Nuclear Instruments and Methods in Physics Research Section B: Beam Interactions with Materials and Atoms*, 2008, **266**, 904–910.

41 C. O. Avci, *Physical Review B*, 2014, **90**, 224427.

42 H. Y. Poh, *Physical Review B*, 2021, **104**, 224416.

43 K. Grochot, L. Karwacki, S. Lazarski, W. Skowronski, J. Kanak,

W. Powroznik, P. Kuswik, M. Kowacz, F. Stobiecki and T. Stobiecki, *Phys. Rev. Applied*, 2021, **15**, 014017.
44 K.-S. Lee, S.-W. Lee, B.-C. Min and K.-J. Lee, *Applied Physics Letters*, 2013, **102**, 112410.
45 M.-H. Nguyen, D. C. Ralph and R. A. Buhrman, *Phys. Rev. Lett.*, 2016, **116**, 126601.
46 D. Ralph and M. Stiles, *Journal of Magnetism and Magnetic Materials*, 2008, **320**, 1190–1216.
47 J. Slonczewski, *Journal of Magnetism and Magnetic Materials*, 1996, **159**, L1–L7.
48 M.-H. Nguyen and C.-F. Pai, *APL Materials*, 2021, **9**, 030902.
49 J. Mojsiejuk, S. Ziętek, K. Grochot, W. Skowroński and T. Stobiecki, *A comprehensive simulation package for analysis of multilayer spintronic devices*, 2022, `https://arxiv.org/abs/2207.11606`.
50 J. Kim, P. Sheng, S. Takahashi, S. Mitani and M. Hayashi, *Phys. Rev. Lett.*, 2016, **116**, 097201.
51 K. Yue, Y. Liu, R. K. Lake and A. C. Parker, *Science Advances*, 2019, **5**, eaau8170.

Section summary

This section reports our studies on the Co/Pt/Co trilayer system, where the Pt spacer acts as a spin current source and a coupling tuner. We have explored how the Pt thickness affects the magnetic properties, spin transport effects, and magnetization dynamics of the system by various methods, such as magnetoresistance measurements, spin diode (SD)-FMR, CIMS and p-MOKE microscopy. We have also used a spin diffusion model and simulations to support our experiments and estimate the system parameters.

We have found that IEC between Co layers is ferromagnetic. We have also found that the Pt thickness influences the anisotropy and saturation magnetization of the Co layers and their interface transparency and mixing conductance. These parameters affect the spin transport effects, such as SMR and AMR and the SOT fields of the Co layers. We have determined the effective SHA as a function of Pt thickness and found a maximum value of about 14% for $t_{\mathrm{Pt}} = 3.24$ nm.

We studied the magnetization dynamics of the Co/Pt/Co trilayer by measuring the dispersion relations of the resonance modes as a function of the magnetic field. We have used these results to estimate the IEC by fitting an LLGS macrospin model. We also observed a fine-grained domain structure in strongly coupled devices using p-MOKE microscopy.

We have shown a four-state current-induced magnetization switching in devices with strong ferromagnetic IEC and asymmetric interfaces. We have explained this phenomenon by a phenomenological model that considers the different effective fields on each Co layer because of their different anisotropies and interface properties. We have analyzed the critical switching current densities as a function of the magnetic field and Pt thickness.

4.3 | Heavy metal/ferromagnet/antiferromagnet (HM/FM/AFM) system

The last type of thin-film hybrid system described in this dissertation is HM/FM/AFM system, where the NiO layer is an insulating AFM. This made it possible to achieve field-free magnetization switching by inducing an in-plane exchange bias field. This chapter is mainly based on the publication [P5], which reports the study of CIMS in W(Pt)/Co/NiO systems with variable-thickness W and Pt layers, Co perpendicularly magnetized and an antiferromagnetic NiO layer. The influence of the antiferromagnetic layer on the dependence of SMR as a function of the thickness of Pt was analyzed. The layer system is schematically depicted in Fig.4.8.

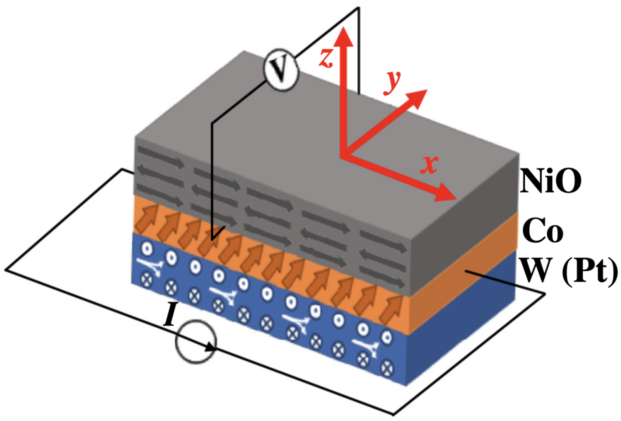

Figure 4.8: Schematic sketch of the HM/FM/AFM system. Orange arrows represent the perpendicularly magnetized Co layer, while the out-of-plane white vectors on W(Pt)/Co interfaces show the accumulated spins due to the SHE.

4.3.1 | Spin Hall Magnetoresistance

The goal of the SMR investigation in a AFM hybrid structure was to examine the effect of spin ordering in the NiO layer on the spin current generated in Pt after passing through a thin Co layer. For this purpose, the dependence of the relative SMR as a function of Pt thickness was measured. The maximum value of |SMR| of approximately 0.42% is comparable to the |SMR|$\approx$ 0.33%. obtained for the Pt(t_{Pt})/Co(0.6)/MgO bilayer [166].

By comparing the thickness of the Pt layer for which the maximum SMR occurs, we

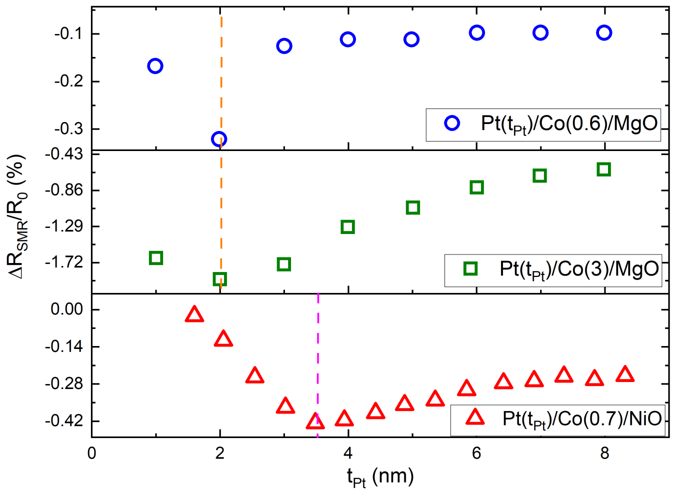

Figure 4.9: Dependence of SMR as a function of the Pt thickness for Pt(t_{Pt})/Co(0.6)/MgO [166] (blue points), Pt(t_{Pt})/Co(3)/MgO [166] (green points) and Pt(t_{Pt})/Co(0.7)/NiO (red points).

can see that in systems without AFM layers, it occurs $t_{\mathrm{Pt}} \approx 2$ nm while in the Pt/Co/NiO system for $t_{\mathrm{Pt}} \approx 3.5$ nm (Fig.4.9). Note that in a Pt/Co bilayer system, the minimum position practically does not depend on the thickness of Co, as shown in [166]. This can be explained by replacing a nonmagnetic MgO layer with an antiferromagnetic NiO layer. This causes an increase in spin current absorption at the FM/AFM interface, with the result that a reduced part of the current is reflected due to the inverse SHE. To analyze the dependence of SMR on t_{Pt}, the theoretical SMR model from Karwacki, Grochot, et al. [P1] paper was developed. The model extension relies on the introduction of an additional layer and, thus, reformulation of boundary conditions at this new FM/AFM interfaces:

$$\mathbf{J}_{\mathrm{s},z}^{\mathrm{FM}}(t_{\mathrm{FM}}) = \mathbf{m} \cdot \mathbf{J}_{\mathrm{s}}^{\mathrm{FM/AFM}}(t_{\mathrm{FM}}) \tag{4.2}$$

where $\mathbf{J}_{\mathrm{s}}^{\mathrm{FM/AFM}} = G_{\perp}^{\mathrm{AFM}} \mu_{\mathrm{s}}^{\mathrm{FM}}(t_{\mathrm{FM}})(\mathbf{n} \times \mathbf{n} \times \mathbf{m})$, $\mu_{\mathrm{s}}^{\mathrm{FM}}$ is the spin accumulation, $\mathbf{n}$ is Néel vector of AFM layer and $\mathbf{m}$ is magnetization of FM.

The spin current was also assumed to be completely absorbed in the HM/FM interface and does not flow into the AFM layer. Parameters used to fit the model to experimental points: t_{Co} = 0.7 nm, ρ_{Pt} = 30 $\mu\Omega$cm, ρ_{Co} = 28 $\mu\Omega$cm, λ_{Co} = 7 nm, θ_{SH} = 13% $G_{\uparrow}$ = $G_{\downarrow}$ = 10^{15}, G_r = $+\infty$ and G_i = 0, θ_{AMR} = 0 and mean free path of spin in HM λ_{Pt}, whose value was fixed at 1.7 nm, as optimal due to the position of the minimum |SMR|.

The model was fitted to the experimental points for the Néel vector ($\mathbf{n}$) components: n_{y} = (0,1,0) (blue line), n_{x} = (1,0,0) (red line) and for the variable direction vector $\mathbf{n}$ (black line). It was assumed that for the variable direction vector $\mathbf{n}$, its components in the x-y plane as a function of Pt thickness varied with Pt thickness. For thin Pt, it is oriented in the y direction, while for thicker Pt, it is oriented in the x direction (Fig.4.10(a)).

As shown in Fig.4.10(b), the three assumptions for small Pt thicknesses are almost identical. However, the fit is at an acceptable level for $t_{Pt} > 4$ nm only in the case of a variable **n** direction. The theoretical line deviates significantly from the measurement points in the remaining cases. The change in $H^{(x)}_{\text{exb}}$ and $H^{(z)}_{\text{exb}}$ (shown in Fig.3 in [P5] and Fig.S7(b) in Supplementary Materials to [P5]) may suggest that the assumption of a change in the direction of the vector **n** is correct. However, introducing a different orientation of the Néel vector was aimed at checking which parameter improves the model fit. The dependence of the **n**-vector components on t_{Pt} and an attempt to relate it to the ExB field require further analysis.

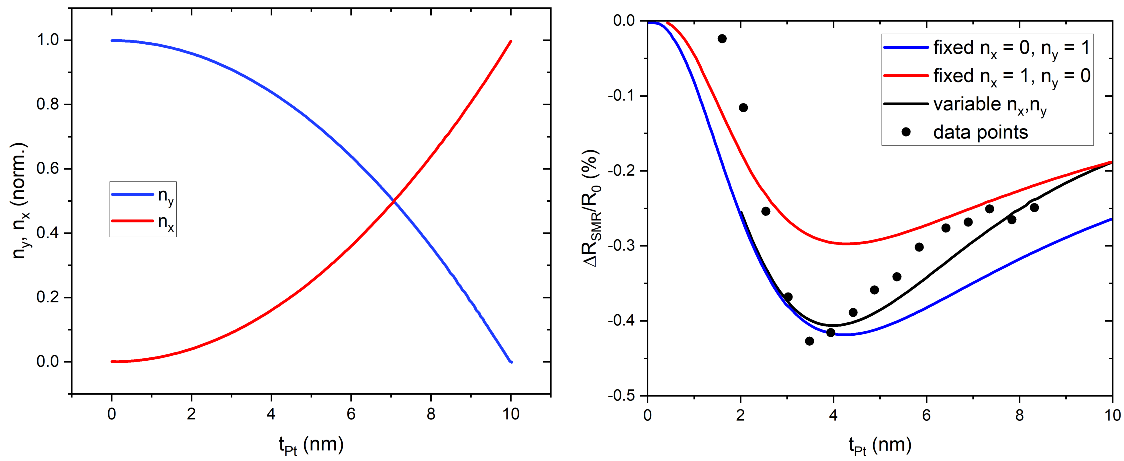

(a) (b)

Figure 4.10: The n_{x} and n_{y} components of the Néel vector as a function of Pt thickness (a) used to fit the theoretical model to the experimental points of $\Delta R_{\text{SMR}}/R_0$ (b).

4.3.2 | Field-free CIMS

In this subsection, we demonstrate that in both the Pt/Co/NiO and the W/Co/NiO systems deterministic Co magnetization switching without an external magnetic field is replaced by $H^{(x)}_{\text{exb}}$. However, we demonstrated the simultaneous occurrence of $H^{(x)}_{\text{exb}}$ and $H^{(z)}_{\text{exb}}$ components of the exchange bias field. As our XAS studies (for details, see Chapter 2 in Supplementary Materials to [P5]) have shown, the single Co monolayer is oxidized to stoichiometric CoO (see Fig.S3 in the Supplementary Materials to [P5]) and is in a paramagnetic state (see Fig.S5 in the Supplementary Materials to [P5]) which can increase the effect of exchange bias [167]. For this reason, it can be assumed that the ExB originates from the antiferromagnetic CoO/NiO bilayer.

Firstly, $H_{\mathrm{exb}}^{(z)}$ was determined from the AHE loop (Fig.S6 in Supplementary Materials to [P5]). The maximum value for both systems occurs for $t_{\mathrm{Pt(W)}} \approx 5$ nm and then decreases for larger thicknesses. However, in the W system, $H_{\mathrm{exb}}^{(z)}$ is about two times smaller than in the Pt-based system. Details can be found in Fig.S7 in the Supplementary Materials to [P5].

To determine the in-plane $H_{\mathrm{exb}}^{(x)}$ component, CIMS loops were measured for a series of magnetic field values applied in-plane in the x direction (H_{x}), as described in Sect.3.6.3. An example set of loops are presented in Fig.2(a,b) in [P5] for Pt-based and W-based systems, respectively. As you can see, the amplitude of the loops (ΔR) varies with the value of the external field, and the loops completely disappear for a specific (H_{x}). By analyzing the ratio of $\Delta R/\Delta R_{\mathrm{AHE}}$ (where ΔR_{AHE} is the amplitude of AHE loop) as a function of the H_{x}, we obtained linear dependencies for both systems as presented in Fig.2(c-d) in [P5] and in Fig.S10 in Supplementary Materials to [P5]. Based on this, we showed that $\Delta R/\Delta R_{\mathrm{AHE}}$ is about twice as high in W-based devices than in Pt-based devices due to a higher effective SHA in W than in Pt. The field H_{x}, for which the fitted line takes the value of $\Delta R/\Delta R_{\mathrm{AHE}} = 0$, is the equivalent of $H_{\mathrm{exb}}^{(x)}$, which is of equal magnitude but with the opposite sign [119]. The resulting values as a function of $t_{\mathrm{Pt(W)}}$ are shown in Fig.3 in [P5] and Fig.S10 in the Supplementary Materials to [P5]. The maximum of $H_{\mathrm{exb}}^{(x)}$ = 392 Oe in the Pt-based system is found for $t_{\mathrm{Pt}} = 4.9$ nm (Fig.S10(a) in Supplementary Materials in [P5]). When for the W-based system, which was annealed in the presence of an external magnetic applied perpendicular to the sample plane, obtained $H_{\mathrm{exb}}^{(x)}$= -148 Oe (see Fig.S10(b) in Supplementary Materials to [P5] and Fig.4(g) in [P5]) and reaching field-free magnetization switching.

A description of the critical current was available with an extended SOT threshold current model from the Lee et al. paper [93] by a term related to the $H_{\mathrm{exb}}^{(x)}$. Starting from the LLGS equation and assuming a strong magnetic field applied in the x-direction, an ideal HM/FM interface ($G_{\mathrm{r}} \rightarrow \infty$), and $t_{\mathrm{HM}} >> \lambda_{\mathrm{HM}}$, a simple formula for the critical switching current (Eq.4.3) was obtained.

$$j_{\mathrm{c}}^{\mathrm{sw}} \approx \frac{2e\mu_0 M_{\mathrm{s}} t_{\mathrm{FM}}}{\hbar\theta_{\mathrm{SH}}} \left(\frac{H_{\mathrm{K,eff}}}{2} - \frac{H_{\mathrm{x}} - H_{\mathrm{exb}}^{(x)}}{\sqrt{2}} \right) \tag{4.3}$$

A more detailed description of the derivation and assumptions can be found in the paper [P5]. $j_{\mathrm{c}}^{\mathrm{sw}}$ was determined from the CIMS loops measurements for H_{x} field in both systems to analyze the critical switching current. As a result, linear dependencies $j_{\mathrm{c}}^{\mathrm{sw}}(H_{\mathrm{x}})$ were obtained, to which the model was fitted with Eq. 4.3 (see Fig.6 in [P5]). A

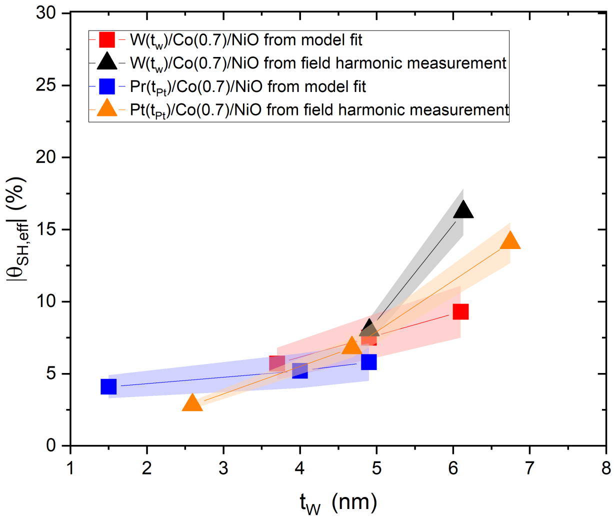

Figure 4.11: Spin Hall angle as a function of HM obtained by the field harmonics method and from the critical switching current model for as-deposited W(t_W)/Co(0.7)/NiO and Pt(t_{Pt})/Co(0.7)/NiO systems.

deviation from the linear dependence of the experimental points in both systems was observed; however, in the case of W, it occurs in smaller H_x due to the smaller value of $H_{K,eff}$.

The effective SHA ($\theta_{SH,eff}$) was determined based on fitting the theoretical model of the current switching current to the experimental data. The resulting values were collected in Tab.1 in [P5]. The effective SHA in all as-deposited systems is consistent with data from the literature [168, 169]. Moreover, the values for the as-deposited Pt(W)/Co/NiO system follow the dependence derived by the field harmonics method quite well and are shown in Fig.4.11. The effective SHA of the as-deposited system based on W is slightly higher than that found for the system with Pt, which, combined with the much lower value of $H_{K,eff}$, results in a lower j_c^{sw} by about one order of magnitude. The annealed W/Co/NiO system is characterized by a high effective SHA that reaches $\theta_{SH,eff}$ = -44% [170, 171] and a double of $H_{K,eff}$. This result was confirmed in another annealed sample from the same series (see Fig.S9 in the Supplemental Materials to the paper [P5]). We attribute such a high value of effective SHA after annealing due to the high resistive phase β-W [172] and the presence of interstitial zero dopants, which stabilize grains β -W [173]. In addition, we studied the effect of training to investigate the thermal stability of the investigated devices. Both systems showed a decrease in j_c^{sw} and ΔR with an increase in the number of switches (Fig.7 in [P5]) due to an increase in the temperature of the system associated with Joule heat and switching durability. We also showed that during long-term current switching with high current density in the presence of an H_x, the $H_\mathrm{exb}^{(\mathrm{x})}$ could increase (Fig.8 in [P5]) and the $H_\mathrm{exb}^{(\mathrm{z})}$ decreases (Fig.9 in [P5]) due to significant Joule heat which can exceed the Néel temperature.

Current-Induced Magnetization Switching of Exchange-Biased NiO Heterostructures Characterized by Spin-Orbit Torque

Krzysztof Grochot,[1,2,*] Łukasz Karwacki,[3,†] Stanisław Łazarski,[1] Witold Skowroński,[1] Jarosław Kanak,[1] Wiesław Powroźnik,[1] Piotr Kuświk,[3] Mateusz Kowacz,[3] Feliks Stobiecki,[3] and Tomasz Stobiecki[1,2]

[1] *Department of Electronics, AGH University of Science and Technology, Al. Mickiewicza 30, 30-059 Kraków, Poland*
[2] *Faculty of Physics and Applied Computer Science, AGH University of Science and Technology, Al. Mickiewicza 30, 30-059 Kraków, Poland*
[3] *Institute of Molecular Physics, Polish Academy of Sciences, ul. Smoluchowskiego 17, 60-179 Poznań, Poland*

(Received 7 July 2020; revised 23 November 2020; accepted 8 December 2020; published 11 January 2021)

In this work, we study magnetization switching induced by spin-orbit torque in W (Pt)/Co/NiO heterostructures with variable thickness of W and Pt heavy-metal layers, a perpendicularly magnetized Co layer, and an antiferromagnetic NiO layer. Using current-driven switching and magnetoresistance and anomalous-Hall-effect measurements, we determine the perpendicular and in-plane exchange-bias field. Several Hall-bar devices possessing in-plane exchange bias from both systems are selected and analyzed in relation to our analytical switching model of the critical current density as a function of Pt and W thickness, resulting in estimation of the effective spin Hall angle and perpendicular effective magnetic anisotropy. We demonstrate in both the Pt/Co/NiO system and the W/Co/NiO system deterministic Co magnetization switching without an external magnetic field, which is replaced by an in-plane exchange-bias field. Moreover, we show that due to a higher effective spin Hall angle in the W-based system than in the Pt-based system, the relative difference between the resistance states in the magnetization current switching to the difference between the resistance states in magnetic field switching determined by the anomalous Hall effect ($\Delta R/\Delta R_{\mathrm{AHE}}$) is about twice as high in W-based devices than in Pt-based devices, while the critical switching-current density in W-based devices is 1 order lower than in Pt-based devices. The current-switching stability and the training process are discussed in detail.

DOI: 10.1103/PhysRevApplied.15.014017

I. INTRODUCTION

Spin-orbit-torque (SOT) random-access memories (RAMs) are anticipated as a next generation of low-power, high-endurance, nonvolatile, and energy-efficient magnetic RAMs, which fit into the modern trend of green information technology [1,2]. Spintronic data-storage devices, in contrast to their conventional semiconductor counterparts, need not be continuously refreshed, leading to the reduction of heat dissipation and lower energy consumption [3]. Recently, SOT-based technologies have evolved as one of the most promising, because they require neither high current densities nor high voltages applied to the thin tunnel barriers [4,5], and enable magnetization switching below 1 ns [6]. Such memory cells constitute an efficient alternative to spin-transfer-torque magnetoresistive RAM.

Significant progress has been achieved in understanding and utilizing the spin Hall effect [7–9] in heavy metals (HMs) or topological insulators [10] to control magnetic states of ferromagnets (FMs) and antiferromagnets (AFMs) [11]. The mechanism relies on SOT-induced switching due to accumulated spin density noncollinear with magnetization. However, the torque itself cannot switch the magnetization between two stable states without the up-down degeneracy along the charge-current flow direction being broken. It can be achieved by applying an external magnetic field collinear with the current (but noncollinear with the magnetization), which, however, is impractical in device applications and technologically unattractive. Several approaches have been proposed to replace the external magnetic field and achieve field-free switching: for example, magnetization switching controlled by the electric field in a hybrid ferromagnetic/ferroelectric structure [12], two coupled FM layers exhibiting magnetization easy axes orthogonal to each other [13–19], or introducing a lateral symmetry breaking

*grochot@agh.edu.pl
†karwacki@ifmpan.poznan.pl

by asymmetric layers [20–24]. However, one of the most-promising solutions is still the well-known exchange bias induced by interfacial exchange coupling a ferromagnet with an antiferromagnetic layer [25–28]. The use of a metallic antiferromagnet for this purpose has already been described in the literature [13,29], and it was shown to support both the spin Hall effect and exchange bias in a single layer. This setup, however, makes further optimization of SOT-induced switching of a ferromagnet difficult as the electron spin density generated in an AFM acts not only on the ferromagnet but also on the Néel order as well [30]. To distinguish between torques acting on ferromagnetic layers from the spin-orbit–induced effect and the exchange-bias effect, one can use a HM/FM coupled with an antiferromagnetic insulator such as NiO. It not only induces exchange bias [31–33] but also can enhance the perpendicular magnetic anisotropy (PMA) of the ferromagnetic layer [34] and allow one to achieve a lower critical switching current than in the case of metallic AFMs.

Use of HM/FM/NiO heterostructures as one of the elements in magnetoresistive RAMs is possible, as a recent study on NiO/MgO tunnel junctions has shown that there is a sizable tunneling magnetoresistance (TMR) [35], although its appearance is more complex than with use of a MgO barrier alone—the insertion of NiO leads to the appearance of a strong asymmetry in TMR and in particular to negative TMR [35]. It has also been shown that NiO alone can support large TMR in various magnetic tunnel junctions [36,37]. Moreover, there is a possibility for a novel type of memory cells, as it has been shown that NiO can mediate antidamping spin-transfer torque between metallic layers [38].

Motivated by the above-mentioned considerations, we present here a study of magnetization switching induced by spin-orbit torque in W (Pt)/Co/NiO heterostructures with variable thickness of the W and Pt layers, a perpendicularly magnetized Co layer, and an antiferromagnetic NiO layer. Using magnetoresistance measurements and current-driven magnetization switching, we demonstrate the simultaneous occurrence of in-plane ($H_{\mathrm{exb}}^{(x)}$) and perpendicular ($H_{\mathrm{exb}}^{(z)}$) components of the exchange-bias field. We show Co magnetization switching without an external magnetic field, which is replaced by an in-plane exchange-bias field, and for this case we develop an analytical magnetization-switching model of the critical current density. Finally, we discuss the current-switching stability and training process conducted on Hall-bar devices of Pt/Co/NiO and W/Co/NiO.

The remainder of this paper is organized as follows: Sec. II provides details of sample fabrication, and explains the experimental techniques used to characterize the samples, Sec. III describes the theoretical model for spin Hall threshold currents adopted for exchange-biased samples; Sec. IV contains the results and their discussion; and Sec. VI concludes and summarizes the paper.

II. EXPERIMENT

Two HM/FM/AFM multilayer systems consisting of two different heavy metals, W and Pt, are deposited. As shown schematically in Fig. 1(a) the bottom-up heterostructure is sequenced as Si/SiO_2/W(Pt)/Co/NiO. The heavy-metal layer is deposited in wedge-shaped form with thickness ranging from 0 to 10 nm along the 20-mm-long sample edge (x coordinate). The resulting thickness gradient is achieved by controlled movement of a shutter. The thicknesses of the two other layers, namely, Co and NiO, are 0.7 and 7 nm, respectively. We also deposit the Pt(4 nm)/Co(1 nm)/MgO system as a reference sample for further analysis. All metallic layers are deposited by magnetron sputtering at room temperature.

In the case of W sputtering, low dc power of 4 W and a 6-cm target-sample distance are used, which results in a deposition rate of 0.01 nm/s. Such conditions are essential for the growth of the W layer in the cubic β phase. Pt and Co are deposited with dc power of 8 and 15 W, respectively.

The stoichiometric NiO layer deposited on the top of Co layer is prepared from a NiO target by a pulsed-laser-deposition technique. The process is performed in a controlled oxygen atmosphere under O_2 partial pressure 1.5×10^{-5} mbar in a separate UHV chamber and samples are transferred between chambers without our breaking the UHV conditions. To induce exchange-bias coupling, a perpendicular magnetic field of 1.1 kOe is applied during deposition of the whole multilayer. Systematic studies of the perpendicular exchange-bias effect in the Au/Co/NiO/Au system by magneto-optical Kerr rotation, published in Ref. [34], have shown that the Co underlayer is oxidized due to deposition of NiO in an oxygen-rich atmosphere. Our x-ray-absorption-spectroscopy (XAS) studies at room temperature also confirm the surface oxidation of the Co layer to stoichiometric CoO [39,40] and prove that it is in a paramagnetic state (for details, see

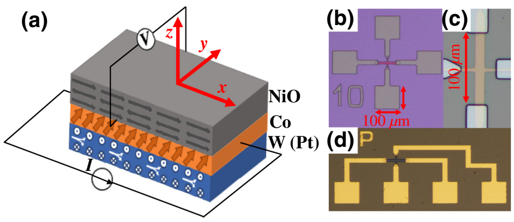

FIG. 1. (a) Our multilayer system. The orange arrows indicate the perpendicularly magnetized Co layer. The out-of-plane vectors on W (Pt)/Co interfaces show the accumulated spin as a result of the spin Hall effect. Optical microscopic images of the patterned Hall-bar device: (b) Hall-bar for magnetoresistance measurements, (c) detailed dimensions of the Hall bar, (d) Hall bar for SOT-induced magnetization-switching measurements.

Supplemental Material [41]). As shown in previous experimental work, exchange bias can not only be preserved but can also be enhanced by an insulating paramagnetic spacer [42,43]. On the other hand, XAS studies of the ordering of interfacial spins for antiferromagnetic bilayer Co/NiO show that an adjacent NiO layer can increase the CoO layer's Néel temperature (T_N) due to the strong exchange interaction at the CoO/NiO interface [44,45]. For this reason, it cannot be definitely ruled out that the exchange bias on the Co layer may come from the antiferromagnetic CoO/NiO bilayer. Moreover, in both cases, the oxidation process effectively reduces the ferromagnetic thickness of Co, which leads to an increase in the surface anisotropy, revealing strong PMA of Co. Nevertheless, this issue requires further investigations, which is beyond the scope of this paper.

The thicknesses of all layers are determined from the deposition growth rate of particular materials calibrated by x-ray-reflectivity measurements. Next, all as-deposited samples are characterized before patterning by x-ray diffraction ($\theta - 2\theta$) and grazing-incidence x-ray diffraction (for details, see Supplemental Material [41]). All systems are also examined with a polar Kerr magnetometer to determine the range of HM thicknesses for which PMA occurs. Square hysteresis loops are observed, which indicate the presence of PMA in both systems for Pt-layer thickness t_{Pt} between 1 and 9 nm and for W-layer thickness t_{W} between 3.5 and 8 nm, which is confirmed by anomalous-Hall-effect (AHE) measurements (see Supplemental Material [41]).

After basic characterization of continuous samples, both heterostructures are patterned by optical direct-imaging lithography and ion etching to create a matrix of Hall-bar devices with different t_{HM} for subsequent electrical measurements [Figs. 1(b)–1(d)]. The sizes of the prepared structures are 100×10 μm^2 for magnetoresistance and AHE measurements and 30×30 μm^2 for current-induced-magnetization-switching experiments. Al(20 nm)/Au(30 nm) electrical leads of 100×100 μm^2 are deposited in a second lithography step followed by the lift-off process. Specific locations of pads near the Hall-bars are designed for measurement in a custom-made rotating probe station allowing two-point or four-point measurement of electrical transport properties in the presence of the magnetic field applied at arbitrary azimuthal and polar angles with respect to the Hall-bar axis.

The resistance of each Hall bar is measured by a four-point method [46] and the resistivities of the Pt and W layers are determined with a parallel-resistor model and the method described by Kawaguchi *et al.* [47]. Analysis of the Pt and W resistivities yielded 30 $\mu\Omega\,\text{cm}$ [14,47–49] and 170 $\mu\Omega\,\text{cm}$ [49–52], respectively. The Co resistivity is 28 $\mu\Omega\,\text{cm}$ when Co is deposited on Pt [14] and 58 $\mu\Omega\,\text{cm}$ when Co is deposited on W. The details of the resistivity measurements are presented in Supplemental Material [41].

III. CRITICAL-CURRENT MODEL

To determine the influence of exchange bias on the threshold current in our system, we follow the analysis for spin Hall threshold currents first derived by Lee *et al.* [53,54].

We start with the Landau-Lifshitz-Gilbert equation for macrospin magnetization: $\hat{\mathbf{m}} = (m_x, m_y, m_z) = (\cos\phi \sin\theta, \sin\phi \sin\theta, \cos\theta)$,

$$\frac{d\hat{\mathbf{m}}}{dt} - \alpha\hat{\mathbf{m}} \times \frac{d\hat{\mathbf{m}}}{dt} = \mathbf{\Gamma}, \tag{1}$$

where α is the Gilbert damping constant.

The general torque exerted on magnetization assumes the following form:

$$\mathbf{\Gamma} = -\gamma_0 \hat{\mathbf{m}} \times \mathbf{H}_{\text{eff}} - \gamma_0 H_{\text{DL}} \hat{\mathbf{m}} \times \hat{\mathbf{m}} \times \hat{\mathbf{y}}, \tag{2}$$

where γ_0 is the gyromagnetic constant, and the first term comes from the effective field, $\boldsymbol{H}_{\text{eff}} = -\nabla_{\boldsymbol{m}} u$, where free energy of the FM has the form

$$u = -\frac{1}{2} H_{K,\text{eff}} m_z^2 - \frac{1}{2} H_A m_y^2 - m_x H_x - m_x H_{\text{exb}}^{(x)}, \tag{3}$$

where $H_{K,\text{eff}}$ is the field of the effective perpendicular magnetic anisotropy, H_A is field of the effective in-plane anisotropy, H_x is the magnetic field along the x direction, and $H_{\text{exb}}^{(x)}$ is the in-plane exchange bias.

The second torque term in Eq. (2) comes from the dampinglike field,

$$H_{\text{DL}} = \frac{\hbar}{2e\mu_0 M_s t_{\text{FM}}} \theta_{\text{SH}} j_{\text{HM}} \left(1 - \operatorname{sech} \frac{t_{\text{HM}}}{\lambda_{\text{HM}}}\right) \frac{g_r}{1 + g_r}, \tag{4}$$

where $\hbar$ is the reduced Planck's constant, e is the elementary charge, $\mu_0 M_s$ is saturation magnetization, t_{FM} is the thickness of ferromagnetic layer, θ_{SH} is the spin Hall angle, j_{HM} is the current density flowing through HM, and $g_r = 2\lambda_{\text{HM}} \rho_{\text{HM}} G_r \coth(t_{\text{HM}}/\lambda_{\text{HM}})$ is the unitless real part of the spin-mixing conductivity, G_r, where λ_{HM}, ρ_{HM}, and t_{HM} are the HM's spin diffusion length, resistivity, and thickness, respectively. The dampinglike field is induced by $\hat{\mathbf{y}}$-polarized spin accumulation due to the spin Hall effect in the HM.

The stationary solution of the Landau-Lifshitz-Gilbert equation (1) leads to the torque equilibrium condition, $\mathbf{\Gamma} = 0$. For a strong magnetic field applied along the x direction, we assume $\phi \approx 0$, which leads to the following condition for the dampinglike field:

$$H_{\mathrm{DL}} = \cos\theta \left(H_{\mathrm{exb}}^{(x)} - H_{K,\mathrm{eff}} \sin\theta + H_x\right). \tag{5}$$

By analyzing the stability of the above equation, we obtain a simplified relation for the critical dampinglike field:

$$H_{\mathrm{DL}}^{\mathrm{sw}} \approx \frac{H_{K,\mathrm{eff}}}{2} - \frac{H_x - H_{\mathrm{exb}}^{(x)}}{\sqrt{2}}. \tag{6}$$

Inserting into the above equation the explicit formula for the dampinglike field, Eq. (4), we obtain the following expression for the critical current density:

$$j_c^{\mathrm{sw}} \approx \frac{2e\mu_0 M_s t_{\mathrm{FM}}\,(1+g_r)}{\hbar\theta_{\mathrm{SH}} g_r \left(1 - \mathrm{sech}\,\frac{t_{\mathrm{HM}}}{\lambda_{\mathrm{HM}}}\right)} \left(\frac{H_{K,\mathrm{eff}}}{2} - \frac{H_x - H_{\mathrm{exb}}^{(x)}}{\sqrt{2}}\right). \tag{7}$$

Assuming a perfect HM/FM interface (i.e., $G_r \to \infty$) and assuming $t_{\mathrm{HM}} \gg \lambda_{\mathrm{HM}}$ leads to the simplified expression

$$j_c^{\mathrm{sw}} \approx \frac{2e\mu_0 M_s t_{\mathrm{FM}}}{\hbar\theta_{\mathrm{SH}}} \left(\frac{H_{K,\mathrm{eff}}}{2} - \frac{H_x - H_{\mathrm{exb}}^{(x)}}{\sqrt{2}}\right), \tag{8}$$

which is used later to fit the experimental data. Our model does not take into account the switching mechanism due to creation and motion of domain walls, which has been observed in the Pt/Co system [55] and results in a smaller switching-current density than that estimated by the model above. Our estimate can, however, be treated as the upper limit.

IV. RESULTS AND DISCUSSION

A. SOT-induced current switching

The anomalous Hall effect is used to determine the current-driven magnetization switching between high-stable-resistance and low-stable-resistance states. The measurement setup is shown in Fig. 1(a). Initially, the sample is magnetized by an external magnetic field applied along the z direction to the state corresponding to low resistance of the AHE loop.

Then, a sequence of current pulses with 10-ms duration and 20-ms intervals in the x direction is applied to drive the magnetization switching. The current is swept from negative to positive and back to negative and simultaneously the transverse voltage is measured in the presence of an in-plane magnetic field, collinear with the current direction (H_x). The value of H_x is changed sequentially after each switching loop.

As a result, we obtain the current-switching loops for Pt-based and W-based Hall-bar devices [Figs. 2(a) and 2(b)].

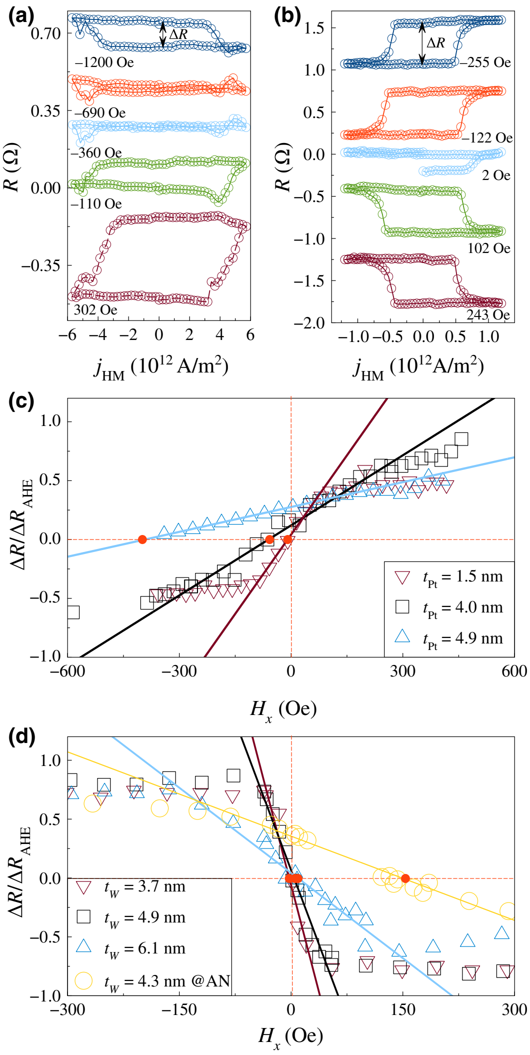

FIG. 2. Examples of the current-switching loops for different values of the external magnetic field H_x in the Pt(4.9 nm)/Co/NiO system (a) and the W(4.9 nm)/Co/NiO system (b). The ratio $\Delta R/R_{\mathrm{AHE}}$ is depicted in (c),(d); the intersection is marked by a red dot. $H_{\mathrm{exb}}^{(x)}$ in the Pt-based system is 5 Oe for $t_{\mathrm{Pt}} = 1.5$ nm, 60 Oe for $t_{\mathrm{Pt}} = 4.0$ nm, and 392 Oe for $t_{\mathrm{Pt}} = 4.9$ nm. For all analyzed W elements, the values are approximately 0 Oe in the measurement error limit and −148 Oe for the annealed sample (@AN).

Opposite loop polarities result in Pt having a positive spin Hall angle and W having a negative one.

By analyzing the difference between high and low AHE resistance from the AHE loop for different thicknesses of Pt-based and W-based devices, we determine ΔR_{AHE}. Next, the current-switching loop opening ΔR is measured, for each value of the applied magnetic field H_x, which shows a closing loop with decreasing H_x [Figs. 2(a) and 2(b)]. The $\Delta R/\Delta R_{\mathrm{AHE}}$ ratio as a function of H_x, which is a measure of the effectiveness of current-induced magnetization switching for Pt-based and W-based devices, is shown in Figs. 2(c) and 2(d). The dependence obtained is approximately linear for small positive and negative H_x. As can be seen, ΔR does not reach ΔR_{AHE}, even when a large magnetic field is applied (see also Fig. S10 in Supplemental Material [41]).

The intersection of the linear function with zero $\Delta R/\Delta R_{\mathrm{AHE}}$, corresponding to the magnetic field for which the loop is closed, can be identified as the value of H_x that compensates the in-plane component of the exchange-bias field ($H_{\mathrm{exb}}^{(x)}$) and allows us to indirectly determine the value of $H_{\mathrm{exb}}^{(x)}$, because the aforementioned in-plane compensation field has the same value, but the opposite sign.

The intersection points for the Pt-based system depend on the Pt-layer thickness, reaching maximal compensation-field magnitude for $t_{\mathrm{Pt}} = 4.9$ nm, while in the W-based structure, intersection occurs roughly at zero H_x field in a wide range of W-layer thicknesses, as shown in Fig. 3. In high H_x fields, ΔR saturates, for W-based devices reaching about $0.8\Delta R_{\mathrm{AHE}}$ [Fig. 2(d)], while for Pt-based devices it changes with increasing Pt thickness from about $0.5\Delta R_{\mathrm{AHE}}$ to $0.28\Delta R_{\mathrm{AHE}}$ [Fig. 2(c) and Fig. S10(a) in Supplemental Material [41]]. The perpendicular exchange-bias field ($H_{\mathrm{exb}}^{(z)}$), determined by AHE hysteresis, is highest for a HM thickness of about 5 nm in both systems, but $H_{\mathrm{exb}}^{(z)}$ in the W-based system is 2 times smaller than in the Pt-based system (see Fig. S7 in Supplemental Material [41]).

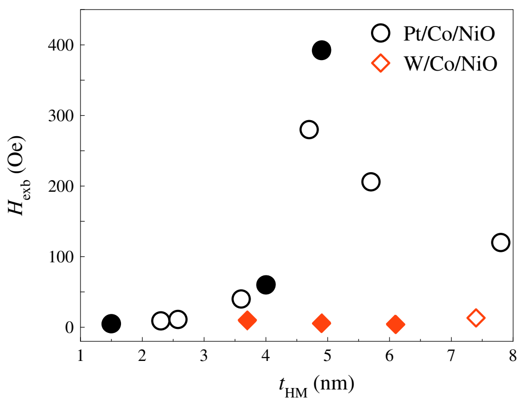

FIG. 3. $H_{\mathrm{exb}}^{(x)}$ obtained from ΔR zero shifts for the as-deposited W(Pt)/Co/NiO system. Filled points mark the elements for which the theoretical threshold-current model is fitted.

Because in the as-deposited W/Co/NiO heterostructure the magnitude of $H_{\mathrm{exb}}^{(x)}$ is negligible, field-free SOT-induced magnetization switching is not achieved. Therefore, to induce the in-plane component of exchange bias, the system is annealed at 100 °C (i.e., at a temperature slightly higher than the blocking temperature of 373 K but lower than T_N of 525 K) for 15 min and then cooled to room temperature in the presence of an external magnetic field of 4 kOe applied perpendicularly to the sample. Afterward, the remeasured AHE loop for the selected HM thickness indicates the presence of the PMA and $H_{\mathrm{exb}}^{(z)}$ in the Co layer, manifested by a rectangular-shape shift of −67 Oe [see Fig. S6(b) in Supplemental Material [41]]. In the next step, the current-switching experiments are repeated and results are analyzed as described above. Finally, $H_{\mathrm{exb}}^{(x)} = -148$ Oe is obtained from ΔR measurements [see Fig. S10(b) in Supplemental Material [41]]. For further analysis and fitting our threshold-current model in an exchange-biased system, three as-deposited Pt/Co/NiO Hall-bar devices with Pt thicknesses of 1.5, 4.0, and 4.9 nm are selected and denoted as A2, A3, and A4, respectively. We select also three as-deposited W/Co/NiO Hall-bar devices of with W thicknesses of 3.7, 4.9, and 6.1 nm which are denoted as B1, B2, and B3, respectively, and chose the annealed W(4.3 nm)/Co/NiO device (C1). We also fit our model to the reference sample (denoted A1), which is used to verify the model, as indicated earlier.

B. In-plane exchange bias

To confirm the above-discussed $H_{\mathrm{exb}}^{(x)}$, the resistance along the Hall bar (R_{xx}) is measured with the external magnetic field being swept along the x direction and is modeled with the equation

$$R_{xx} = R_0 + \Delta R_{\mathrm{AMR}} m_x^2, \tag{9}$$

where R_0 is the magnetization-independent resistance and ΔR_{AMR} denotes changes due to the anisotropic magnetoresistance effect. Considering the equilibrium condition of energy density [Eq. (3)] with respect to angle ϕ, the longitudinal resistance is reformulated to

$$R_{xx} \approx R_0 + \Delta R_{\mathrm{AMR}} \frac{(H_{\mathrm{exb}}^{(x)} + H_x)^2}{H_A^2}. \tag{10}$$

Measured R_{xx} for samples A2–A4, B1–B3, and C1 is shown in Fig. 4. A parabolic function is fitted to the data points, and minima of the functions are indicated with arrows. According to Eq. (10), the minima can be identified as the $H_{\mathrm{exb}}^{(x)}$ field, as discussed in the previous section. The resulting values for samples A2, A3 and A4 of about 6, 176, and 522 Oe [Figs. 4(d)–4(f)], respectively, are consistent with the ones obtained in the ΔR opening loop of the current-switching experiment described in Sec. IV A.

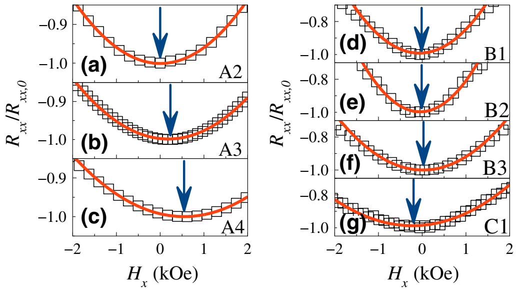

FIG. 4. $H_{\rm exb}^{(x)}$ obtained from $R_{xx}(H_x)$ measurements for as-deposited Pt-based systems (a)–(c) and W-based systems (d)–(f) and the annealed W/Co/NiO system (g). The blue arrows indicate the position of in-plane $H_{\rm exb}^{(x)}$. Experimental data are normalized to a minimum point. The red lines are fits according to Eq. (10).

As-deposited B-series Hall bars still exhibit negligible loop shifts [Figs. 4(d)–4(f)]. The only exception is the annealed C1 element, for which the value is −158 Oe [Fig. 4(g)]. $H_{\rm exb}^{(x)}$ values obtained from magnetoresistance measurements are in general less noisy and are used for further analysis.

C. Fitting procedure

For the analysis of the SOT-induced magnetization switching, we use AHE resistance hysteresis loops versus applied current densities in the HM layer ($j_{\rm HM}$) measured in a different external magnetic field H_x; examples are depicted in Fig. 5.

First, using a derivative of ($\partial V_{\rm AHE}/\partial j_{\rm HM}$), we calculate the threshold switching current ($j_c^{\rm sw}$) separately for each H_x. As a result, linear dependencies of $j_c^{\rm sw}$ versus H_x are obtained for selected Pt and W thicknesses. Nevertheless, a large number of free parameters in the model equation [Eq. (8)] may cause large uncertainties in the determined values. For this reason, the first part of Eq. (8) is replaced by a single parameter a, which is fixed and calculated as the linear slope coefficient determined by numerical differentiation of the $j_c^{\rm sw}$ dependence. Therefore, Eq. (8) can be rewritten as

$$j_c^{\rm sw} \approx a\left(\frac{H_{K,\rm eff}}{2} - \frac{H_x - H_{\rm exb}^{(x)}}{\sqrt{2}}\right), \tag{11}$$

where a is a fixed parameter obtained from differing $j_c^{\rm sw}$-dependence data points.

This ensures that the only free-fit parameter is $H_{K,\rm eff}$. As mentioned earlier, $H_{\rm exb}^{(x)}$ is a fixed parameter obtained from the magnetoresistance measurements.

Initially, the model is verified on the reference sample A1, which is characterized by zero $H_{\rm exb}^{(x)}$. In this particular case, both $H_{\rm exb}^{(x)}$ and $H_{K,\rm eff}$ are set as free parameters to check the validity of the parameters obtained from fitting. As expected, $H_{\rm exb}^{(x)} = 0$ Oe and $H_{K,\rm eff} = 2508$ Oe are obtained with a very good compliance level of $R^2 = 0.93$.

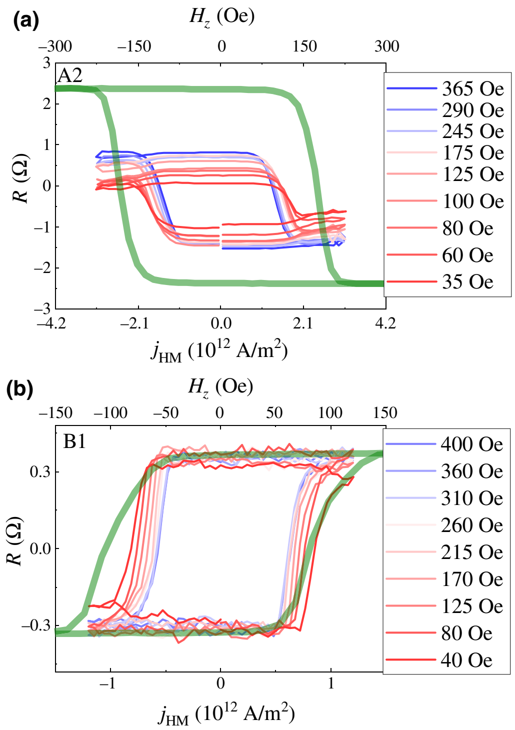

FIG. 5. Examples of a series of current-switching hysteresis loops for sequentially changed values of H_x in two selected elements, A2 (a) and B1 (b). Anomalous Hall resistances are represented by the green line.

Next, a simplified model equation [Eq. (11)] is fitted to all selected Pt/Co/NiO and W/Co/NiO samples. As indicated, $H_{\rm exb}^{(x)}$ is fixed and set in accordance with Table I. The fitting results are depicted in Fig. 6, where the solid lines correspond to the model equation for all devices investigated. As shown, the model exhibits good correlation with the data points. All of the R^2 coefficients are above 0.90, ensuring a low uncertainty level. For higher H_x, there are deviations from a linear dependence in both systems.

In case of W-based devices, the deviations appear at lower H_x field than in Pt-based devices. This can be explained by the lower $H_{K,\rm eff}$ (see Table I) for as-deposited W/Co/NiO systems than for as-deposited Pt/Co/NiO systems. Devices of the A series are characterized by increased $H_{K,\rm eff}$ and H_c with increasing Pt thickness [Figs. 6(b)–6(d)]. Additionally, annealing of the B-series

TABLE I. In-plane exchange-bias field ($H_{\text{exb}}^{(x)}$), effective anisotropy field ($H_{K,\text{eff}}$), spin Hall angle ($\theta_{\text{SH,eff}}$), and saturation magnetization ($\mu_0 M_s$) obtained as a result of magnetoresistance measurements and fitting the threshold-current model to the experimental data.

			Pt/Co/MgO		
Sample	t_{Pt} (nm)	$H_{\text{exb}}^{(x)}$ (Oe)	$H_{K,\text{eff}}$—fit (Oe)	$\theta_{\text{SH,eff}}$—fit (%)	$\mu_0 M_s$ (T)
A1	4.0	0	2508$\pm$ 80	13.5 $\pm$ 1	0.5
			Pt/Co/NiO		
Sample	t_{Pt} (nm)	$H_{\text{exb}}^{(x)}$ (Oe)	$H_{K,\text{eff}}$—fit (Oe)	$\theta_{\text{SH,eff}}$—fit (%)	$\mu_0 M_s$ (T)
A2	1.5	6 $\pm$ 1	2141 $\pm$ 10	4.1 $\pm$ 0.8	0.5
A3	4.0	176 $\pm$ 3	4130 $\pm$ 10	5.2 $\pm$ 1.2	0.5
A4	4.9	522 $\pm$ 14	4638 $\pm$ 10	5.8 $\pm$ 1.3	0.5
			W/Co/NiO		
Sample	t_{W} (nm)	$H_{\text{exb}}^{(x)}$ (Oe)	$H_{K,\text{eff}}$—fit (Oe)	$\theta_{\text{SH,eff}}$—fit (%)	$\mu_0 M_s$ (T)
B1	3.7	0	1132 $\pm$ 20	-5.7 ± 1.1	0.5
B2	4.9	30 $\pm$ 15	1031 $\pm$ 10	-7.5 ± 1.5	0.5
B3	6.1	7 $\pm$ 1	1035 $\pm$ 11	-9.3 ± 1.8	0.5
C1	4.3	-158 ± 29	2584 $\pm$ 2	-44.0 ± 5	0.5

devices results in doubling of the $H_{K,\text{eff}}$ value with increasing H_c.

Finally, we calculate the effective spin Hall angles ($\theta_{\text{SH,eff}}$) in the HM layer. For the calculations we use magnetization saturation ($\mu_0 M_s$) of 0.5 T in both systems, obtained from VSM measurements (see Fig. S11 in Supplemental Material [41]). We also assume an infinite value of mixing conduction (g_r), which is mostly valid for metallic interfaces [56].

The assumptions we make allow us to calculate the effective spin Hall angle from the following formula:

$$\theta_{\text{SH,eff}} = \frac{2e\mu_0 M_s t_F}{\hbar a}. \tag{12}$$

The values of $\theta_{\text{SH,eff}}$ obtained are listed in Table I and agree with the ones found in the literature [14,48,49,51,57–65]. $\theta_{\text{SH,eff}}$ values in as-deposited B-series devices are slightly higher than the values calculated for A-series devices, which combined with significantly lower $H_{K,\text{eff}}$ results in critical switching-current densities that are approximately approximately 1 order of magnitude smaller in this system. It is also worth noting that annealing of the W-based system, apart from inducing $H_{\text{exb}}^{(x)}$, also increases $\theta_{\text{SH,eff}}$ to -44% [51,62–64] and reduces j_c^{sw} by 1 order of magnitude [Fig. 6(h)]. To confirm the high value of $\theta_{\text{SH,eff}}$, a current-switching experiment is performed on another annealed sample from the same series. A similar $\theta_{\text{SH,eff}}$ value is obtained (see Fig. S9 in Supplemental Material [41]). We attribute a high value of the effective spin Hall angle of W similarly as in Refs. [49,51,63,64] to the highly resistive β-W phase. For example $\theta_{\text{SH,eff}}$ is approximately -30% at room temperature and more than -50% at 50 K in Ref. [62], while in Ref. [64] it is approximately -44%. Recently, McHugh *et al.* [65] showed, from first-principles calculations, that interstitial O and N dopants help to stabilize β-W grains during film deposition, and this process leads to high spin Hall angles.

D. Training effect

The training effect in both systems is also investigated for verification of the thermal stability of the heterostructures examined. To do this, pulses 10 times longer than those used in the experiments described in Sec. IV A are used. For this purpose, multiple current switching in a fixed external H_x field is performed by 100-ms current pulses with a 200-ms interval between them. The magnitude of the external H_x field is chosen to obtain magnetization switching. The series of current-switching loops depicted in Figs. 7(a) and 7(b) are obtained. Next, loop opening ΔR and critical current densities j_c^{sw} are determined as a function of loop numbers. The results are presented in Figs. 7(c) and 7(d).In both systems, j_c^{sw} and ΔR decrease with increasing number of magnetization switches, and their dependence on the number of loops is similar. During the first few switching events, a significant reduction in both ΔR and j_c^{sw} is observed. These phenomena can be explained by the progressively increasing temperature in both systems due to Joule heating [29] and the training effect [28,66,67], witnessed also during magnetic field switching [28,68,69]. It is worth mentioning that the Joule-heating effect leads to a reduction of the switching current and anisotropy. Saturation of the dependence is caused by achieving a balance between the generated heat and the emitted heat. This saturation occurs for smaller repetition number in the system with Pt (after about 20 switches) in contrast to the Pt-based system, in which it is not reached even after 35 switches.

Furthermore, for the Pt-based system we investigate how the number of switches affects $H_{\text{exb}}^{(x)}$. For this purpose, we measure the longitudinal magnetoresistance signal, R_{xx}, as in Sec. IV B, before the current-switching experiment, and we find that $H_{\text{exb}}^{(x)}$ is 302 Oe [Fig. 8(a)]. First, the current is switched several times in zero external magnetic field. It is found that $H_{\text{exb}}^{(x)}$ decreases to 0 Oe [Fig. 8(b)]. This proves that thermal energy generated during the pulses

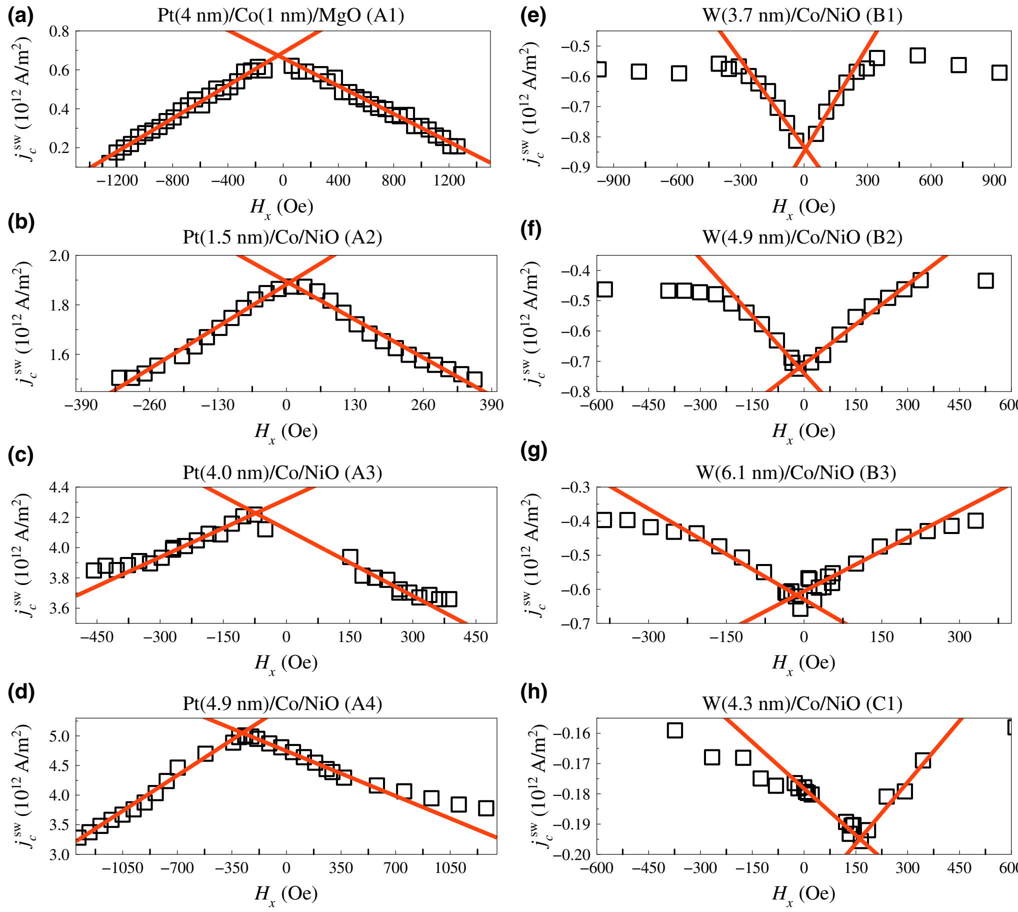

FIG. 6. Critical switching-current densities, j_c^{sw}, as a function of applied external magnetic field H_x for Pt/Co/NiO (a)–(d) and W/Co/NiO (e)–(h) differing by the HM layer thickness. (h) The annealed W-based system. The red line represents the model equation fitted to the data points. Parameters used for theoretical-model lines are given in Table I.

leads to degradation of the $H_{exb}^{(x)}$ component. The same $H_{exb}^{(x)}$-reduction effect on switching without an external magnetic field was noticed by Razavi *et al.* [29]. Then, by applying an in-plane H_x field of −200 Oe, we repeated the multiple switching events. It turns out that as the number of switching cycles increases, $H_{exb}^{(x)}$ rises to 430 Oe after 25 switching loops as depicted in Fig. 8(c). Finally, the AHE loop shapes and $H_{exb}^{(z)}$ in both systems are analyzed by our comparing the loops before and after the current-switching experiments. No significant degradation of PMA is found; however, $H_{exb}^{(z)}$ is reduced in both cases, as shown in Fig. 9, to 0 and −3 Oe, respectively for Pt-based and W-based devices. We conclude that during the switching events, significant Joule heating is generated, which may lead to the temperature increase above T_N. If an in-plane magnetic field is applied, an increase of in-plane exchange bias is accompanied by a decrease of the perpendicular exchange-bias component.

V. SUMMARY

In summary, the SOT-induced magnetization switching of W (Pt)/Co/NiO with a perpendicularly magnetized Co layer and various HM thicknesses is examined. Both the in-plane $H_{exb}^{(x)}$ and the perpendicular $H_{exb}^{(z)}$ exchange bias are determined by current-driven-switching, magnetoresistance, and AHE methods. We demonstrate in the

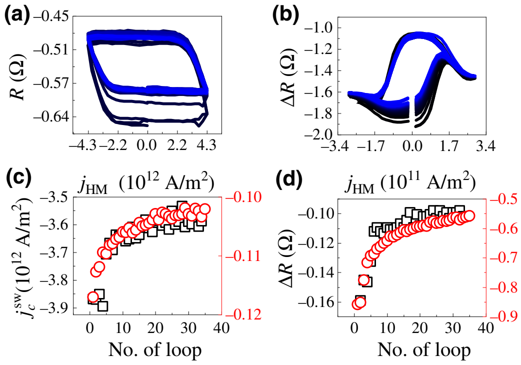

FIG. 7. A series of successive switching loops in a measurement sequence for Pt(5.1 nm)/Co(0.7 nm)/NiO(7 nm) (a) and the annealed W(4.3 nm)/Co(0.7 nm)/NiO(7 nm) device (b). The color of each subsequent loop in the sequence changes with increasing magnetic field from black to blue. Critical switching current, j_c^{sw}, versus number of repeated loops (c) and magnetoresistance, ΔR, (d) for Pt-based devices (black points) and W-based devices (red points).

Pt/Co/NiO and W/Co/NiO systems deterministic Co magnetization switching without an external magnetic field, which is replaced by an in-plane exchange-bias field. For several selected Hall-bar devices in both systems, threshold current densities are analyzed on the basis of our theoretical model, allowing us to estimate effective parameters $\theta_{SH,eff}$ and $H_{K,eff}$. Because of higher $\theta_{SH,eff}$ in the W-based system than in the Pt-based system, a critical switching-current density approximately 1 order of magnitude smaller is found. The switching stability experiments confirm the ability to induce $H_{exb}^{(x)}$ by thermal effects. Finally, we show a wide range of resistance changes in field-free magnetization switching in the case of the W (Pt)/Co/NiO system.

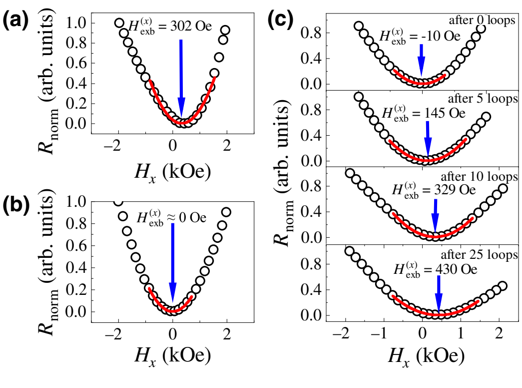

FIG. 8. Normalized longitudinal magnetoresistance of the Pt(5.1 nm)/Co(0.7 nm)/NiO(7 nm) device: (a) before the current-switching experiment, (b) after current switching without an external magnetic field, and (c) measured after a specified number of switching cycles. The red line corresponds to a quadratic function fitted to the data to determine the shift.

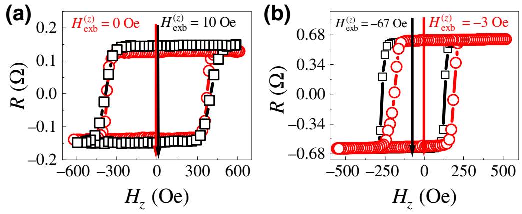

FIG. 9. AHE loops before switching experiments (black points) and after multiple switching cycles (red points) for Pt(5.1 nm)/Co(0.7 nm)/NiO(7 nm) (a) and the annealed W(4.3 nm)/Co(0.7 nm)/NiO(7 nm) (b) system.

ACKNOWLEDGMENTS

This work was supported by the National Science Centre, Poland, Grant No. 2016/23/B/ST3/01430 (SPINORBITRONICS). W.S. acknowledges National Science Centre Grant No. 2015/17/D/ST3/00500. J.K. and W.P. acknowledge National Science Centre Grant No. 2012/05/E/ST7/00240. P.K. and M.K. acknowledge National Science Centre Grant No. 2015/18/E/ST3/00557. The authors express their gratitude to Dr. A. Kozioł-Rachwał and Dr. M. Ślęzak for fruitful discussions and technical assistance with the XAS measurements. Nanofabrication was performed at the Academic Center for Materials and Nanotechnology of AGH University of Science and Technology. The XAS experiment was performed at the SOLARIS National Synchrotron Radiation Centre Grant No. XAS–192051.

[1] A. Brataas and K. M. D. Hals, Spin–orbit torques in action, Nat. Nanotechnol. **9**, 86 (2014).

[2] T. Wang, J. Q. Xiao, and X. Fan, Spin–orbit torques in metallic magnetic multilayers: Challenges and new opportunities, SPIN **07**, 1740013 (2017).

[3] B. Dieny *et al.*, Opportunities and challenges for spintronics in the microelectronics industry, Nat. Electron. **3**, 446 (2020).

[4] K. Garello, C. O. Avci, I. M. Miron, M. Baumgartner, A. Ghosh, S. Auffret, O. Boulle, G. Gaudin, and P. Gambardella, Ultrafast magnetization switching by spin-orbit torques, Appl. Phys. Lett. **105**, 212402 (2014).

[5] S. Fukami, T. Anekawa, C. Zhang, and H. Ohno, A spin–orbit torque switching scheme with collinear magnetic

easy axis and current configuration, Nat. Nanotechnol. **11**, 621 (2016).

[6] E. Grimaldi, V. Krizakova, G. Sala, F. Yasin, S. Couet, G. Sankar Kar, K. Garello, and P. Gambardella, Single-shot dynamics of spin–orbit torque and spin transfer torque switching in three-terminal magnetic tunnel junctions, Nat. Nanotechnol. **15**, 111 (2020).

[7] J. E. Hirsch, Spin Hall Effect, Phys. Rev. Lett. **83**, 1834 (1999).

[8] S. Zhang, Spin Hall Effect in the Presence of Spin Diffusion, Phys. Rev. Lett. **85**, 393 (2000).

[9] J. Sinova, S. O. Valenzuela, J. Wunderlich, C. H. Back, and T. Jungwirth, Spin hall effects, Rev. Mod. Phys. **87**, 1213 (2015).

[10] Y. Fan, P. Upadhyaya, X. Kou, M. Lang, S. Takei, Z. Wang, J. Tang, L. He, L.-T. Chang, M. Montazeri, G. Yu, W. Jiang, T. Nie, R. N. Schwartz, Y. Tserkovnyak, and K. L. Wang, Magnetization switching through giant spin–orbit torque in a magnetically doped topological insulator heterostructure, Nat. Mater. **13**, 699 (2014).

[11] A. Manchon, J. Železný, I. Miron, T. Jungwirth, J. Sinova, A. Thiaville, K. Garello, and P. Gambardella, Current-induced spin-orbit torques in ferromagnetic and antiferromagnetic systems, Rev. Mod. Phys. **91**, 035004 (2019).

[12] K. Cai, M. Yang, H. Ju, S. Wang, Y. Ji, B. Li, K. W. Edmonds, Y. Sheng, B. Zhang, N. Zhang, S. Liu, H. Zheng, and K. Wang, Electric field control of deterministic current-induced magnetization switching in a hybrid ferromagnetic/ferroelectric structure, Nat. Mater. **16**, 712 (2017).

[13] Y.-C. Lau, D. Betto, K. Rode, J. M. D. Coey, and P. Stamenov, Spin–orbit torque switching without an external field using interlayer exchange coupling, Nat. Nanotechnol. **11**, 758 (2016).

[14] S. Łazarski, W. Skowroński, J. Kanak, Ł. Karwacki, S. Zietek, K. Grochot, T. Stobiecki, and F. Stobiecki, Field-Free Spin-Orbit-Torque Switching in Co/Pt/Co Multilayer with Mixed Magnetic Anisotropies, Phys. Rev. Appl. **12**, 014006 (2019).

[15] S.-h. C. Baek, V. P. Amin, Y.-W. Oh, G. Go, S.-J. Lee, G.-H. Lee, K.-J. Kim, M. D. Stiles, B.-G. Park, and K.-J. Lee, Spin currents and spin–orbit torques in ferromagnetic trilayers, Nat. Mater. **17**, 509 (2018).

[16] Y. Sheng, K. W. Edmonds, X. Ma, H. Zheng, and K. Wang, Adjustable current-induced magnetization switching utilizing interlayer exchange coupling, Adv. Electron. Mater. **4**, 1800224 (2018).

[17] X. Wang, C. Wan, W. Kong, X. Zhang, Y. Xing, C. Fang, B. Tao, W. Yang, L. Huang, H. Wu, M. Irfan, and X. Han, Field-free programmable spin logics via chirality-reversible spin–orbit torque switching, Adv. Mater. **30**, 1801318 (2018).

[18] T. Chuang, C. Pai, and S. Huang, Cr -induced Perpendicular Magnetic Anisotropy and Field-Free Spin-Orbit-Torque Switching, Phys. Rev. Appl. **11**, 061005 (2019).

[19] Y. Cao, A. Rushforth, Y. Sheng, H. Zheng, and K. Wang, Tuning a binary ferromagnet into a multistate synapse with spin–orbit-Torque-Induced plasticity, Adv. Funct. Mater. **29**, 1808104 (2019).

[20] S. Chen, J. Yu, Q. Xie, X. Zhang, W. Lin, L. Liu, J. Zhou, X. Shu, R. Guo, Z. Zhang, and J. Chen, Free field electric switching of perpendicularly magnetized thin film by spin current gradient, ACS Appl. Mater. Interfaces **11**, 30446 (2019).

[21] C. K. Safeer, E. Jué, A. Lopez, L. Buda-Prejbeanu, S. Auffret, S. Pizzini, O. Boulle, I. M. Miron, and G. Gaudin, Spin–orbit torque magnetization switching controlled by geometry, Nat. Nanotechnol. **11**, 143 (2016).

[22] L. You, O. Lee, D. Bhowmik, D. Labanowski, J. Hong, J. Bokor, and S. Salahuddin, Switching of perpendicularly polarized nanomagnets with spin orbit torque without an external magnetic field by engineering a tilted anisotropy, Proc. Natl. Acad. Sci. **112**, 10310 (2015).

[23] G. Yu, L.-T. Chang, M. Akyol, P. Upadhyaya, C. He, X. Li, K. L. Wong, P. K. Amiri, and K. L. Wang, Current-driven perpendicular magnetization switching in Ta/CoFeB/[TaOx or MgO/TaOx] films with lateral structural asymmetry, Appl. Phys. Lett. **105**, 102411 (2014).

[24] G. Yu, P. Upadhyaya, Y. Fan, J. G. Alzate, W. Jiang, K. L. Wong, S. Takei, S. A. Bender, L.-T. Chang, Y. Jiang, M. Lang, J. Tang, Y. Wang, Y. Tserkovnyak, P. K. Amiri, and K. L. Wang, Switching of perpendicular magnetization by spin–orbit torques in the absence of external magnetic fields, Nat. Nanotechnol. **9**, 548 (2014).

[25] S. Maat, K. Takano, S. S. P. Parkin, and E. E. Fullerton, Perpendicular Exchange Bias of Co/Pt Multilayers, Phys. Rev. Lett. **87**, 087202 (2001).

[26] Y.-W. Oh, S.-h. Chris Baek, Y. M. Kim, H. Y. Lee, K.-D. Lee, C.-G. Yang, E.-S. Park, K.-S. Lee, K.-W. Kim, G. Go, J.-R. Jeong, B.-C. Min, H.-W. Lee, K.-J. Lee, and B.-G. Park, Field-free switching of perpendicular magnetization through spin–orbit torque in antiferromagnet/ferromagnet/oxide structures, Nat. Nanotechnol. **11**, 878 (2016).

[27] S. Fukami, C. Zhang, S. DuttaGupta, A. Kurenkov, and H. Ohno, Magnetization switching by spin–orbit torque in an antiferromagnet–ferromagnet bilayer system, Nat. Mater. **15**, 535 (2016).

[28] A. van den Brink, G. Vermijs, A. Solignac, J. Koo, J. Kohlhepp, H. Swagten, and B. Koopmans, Field-free magnetization reversal by spin-hall effect and exchange bias, Nat. Commun. **7**, 10854 (2016).

[29] S. A. Razavi, D. Wu, G. Yu, Y.-C. Lau, K. L. Wong, W. Zhu, C. He, Z. Zhang, J. M. D. Coey, P. Stamenov, P. Khalili Amiri, and K. L. Wang, Joule Heating Effect on Field-Free Magnetization Switching by Spin-Orbit Torque in Exchange-Biased Systems, Phys. Rev. Appl. **7**, 024023 (2017).

[30] A. Manchon, Spin diffusion and torques in disordered antiferromagnets, J. Phys.: Condens. Matter **29**, 104002 (2017).

[31] P. Kuświk, M. Matczak, M. Kowacz, K. Szuba-Jabński, N. Michalak, B. Szymański, A. Ehresmann, and F. Stobiecki, Asymmetric domain wall propagation caused by interfacial dzyaloshinskii-moriya interaction in exchange biased Au/Co/NiO layered system, Phys. Rev. B **97**, 024404 (2018).

[32] P. Kuświk, A. Gaul, M. Urbaniak, M. Schmidt, J. Aleksiejew, A. Ehresmann, and F. Stobiecki, Tailoring perpendicular exchange bias coupling in Au/Co/NiO systems by ion bombardment, Nanomaterials **8**, 813 (2018).

[33] P. Mazalski, B. Anastaziak, P. Kuświk, Z. Kurant, I. Sveklo, and A. Maziewski, Demagnetization of an ultrathin Co/NiO bilayer with creation of submicrometer domains controlled by temperature-induced changes of magnetic anisotropy, J. Magn. Magn. Mater. **508**, 166871 (2020).

[34] P. Kuświk, B. Szymański, B. Anastaziak, M. Matczak, M. Urbaniak, A. Ehresmann, and F. Stobiecki, Enhancement of perpendicular magnetic anisotropy of Co layer in exchange-biased Au/Co/NiO/Au polycrystalline system, J. Appl. Phys. **119**, 215307 (2016).

[35] H. Yang, S.-H. Yang, D.-C. Qi, A. Rusydi, H. Kawai, M. Saeys, T. Leo, D. J. Smith, and S. S. P. Parkin, Negative Tunneling Magnetoresistance by Canted Magnetization in MgO / NiO Tunnel Barriers, Phys. Rev. Lett. **106**, 167201 (2011).

[36] K. Ono, H. Shimada, S.-i. Kobayashi, and Y. Ootuka, Magnetoresistance of Ni/NiO/Co small tunnel junctions in coulomb blockade regime, J. Phys. Soc. Jpn. **65**, 3449 (1996).

[37] A. Sokolov, I. F. Sabirianov, E. Y. Tsymbal, B. Doudin, X. Z. Li, and J. Redepenning, Resonant tunneling in magnetoresistive Ni/NiO/Co nanowire junctions, J. Appl. Phys. **93**, 7029 (2003).

[38] T. Moriyama, S. Takei, M. Nagata, Y. Yoshimura, N. Matsuzaki, T. Terashima, Y. Tserkovnyak, and T. Ono, Anti-damping spin transfer torque through epitaxial nickel oxide, Appl. Phys. Lett. **106**, 162406 (2015).

[39] J. Wu, J. S. Park, W. Kim, E. Arenholz, M. Liberati, A. Scholl, Y. Z. Wu, C. Hwang, and Z. Q. Qiu, Direct Measurement of Rotatable and Frozen CoO Spins in Exchange Bias System of CoO/Fe/Ag (001), Phys. Rev. Lett. **104**, 217204 (2010).

[40] M. Ślęzak, T. Ślęzak, P. Dróżdż, B. Matlak, K. Matlak, A. Kozioł-Rachwał, M. Zając, and J. Korecki, How a ferromagnet drives an antiferromagnet in exchange biased CoO/Fe(110) bilayers, Sci. Rep. **9**, 889 (2019).

[41] See Supplemental Material at http://link.aps.org/supplemental/10.1103/PhysRevApplied.15.014017 for a detailed description of the structural characterization, the resistivity analysis, x-ray-absorption-spectroscopy measurements, the spin Hall angle, and perpendicular-exchange-bias analysis.

[42] A. Tan, J. Li, C. A. Jenkins, E. Arenholz, A. Scholl, C. Hwang, and Z. Q. Qiu, Exchange bias in epitaxially grown CoO/MgO/Fe/Ag(001), Phys. Rev. B **86**, 064406 (2012).

[43] A. Kozioł-Rachwał, W. Janus, M. Szpytma, P. Dróżdż, M. Ślęzak, K. Matlak, M. Gajewska, T. Ślęzak, and J. Korecki, Interface engineering towards enhanced exchange interaction between Fe and FeO in Fe/MgO/FeO epitaxial heterostructures, Appl. Phys. Lett. **115**, 141603 (2019).

[44] J. Zhu, Q. Li, J. X. Li, Z. Ding, J. H. Liang, X. Xiao, Y. M. Luo, C. Y. Hua, H.-J. Lin, T. W. Pi, Z. Hu, C. Won, and Y. Z. Wu, Antiferromagnetic spin reorientation transition in epitaxial NiO/CoO/MgO(001) systems, Phys. Rev. B **90**, 054403 (2014).

[45] Q. Li, J. H. Liang, Y. M. Luo, Z. Ding, T. Gu, Z. Hu, C. Y. Hua, H.-J. Lin, T. W. Pi, S. P. Kang, C. Won, and Y. Z. Wu, Antiferromagnetic proximity effect in epitaxial CoO/NiO/MgO(001) systems, Sci. Rep. **6**, 22355 (2016).

[46] F. Smits, Measurement of sheet resistivities with the four-point probe, Bell Syst. Tech. J. **34**, 711 (1958).

[47] M. Kawaguchi, D. Towa, Y.-C. Lau, S. Takahashi, and M. Hayashi, Anomalous spin hall magnetoresistance in Pt/Co bilayers, Appl. Phys. Lett. **112**, 202405 (2018).

[48] E. Sagasta, Y. Omori, M. Isasa, M. Gradhand, L. E. Hueso, Y. Niimi, Y. Otani, and F. Casanova, Tuning the spin hall effect of Pt from the moderately dirty to the superclean regime, Phys. Rev. B **94**, 060412 (2016).

[49] W. Skowroński, Ł. Karwacki, S. Zietek, J. Kanak, S. Łazarski, K. Grochot, T. Stobiecki, P. Kuświk, F. Stobiecki, and J. Barnaś, Determination of Spin Hall Angle in Heavy-Metal/Co-Fe-B-based Heterostructures with Interfacial Spin-Orbit Fields, Phys. Rev. Appl. **11**, 024039 (2019).

[50] Q. Hao, W. Chen, and G. Xiao, Beta (β) tungsten thin films: Structure, electron transport, and giant spin hall effect, Appl. Phys. Lett. **106**, 182403 (2015).

[51] Q. Hao and G. Xiao, Giant Spin Hall Effect and Switching Induced by Spin-Transfer Torque in a $W/Co_{40}Fe_{40}B_{20}$/MgO Structure with Perpendicular Magnetic Anisotropy, Phys. Rev. Appl. **3**, 034009 (2015).

[52] L. Neumann, D. Meier, J. Schmalhorst, K. Rott, G. Reiss, and M. Meinert, Temperature dependence of the spin hall angle and switching current in the $nc - W(O)/CoFeB/MgO$ system with perpendicular magnetic anisotropy, Appl. Phys. Lett. **109**, 142405 (2016).

[53] K.-S. Lee, S.-W. Lee, B.-C. Min, and K.-J. Lee, Threshold current for switching of a perpendicular magnetic layer induced by spin hall effect, Appl. Phys. Lett. **102**, 112410 (2013).

[54] T. Taniguchi, Theoretical condition for switching the magnetization in a perpendicularly magnetized ferromagnet via the spin hall effect, Phys. Rev. B **100**, 174419 (2019).

[55] M. Baumgartner, K. Garello, J. Mendil, C. O. Avci, E. Grimaldi, C. Murer, J. Feng, M. Gabureac, C. Stamm, Y. Acremann, S. Finizio, S. Wintz, J. Raabe, and P. Gambardella, Spatially and time-resolved magnetization dynamics driven by spin–orbit torques, Nat. Nanotechnol. **12**, 980 (2017).

[56] J. Kim, P. Sheng, S. Takahashi, S. Mitani, and M. Hayashi, Spin Hall Magnetoresistance in Metallic Bilayers, Phys. Rev. Lett. **116**, 097201 (2016).

[57] J.-C. Rojas-Sánchez, N. Reyren, P. Laczkowski, W. Savero, J.-P. Attané, C. Deranlot, M. Jamet, J.-M. George, L. Vila, and H. Jaffrès, Spin Pumping and Inverse Spin Hall Effect in Platinum: The Essential Role of Spin-Memory Loss at Metallic Interfaces, Phys. Rev. Lett. **112**, 106602 (2014).

[58] C. F. Pai, L. Liu, Y. Li, H. W. Tseng, D. C. Ralph, and R. A. Buhrman, Spin transfer torque devices utilizing the giant spin hall effect of tungsten, Appl. Phys. Lett. **101**, 122404 (2012).

[59] Y. Takeuchi, C. Zhang, A. Okada, H. Sato, S. Fukami, and H. Ohno, Spin-orbit torques in high-resistivity-$W/CoFeB/MgO$, Appl. Phys. Lett. **112**, 192408 (2018).

[60] S. Cho, S.-h. C. Baek, K.-D. Lee, Y. Jo, and B.-G. Park, Large spin hall magnetoresistance and its correlation to the spin-orbit torque in W/CoFeB/MgO structures, Sci. Rep. **5**, 14668 (2015).

[61] C. Zhang, S. Fukami, K. Watanabe, A. Ohkawara, S. DuttaGupta, H. Sato, F. Matsukura, and H. Ohno, Critical role of w deposition condition on spin-orbit torque induced magnetization switching in nanoscale W/CoFeB/MgO, Appl. Phys. Lett. **109**, 192405 (2016).

[62] W. Skowroński, M. Cecot, J. Kanak, S. Ziętek, T. Stobiecki, L. Yao, S. van Dijken, T. Nozaki, K. Yakushiji, and S. Yuasa, Temperature dependence of spin-orbit torques in W/CoFeB bilayers, Appl. Phys. Lett. **109**, 062407 (2016).

[63] W. Chen, G. Xiao, Q. Zhang, and X. Zhang, Temperature study of the giant spin hall effect in the bulk limit of β-W, Phys. Rev. B **98**, 134411 (2018).

[64] R. Bansal, G. Nirala, A. Kumar, S. Chaudhary, and P. K. Muduli, Large spin hall angle in β-W thin films grown on CoFeB without oxygen plasma, SPIN **8**, 1850018 (2018).

[65] O. L. W. McHugh, W. F. Goh, M. Gradhand, and D. A. Stewart, Impact of impurities on the spin hall conductivity in β -W, Phys. Rev. Mater. **4**, 094404 (2020).

[66] K. Zhang, T. Zhao, and H. Fujiwara, Training effect of exchange biased iron–oxide/ferromagnet systems, J. Appl. Phys. **89**, 6910 (2001).

[67] S. Brems, K. Temst, and C. Van Haesendonck, Origin of the Training Effect and Asymmetry of the Magnetization in Polycrystalline Exchange Bias Systems, Phys. Rev. Lett. **99**, 067201 (2007).

[68] C. Binek, Training of the exchange-bias effect: A simple analytic approach, Phys. Rev. B **70**, 014421 (2004).

[69] A. Hochstrat, C. Binek, and W. Kleemann, Training of the exchange-bias effect in nio-fe heterostructures, Phys. Rev. B **66**, 092409 (2002).

Current-induced magnetization switching of exchange-biased NiO heterostructures characterized by spin-orbit torque

Krzysztof Grochot [1,2], Łukasz Karwacki [3], Stanisław Łazarski [1], Witold Skowroński [1], Jarosław Kanak [1], Wiesław Powroźnik [1], Piotr Kuświk [3], Mateusz Kowacz [3], Feliks Stobiecki [3], and Tomasz Stobiecki [1,2]

[1] *AGH University of Science and Technology, Department of Electronics, Al. Mickiewicza 30, 30-059 Kraków, Poland*
[2] *AGH University of Science and Technology, Faculty of Physics and Applied Computer Science, 30-059 Kraków, Poland*
[3] *Institute of Molecular Physics, Polish Academy of Sciences, ul. Smoluchowskiego 17, 60-179 Poznań, Poland*

1. Structural characterization

The multilayers investigated in this paper were deposited on 20 mm × 20 mm Si/SiO_2 wafer using a magnetron sputtering technique. The as-deposited samples were measured by the polar magnetooptical Kerr effect (p-MOKE) in order to determine the range of heavy metal (HM) thicknesses for which perpendicular magnetic anisotropy (PMA) occurs. Next, the multilayer was divided into two equal halves, one of which was intended for fabrication of Hall-bar devices and the other for structural characterization.

The structure of the multilayers Si/SiO_2/wedge-W/Co/NiO and Si/SiO_2/wedge-Pt/Co/NiO was characterized using a X'Pert–MPD diffractometer with Cu-anode. Figure S1 shows the x-ray diffraction (XRD) θ−2θ (a) and GIXD@1° (b) profiles for Si/SiO2/W(0-10)/Co (0.7)/NiO(7) (thickness in nanometers) measured in three positions of the W wedge (1 nm, 5 nm and 9 nm). The grazing incidence X-ray diffraction (GIXD) method was used in order to minimize the influence of Si/SiO_2 substrate background.

The antiferromagnetic NiO layer grows in cubic fcc (space group: Fm3m) structure whereas W in cubic (space group: Pm3n) β-W structure. The θ−2θ measurements show preferred growth of the NiO in [111] direction, while GIXD diffraction patterns, measured at 1° incidence beam, reveal more NiO and W structural peaks characteristic for polycrystalline structure. The GIXD profiles of 1 nm thick W layer show a very broad low-intensity peak, indicating an amorphous-like disordered structure, while the profiles of thicker W layers 5 nm, and 9 nm contain peaks that originate from a polycrystalline W β-phase.

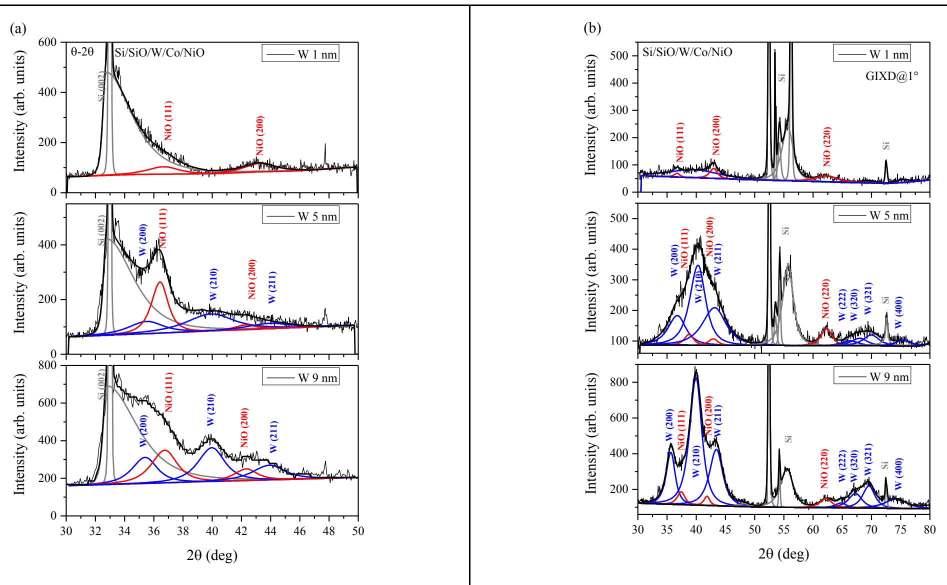

Fig. S1. The θ−2θ (a) and GIXD (b) diffraction profiles for Si/SiO_2/wedge-W/Co/NiO measured in thin (1 nm), middle (5 nm), and thick (9 nm) position of the wedge of W layer. Black lines depict the experimental data, blue and red lines are fits, which represent the distribution of W and NiO peaks for different crystallographic orientations of polycrystalline samples.

The XRD profiles of Si/SiO_2/Pt(0-10)/Co (0.7)/NiO(7) multilayer measured in different positions of the Pt wedge, which grows in cubic fcc (space group: Fm3m), are shown in Fig. S2 (a) θ−2θ and GIXD@1° (b). In this case the θ−2θ diffraction patterns shown preferred growth of the NiO in [200] direction and Pt in [111], while the GIXD profiles, similarly to W system, reveal more the NiO and Pt structural peaks characteristic for polycrystalline structure. The diffraction peaks from the Co layer are not visible due to its low thickness.

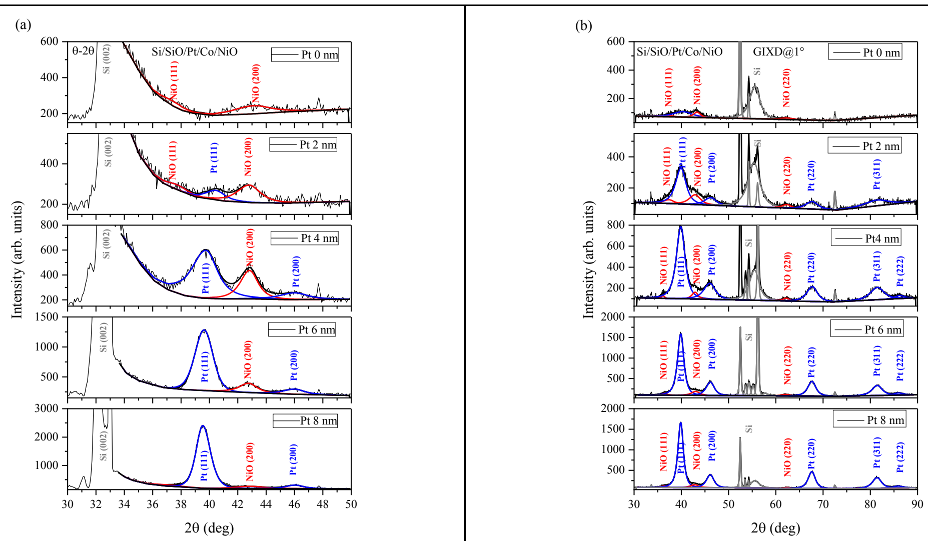

Fig. S2. The θ−2θ (a) and GIXD (b) diffraction profiles for Si/SiO_2/wedge-Pt/Co/NiO measured at different positions of the Pt wedge. Black lines depict the experimental data, blue and red lines are fits, which represent the distribution of Pt and NiO peaks for different crystallographic orientations of polycrystalline samples.

2. X-ray absorption spectroscopy measurements

In Fig. S3 a and b are shown X-ray absorption spectra (XAS) spectra on the samples: Pt(3)/Co(0.7)/NiO(4) and Pt(3)/Co(2.3)/NiO(3), respectively. The characteristic peak structure at the L_3 of Co absorption edge corresponds to the stoichiometric CoO [S1 – S4]. Comparison of the XAS spectra acquired at room temperature (RT) for two samples with different Co thicknesses (0.7nm and 2.3nm, a and b respectively) indicates that roughly one monolayer of CoO exists at the Co/NiO interface. With increasing thickness of Co a contribution of metallic Co dominates the XAS spectra and so the characteristic CoO peaks structure are less evident (Fig.S3 b).

In our studies, we noted the presence of RT perpendicular exchange bias in P-MOKE measurements (Fig. S4 a), which is additionally confirmed by the hysteresis loop measured by XMCD at the Co absorption edge (Fig. S4 b).
To elucidate the magnetic state of the interfacial CoO monolayer we have performed angle-dependent XAS measurements with linearly polarized incoming X-rays (XMLD). Two XMLD spectra collected at normal and grazing incidence angles geometries are almost perfectly identical which proves paramagnetic state of CoO layer at RT (Fig. S5). At low temperatures CoO can order antiferromagnetically, and it has been shown that an adjacent NiO layer can enhance CoO layer's Néel temperature [S3, S4], so further systematic XAS studies are necessary to investigate interfacial spin ordering as well as magnetic coupling between CoO and NiO. These effects will be studied during future beam times and published elsewhere.

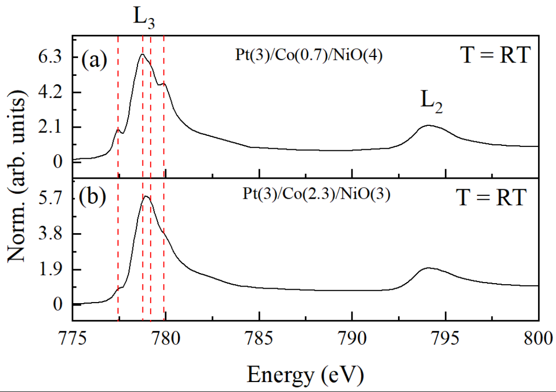

Fig. S3. XMCD spectra acquired at the L_3 (779 eV) and L_2 (793.8 eV) absorption edge of Co. Red dashed lines indicate CoO absorption lines at 777.5 eV, 778.75 eV, 779.2 eV and 779.9 eV.

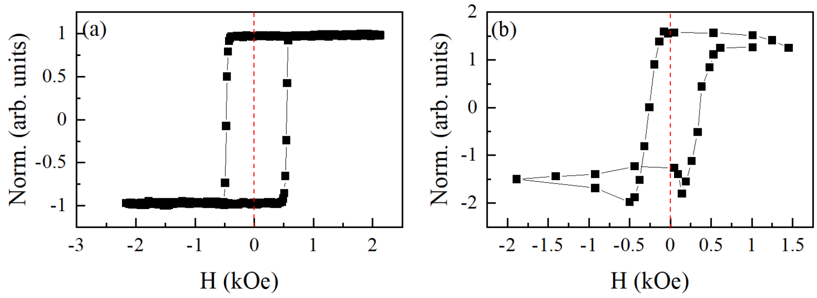

Fig. S4. (a) p-MOKE Hysteresis loop H_{EB}= 45 Oe and (b) XMCD Hysteresis loop H_{EB} = 48 Oe.

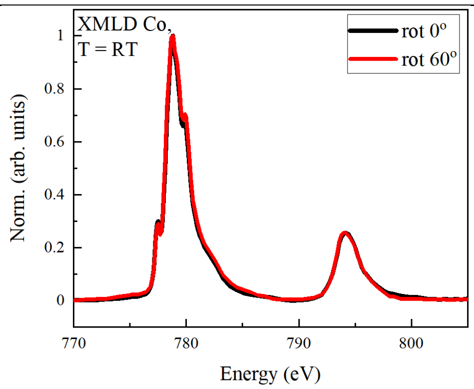

Fig. S5. XMLD spectra of CoO.

3. Perpendicular magnetic anisotropy, coercive field and perpendicular exchange bias

Both Pt(t_{Pt})/Co/NiO and W(t_W)/Co/NiO systems were patterned to create a matrix of 100 µm × 10 µm or 30 µm × 30 µm Hall-bar devices. Every next element in the column along the wedge was characterized by gradually increased in a thickness of HM layer. Anomalous Hall effect (AHE) hysteresis loops for selected thicknesses of W- and Pt-based Hall-bar devices are depicted in Fig. S6. The square-shape loops in both systems prove the perpendicular magnetic anisotropy (PMA) in t_{Pt} between 1 nm and 9 nm and in t_W between 3.5 nm and 8 nm.

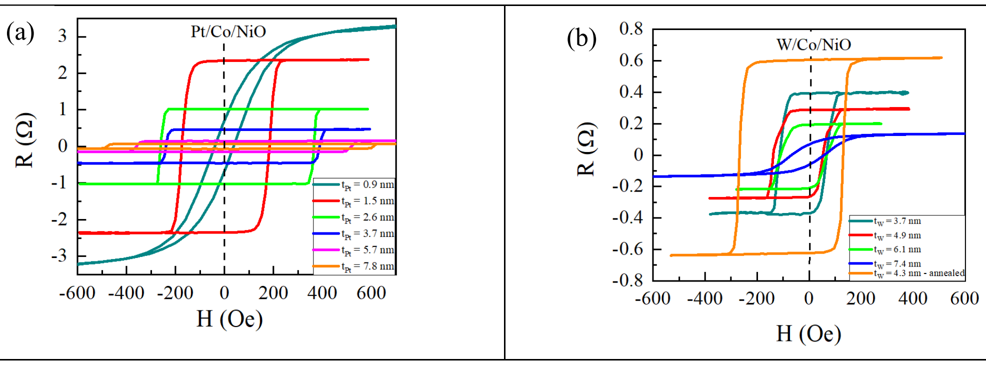

Fig. S6. The AHE loops for several thicknesses of HM layer: Pt (a) and W (b) where the orange loop corresponds to an annealed Hall-bar W(4.3)/Co(0.7)/NiO(7), marked as C1 in the main text.

The coercive field (H_c) as a function of Pt thicknesses increases up to 600 Oe, while for W-based devices H_c is independent for thicknesses up to 6 nm and amounts to 180 Oe then gradually decreases (Fig. S7a). The perpendicular exchange bias (H_{exb}), as shown in Fig. S7b, is highest for HM thickness of about 5 nm in both systems with about two times higher values are achieved for Pt-based devices.

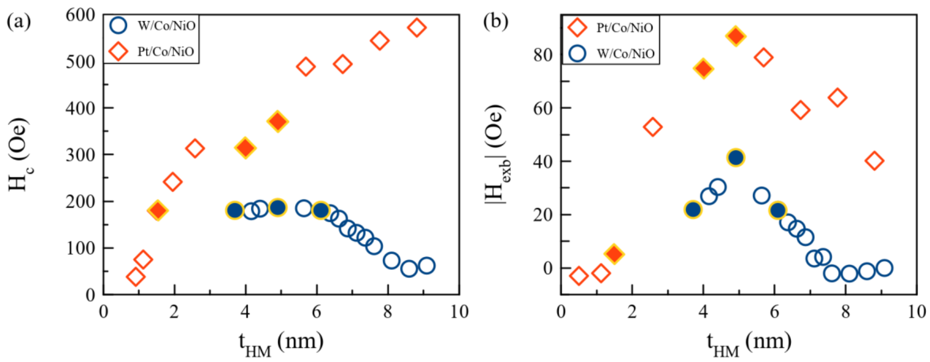

Fig. S7. The coercive field H_c (a) and perpendicular exchange bias H_{exb} (b) of Pt/Co/NiO and W/Co/NiO determined from AHE hysteresis loops. Points with yellow border correspond to the devices analyzed in the main text.

4. Resistivity

The resistivity of each material was calculated based on sheet conductance (G = L/(w·R)), where L is length, w is width and R is the resistance of the Hall-bar measured by the four-probe method according to the procedure described in Ref.[S5]. The distance between voltage pads was 100 µm, and the Hall bar width was fixed to 10 µm. Sheet conductance G as a function of HM thickness was presented in Fig. S8.

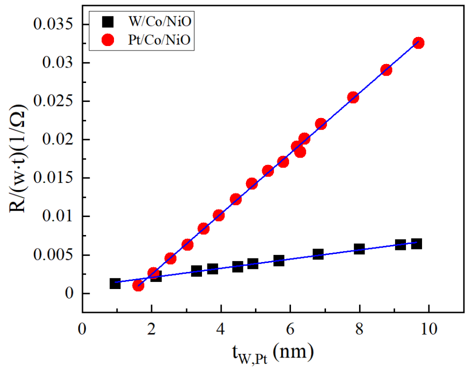

Fig. S8. The sheet conductance W(t_w)/Co/NiO (black squares) and Pt(t_{Pt})/Co/NiO (red dots).

The dependence of G is a linear function of HM thickness for both W(t_w)/Co/NiO and Pt(t_{Pt})/Co/NiO system, therefore the resistivities of W and Pt, calculated using parallel resistors model, are 170 µΩcm and 30 µΩcm, respectively, while Co resistivity varied from 28 µΩcm on Pt to 58 µΩcm on W underlayer.

5. Spin Hall angle in annealed W/Co/NiO system

To confirm the high spin Hall angle obtained from the threshold current model for the C1 device (Fig. S9 (a)), we selected another device (W(4.3)/Co(0.8)/NiO) from the same sample series. The sample has been annealed in the same condition as C1. Next, we performed current-induced magnetization switching with the same measurement parameters, and the model was fitted to an obtained current density data point. As a result, we obtained θ_{SH} = -46 ± 5% (Fig. S9(b)).

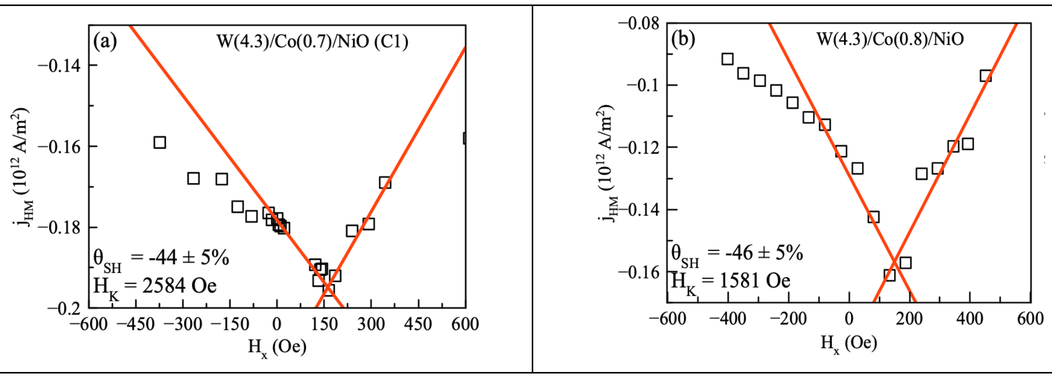

Fig. S9: Critical threshold current density as a function of external magnetic field (H_x) for W(4.3)/Co(0.7)/NiO (labeled as C1) (a) and W(4.3)/Co(0.8)/NiO (b).

6. ΔR/ΔR$_{AHE}$ ratio

Current magnetization switching of the studied systems, although it occurs in a zero external magnetic field, does not reach the full switching defined by the difference of resistance in the AHE loop (ΔR$_{AHE}$). The maximum value of the ΔR/ΔR_{AHE} ratio is about 40% for Pt-based devices and about 80% for W-based devices (see Fig. 2 in main text). However, when samples were field-free switching, the maximum obtained values were 28% in the A4 (Fig. S10(a)) and 38% in the C1 device (Fig. S10(b)) with the highest value of in-plane exchange bias, respectively.

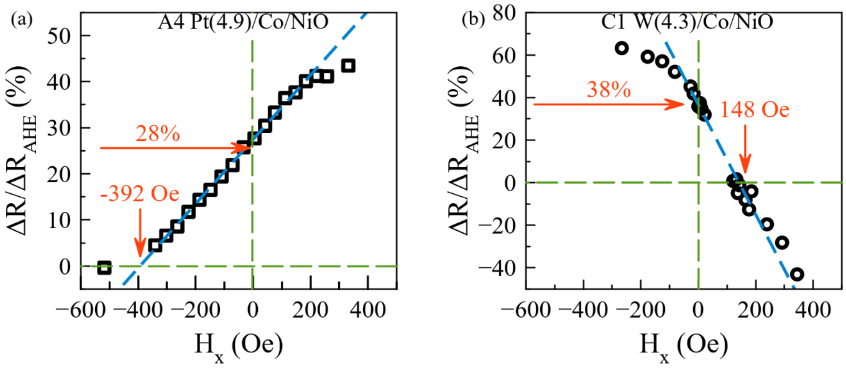

Fig. S10: ΔR/ΔR_{AHE} field dependence obtained for A4 (a) and C1 (b) devices. Red arrows indicate ΔR/ΔR_{AHE} in field-free switching cases.

7. Saturation of magnetization

In order to determine the dependence of the saturation magnetization ($\mu_0 M_s$) as a function of the Co layers thickness, following multilayer systems: Ti(2)/Co (t_{Co}: 0.9, 1.65, 2.19, 3.4, 9.05)/Pt(4) were deposited. Ti buffer layer was oxidized and provided a smooth interface. Thickness of Co layer was determined by x-ray reflectivity analysis. Magnetization hysteresis loop measurements were carried out using VSM (Vibrating Sample Magnetometer) in 20 kOe magnetic field applied in-plane (HIP) and perpendicular to the sample plane (HPP). Below 2 nm Co thickness (Fig. S11) $\mu_0 M_s$ decreases approximately linearly, reaching about 0.5 T, above 3 nm is approximately independent of the Co layer thickness by setting 2 T.

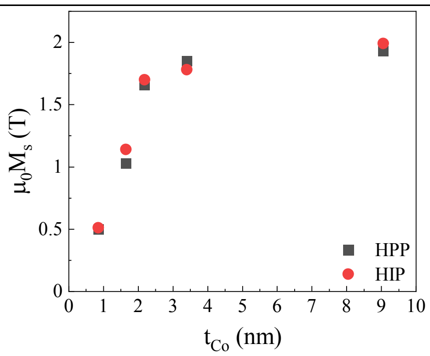

Fig.S11: The saturation magnetization $\mu_0 M_S$ as a function of Co thickness in Co(t_{Co})/Pt(4).

[S1] J. Wu, J. S. Park, W. Kim, E. Arenholz, M. Liberati, A. Scholl, Y. Z. Wu, C. Hwang, and Z. Q. Qiu, *Direct Measurement of Rotatable and Frozen CoO Spins in Exchange Bias System of CoO/Fe/Ag(001)*, Phys. Rev. Lett. 104, 217204 (2010)
[S2] J. Zhu, Q. Li, J. X. Li, Z. Ding, J. H. Liang, X. Xiao, Y. M. Luo, C. Y. Hua, H.-J. Lin, T. W. Pi, Z. Hu, C. Won, and Y. Z. Wu, *Antiferromagnetic spin reorientation transition in epitaxial NiO/CoO/MgO(001) systems*, Phys. Rev. B **90**, 054403 (2014).
[S3] Q. Li, J. H. Liang, Y. M. Luo, Z. Ding, T. Gu, Z. Hu, C. Y. Hua, H.-J. Lin, T. W. Pi, S. P. Kang,C. Won andY. Z. Wu , *Antiferromagnetic proximity effect in epitaxial CoO/NiO/MgO(001) system,* Sci. Rep. **6**, 22355 (2016)
[S4] M. Ślęzak, T. Ślęzak, P. Dróżdż, B. Matlak, K. Matlak, A. Kozioł-Rachwał, M. Zając, and J. Korecki, *How a Ferromagnet Drives an Antiferromagnet in Exchange Biased CoO/Fe(110) Bilayers*, Sci Rep **9**, 889 (2019).

[S5] M. Kawaguchi, D. Towa, Y.-C. Lau, S. Takahashi, and M. Hayashi, *Anomalous Spin Hall Magnetoresistance in Pt/Co Bilayers*, Appl. Phys. Lett. **112**, 202405 (2018).

Section summary

In this section, we describe our study on CIMS in thin-film hybrid systems with HM, FM, and AFM layers. We studied two systems: Pt/Co/NiO and W/Co/NiO, where the NiO layer induces an ExB fields on the Co layer. We measured the SMR and the CIMS and developed theoretical models to describe them. We also studied the effect of annealing and long-term current switching on the thermal stability of these systems and the ExB fields.

We have found that the SMR depends on the thickness of the Pt layer and the spin ordering via Néel vector of the NiO layer. We observed a shift in the position of the minimum |SMR| value from 2 nm to 3.5 nm for the Pt/Co/NiO system compared to the Pt/Co/MgO system, which we attributed to the spin current absorption at the FM/AFM interface. We fitted our experimental data with an extended SMR model that accounts for a variable direction of the Néel vector in the NiO layer.

Next, we showed that the ExB field has both in-plane ($H_{\mathrm{exb}}^{(\mathrm{x})}$) and perpendicular ($H_{\mathrm{exb}}^{(\mathrm{z})}$) components that affect the CIMS. In-plane $H_{\mathrm{exb}}^{(\mathrm{x})}$ field could achieve field-free magnetization switching in as-deposited Pt/Co/NiO, and W-based systems annealed with a perpendicular magnetic field. We attributed the origin of the ExB field to the antiferromagnetic CoO/NiO bilayer that forms at the interface due to Co oxidation. The critical switching current was modeled by extending the SOT threshold current model with a term related to the $H_{\mathrm{exb}}^{(\mathrm{x})}$ field. We determined the effective SHA from this model and compared it with data from the literature and the field harmonics method. Effective SHA is higher in the W-based system than in the Pt-based system, especially for annealed W/Co/NiO system it increases significantly to -44%, which we attributed to the formation of β-W phase. The effect of Joule heating and training on magnetization switching durability affects the thermal stability of systems, which can change the ExB fields and reduce the CIMS amplitude.

5

Summary & Outlook

Spin electronics memories, such as SOT-RAMs and STT-RAMs, are promising alternatives to conventional RAMs because they have the advantages of non-volatility, energy efficiency, and compatibility with modern silicon technologies. These features align well with the green IT industry trends. However, these emerging technologies need further research to optimize the materials and thin-film structures for SOT generation efficiency, field-free magnetization switching, and understanding the mechanisms of magnetization dynamics. These aspects are crucial for practical applications. This dissertation presents an experimental study of thin-film hybrid systems of HM/FM bilayer, coupled FM/HM/FM trilayer, and HM/FM/AFM system, supported by theoretical models. The aim of this study was to enhance the understanding of spin electronics phenomena.

We used a theoretical spin diffusion model that we modified according to the type of system we studied. This allowed us to separate the contributions of SMR and AMR to the total magnetoresistance. In the [P1] publication, we analyzed ten bilayer systems with different compositions and crystal structures of the individual layers. We found that SMR dominates over AMR in systems with W as the HM layer and amorphous CoFeB and crystalline Co as the FM layer. This is because W has a high SHA. However, in systems with Pt or Au as the HM layer and Co as the FM layer, AMR dominates over SMR. This is because of the significant difference in the resistivities of the layers and the different crystallinities of the Co and W layers. We also showed that the thickness of the Pt spacer in Co/Pt/Co trilayer affects the IEC between the two Co layers, which influences anisotropy, saturation magnetization, interface transparency, and mixing conductance. These factors affect spin transport effects, such as SMR and AMR, as shown in the [P3]. Furthermore, we showed that the NiO layer in the Pt(t_{Pt})/Co/NiO system affects SMR as a function of the Pt thickness. We modeled this by using the variable direction of the Néel vector components of the AFM layer. However, this issue needs more research.

In this dissertation, we also analyzed spin-dependent transport phenomena in the systems described in papers [P2] and [P3]. We determined the SHA and SHC (σ_{SH}) of Pt-based bilayer systems with different interface structures. We showed that inserting thin Ti layers between Pt can increase the SHA of the system by increasing the number of interfaces. This suggests that the Pt-Ti superlattice is a promising material for spintronics applications. We also investigated the effect of the interface and coupling parameters on the SOT effective fields and SHE in the trilayer Pt/Co/Pt system. We obtained the maximum value of SHA of about 14% for t_{Pt} = 3.24 nm. Moreover, we studied the magnetization dynamics of the Co/Pt/Co trilayer and estimated the IEC by fitting a LLGS macrospin model. Finally, we have shown that SHA in the W/Co/NiO system is several times higher than in the Pt-based system.

Last aspect that we investigated in this dissertation is CIMS based on [P4] and [P5]. We analyzed the CIMS loop in three magnetic field ranges H_x for the Pt/Co bilayer system. We used a phenomenological model to show that the CIMS loop deviates from a rectangular shape due to the characteristic domain structure induced by the DMI. We determined the DMI field from the CIMS loops to be around 1200 Oe, which corresponds to the DMI energy density D=1.1 mJ/m^2 typical for the Pt/Co system. We have also shown multilevel magnetization switching in the Co/Pt/Co trilayer. We demonstrated a four-state CIMS in devices with strong IEC and asymmetric interfaces. We explained this phenomenon by the different effective fields acting on each Co layer due to their different anisotropies and interface properties. We examined the critical switching current densities as a function of the magnetic field and the Pt thickness. Furthermore, we studied the effect of the in-plane and perpendicular ExB components on CIMS. The in-plane component enables field-free switching in Pt/Co/NiO and annealed W-based systems with perpendicular anisotropy. The ExB field originates from the antiferromagnetic CoO/NiO bilayer at the interface due to Co oxidation. We modified the SOT threshold current model with a term for the ExB in-plane component. We estimated the effective SHA from this model and show that it is higher in the W-based system than in the Pt-based system, especially for the annealed W/Co/NiO system where it reaches -44%, due to β-W phase formation. On the other hand, the effects of Joule heating and training reduce switching durability and thermal stability of the systems what needs to be considered in the design of practical devices. Nevertheless, the research carried out in this dissertation brings a number of very important tips important for practical solutions.

References

[1] Puebla, J., Kim, J., Kondou, K., and Otani, Y.: Spintronic devices for energy-efficient data storage and energy harvesting. *Communications Materials* 1, 1–9 (2020)

[2] Grollier, J., Querlioz, D., Camsari, K. Y., Everschor-Sitte, K., Fukami, S., and Stiles, M. D.: Neuromorphic spintronics. *Nature Electronics* 3, 360–370 (2020)

[3] Chen, X., Kang, W., Zhu, D., Zhang, X., Lei, N., Zhang, Y., Zhou, Y., and Zhao, W.: A compact skyrmionic leaky–integrate–fire spiking neuron device. *Nanoscale* 10, 6139–6146 (2018)

[4] Li, S., Kang, W., Huang, Y., Zhang, X., Zhou, Y., and Zhao, W.: Magnetic skyrmion-based artificial neuron device. *Nanotechnology* 28, 31LT01 (2017)

[5] Pinna, D., Abreu Araujo, F., Kim, J.-V., Cros, V., Querlioz, D., Bessiere, P., Droulez, J., and Grollier, J.: Skyrmion Gas Manipulation for Probabilistic Computing. *Physical Review Applied* 9, 064018 (2018)

[6] Allwood, D. A., Xiong, G., Faulkner, C. C., Atkinson, D., Petit, D., and Cowburn, R. P.: Magnetic Domain-Wall Logic. *Science* 309, 1688–1692 (2005)

[7] Yang, J. J., Strukov, D. B., and Stewart, D. R.: Memristive devices for computing. *Nature Nanotechnology* 8, 13–24 (2013)

[8] Fukami, S. and Ohno, H.: Magnetization switching schemes for nanoscale three-terminal spintronics devices. *Japanese Journal of Applied Physics* 56, 0802A1 (2017)

[9] Prenat, G., Jabeur, K., Vanhauwaert, P., Pendina, G. D., Oboril, F., Bishnoi, R., Ebrahimi, M., Lamard, N., Boulle, O., Garello, K., Langer, J., Ocker, B., Cyrille, M.-C., Gambardella, P., Tahoori, M., and Gaudin, G.: Ultra-Fast and High-Reliability SOT-MRAM: From Cache Replacement to Normally-Off Computing. *IEEE Transactions on Multi-Scale Computing Systems* 2, 49–60 (2016)

[10] Kato, Y., Saito, Y., Yoda, H., Inokuchi, T., Shirotori, S., Shimomura, N., Oikawa, S., Tiwari, A., Ishikawa, M., Shimizu, M., Altansargai, B., Sugiyama, H., Koi, K., Ohsawa, Y., and Kurobe, A.: Improvement of Write Efficiency in Voltage-Controlled Spintronic Memory by development of a $Ta-B$ Spin Hall Electrode. *Physical Review Applied* 10, 044011 (2018)

[11] Oboril, F., Bishnoi, R., Ebrahimi, M., and Tahoori, M. B.: Evaluation of Hybrid Memory Technologies Using SOT-MRAM for On-Chip Cache Hierarchy. *IEEE Transactions on Computer-Aided Design of Integrated Circuits and Systems* 34, 367–380 (2015)

[12] Chen, E., Lottis, D., Driskill-Smith, A., Druist, D., Nikitin, V., Watts, S., Tang, X., and Apalkov, D.: Non-volatile spin-transfer torque RAM (STT-RAM). In *68th Device Research Conference*, 249–252 (2010)

[13] Endoh, T., Honjo, H., Nishioka, K., and Ikeda, S.: Recent Progresses in STT-MRAM and SOT-MRAM for Next Generation MRAM. In *2020 IEEE Symposium on VLSI Technology*, 1–2 (2020)

[14] Zeissler, K.: STT-MRAM that works at high temperatures. *Nature Electronics* 6, 180–180 (2023)

[15] Worledge, D. C.: Spin-Transfer-Torque MRAM: the Next Revolution in Memory. In *2022 IEEE International Memory Workshop (IMW)*, 1–4 (2022)

[16] Ikeda, S., Miura, K., Yamamoto, H., Mizunuma, K., Gan, H. D., Endo, M., Kanai, S., Hayakawa, J., Matsukura, F., and Ohno, H.: A perpendicular-anisotropy CoFeB–MgO magnetic tunnel junction. *Nature Materials* 9, 721–724 (2010)

[17] Tsoi, M., Jansen, A. G. M., Bass, J., Chiang, W.-C., Tsoi, V., and Wyder, P.: Generation and detection of phase-coherent current-driven magnons in magnetic multilayers. *Nature* 406, 46–48 (2000)

[18] Kiselev, S. I., Sankey, J. C., Krivorotov, I. N., Emley, N. C., Schoelkopf, R. J., Buhrman, R. A., and Ralph, D. C.: Microwave oscillations of a nanomagnet driven by a spin-polarized current. *Nature* 425, 380–383 (2003)

[19] Rippard, W. H., Pufall, M. R., Kaka, S., Russek, S. E., and Silva, T. J.: Direct-Current Induced Dynamics in $Co_{90}Fe_{10}/Ni_{80}Fe_{90}$ Point Contacts. *Physical Review Letters* 92, 027201 (2004)

[20] Demidov, V. E., Urazhdin, S., de Loubens, G., Klein, O., Cros, V., Anane, A., and Demokritov, S. O.: Magnetization oscillations and waves driven by pure spin currents. *Physics Reports* 673, 1–31 (2017)

[21] Madami, M., Bonetti, S., Consolo, G., Tacchi, S., Carlotti, G., Gubbiotti, G., Mancoff, F. B., Yar, M. A., and Åkerman, J.: Direct observation of a propagating spin wave induced by spin-transfer torque. *Nature Nanotechnology* 6, 635–638 (2011)

[22] Demidov, V. E., Urazhdin, S., and Demokritov, S. O.: Direct observation and mapping of spin waves emitted by spin-torque nano-oscillators. *Nature Materials* 9, 984–988 (2010)

[23] Cheng, R., Xiao, D., and Brataas, A.: Terahertz Antiferromagnetic Spin Hall Nano-Oscillator. *Physical Review Letters* 116, 207603 (2016)

[24] Salikhov, R., Ilyakov, I., Körber, L., Kákay, A., Gallardo, R. A., Ponomaryov, A., Deinert, J.-C., de Oliveira, T. V. A. G., Lenz, K., Fassbender, J., Bonetti, S., Hellwig, O., Lindner, J., and Kovalev, S.: Coupling of terahertz light with nanometre-wavelength magnon modes via spin–orbit torque. *Nature Physics* 1–7 (2023)

[25] Rzeszut, P., Chęciński, J., Brzozowski, I., Ziętek, S., Skowroński, W., and Stobiecki, T.: Multi-state MRAM cells for hardware neuromorphic computing. *Scientific Reports* 12, 7178 (2022)

[26] Borders, W. A., Pervaiz, A. Z., Fukami, S., Camsari, K. Y., Ohno, H., and Datta, S.: Integer factorization using stochastic magnetic tunnel junctions. *Nature* 573, 390–393 (2019)

[27] Jan, J. P.: Galvamomagnetic and Thermomagnetic Effects in Metals. In Seitz, F. and Turnbull, D., eds., *Solid State Physics*, vol. 5, 1–96. Academic Press (1957)

[28] Yamaguchi, A., Motoi, K., Hirohata, A., and Miyajima, H.: Anomalous Hall voltage rectification and quantized spin-wave excitation induced by simultaneous application of dc and rf currents in a single-layered $Ni_{81} - Fe_{19}$ nanoscale wire. *Physical Review B* 79, 224409 (2009)

[29] Thomson, W.: XIX. On the electro-dynamic qualities of metals:—Effects of magnetization on the electric conductivity of nickel and of iron. *Proceedings of the Royal Society of London* 8, 546–550 (1997)

[30] Smit, J.: Magnetoresistance of ferromagnetic metals and alloys at low temperatures. *Physica* 17, 612–627 (1951)

[31] McGuire, T. and Potter, R.: Anisotropic magnetoresistance in ferromagnetic 3d alloys. *IEEE Transactions on Magnetics* 11, 1018–1038 (1975)

[32] Stobiecki, T., Kossacki, P., and Szymczak, H.: Sign reversal of the Hall coefficient in amorphous Co-Zr thin films. *Journal of Magnetism and Magnetic Materials* 101, 211–212 (1991)

[33] Nagaosa, N., Sinova, J., Onoda, S., MacDonald, A. H., and Ong, N. P.: Anomalous Hall effect. *Reviews of Modern Physics* 82, 1539–1592 (2010)

[34] Karplus, R. and Luttinger, J. M.: Hall Effect in Ferromagnetics. *Physical Review* 95, 1154–1160 (1954)

[35] Jungwirth, T., Niu, Q., and MacDonald, A. H.: Anomalous Hall Effect in Ferromagnetic Semiconductors. *Physical Review Letters* 88, 207208 (2002)

[36] Onoda, M. and Nagaosa, N.: Topological Nature of Anomalous Hall Effect in Ferromagnets. *Journal of the Physical Society of Japan* 71, 19–22 (2002)

[37] Berger, L.: Side-Jump Mechanism for the Hall Effect of Ferromagnets. *Physical Review B* 2, 4559–4566 (1970)

[38] Nakayama, H., Althammer, M., Chen, Y.-T., Uchida, K., Kajiwara, Y., Kikuchi, D., Ohtani, T., Geprägs, S., Opel, M., Takahashi, S., Gross, R., Bauer, G. E. W., Goennenwein, S. T. B., and Saitoh, E.: Spin Hall Magnetoresistance Induced by a Nonequilibrium Proximity Effect. *Physical Review Letters* 110, 206601 (2013)

[39] Althammer, M., Meyer, S., Nakayama, H., Schreier, M., Altmannshofer, S., Weiler, M., Huebl, H., Geprägs, S., Opel, M., Gross, R., Meier, D., Klewe, C., Kuschel, T., Schmalhorst, J.-M., Reiss, G., Shen, L., Gupta, A., Chen, Y.-T., Bauer, G. E. W., Saitoh, E., and Goennenwein, S. T. B.: Quantitative study of the spin Hall magnetoresistance in ferromagnetic insulator/normal metal hybrids. *Physical Review B* 87, 224401 (2013)

[40] Chen, Y.-T., Takahashi, S., Nakayama, H., Althammer, M., Goennenwein, S. T. B., Saitoh, E., and Bauer, G. E. W.: Theory of spin Hall magnetoresistance (SMR) and related phenomena. *Journal of Physics: Condensed Matter* 28, 103004 (2016)

[41] Saitoh, E., Ueda, M., Miyajima, H., and Tatara, G.: Conversion of spin current into charge current at room temperature: Inverse spin-Hall effect. *Applied Physics Letters* 88, 182509 (2006)

[42] Kim, J., Sheng, P., Takahashi, S., Mitani, S., and Hayashi, M.: Spin Hall Magnetoresistance in Metallic Bilayers. *Physical Review Letters* 116, 097201 (2016)

[43] Dicke, R. H. and Wittke, J. P.: *Introduction to Quantum Mechanics*. Addison-Wesley Publishing Company (1960). ISBN 978-0-201-01510-2

[44] Bohr, N.: I. On the constitution of atoms and molecules. *The London, Edinburgh, and Dublin Philosophical Magazine and Journal of Science* 26, 1–25 (1913)

[45] Coey, J.: *Magnetism and magnetic materials*. Cambridge. University Press (2010)

[46] Darby, M. and Isaac, E.: Magnetocrystalline anisotropy of ferro- and ferrimagnetics. *IEEE Transactions on Magnetics* 10, 259–304 (1974)

[47] Ricodeau, J. A.: Magnetocrystalline Anisotropy and Spin-Orbit Coupling in Nonspherical Crystal Potentials. *Physical Review B* 7, 4950–4958 (1973)

[48] Hashimoto, S., Ochiai, Y., and Aso, K.: Perpendicular magnetic anisotropy and magnetostriction of sputtered Co/Pd and Co/Pt multilayered films. *Journal of Applied Physics* 66, 4909–4916 (1989)

[49] Slonczewski, J. C.: Anisotropy and Magnetostriction in Magnetic Oxides. *Journal of Applied Physics* 32, S253–S263 (1961)

[50] Goodenough, J. B.: Spin-Orbit-Coupling Effects in Transition-Metal Compounds. *Physical Review* 171, 466–479 (1968)

[51] Ashworth, H., Sengupta, D., Schnakenberg, G., Shapiro, L., and Berger, L.: Galvanomagnetic Effects, Magnetostriction, and Spin-Orbit Interaction in Cu-Ni-Fe and Other Ferromagnetic Nickel Alloys. *Physical Review* 185, 792–797 (1969)

[52] Song, J. H., Park, J.-H., Kim, J.-Y., Park, B.-G., Jeong, Y. H., Noh, H.-J., Oh, S.-J., Lin, H.-J., and Chen, C. T.: Spin-orbit-lattice coupling and magnetostriction of strained $La_{0.7}Ca_{0.3}Mn0_3$ films. *Physical Review B* 72, 060405 (2005)

[53] Zhang, W., Jungfleisch, M. B., Jiang, W., Pearson, J. E., and Hoffmann, A.: Spin pumping and inverse Rashba-Edelstein effect in NiFe/Ag/Bi and NiFe/Ag/Sb. *Journal of Applied Physics* 117, 17C727 (2015)

[54] Ghiasi, T. S., Kaverzin, A. A., Blah, P. J., and van Wees, B. J.: Charge-to-Spin Conversion by the Rashba–Edelstein Effect in Two-Dimensional van der Waals Heterostructures up to Room Temperature. *Nano Letters* 19, 5959–5966 (2019)

[55] Gambardella, P. and Miron, I. M.: Current-induced spin–orbit torques. *Philosophical Transactions of the Royal Society A: Mathematical, Physical and Engineering Sciences* 369, 3175–3197 (2011)

[56] Schliemann, J. and Loss, D.: Anisotropic transport in a two-dimensional electron gas in the presence of spin-orbit coupling. *Physical Review B* 68, 165311 (2003)

[57] Rojas-Sánchez, J.-C., Oyarzún, S., Fu, Y., Marty, A., Vergnaud, C., Gambarelli, S., Vila, L., Jamet, M., Ohtsubo, Y., Taleb-Ibrahimi, A., Le Fèvre, P., Bertran, F., Reyren, N., George, J.-M., and Fert, A.: Spin to Charge Conversion at Room Temperature by Spin Pumping into a New Type of Topological Insulator. *Physical Review Letters* 116, 096602 (2016)

[58] Edelstein, V. M.: Spin polarization of conduction electrons induced by electric current in two-dimensional asymmetric electron systems. *Solid State Communications* 73, 233–235 (1990)

[59] Murakami, S., Nagaosa, N., and Zhang, S.-C.: Dissipationless Quantum Spin Current at Room Temperature. *Science* 301, 1348–1351 (2003)

[60] Kimura, T., Otani, Y., Sato, T., Takahashi, S., and Maekawa, S.: Room-Temperature Reversible Spin Hall Effect. *Physical Review Letters* 98, 156601 (2007)

[61] Hirsch, J. E.: Spin Hall Effect. *Physical Review Letters* 83, 1834–1837 (1999)

[62] Dyrdał, A.: Rozprawa doktorska: Spinowy efekt Halla. Wydział Fizyki, Uniwersytet im. Adama Mickiewicza w Poznaniu, 2013

[63] Dyrdał, A. and Barnaś, J.: Spin Hall effect in graphene due to random Rashba field. *Physical Review B* 86, 161401 (2012)

[64] Dyakonov, M. I. and Perel, V. I.: Current-induced spin orientation of electrons in semiconductors. *Physics Letters A* 35, 459–460 (1971)

[65] Berry, M. V.: Quantal phase factors accompanying adiabatic changes. *Proceedings of the Royal Society of London A Mathematical and Physical Sciences* 392, 45–57 (1997)

[66] Sinova, J., Valenzuela, S. O., Wunderlich, J., Back, C., and Jungwirth, T.: Spin Hall effects. *Reviews of Modern Physics* 87, 1213–1260 (2015)

[67] Tanaka, T., Kontani, H., Naito, M., Naito, T., Hirashima, D. S., Yamada, K., and Inoue, J.: Intrinsic spin Hall effect and orbital Hall effect in 4d and 5d transition metals. *Physical Review B* 77, 165117 (2008)

[68] Liu, L., Moriyama, T., Ralph, D. C., and Buhrman, R. A.: Spin-Torque Ferromagnetic Resonance Induced by the Spin Hall Effect. *Physical Review Letters* 106, 036601 (2011)

[69] Fache, T., Rojas-Sanchez, J. C., Badie, L., Mangin, S., and Petit-Watelot, S.: Determination of spin Hall angle, spin mixing conductance, and spin diffusion length in CoFeB/Ir for spin-orbitronic devices. *Physical Review B* 102, 064425 (2020)

[70] Wang, X., Pauyac, C. O., and Manchon, A.: Spin-orbit-coupled transport and spin torque in a ferromagnetic heterostructure. *Physical Review B* 89, 054405 (2014)

[71] Liu, L., Pai, C.-F., Li, Y., Tseng, H. W., Ralph, D. C., and Buhrman, R. A.: Spin-Torque Switching with the Giant Spin Hall Effect of Tantalum. *Science* 336, 555–558 (2012)

[72] Pai, C.-F., Liu, L., Li, Y., Tseng, H. W., Ralph, D. C., and Buhrman, R. A.: Spin transfer torque devices utilizing the giant spin Hall effect of tungsten. *Applied Physics Letters* 101, 122404 (2012)

[73] Landau, L. and Lifshitz, E.: On the Theory of the Dispersion of Magnetic Permeability in Ferromagnetic Bodies. *Phys Z Sowjetunion* 8, 153–164 (1935)

[74] Gilbert, T.: A phenomenological theory of damping in ferromagnetic materials. *IEEE Transactions on Magnetics* 40, 3443–3449 (2004)

[75] Slonczewski, J. C.: Current-driven excitation of magnetic multilayers. *Journal of Magnetism and Magnetic Materials* 159, L1–L7 (1996)

[76] Yuasa, S., Nagahama, T., Fukushima, A., Suzuki, Y., and Ando, K.: Giant room-temperature magnetoresistance in single-crystal Fe/MgO/Fe magnetic tunnel junctions. *Nature Materials* 3, 868–871 (2004)

[77] Ando, K., Takahashi, S., Harii, K., Sasage, K., Ieda, J., Maekawa, S., and Saitoh, E.: Electric Manipulation of Spin Relaxation Using the Spin Hall Effect. *Physical Review Letters* 101, 036601 (2008)

[78] Miron, I. M., Moore, T., Szambolics, H., Buda-Prejbeanu, L. D., Auffret, S., Rodmacq, B., Pizzini, S., Vogel, J., Bonfim, M., Schuhl, A., and Gaudin, G.: Fast current-induced domain-wall motion controlled by the Rashba effect. *Nature Materials* 10, 419–423 (2011)

[79] Lee, J., Park, J., Yuk, J., and Park, B.-G.: Spin-Orbit Torque in a Perpendicularly Magnetized Ferrimagnetic Tb - Co Single Layer. *Physical Review Applied* 13 (2020)

[80] Wang, W., Wang, T., Amin, V. P., Wang, Y., Radhakrishnan, A., Davidson, A., Allen, S. R., Silva, T. J., Ohldag, H., Balzar, D., Zink, B. L., Haney, P. M., Xiao, J. Q., Cahill, D. G., Lorenz, V. O., and Fan, X.: Anomalous spin–orbit torques in magnetic single-layer films. *Nature Nanotechnology* 14, 819–824 (2019)

[81] Manchon, A., Železný, J., Miron, I., Jungwirth, T., Sinova, J., Thiaville, A., Garello, K., and Gambardella, P.: Current-induced spin-orbit torques in ferromagnetic and antiferromagnetic systems. *Reviews of Modern Physics* 91, 035004 (2019)

[82] Ralph, D. C. and Stiles, M. D.: Spin transfer torques. *Journal of Magnetism and Magnetic Materials* 320, 1190–1216 (2008)

[83] Brataas, A., Bauer, G. E. W., and Kelly, P. J.: Non-collinear magnetoelectronics. *Physics Reports* 427, 157–255 (2006)

[84] Baumgartner, M., Garello, K., Mendil, J., Avci, C. O., Grimaldi, E., Murer, C., Feng, J., Gabureac, M., Stamm, C., Acremann, Y., Finizio, S., Wintz, S., Raabe, J., and Gambardella, P.: Spatially and time-resolved magnetization dynamics driven by spin–orbit torques. *Nature Nanotechnology* 12, 980–986 (2017)

[85] Rojas-Sánchez, J.-C., Reyren, N., Laczkowski, P., Savero, W., Attané, J.-P., Deranlot, C., Jamet, M., George, J.-M., Vila, L., and Jaffrès, H.: Spin Pumping and Inverse Spin Hall Effect in Platinum: The Essential Role of Spin-Memory Loss at Metallic Interfaces. *Physical Review Letters* 112, 106602 (2014)

[86] Bose, A., Singh, H., Kushwaha, V. K., Bhuktare, S., Dutta, S., and Tulapurkar, A. A.: Sign Reversal of Fieldlike Spin-Orbit Torque in an Ultrathin Cr/Ni Bilayer. *Physical Review Applied* 9, 014022 (2018)

[87] Gao, T., Qaiumzadeh, A., An, H., Musha, A., Kageyama, Y., Shi, J., and Ando, K.: Intrinsic Spin-Orbit Torque Arising from the Berry Curvature in a Metallic-Magnet/Cu-Oxide Interface. *Physical Review Letters* 121, 017202 (2018)

[88] Li, H., Gao, H., Zârbo, L. P., Výborný, K., Wang, X., Garate, I., Doğan, F., Čejchan, A., Sinova, J., Jungwirth, T., and Manchon, A.: Intraband and interband spin-orbit torques in noncentrosymmetric ferromagnets. *Physical Review B* 91, 134402 (2015)

[89] Saidaoui, H. B. M. and Manchon, A.: Spin-Swapping Transport and Torques in Ultrathin Magnetic Bilayers. *Physical Review Letters* 117, 036601 (2016)

[90] Onur Avci, C., Garello, K., Mihai Miron, I., Gaudin, G., Auffret, S., Boulle, O., and Gambardella, P.: Magnetization switching of an MgO/Co/Pt layer by in-plane current injection. *Applied Physics Letters* 100, 212404 (2012)

[91] Wadley, P., Howells, B., Železný, J., Andrews, C., Hills, V., Campion, R. P., Novák, V., Olejník, K., Maccherozzi, F., Dhesi, S. S., Martin, S. Y., Wagner, T., Wunderlich, J., Freimuth, F., Mokrousov, Y., Kuneš, J., Chauhan, J. S., Grzybowski, M. J., Rushforth, A. W., Edmonds, K. W., Gallagher, B. L., and Jungwirth, T.: Electrical switching of an antiferromagnet. *Science* 351, 587–590 (2016)

[92] Li, P., Liu, T., Chang, H., Kalitsov, A., Zhang, W., Csaba, G., Li, W., Richardson, D., DeMann, A., Rimal, G., Dey, H., Jiang, J. S., Porod, W., Field, S. B., Tang, J., Marconi, M. C., Hoffmann, A., Mryasov, O., and Wu, M.: Spin–orbit torque-assisted switching in magnetic insulator thin films with perpendicular magnetic anisotropy. *Nature Communications* 7, 12688 (2016)

[93] Lee, K.-S., Lee, S.-W., Min, B.-C., and Lee, K.-J.: Threshold current for switching of a perpendicular magnetic layer induced by spin Hall effect. *Applied Physics Letters* 102, 112410 (2013)

[94] Yu, J., Qiu, X., Wu, Y., Yoon, J., Deorani, P., Besbas, J. M., Manchon, A., and Yang, H.: Spin orbit torques and Dzyaloshinskii-Moriya interaction in dual-interfaced Co-Ni multilayers. *Scientific Reports* 6, 32629 (2016)

[95] Lee, J. M., Cai, K., Yang, G., Liu, Y., Ramaswamy, R., He, P., and Yang, H.: Field-Free Spin–Orbit Torque Switching from Geometrical Domain-Wall Pinning. *Nano Letters* 18, 4669–4674 (2018)

[96] Binek, C., Hochstrat, A., and Kleemann, W.: Exchange bias in a generalized Meiklejohn–Bean approach. *Journal of Magnetism and Magnetic Materials* 234, 353–358 (2001)

[97] Yu, G., Upadhyaya, P., Wong, K. L., Jiang, W., Alzate, J. G., Tang, J., Amiri, P. K., and Wang, K. L.: Magnetization switching through spin-Hall-effect-induced chiral domain wall propagation. *Physical Review B* 89, 104421 (2014)

[98] Torrejon, J., Garcia-Sanchez, F., Taniguchi, T., Sinha, J., Mitani, S., Kim, J.-V., and Hayashi, M.: Current-driven asymmetric magnetization switching in perpendicularly magnetized CoFeB/MgO heterostructures. *Physical Review B* 91, 214434 (2015)

[99] You, L., Lee, O., Bhowmik, D., Labanowski, D., Hong, J., Bokor, J., and Salahuddin, S.: Switching of perpendicularly polarized nanomagnets with spin orbit torque without an external magnetic field by engineering a tilted anisotropy. *Proceedings of the National Academy of Sciences* 112, 10310–10315 (2015)

[100] van den Brink, A., Vermijs, G., Solignac, A., Koo, J., Kohlhepp, J. T., Swagten, H. J. M., and Koopmans, B.: Field-free magnetization reversal by spin-Hall effect and exchange bias. *Nature Communications* 7, 10854 (2016)

[101] Fukami, S., Zhang, C., DuttaGupta, S., Kurenkov, A., and Ohno, H.: Magnetization switching by spin–orbit torque in an antiferromagnet–ferromagnet bilayer system. *Nature Materials* 15, 535–541 (2016)

[102] Kurenkov, A., Zhang, C., DuttaGupta, S., Fukami, S., and Ohno, H.: Device-size dependence of field-free spin-orbit torque induced magnetization switching in antiferromagnet/ferromagnet structures. *Applied Physics Letters* 110, 092410 (2017)

[103] Huang, J., Wang, H., Wang, X., Gao, X., Liu, J., and Wang, H.: Exchange Bias in a La0.67Sr0.33MnO3/NiO Heterointerface Integrated on a Flexible Mica Substrate. *ACS Applied Materials & Interfaces* 12, 39920–39925 (2020)

[104] Meiklejohn, W. H. and Bean, C. P.: New Magnetic Anisotropy. *Physical Review* 105, 904–913 (1957)

[105] Nogués, J. and Schuller, I. K.: Exchange bias. *Journal of Magnetism and Magnetic Materials* 192, 203–232 (1999)

[106] Kuświk, P., Gaul, A., Urbaniak, M., Schmidt, M., Aleksiejew, J., Ehresmann, A., and Stobiecki, F.: Tailoring Perpendicular Exchange Bias Coupling in Au/Co/NiO Systems by Ion Bombardment. *Nanomaterials* 8, 813 (2018)

[107] Tian, F., Li, Y., Zhao, Q., Cao, K., Wang, D., Dai, Z., Yu, Z., Ke, X., Zhang, Y., Zhou, C., Zuo, W., Yang, S., and Song, X.: Giant exchange bias induced via tuning interfacial spins in polycrystalline Fe3O4/CoO bilayers. *Physical Chemistry Chemical Physics* 23, 4805–4810 (2021)

[108] Liu, K., Ma, S. C., Zhang, Z. S., Zhao, X. W., Yang, B., Wang, D. H., Ur Rehman, S., and Zhong, Z. C.: Giant exchange bias effect in all-3d-metal Ni38.8Co2.9Mn37.9Ti20.4 thin film. *Applied Physics Letters* 116, 022412 (2020)

[109] Peng, S., Zhu, D., Li, W., Wu, H., Grutter, A. J., Gilbert, D. A., Lu, J., Xiong, D., Cai, W., Shafer, P., Wang, K. L., and Zhao, W.: Exchange bias switching in an antiferromagnet/ferromagnet bilayer driven by spin–orbit torque. *Nature Electronics* 3, 757–764 (2020)

[110] Huckfeldt, H., Gaul, A., Müglich, N. D., Holzinger, D., Nissen, D., Albrecht, M., Emmrich, D., Beyer, A., Gölzhäuser, A., and Ehresmann, A.: Modification of the saturation magnetization of exchange bias thin film systems upon light-ion bombardment. *Journal of Physics: Condensed Matter* 29, 125801 (2017)

[111] Yuan, W., Su, T., Song, Q., Xing, W., Chen, Y., Wang, T., Zhang, Z., Ma, X., Gao, P., Shi, J., and Han, W.: Crystal Structure Manipulation of the Exchange Bias in an Antiferromagnetic Film. *Scientific Reports* 6, 28397 (2016)

[112] Liu, Y., Sun, K., Yang, Y., Yu, Z., Zeng, Y., Chai, Z., Jiang, X., and Lan, Z.: Exchange Bias Effect and Ferromagnetic Resonance Study of NiO/NiFe/NiO Trilayers with Different Thicknesses of NiO Layers. *Journal of Superconductivity and Novel Magnetism* 30, 593–596 (2017)

[113] Meiklejohn, W. H. and Bean, C. P.: New Magnetic Anisotropy. *Physical Review* 102, 1413–1414 (1956)

[114] Stoner, E. C. and Wohlfarth, E. P.: Interpretation of High Coercivity in Ferromagnetic Materials. *Nature* 160, 650–651 (1947)

[115] Takano, K., Kodama, R. H., Berkowitz, A. E., Cao, W., and Thomas, G.: Interfacial Uncompensated Antiferromagnetic Spins: Role in Unidirectional Anisotropy in Polycrystalline $Ni_{81}Fe_{19}/CoO$ Bilayers. *Physical Review Letters* 79, 1130–1133 (1997)

[116] Nowak, U., Misra, A., and Usadel, K. D.: Domain state model for exchange bias. *Journal of Applied Physics* 89, 7269–7271 (2001)

[117] Olsen, F. K., Hallsteinsen, I., Arenholz, E., Tybell, T., and Folven, E.: Coexisting spin-flop coupling and exchange bias in $LaFeO_3/La_{0.7}Sr_{0.3}MnO_3$ heterostructures. *Physical Review B* 99, 134411 (2019)

[118] Maniv, E., Murphy, R. A., Haley, S. C., Doyle, S., John, C., Maniv, A., Ramakrishna, S. K., Tang, Y.-L., Ercius, P., Ramesh, R., Reyes, A. P., Long, J. R., and Analytis, J. G.: Exchange bias due to coupling between coexisting antiferromagnetic and spin-glass orders. *Nature Physics* 17, 525–530 (2021)

[119] Razavi, S. A., Wu, D., Yu, G., Lau, Y.-C., Wong, K. L., Zhu, W., He, C., Zhang, Z., Coey, J. M. D., Stamenov, P., Khalili Amiri, P., and Wang, K. L.: Joule Heating Effect on Field-Free Magnetization Switching by Spin-Orbit Torque in Exchange-Biased Systems. *Physical Review Applied* 7, 024023 (2017)

[120] Zakład Cienkich Warstw, IFM Poznań. `https://www.ifmpan.poznan.pl/pl/jednostki-naukowe/zaklad-cienkich-warstw.html`. [Online; accessed 23-January-2023]

[121] Zakład Cienkich Warstw, IFM Poznań: "Wyposażenie - prezentacja". `https://www.ifmpan.poznan.pl/pl/jednostki-naukowe/zaklad-cienkich-warstw/zaklad-cienkich-warstw-wyposazenie.html`. [Online; accessed 23-January-2023]

[122] Swann, S.: Magnetron sputtering. *Physics in Technology* 19, 67–75 (1988)

[123] Chrisey, D. B. and Hubler, G. K.: *Pulsed laser deposition of thin films*. John Wiley and Sons, New York (1994). ISBN 9780471592181

[124] Kuświk, P., Matczak, M., Kowacz, M., Szuba-Jabłoński, K., Michalak, N., Szymański, B., Ehresmann, A., and Stobiecki, F.: Asymmetric domain wall propagation caused by interfacial Dzyaloshinskii-Moriya interaction in exchange biased Au/Co/NiO layered system. *Physical Review B* 97, 024404 (2018)

[125] Kuświk, P., Matczak, M., Kowacz, M., Lisiecki, F., and Stobiecki, F.: Determination of the Dzyaloshinskii-Moriya interaction in exchange biased Au/Co/NiO systems. *Journal of Magnetism and Magnetic Materials* 472, 29–33 (2019)

[126] Kuświk, P., Szymański, B., Anastaziak, B., Matczak, M., Urbaniak, M., Ehresmann, A., and Stobiecki, F.: Enhancement of perpendicular magnetic anisotropy of Co layer in exchange-biased Au/Co/NiO/Au polycrystalline system. *Journal of Applied Physics* 119, 215307 (2016)

[127] Urbaniak, M., Matczak, M., Chaves-O'Flynn, G., Reginka, M., Ehresmann, A., and Kuświk, P.: Domain wall motion induced magnetophoresis in unpatterned perpendicular magnetic anisotropy Co layers with Dzyaloshinskii-Moriya interactions. *Journal of Magnetism and Magnetic Materials* 519, 167454 (2021)

[128] Kowacz, M., Mazalski, P., Sveklo, I., Matczak, M., Anastaziak, B., Guzowska, U., Dhiman, A. K., Madej, E., Maziewski, A., Kuświk, P., and Gieniusz, R.: Strong interfacial Dzyaloshinskii–Moriya induced in Co due to contact with NiO. *Scientific Reports* 12, 12741 (2022)

[129] Bhattacharya, D., Razavi, S. A., Wu, H., Dai, B., Wang, K. L., and Atulasimha, J.: Creation and annihilation of non-volatile fixed magnetic skyrmions using voltage control of magnetic anisotropy. *Nature Electronics* 3, 539–545 (2020)

[130] Stöhr, J.: X-ray magnetic circular dichroism spectroscopy of transition metal thin films. *Journal of Electron Spectroscopy and Related Phenomena* 75, 253–272 (1995)

[131] Thole, B. T., van der Laan, G., and Sawatzky, G. A.: Strong Magnetic Dichroism Predicted in the $M_{4,5}$ X-Ray Absorption Spectra of Magnetic Rare-Earth Materials. *Physical Review Letters* 55, 2086–2088 (1985)

[132] Dhesi, S. S., van der Laan, G., and Dudzik, E.: Determining element-specific magnetocrystalline anisotropies using x-ray magnetic linear dichroism. *Applied Physics Letters* 80, 1613–1615 (2002)

[133] van der Laan, G.: Magnetic Linear X-Ray Dichroism as a Probe of the Magnetocrystalline Anisotropy. *Physical Review Letters* 82, 640–643 (1999)

[134] Solaris National Synchrotron Radiation Centre: PIRX. `https://synchrotron.uj.edu.pl/en_GB/linie-badawcze/pirx`. [Online; accessed 23-January-2023]

[135] Kozioł-Rachwał, A., Ślęzak, M., Zając, M., Dróżdż, P., Janus, W., Szpytma, M., Nayyef, H., and Ślęzak, T.: Control of spin orientation in antiferromagnetic NiO by epitaxial strain and spin–flop coupling. *APL Materials* 8, 061107 (2020)

[136] Holy´, V., Kuběna, J., Ohli´dal, I., Lischka, K., and Plotz, W.: X-ray reflection from rough layered systems. *Physical Review B* 47, 15896–15903 (1993)

[137] Parratt, L. G.: Surface Studies of Solids by Total Reflection of X-Rays. *Physical Review* 95, 359–369 (1954)

[138] Akademickie Centrum Materiałów i Nanotechnologii: Laboratorium Ablacji Laserowej i Nanolitografii. `http://bitly.pl/mVCq1`. [Online; accessed 23-January-2023]

[139] Allresist: Photoresist AR-N 4340. `https://www.allresist.com/wp-content/uploads/sites/2/2016/12/allresist_produktinfos_ar-n4300_englisch.pdf`. [Online; accessed 23-January-2023]

[140] See: KLayout. `https://www.klayout.de/`. [Online; accessed 23-January-2023]

[141] Allresist: Developer AR 300-475. `https://www.allresist.com/wp-content/uploads/sites/2/2020/03/AR300-40_english_Allresist_product_information.pdf`. [Online; accessed 23-January-2023]

[142] Allresist: Photoresist AR-P 3740. `https://www.allresist.com/wp-content/uploads/sites/2/2020/03/AR-P3700_3800_english_Allresist_product_information.pdf`. [Online; accessed 23-January-2023]

[143] Allresist: Developer AR 300-47. `https://www.allresist.com/portfolio-item/developer-ar-300-47/`. [Online; accessed 23-January-2023]

[144] Hayashi, M., Kim, J., Yamanouchi, M., and Ohno, H.: Quantitative characterization of the spin-orbit torque using harmonic Hall voltage measurements. *Phys Rev B* 89, 144425 (2014)

[145] Magni, A., Basso, V., Sola, A., Soares, G., Meggiato, N., Kuepferling, M., Skowroński, W., Łazarski, S., Grochot, K., Khanjani, M. V., Langer, J., and Ocker, B.: Spin Hall Magnetoresistance and Spin–Orbit Torque Efficiency in Pt/FeCoB Bilayers. *IEEE Transactions on Magnetics* 58, 1–5 (2022)

[146] Ziętek, S., Mojsiejuk, J., Grochot, K., Łazarski, S., Skowroński, W., and Stobiecki, T.: Numerical model of harmonic Hall voltage detection for spintronic devices. *Physical Review B* 106, 024403 (2022)

[147] Skowroński, W., Grochot, K., Rzeszut, P., Łazarski, S., Gajoch, G., Worek, C., Kanak, J., Stobiecki, T., Langer, J., Ocker, B., and Vafaee, M.: Angular Harmonic Hall Voltage and Magnetoresistance Measurements of Pt/FeCoB and Pt-Ti/FeCoB Bilayers for Spin Hall Conductivity Determination. *IEEE Transactions on Electron Devices* 68, 6379–6385 (2021)

[148] Skowroński, W., Karwacki, L., Ziętek, S., Kanak, J., Łazarski, S., Grochot, K., Stobiecki, T., Kuświk, P., Stobiecki, F., and Barnaś, J.: Determination of Spin Hall Angle in Heavy-Metal/CoFeB-Based Heterostructures with Interfacial Spin-Orbit Fields. *Physical Review Applied* 11, 024039 (2019)

[149] Łazarski, S., Skowroński, W., Kanak, J., Karwacki, L., Ziętek, S., Grochot, K., Stobiecki, T., and Stobiecki, F.: Field-Free Spin-Orbit-Torque Switching in Co/Pt/Co Multilayer with Mixed Magnetic Anisotropies. *Physical Review Applied* 12, 014006 (2019)

[150] Łazarski, S., Skowroński, W., Grochot, K., Powroźnik, W., Kanak, J., Schmidt, M., and Stobiecki, T.: Spin-orbit torque induced magnetization dynamics and switching in a CoFeB/Ta/CoFeB system with mixed magnetic anisotropy. *Physical Review B* 103, 134421 (2021)

[151] Avci, C. O., Garello, K., Gabureac, M., Ghosh, A., Fuhrer, A., Alvarado, S. F., and Gambardella, P.: Interplay of spin-orbit torque and thermoelectric effects in ferromagnet/normal-metal bilayers. *Physical Review B* 90, 224427 (2014)

[152] Zhu, L., Ralph, D., and Buhrman, R.: Spin-Orbit Torques in Heavy-Metal–Ferromagnet Bilayers with Varying Strengths of Interfacial Spin-Orbit Coupling. *Physical Review Letters* 122, 077201 (2019)

[153] Kabanov, Y. P., Iunin, Y. L., Nikitenko, V. I., Shapiro, A. J., Shull, R. D., Zhu, L. Y., and Chien, C. L.: In-Plane Field Effects on the Dynamics of Domain Walls in Ultrathin Co Films With Perpendicular Anisotropy. *IEEE Transactions on Magnetics* 46, 2220–2223 (2010)

[154] Hrabec, A., Porter, N. A., Wells, A., Benitez, M. J., Burnell, G., McVitie, S., McGrouther, D., Moore, T. A., and Marrows, C. H.: Measuring and tailoring the Dzyaloshinskii-Moriya interaction in perpendicularly magnetized thin films. *Physical Review B* 90, 020402 (2014)

[155] Cho, J., Kim, N.-H., Lee, S., Kim, J.-S., Lavrijsen, R., Solignac, A., Yin, Y., Han, D.-S., van Hoof, N. J. J., Swagten, H. J. M., Koopmans, B., and You, C.-Y.: Thickness dependence of the interfacial Dzyaloshinskii–Moriya interaction in inversion symmetry broken systems. *Nature Communications* 6, 7635 (2015)

[156] Emori, S., Bauer, U., Ahn, S.-M., Martinez, E., and Beach, G. S. D.: Current-driven dynamics of chiral ferromagnetic domain walls. *Nature Materials* 12, 611–616 (2013)

[157] Ryu, K.-S., Thomas, L., Yang, S.-H., and Parkin, S.: Chiral spin torque at magnetic domain walls. *Nature Nanotechnology* 8, 527–533 (2013)

[158] Kuepferling, M., Casiraghi, A., Soares, G., Durin, G., Garcia-Sanchez, F., Chen, H., Tacchi, S., and Carlotti, G.: Measuring interfacial Dzyaloshinskii-Moriya interaction in ultrathin magnetic films. *Reviews of Modern Physics* 95, 015003 (2023)

[159] Pai, C.-F., Mann, M., Tan, A. J., and Beach, G. S. D.: Determination of spin torque efficiencies in heterostructures with perpendicular magnetic anisotropy. *Physical Review B* 93, 144409 (2016)

[160] Kim, W.-Y., Gweon, H. K., Lee, K.-J., and You, C.-Y.: Correlation between interfacial Dzyaloshinskii–Moriya interaction and interfacial magnetic anisotropy of Pt/Co/MgO structures. *Applied Physics Express* 12, 053007 (2019)

[161] Martinez, E.: The stochastic nature of the domain wall motion along high perpendicular anisotropy strips with surface roughness. *Journal of Physics: Condensed Matter* 24, 024206 (2011)

[162] Vansteenkiste, A., Leliaert, J., Dvornik, M., Helsen, M., Garcia-Sanchez, F., and Van Waeyenberge, B.: The design and verification of MuMax3. *AIP Advances* 4, 107133 (2014)

[163] Tulapurkar, A. A., Suzuki, Y., Fukushima, A., Kubota, H., Maehara, H., Tsunekawa, K., Djayaprawira, D. D., Watanabe, N., and Yuasa, S.: Spin-torque diode effect in magnetic tunnel junctions. *Nature* 438, 339–342 (2005)

[164] Ziętek, S., Ogrodnik, P., Frankowski, M., Chęciński, J., Wiśniowski, P., Skowroński, W., Wrona, J., Stobiecki, T., Żywczak, A., and Barnaś, J.: Rectification of radio-frequency current in a giant-magnetoresistance spin valve. *Physical Review B* 91, 014430 (2015)

[165] Kittel, C.: On the Theory of Ferromagnetic Resonance Absorption. *Physical Review* 73, 155–161 (1948)

[166] Kawaguchi, M., Towa, D., Lau, Y.-C., Takahashi, S., and Hayashi, M.: Anomalous spin Hall magnetoresistance in Pt/Co bilayers. *Applied Physics Letters* 112, 202405 (2018)

[167] Kozioł-Rachwał, A., Janus, W., Szpytma, M., Dróżdż, P., Ślęzak, M., Matlak, K., Gajewska, M., Ślęzak, T., and Korecki, J.: Interface engineering towards enhanced exchange interaction between Fe and FeO in Fe/MgO/FeO epitaxial heterostructures. *Applied Physics Letters* 115, 141603 (2019)

[168] Cho, S., Baek, S.-h. C., Lee, K.-D., Jo, Y., and Park, B.-G.: Large spin Hall magnetoresistance and its correlation to the spin-orbit torque in W/CoFeB/MgO structures. *Scientific Reports* 5, 14668 (2015)

[169] Zhang, C., Fukami, S., Watanabe, K., Ohkawara, A., DuttaGupta, S., Sato, H., Matsukura, F., and Ohno, H.: Critical role of W deposition condition on spin-orbit torque induced magnetization switching in nanoscale W/CoFeB/MgO. *Applied Physics Letters* 109, 192405 (2016)

[170] Hao, Q. and Xiao, G.: Giant Spin Hall Effect and Switching Induced by Spin-Transfer Torque in a $W/Co_{40}Fe_{40}B_{20}/MgO$ Structure with Perpendicular Magnetic Anisotropy. *Physical Review Applied* 3, 034009 (2015)

[171] Chen, W., Xiao, G., Zhang, Q., and Zhang, X.: Temperature study of the giant spin Hall effect in the bulk limit of beta - W. *Physical Review B* 98, 134411 (2018)

[172] Skowroński, W., Cecot, M., Kanak, J., Ziętek, S., Stobiecki, T., Yao, L., van Dijken, S., Nozaki, T., Yakushiji, K., and Yuasa, S.: Temperature dependence of spin-orbit torques in W/CoFeB bilayers. *Applied Physics Letters* 109, 062407 (2016)

[173] McHugh, O. L. W., Goh, W. F., Gradhand, M., and Stewart, D. A.: Impact of impurities on the spin Hall conductivity in beta-W. *Physical Review Materials* 4, 094404 (2020)